Near-Infrared Polarimetry and Stellar Classification in the Galactic Center

INAUGURAL-DISSERTATION

zur

Erlangung des Doktorgrades

der Mathematisch-Naturwissenschaftlichen Fakultät
der Universität zu Köln

vorgelegt von

Rainer Buchholz

aus Köln

Köln 2011

Berichterstatter: Prof. Dr. Andreas Eckart
Prof. Dr. Jan Jolie

Tag der mündlichen Prüfung: 07. 12. 2011

Abstract

The Galactic center (GC) is the closest galactic nucleus, offering the unique possibility of studying the population of a dense stellar cluster surrounding a Supermassive Black Hole (SMBH), as well as stellar and bow-shock polarization effects in a dusty environment.
The goals of the first part of this work are to develop a new method of separating early and late type stellar components of a dense stellar cluster based on intermediate band filters, applying it to the central parsec of the GC, and conducting a population analysis of this area. Adaptive optics assisted observations obtained at the Very Large Telescope (VLT, run by the European Southern Observatory, ESO) in the Near-Infrared (NIR) H-band (1.6 μm) and 7 intermediate bands covering the NIR K-band (2.18 μm) were used for this. A comparison of the resulting Spectral Energy Distributions (SEDs) with a blackbody of variable extinction then allowed to determine the presence and strength of a CO absorption feature to distinguish between early and late type stars. This new method is suitable for classifying K giants (and later), as well as B2 main sequence (and earlier) stars that are brighter than 15.5 mag in the K band in the central parsec. Compared to previous spectroscopic investigations that were limited to 13-14 mag, this represents a major improvement in the depth of the observations and reduces the needed observation time. Extremely red objects and foreground sources could also be reliably removed from the sample. Comparison to sources of known classification indicates that the method has an accuracy of better than ~87%.
312 stars have been classified as early type candidates out of a sample of 5914 sources. Several results, such as the shape of the K-band Luminosity Function (KLF) and the spatial distribution of both early and late type stars, confirm and extend previous works. The distribution of the early type stars can be fitted with a steep power law ($\beta_{1''} = -1.49 \pm 0.12$), alternatively with a broken power law, $\beta_{1-10''} = -1.08 \pm 0.12$, $\beta_{10-20''} = -3.46 \pm 0.58$, since a drop in the early type density seems to occur at ~10". In addition, early type candidates outside of 0.5 pc have been detected in significant numbers for the first time. The late type density function shows an inversion in the inner 6", with a power-law slope of $\beta_{R<6''} = 0.17 \pm 0.09$. The late type KLF has a power-law slope of 0.30±0.01, closely resembling the KLF obtained for the bulge of the Milky Way. The early type KLF has a much flatter slope of (0.14 ± 0.02). These results seem to agree best with an in-situ star formation scenario, although alternatives like the inspiraling cluster scenario cannot be ruled out yet.
The second part of this work aims at providing NIR (H-, Ks-, and Lp-band) polarimetry of the stellar sources in the central parsec at the resolution of an 8m telescope for the first time, along with new insight into the nature of the known bright bow-shock sources.
Using the NAOS-CONICA (NACO) intrument at the ESO VLT in its polarimetric mode and applying both high-precision photometric methods specifically developed for crowded fields along with a newly established polarimetric calibration for NACO, polarization maps covering parts of the central 30"×30" (with different coverage and depth in the three wavelength bands) were produced. In addition, spatially resolved polarimetry and a flux variability analysis on the extended sources in this region were conducted.
It has been confirmed for this larger sample that the foreground polarization mostly follows the orientation of the Galactic plane, with average values of 4.5 - 6.1 % at ~ 26° (in the Ks-band, depending on the Field-of-View, FOV), (9.3 ± 1.3)% at 20° ± 6° (H-band), and (4.5 ± 1.4)% at $20° \pm 5°$ (Lp-band, 3.8 μm). In the east of the FOV, higher polarization degrees and steeper polarization angles have been found: (7.5 ± 1.0)% at $11° \pm 6°$ (Ks-band) and (12.1 ± 2.1)% at $13° \pm 6°$ (H-band). p_H/p_{Ks} peaks at 1.9 ± 0.4, corresponding to a power law index for the wavelength dependency of $\alpha = 2.4 \pm 0.7$. These values also vary over the FOV, with higher values in the center. This may indicate the influence of local effects on the total polarization, possibly dichroic extinction by Northern Arm dust. The relation between the Lp- and Ks-band polarization degrees has an average of 0.7-0.8, consistent with previous measurements on a much smaller number of sources. The polarization efficiency in the H- and Ks-band shows the expected power-law dependency on the local extinction.

Several of the extended sources, namely IRS 1W, IRS 5, IRS 10W, and IRS21 show significant intrinsic polarization in all wavelength bands, as well as spatial polarization patterns that are consistent with emission and/or scattering on aligned grains as a polarization mechanism. The bow-shock structure around IRS 21 could be separated from the central source for the first time in the Ks-band, finding the apex north of the central source and determining a standoff distance of ~400 AU, which matches previous estimates. This source also shows a ~ 50% increase in flux in the NIR over several years. In addition, the Mid-Infrared (MIR) excess sources IRS 5NE, IRS 2L, and IRS 2S have been found to show a significant Lp-band polarization that agrees well with the scenario that these sources are lower luminosity versions of the bright bow-shock sources.

Zusammenfassung

Das Galaktische Zentrum ist der nächst benachbarte galaktische Kern und bietet als solcher die einzigartige Möglichkeit, die stellare Population eines dichten Sternhaufens um ein supermassives schwarzes Loch zu untersuchen. Ebenso kann in dieser Region die Polarisation von Sternen und ausgedehnten Quellen wie sogenannte "bow-shocks" studiert werden.
Das Ziel des ersten Teils dieser Arbeit war es, eine Methode zur Unterscheidung früher und später Sterntypen eines dichten Sternhaufens basiert auf der Verwendung von Schmalbandfiltern zu entwickeln, diese dann im zentralen Parsek des Galaktischen Zentrums anzuwenden und so die stellare Population dieser Region zu analysieren. Dazu wurden am Very Large Telescope (VLT) der Europäischen Südsternwarte (ESO) unter Verwendung Adaptiver Optik im Nahinfraroten aufgenommene Daten verwendet (8 Filter, davon ein H-Band Breitbandfilter (1.6 μm) und 7 das K-Band (2.18 μm) abdeckende Schmalbandfilter). Ein Vergleich der so gewonnenen spektralen Energieverteilungen mit einem Schwarzkörperstrahler mit variabler Extinktion erlaubte es dann, das Vorhandensein und die Stärke der CO-Absorption festzustellen, die wiederum zur Unterscheidung von frühen und späten Sterntypen dienen konnte. Diese neue Methode ist geeignet zur Klassifizierung von Riesen bis hinunter zum Spektraltyp K sowie Hauptreihensternen bis einschliesslich B2. Im zentralen Parsec weisen diese Klassen eine Helligkeit von etwa 15.5 mag im K-band auf, was die untere Grenze dieser Methode darstellt. Dies stellt eine grosse Verbesserung gegenüber früheren spektroskopischen Untersuchungen mit einer Helligkeitsgrenze von 13-14 mag dar, sowohl in der Tiefe wie auch in der benötigten Beobachtungszeit. Extrem gerötete Objekte und Vordergrundsterne konnten ebenso zuverlässig aus der Analyse ausgeschlossen werden. Ein Vergleich mit bereits früher klassifizierten Quellen ergab eine Zuverlässigkeit dieser Klassifizierungsmethode von besser als ~87%
312 von 5914 Sternen wurde ein früher Spektraltyp zugeordnet. Mehrere frühere Resultate, wie die Form der K-Band Helligkeitsfunktion (KLF) und die räumliche Verteilung der frühen und späten Spektraltypen, konnten bestätigt bzw. signifikant erweitert werden. Die Verteilung der Sterne frühen Typs folgt einem steilen Potenzgesetz (mit Exponent $\beta_{1''} = -1.49 \pm 0.12$), oder alternativ einem abschnittsweisen Potenzgesetz mit $\beta_{1-10''} = -1.08 \pm 0.12$, $\beta_{10-20''} = -3.46 \pm 0.58$, da bei etwa 10" ein plötzlicher Abfall in der projizierten stellaren Dichte auftritt. Zusätzlich wurden zum ersten Mal in signifikanter Anzahl Sterne frühen Typs ausserhalb der innersten 0.5 pc detektiert. Die Dichtefunktion der Sterne späten Typs zeigt innerhalb von 6" einen anderen Verlauf als weiter aussen: die projizierte Dichte steigt dort nach aussen hin an anstatt abzufallen, in Form eines Potenzgesetzes mit $\beta_{R<6''} = 0.17 \pm 0.09$. Die KLF der späten Spektraltypen folgt einem Potenzgesetz mit Exponent 0.30±0.01, was der im Bulge der Milchstrasse gemessenen Helligkeitsfunktion entspricht. Die KLF der frühen Typen ist deutlich flacher, mit einem Exponenten von 0.14 ± 0.02. Diese Resultate scheinen am besten zu einer Sternentstehung *in situ* zu passen, d.h. direkt im zentralen Parsec, wobei allerdings alternative Szenarien wie das eines einfallenden jungen Sternhaufens noch nicht ausgeschlossen werden können.
Der zweite Teil dieser Arbeit zielte darauf ab, erstmalig Nahinfrot-Polarimetrie der Sterne im zentralen Parsek mit der Auflösung eines 8m-Teleskops zu liefern, zusammen mit neuen Erkenntnissen über die Natur der bereits bekannten hellen *bow-shock*-Quellen.
Unter Verwendung des polarimetrischen Modus des Instrumentes NACO am ESO VLT und unter Anwendung sowohl von hochpräzisen, speziell für Regionen hoher stellarer Dichte entwickelter photometrischer Methoden als auch einer neu etablierten polarimetrischen Kalibrationsmethode für NACO war es möglich, Polarisationskarten von Teilen der innersten 30"×30" zu erstellen (mit unterschiedlicher Abdeckung dieses Feldes in den verschiedenen Bändern). Zusätzlich wurden räumlich aufgelöste Polarimetrie und eine Variabilitätsanalyse auf den ausgedehnten Quellen in dieser Region durchgeführt.
Für diese gegenüber früheren Untersuchungen deutlich höhere Anzahl an Quellen konnte bestätigt werden, dass die Vordergrundpolarisation grösstenteils der Orientierung der Galaktischen Ebene folgt, mit durschnittlichen Werten von 4.5 - 6.1 % bei $\sim 26°$ (im Ks-Band, abhängig von der betrachteten Region), bzw. (9.3 ± 1.3)% bei $20° \pm 6°$ im H-Band und (4.5 ± 1.4)% bei $20° \pm 5°$

im Lp-Band (3.8 μm). Im Osten der hier untersuchten Region wurden im Mittel höhere Polarisationsgrade und steilere Polarisationswinkel gemessen: (7.5 ± 1.0)% bei 11° ± 6° (Ks-Band) und (12.1 ± 2.1)% bei 13° ± 6° (H-Band). p_H/p_{Ks} ist um 1.9 ± 0.4 verteilt, was einem Exponenten des Potenz-gesetzes der Wellenlängenabhängigkeit der Polarisierung von α = 2.4 ± 0.7 entspricht. Auch diese Werte variieren über das beobachtete Gebiet, mit höheren Werten im Zentrum. Dies kann ein Zeichen sein für den Einfluss lokaler Effekte auf die Gesamtpolarisation, möglicherweise durch Absorption an ausgerichteten Staubkörnern im nördlichen Arm der Minispirale. Das Verhältnis zwischen Lp-Band und Ks-Band Polarisierung nimmt Werte von im Mittel 0.7-0.8 an, ein Wert der konsistent mit früheren Messungen auf einer wesentlich kleineren Anzahl von Sternen ist. Die Polarisierungseffizienz zeigt im H- und Ks-Band die erwartete Abhängigkeit von der lokalen Extinktion in Form eines Potenzgesetzes.
Mehrere der ausgedehnten Quellen, IRS 1W, IRS 5, IRS 10W und IRS21, besitzen eine signifikante intrinsische Polarisierung in allen hier betrachteten Wellenlängenbändern. Räumlich aufgelöste Polarisierungskarten dieser Quellen deuten auf Emission oder Streuung an ausgerichteten Staubkörnern als für die Polarisierung verantwortliche Mechanismen hin. Zum ersten Mal konnte ausserdem im Ks-Band die *bow-shock*-Struktur um IRS 21 von der zentralen Quelle getrennt werden. Der Apex des *bow-shock* wurde so etwa 400 AU nördlich der Zentralquelle festgestellt, was früheren Abschätzungen (basierend auf anderen Wellenlängen) entspricht. Weiterhin zeigt diese Quelle einen Anstieg ihres Flusses im Nahinfraroten um etwa 50% im Laufe mehrerer Jahre. Im Lp-Band wurde ausserdem für die im Mittel-Infraroten sehr hellen Quellen IRS 5NE, IRS 2L und IRS 2S eine signifikante intrinsische Polarisierung gemessen, die sehr gut dazu passen würde, dass es sich bei diesen Quellen um weniger helle Varianten der hellen *bow-shock*-Quellen handelte.

Contents

1 Introduction **13**

2 The Galactic Center **15**
2.1 The Nuclear Stellar Cluster . . . 15
2.1.1 Stellar composition . . . 15
2.1.2 Star Formation in the GC? . . . 16
2.2 Extinction . . . 17
2.3 Polarization . . . 17
2.3.1 Foreground polarization . . . 17
2.3.2 Local polarization . . . 18
2.3.3 Polarization of GC sources . . . 20

3 Data reduction techniques **23**
3.1 Cleaning the Image . . . 23
3.1.1 Standard procedure . . . 23
3.1.2 Pattern removal . . . 23
3.2 Deconvolution . . . 24
3.3 Linear Deconvolution . . . 24
3.4 Lucy-Richardson Deconvolution . . . 25

4 Observations **27**
4.1 General parameters . . . 27
4.2 Intermediate band data . . . 27
4.3 Polarimetric data . . . 27
4.4 Imaging data . . . 30

5 Photometry and calibration **33**
5.1 Intermediate band data . . . 33
5.1.1 Double deconvolution photometry . . . 33
5.1.2 Primary Calibration . . . 33
5.1.3 CO band depth as a classification feature . . . 36
5.1.4 Cutoff determination . . . 39
5.1.5 Local calibration . . . 40
5.1.6 Source classification . . . 41
5.2 Polarimetric datasets . . . 44
5.2.1 Deconvolution-assisted large scale photometry . . . 44
5.2.2 Error estimation . . . 45
5.2.3 Photometry on extended sources . . . 47
5.2.4 LR deconvolution: useful for extended structures? . . . 48
5.2.5 Large scale aperture photometry . . . 51
5.2.6 Polarimetry . . . 54
5.2.7 Calibration of the measured polarization . . . 55
5.2.8 Correcting for foreground polarization . . . 56

6 The stellar population in the central parsec **59**
6.1 Stellar classification . . . 59
6.2 Comparison with spectroscopic results and uncertainty estimation . . . 59
6.3 Structure of the cluster . . . 61
6.4 Evidence for giant depletion in the center . . . 65
6.5 K band luminosity function . . . 67

6.6 Extinction . . . 68
6.7 Early type stars outside of 0.5 pc . . . 70

7 Stellar polarization 71
7.1 Ks-band polarization . . . 71
7.1.1 2009 data-set (P2) . . . 71
7.1.2 2007 data-set, rotated FOV (P4) . . . 71
7.1.3 2011 data-set (P18) . . . 72
7.1.4 Comparing the common sources . . . 74
7.2 H-band polarization (P1) . . . 74
7.3 Lp-band polarization (P16) . . . 76
7.4 Comparison to previous results . . . 77
7.5 Comparison between the wavelength bands . . . 80
7.5.1 H- and Ks-band . . . 80
7.5.2 Ks- and Lp-band . . . 85
7.5.3 Sources found in H-, Ks- and Lp-band . . . 87
7.6 Correlation with extinction . . . 87

8 Bow-shocks and dusty sources in the central parsec 91
8.1 Extremely red objects . . . 91
8.2 Examining the extended sources . . . 91
8.2.1 IRS 1W . . . 91
8.2.2 IRS 21 . . . 98
8.2.3 IRS 10 . . . 103
8.2.4 IRS 5 . . . 105
8.2.5 IRS 2 . . . 106
8.2.6 IRS 5NE . . . 107

9 Summary and Conclusions 109
9.1 Stellar Classification . . . 109
9.2 Polarimetric results . . . 111

List of Figures

2.1 Relation between emission at different NIR wavelengths 19

4.1 Ks-band field-of-view 28
4.2 Lp-band field-of-view 29

5.1 Strehl ratio over one intermediate band image 34
5.2 Primary calibration sources 35
5.3 Conversion of continuous spectra into template SEDs 37
5.4 Typical Ks-band spectra of late type stars 38
5.5 CO band depth of reference sources 39
5.6 Effects of the local calibration 40
5.7 Local calibration maps 41
5.8 CO band depth of the sources in the central parsec 42
5.9 Density of stars with noisy SEDs 43
5.10 PSF polarization pattern 45
5.11 H/Ks-band flux errors (P1/P2) 46
5.12 Wiregrid flat-field Stokes parameters 47
5.13 Stokes parameter Q in flat-field with/without Wollaston prism 48
5.14 Fluxes and polarization parameters of IRS 16C (P2) 49
5.15 Fluxes and polarization parameters of IRS 1C (P2) 50
5.16 H/Ks-band lightcurve of non-variable source IRS 16C 51
5.17 Recovered polarization parameters after LR deconvolution 52
5.18 Ks-band flux errors (P18) 53
5.19 Lp-band flux errors (P16) 54
5.20 Lp-band luminosity function of detected sources 55

6.1 Stellar classification map of the GC 60
6.2 Early and late type stellar densities 61
6.3 Stellar surface density map (all stars with $m_{Ks} < 15$) 62
6.4 Stellar surface density map (late type stars) 63
6.5 Stellar surface density map (early type stars) 64
6.6 Ks-band luminosity function of classified stars 66
6.7 Extinction map from fitted extinction values 67
6.8 Early type SEDs of outlying stars 68

7.1 Ks-band polarization map (P2,P4,P18) 72
7.2 Ks-band polarization parameters (P2) 73
7.3 Ks-band polarization parameters (P4) 74
7.4 Ks-band polarization parameters (P18) 75
7.5 Comparing the polarization of the common sources (P2/P4) 76
7.6 H-band polarization map (P1) 76
7.7 H-band polarization parameters (P1) 77
7.8 Lp-band polarization map (P16) 78
7.9 Lp-band polarization parameters (P16) 79
7.10 Polarization angle vs. polarization degree (P1,P2) 80
7.11 Relation between H/Ks polarization parameters (P1/P2) 80
7.12 Polarization parameters of pK^+ and pK^- sources 81
7.13 Polarization parameters of pK-E and pK-W sources 82
7.14 H/Ks-band polarization parameters averaged along the East-West-axis 83
7.15 Relation between Ks/Lp polarization parameters (P2/P16) 84
7.16 H/Ks/Lp-band polarization degrees 85

7.17 Polarization efficiency (P1,P2) 86
7.18 Polarization efficiency (P4,P18) 87
7.19 Polarization efficiency (all Ks-band sources) 89
7.20 Extinction of pK^+ and pK^- sources 90

8.1 SEDs of Extremely Red Objects 92
8.2 Polarization map of IRS 1W (Ks) 93
8.3 Polarization map of IRS 1W (H) 94
8.4 Polarization map of IRS 1W (Lp) 95
8.5 H/Ks/Lp-band lightcurves of IRS 1W 96
8.6 IRS 21 before and after LR deconvolution (2004-08-30) 97
8.7 IRS 21 before and after LR deconvolution (2005-05-14) 98
8.8 Polarization map of IRS 21 (Ks) 99
8.9 Polarization map of IRS 21 (Lp) 100
8.10 H/Ks/Lp-band lightcurves of IRS 21 101
8.11 Polarization map of IRS 10W (Lp) 102
8.12 H/Ks/Lp-band lightcurves of IRS 10W 103
8.13 H/Ks/Lp-band lightcurves of IRS 10E* 104
8.14 Polarization map of IRS 5 (Lp) 105
8.15 H/Ks/Lp-band lightcurves of IRS 5 106
8.16 IRS 2L and 2S (Lp-band) 107
8.17 IRS 5NE before and after LR deconvolution (Lp) 108

List of Tables

4.1 Observations 30

5.1 Primary calibration stars 35
5.2 Stellar types expected in the central parsec 36
5.3 HB/RC template stars 37

6.1 Classified stars 60
6.2 Density power law parameters 65
6.3 KLF power law parameters 66
6.4 Early type stars detected outside of 0.5 pc 69

7.1 Fitting results for polarization parameters (P1,P2) 81
7.2 Polarization parameters for sources common to Ks/Lp-band 88
7.3 Polarization parameters for sources common to H/Ks/Lp-band 89

8.1 Polarization parameters measured for IRS 21 (Ks-band) 97

Table of Abbreviations

AGB	Asymptotic Giant Branch
AGN	Active Galactic Nucleus
AO	Adaptive Optics
CBD	CO band depth
CND	Circumnuclear Disk
ESO	European Southern Observatory
FOV	Field of View
FWHM	Full Width at Half Maximum
GC	Galactic Center
HB	Horizontal Branch
IB	Intermediate Band
IMBH	Intermediate Mass Black Hole
IMF	Initial Mass Function
IRS	Infrared Source
ISM	Interstellar Medium
KLF	K-band Luminosity Function
LR	Lucy-Richardson (deconvolution)
MIR	Mid-Infrared
NA	Northern Arm (of the minispiral)
NB	Narrow Band
NIR	Near-Infrared
NSC	Nuclear Stellar Cluster
PSF	Point Spread Function
RC	Red Clump
SED	Spectral Energy Distribution
SFR	Star Formation Rate
Sgr A*	Sagittarius A*
SMBH	Supermassive Black Hole
VLT	Very Large Telescope
YSO	Young Stellar Object
ZAMS	Zero Age Main Sequence

1 Introduction

The center of our own Galaxy, the only Nuclear Cluster so far accessible at this level of detail, has been the subject of a multitude of studies over the past decades, since infrared and radio observations first opened up this region to the eyes of astronomers. Evolving observational capabilities, especially the construction of 8m class telescopes like the VLT in Chile and Keck in Hawaii, aided by the development of Adaptive Optics and new detector techniques, have allowed a more and more detailed and precise insight into the ”heart” of the Milky Way. And while a new and even larger telescope generation is on the horizon, there are still large blank spots to be filled, even in this well-observed region. The scope of this thesis encompasses two of these formerly blank spots: large-scale, deep stellar classification and high resolution stellar polarization measurements.
Classification of stars based on spectral features has been done in the GC before, and at much higher spectral resolution than what is presented here. So what is new about the method presented in this work, and what new results can it provide? One crucial weakness of spectroscopic instruments is their small field-of-view. Even with an integral field spectrometer like SINFONI (ESO VLT), covering the innermost 1.5 pc as it was done here requires unrealistic amounts of observation time, if sufficient depth and spatial resolution are to be achieved.
This is the advantage of the method used in this work, intermediate-band photometry: the entire region can be observed simultaneously, at the sacrifice of spectral resolution. But the result is sufficient to separate early and late type stars, and based on this, a population analysis can reveal several new aspects: does the old, supposedly relaxed stellar population indeed follow the assumptions for such a population in the vicinity of a Supermassive Black Hole? A so-called *cusp* has been predicted for the very center, an increase in projected density of the late type stars, but as will be shown below, this is clearly not the case. Another aspect is the still ongoing discussion on star formation in the central region, and how this work can contribute to the constraints that have to be placed on stellar evolution models for the GC. The early type density distribution and luminosity function have been investigated before for the brightest of these sources, but can these findings of a steep power law density distribution and a top-heavy initial-mass-function be confirmed on this much larger sample? Are there any signs of tidal tails left behind by an inspiraling cluster of young stars formed elsewhere, as some models suggest? Or, if star formation indeed takes place in the innermost region, are there any signs of Young Stellar Objects (YSOs)?
The latter question leads to the second part of this work: measuring the polarization parameters of an unprecedented number of sources in the GC in the H-, Ks-, and Lp-band. Observations like that have been undertaken in the past, but only at much lower resolution. Especially in the H- and Lp-band, the latest observations were obtained 25-30 years ago, with the depth and spatial resolution available at that time (a few arcseconds, at that resolution the IRS 16 complex for instance is seen as a single source). High resolution polarimetric observations in the GC can provide new insight in several areas: the line-of-sight polarization and its relation to the extinction can be investigated, intrinsic polarization of compact sources yields information on the processes in the vicinity of these objects and the properties of the surrounding material. The central parsec offers several promising targets in all three observed wavelength bands, such as the extended bow-shock sources (most likely mass-losing stars plowing through the local medium), dust streamers in the mini-spiral, and candidates for YSOs. Some of these issues could not be explored in depth in this work due to a lack of suitable data, but in addition to the findings already shown here, interesting targets for follow-up observations can be determined (such as the IRS 13N cluster and several bow-shock sources). In addition, the proven feasibility of Lp-band polarimetry with NACO opens up new possibilities to explore the nature of these sources (while NACO is still operational, but the methods developed here could easily be adapted to a successor instrument).
In the following, §2 gives a short overview of the Galactic Center and introduces some basic concepts and processes. §3 details the data reduction methods that were applied to the observational data, which are presented in §4. §5 explains the photometric, polarimetric and calibration

procedures that were used to achieve the results, which are in turn presented in §6 (stellar classification and popualtion analysis), §7 (stellar polarization), and §8 (polarization and variability of extended sources). Finally, conclusions and a summary are contained in §9.

2 The Galactic Center

2.1 The Nuclear Stellar Cluster

The Galactic center (GC) is located at a distance of $\sim$ 8.0 kpc (Reid, 1993; Eisenhauer et al., 2005; Groenewegen et al., 2008; Ghez et al., 2008; Gillessen et al., 2009; Fritz et al., 2011) from the sun. This value is adopted throughout this work. At this distance, it is much closer than the next closest galactic nucleus in M31 (with 784 kpc, see Holland et al., 1998). The next AGN is even further away ($\sim$ 10 times further out than M31).
The immediate center of the GC contains the densest star cluster in the Galaxy with a $\sim 4.0\times10^6$ $M_\odot$ supermassive black hole at its dynamical center (Eckart et al., 2002; Schödel et al., 2002, 2003; Ghez et al., 2003, 2008; Gillessen et al., 2009). This cluster shows similar properties as the NSCs found at the dynamical and photometric centers of other galaxies (Böker, 2010; Schödel, 2010c). The projected density distribution of the observed stars in this cluster has been described by a broken power law (break radius $R_{break} = 6''.0 \pm 1''.0$, all values given here are projected radii), with a power-law slope of $\Gamma = 0.19 \pm 0.05$ within the break radius and $\Gamma = 0.75 \pm 0.10$ towards the outside of the cluster (Schödel et al., 2007).
Around the central parsec itself, a structure made up of dense and warm molecular gas (10^4 – $10^7 cm^{-3}$, several hundred K) is located in several clumps/clouds/filaments moving on a circular orbit around the center, the *circum nuclear disk* (CND). This structure stretches from about 1.5 pc to 7 pc from the center. The inner edge is relatively steep. Inside this radius, a cavity of mainly atomic and ionized gas (but almost no molecular gas) can be found. From the inner edge, several streamers of gas and dust seem to be on infalling trajectories towards the center. They are interacting with the winds emanating from the stars in the nuclear star cluster. This so-called "mini-spiral" (Lacy et al., 1991) appears to consist of a complex threedimensional structure (Paumard et al., 2004) with several sub-components (e.g. the Northern Arm to the north-east of the center). The influence of this structure can be seen on several individual sources (for instance the bow-shock sources in the Northern Arm, see Tanner et al., 2005), as well as in extinction maps of this area (Scoville et al., 2003; Schödel et al., 2010b).

2.1.1 Stellar composition

The stellar composition of the cluster depends on the distance to the center. This has been observed first as a drop in CO absorption strength towards Sgr A* in seeing-limited observations (Allen et al., 1990; Sellgren et al., 1990; Haller et al., 1996). Two explanations have been discussed for this: a significantly lower density of late type stars in the central few arcseconds and/or the presence of a large number of bright early type stars. Adaptive optics assisted observations with high spatial resolution have shown that there is indeed an increased number of early-type stars in this region, while the relative number of late type stars decreases (Genzel et al., 2003; Eisenhauer et al., 2005; Paumard et al., 2006; Lu et al., 2009). Several authors have tried to explain this finding by collisions between stars (or between stellar mass black holes and stars), which may lead to the destruction of the envelopes of giant stars in the central region (Davies et al., 1991; Bailey & Davies, 1999; Rasio & Shapiro, 1990; Davies et al., 1998; Alexander et al., 1999; Dale et al., 2008).
Several stellar populations have been detected in the central parsec: the oldest observable objects that make up the bulk of the visible sources outside of the innermost few arcseconds are old, metal-rich M, K and G type giants with ages of $1 - 10 \times 10^9$ years. The helium-burning *red clump* sources are also present, although they have not been discussed in detail until recently (Maness et al., 2007), because older works on the stellar population did not reach the necessary lower magnitude limit. A number of intermediate-bright ($mag_K \sim 10 - 12$) stars that are now on the AGB (Krabbe et al., 1995; Blum et al., 1996, 2003) have been produced by a star formation event $\geq 100 \times 10^6$ years ago. These stars can be distinguished from late type giants by the H_2O

absorption bands in their spectra that are detectable even at low spectral resolution. Very few supergiants like IRS 7 are also present in the central parsec. Several objects with featureless, but very red spectra have also been detected (Becklin et al., 1978; Krabbe et al., 1995; Genzel et al., 1996), namely IRS1W, 3, 9, 10W and 21. With high-resolution imaging, most of these sources have been resolved. They are mostly associated with the mini-spiral, and can be interpreted as young and bright stars with rapid mass loss interacting with the interstellar medium in the GC, so called bowshock sources (Tanner et al. (2002, 2003); Geballe et al. (2004), see also Perger et al. (2008)). In the central ~0.5 pc there exists yet another distinct stellar population: massive, young stars created in a starburst $3 - 7 \times 10^6$ years ago (e.g., Krabbe et al., 1995). These stars can be found, e.g., in the IRS 16 and IRS 13 associations (e.g., Eckart et al., 2004a; Maillard et al., 2004; Lu et al., 2005).The brightest of those young stars have been described as stars in a transitional phase between O supergiants and Wolf-Rayet stars (WN9/Ofpe according to e.g. Allen et al., 1990), with high mass-loss during this phase (Najarro et al., 1994; Krabbe et al., 1995; Morris et al., 1996; Najarro et al., 1997; Paumard et al., 2001; Moultaka et al., 2005). These stars account for a large part of the luminosity of the central cluster and also contribute half of the excitation/ionizing luminosity in this region (Rieke, Rieke & Paul , 1989; Najarro et al., 1997; Eckart et al., 1999; Paumard et al., 2006; Martins et al., 2007). Recently, Muzic et al. (2008) have identified a co-moving group of highly reddened stars north of IRS 13 that may be even younger objects, the IRS 13N cluster. These sources are maybe the best candidates for very recent star formation in the central parsec itself, and might therefore provide valuable insight into the star formation mechanism so close to Sgr A*.
Besides the most massive early type stars, a large number of OB stars with masses of ~10-60 $M_\odot$ have been examined by Levin & Beloborodov (2003); Genzel et al. (2003); Paumard et al. (2006); Lu et al. (2009). At least 50% of the early-type stars in the central 0.5 pc appear to be located within a clockwise (in projection on the sky) rotating disk, which was first detected by Levin & Beloborodov (2003). Later, Genzel et al. (2003); Paumard et al. (2006) claimed the existence of a second, counter-clockwise rotating disk. A very detailed analysis by Lu et al. (2009), based on the fitting of individual stellar orbits, shows only one disk and a more randomly distributed off-disk population (with the number of stars in the disk similar to that on random orbits). Bartko et al. (2009), however, claim that they at least observe a counter-clockwise structure that could be a strongly warped, possibly dissolving second disk. In the immediate vicinity of Sgr A*, there is yet another distinct group of stars, which form a small cluster of what appear to be early B-type stars (Eckart et al., 1999; Ghez et al., 2003; Eisenhauer et al., 2005). These so-called “S-stars” stars are on closed orbits around Sgr A*, with velocities of up to a few thousand km/s and at distances as close as a few lightdays (Schödel et al., 2003; Ghez et al., 2003, 2005; Eisenhauer et al., 2005; Ghez et al., 2008; Gillessen et al., 2009). Their orbits have been used to determine the mass of the black hole and the distance to the GC.
Detailed spectroscopic studies of the stellar population in the central parsec have so far only been conducted in the innermost few arcseconds and on small areas in the outer regions of the cluster (see Ghez et al. (2003, 2008); Eisenhauer et al. (2005); Paumard et al. (2006); Maness et al. (2007)). Here the main limitation is that the high surface density of sources in the GC forces the observers to use high spatial resolution observations in order to be able to examine all but the brightest stars. However, the field-of-view of integral field spectrometers is quite small at the required angular resolutions (e.g., between $3'' \times 3''$ and $0.8'' \times 0.8''$ for the ESO SINFONI instrument).

2.1.2 Star Formation in the GC?

How exactly star formation can take place in the central parsec under the observed conditions is still a debated issue. Classical star formation from gas of the observed density is severely impeded by the tidal shear exerted by the black hole and the surrounding dense star cluster (Morris et al., 1993). Two scenarios are being discussed to explain the presence of the early type stars: Genzel et al. (2003); Goodman (2003); Levin & Beloborodov (2003); Milosavljevic & Loeb (2004); Nayakshin & Cuadra (2005); Paumard et al. (2006) suggest a model of in-situ star formation, where the infall and cooling of a large interstellar cloud could lead to the formation of a gravitationally unstable disk and the stars would be formed directly out of the fragmenting disk. An alternative scenario has been proposed by Gerhard (2001); McMillan & Portegies Zwart

(2003); Portegies Zwart et al. (2003); Kim & Morris (2003); Kim et al. (2004); Guerkan & Rasio (2005) with the *infalling cluster scenario*, where the actual star formation takes place outside of the hostile environment of the central parsec. Bound, massive clusters of young stars can then be transported towards the center within a few Myr (dynamical friction in a massive enough cluster lets it sink in much more rapidly than individual stars, see Gerhard (2001)). Recent data seem to favor continuous, in-situ star-formation (e.g. Nayakshin & Sunyaev (2005); Paumard et al. (2006); Lu et al. (2009)
The existence of the S stars so close to Sgr A* is yet another matter, known as the ”paradox of youth” (Ghez et al., 2003). Two explanations are discussed for the presence of these stars, though neither is satisfactory: formation out of colliding or interacting giants (Eckart et al., 1993; Genzel et al., 2003; Ghez et al., 2003, 2005) or scattering from the disk of young stars (Alexander & Livio , 2004).

2.2 Extinction

Radiation from distant sources passes through the interstellar medium (ISM) between the source and the observer, and the influence of this medium can be quite significant. Depending on the wavelength, different components of the ISM and different processes become important, such as emission/absorption and scattering on electrons, ions, atoms, molecules and/or dust grains. For broadband near-infrared observations as they were conducted here, the dominant influence that has to be considered is the absorption and scattering of light on dust grains, termed *extinction*.
Extinction has to main effects on the observations: sources behind a lot of dust appear fainter than expected from their distance and intrinsic brightness. This has to be considered when e.g. distances are calculated from the apparent brightness of sources of known type:

$$m_\lambda = M_\lambda + 5log(d) - 5 + A_\lambda \tag{2.1}$$

Here, m_λ and M_λ denote the apparent respectively absolute magnitude of a source, d is the distance in parsec, and A_λ is the extinction in magnitudes at a particular wavelength. If the extinction is high enough, the source becomes too faint to be observed any more. This is the case, for instance, with the Galactic Center in the optical, where the extinction reaches 40-50 mag (see below). But the extinction is also wavelength dependent, with much lower values of $A_{Ks} \sim 3$ mag towards the GC in the NIR. While this allows observing the GC in these wavelength bands, it leads to another effect: the spectrum of an extincted source is shifted towards the red, since shorter wavelengths suffer higher extinction. The wavelength dependence is complex in general, but in the NIR it can be described by a simple power law (Draine, 1989; Schödel et al., 2010b; Fritz et al., 2011):

$$A_\lambda \propto \lambda^\beta \tag{2.2}$$

Draine (1989) proposed $\beta = -1.75$, but recent results by Gosling et al. (2009); Schödel et al. (2010b); Fritz et al. (2011) suggest a slightly steeper power law with $\beta \sim 2.0$.

2.3 Polarization

In general, three effects can produce polarized NIR radiation in GC sources: (re)emission by heated, non-spherical grains, scattering (on spherical and/or aligned non-spherical grains), and dichroic extinction by aligned dust grains. The first two cases can be, for the purposes of this work, regarded as intrinsic to the source, thereby allowing conclusions about the source itself and its immediate environment, while the third effect is the result of grain alignment averaged along the LOS. For sources enclosed in an optically thick dust shell, dichroic extinction can also contribute significantly as a local effect (see e.g. Whitney & Wolff , 2002).

2.3.1 Foreground polarization

As the basic mechanism that could cause the observed, large scale grain alignment, Davis & Greenstein (1951) suggested paramagnetic dissipation, which basically aligns the angular momentum of spinning grains with the magnetic field. But even almost 60 years later, the issue of

grain alignment is by no means completely solved, and it remains difficult to reach exact conclusions for dust parameters and magnetic field strength, but at least determining the magnetic field orientation is possible. If the parameters change along the LOS, this further complicates the issue. See e.g. Purcell et al. (1971); Lazarian (2003); Lazarian et al. (2007) and references therein for a review of the different possible causes of grain alignment expected to be relevant in different environments.
It is therefore possible to use polarimetric measurements to map at least the direction of the magnetic fields responsible for dust alignment through the Davis-Greenstein effect, as e.g. Nishiyama et al. (2009, 2010) showed for the innermost 20' respectively 2° of the GC, but these studies did not cover the central parsec due to insufficient resolution.
Observations of the galactic center suffer from strong extinction caused by dust grains on the LOS, with values of up to $A_V = 40$ mag at optical wavelengths (or even higher values of up to 50 mag if a steeper extinction law is assumed) and still around 3 mag in the Ks-band (e.g. Scoville et al., 2003; Schödel et al., 2010b). The aligned interstellar dust grains responsible for the polarization cause extinction as well, but non-aligned grains can also contribute. Therefore, the same particles are not necessarily responsible for both effects (e.g. Martin et al., 1990). Universal power laws have been claimed for polarization (Martin et al., 1990) (in a similar way as for NIR extinction, see Draine, 1989), who also showed that the law applicable to polarization in the optical domain (Serkowski et al., 1975) is a poor approximation in the NIR. The power law indices presented in these works for the extinction and the polarization power law are almost the same (1.5-2.0). It also appears that there is a correlation between the measured extinction of an intrinsically unpolarized source and foreground polarization (Serkowski et al., 1975), but this relation is quite complex. In the light of new results for the extinction law which seem to deviate consistently from the Draine law (e.g. Gosling et al., 2009; Schödel et al., 2010b), new polarimetric measurements may be useful to further clarify the relation between extinction and polarization. The central parsec of the GC is a well suited but challenging environment to study this relation, since it contains a large number of sources which exhibit large variances in extinction (1-2 mag, see Buchholz et al., 2009; Schödel et al., 2010b), which is produced along a long line-of-sight by a large number of dust clouds with possibly different grain alignment and composition. A new Ks-band extinction map of the central parsec recently been presented by Schödel et al. (2010b) is used as a reference in this work.

2.3.2 Local polarization

In the context of this work, *local polarization* refers to processes taking place in the innermost region of the GC itself, either around individual sources or in extended local structures such as the arms of the minispiral.Specifically, this encompasses effects of dusty stellar envelopes or disks, the interaction of stellar outflows with the local ISM in bow-shocks, and the emission by heated, aligned grains in dust streamers such as the Northern Arm.
Three basic processes can produce polarization in such environments: emission from elongated and aligned grains, dichroic extinction (also needs grain alignment and elongation), and scattering, either in the form of Mie-scattering on spherical grains or scattering on elongated and aligned grains as well. The relative importance of these processes depends on the local dust properties, such as grain size distribution, dust temperature, dust density, magnetic fields, and streaming velocities.

Emission

While a spherical grain would emit radiation isotropically, elongated grains emit preferably along their long axis. If the grain population is aligned, this leads to the radiation being polarized parallel to the mean orientation of the long grain axes. In the case of magnetic alignmment, spinning grains would align their angular momentum with the field (Davis & Greenstein, 1951), so their long axes and thus the polarization are perpendicular to the aligning field.
For a given grain alignment efficiency, the relative importance of polarized emission over the wavelength bands depends on the size distribution and the temperature of the grains. These two parameters are related as well, since smaller grains can reach higher temperatures more easily by absorption of high energy photons or stochastic collisions with high energy electrons or ions

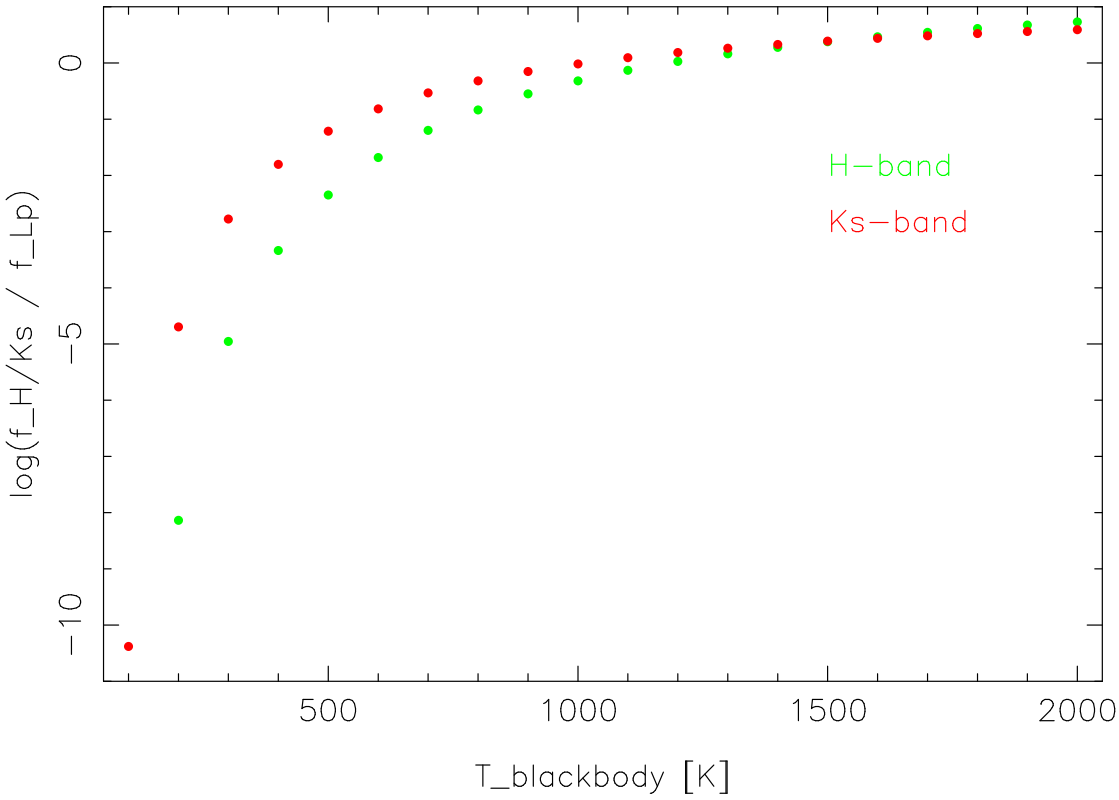

Figure 2.1: Blackbody emission in the H- and Ks-band compared to the Lp-band emission, logarithmic plot. Green dots represent H-band, red dots Ks-band. All fluxes were normalized to the flux in the Lp-band.

(Geballe et al., 2004). Fig.2.1 shows the relation between the emission in the H-, Ks-, and Lp-band at different temperatures. This is only a rough approximation, since the grains are treated as blackbodies here, but it already shows some general trends: for grain temperatures as they are common in the Northern Arm of the minispiral (200-300K, see Smith et al., 1990; Gezari, 1992), emission in the H- and Ks-band is negligible compared to the Lp-band. For higher temperatures of 900-1000K, however, H- and Ks-band emission becomes important as well. Assuming that these trends are essentially the same for the dust grains in the GC, significant emission in the two shorter wavelength bands requires much higher temperatures than what has been observed. Where such emission is detected, such as around the bright bow-shock sources, the temperatures must be higher due to heating from the central source or in a shock front, and/or scattering must play a significant role.

Local dichroic extinction

As it is the case along the LOS, dichroic extinction can take place locally if the dust column density is high enough. But unlike in the dust clouds along the LOS, where individual sections may show different alignment that cancels out parts of the effect and leaves only a net component of polarization, alignment of local dust can be regarded as uniform on small scales (depending on the local magnetic fields). The local field strength also determines the efficiency of the alignment, and this can also be much higher than what is found in a LOS cloud. In total, the polarization efficiency, i.e. the relation between dust extinction and absorptive polarization, can be far higher than the values found for the foreground polarization: essentially, even a small dust column density can produce dichroic extinction of the same order of magnitude as the foreground polarization, if the grains are aligned efficiently.
For a given grain alignment, the polarization produced by this process is perpendicular to the long axes of the grains (as this is the preferential direction of absorption). Therefore, dichroic extinction and dust emission from the same grains produce polarization with perpendicular polarization angles. If the alignment of the grains is known (e.g. from the magnetic fields and

the streaming motions), and if scattering is not important, the polarization angle can be used to estimate the relative importance of these two processes and thus give an indication of the local dust density.

Scattering

While only non-spherical and aligned grains can produce polarization by emission and dichroic extinction, scattering can take place on spherical grains as well. In this so-called *Mie-scattering* process, unpolarized light is partly scattered forward on a dust grain (assuming a particle size of the order of magnitude of the wavelength) and partly scattered away perpendicular to its angle of incidence. This latter part is linearly polarized. If a central source is surrounded by an isotropic shell of spherical grains, the scattered light produces a *reflection nebula*, and this structure shows polarization in a centrosymmetric pattern, with the polarization vectors tangential to concentric circles around the central source. An unresolved source of this kind shows its maximum in polarization if viewed edge-on, while if viewed face-on, it exhibits no linear polarization at all since the contributions from different regions cancel each other out. For a more complicated geometry, such as a dusty disk around a central object as one would expect it in YSOs, the resulting polarization patterns can be more complicated (see e.g. Murakawa, 2010).
Scattering on elongated dust grains is a far less simple problem, and has only recently been modeled: Whitney & Wolff (2002) showed the effects of optical depth, grain geometry and inclination angle on the polarization patterns of dusty disks and spherical structures, using a method developed by Mishchenko et al. (2000) to calculate the scattering properties of non-spherical grains. This study did not cover bow-shock-like structures, however, and while there are theoretical models of bow-shocks (e.g. most recently by Gustafson et al., 2010; van Marle et al., 2011), these do not consider polarization. Therefore, the results obtained in §8.2 could not be compared directly to theory or models.

2.3.3 Polarization of GC sources

Less than a decade after the first near-infrared (NIR) imaging observations of the Galactic center (GC) by Becklin & Neugebauer (1968), the polarization of 10 sources within ≤2 pc of Sagittarius A* was measured by Capps & Knacke (1976); Knacke & Capps (1977), observing in the K-, L- and 11.5 μm-band. These observations revealed similar polarization degrees and angles for the 4 sources observed in the K-band, with the polarization angles roughly parallel to the galactic plane (∼4% at 15° East-of-North, while the projection of the galactic plane is at a position angle of ∼31.4° at the location of the GC, see Reid et al., 2004). This was interpreted as polarization induced by aligned dust grains in the Milky Way spiral arms along the line-of-sight (LOS). The 11.5 μm polarization, however, was found to be almost perpendicular to the galactic plane and was therefore classified as intrinsic. The values found for the L-band showed intermediate values, which was attributed to a superposition of both effects. The GC therefore offers the possibility to study both interstellar polarization as well as the properties of intrinsically polarized sources.
Kobayashi et al. (1980) conducted a survey of K-band polarization in a much wider field of view (7'×7'), finding largely uniform polarization along the galactic plane. Lebofsky et al. (1982) confirmed these findings in the H- and K-band for 17 sources in the central cluster. The latest H-band survey was conducted by Bailey et al. (1984), who examined ∼10 sources with a 4.5" resolution, finding similar results. While these surveys could only resolve a small number of sources in the central region, higher resolution observations (0.25") enabled Eckart et al. (1995) to measure the polarization of 160 sources in the central 13"×13", while Ott et al. (1999) examined ∼ 40 bright sources in the central 20"×20" at 0.5" resolution. These two studies confirmed the known largely uniform foreground polarization, but already revealed a more complex picture: individual sources showed different polarization parameters, such as a significantly higher polarization degree (IRS 21).
These results already illustrated that in addition to the foreground polarization, intrinsic polarization plays a role in the Ks-band as well, and not only at longer wavelengths. Especially sources embedded in the Northern Arm and other bow-shock sources (see Fig.4.2 for an overview of the bright bow-shock sources in the central 20") show signs of intrinsic polarization. Among these objects, IRS 21 shows the strongest total Ks-band polarization of a bright GC source detected to

date (~ 10-16% at 16° Eckart et al., 1995; Ott et al., 1999). Tanner et al. (2002) described IRS 21 as a bow-shock most likely created by a mass-losing Wolf-Rayet star. The observed polarization is a superposition of foreground polarization and source intrinsic polarization. It is still unclear what process(es) cause the latter component: (Mie)-scattering in the dusty environment of the Northern Arm and/or emission from magnetically aligned dust. The latter is known to occur at 12.5 μm (Aitken et al., 1998), but should be negligible at shorter wavelengths.

3 Data reduction techniques

3.1 Cleaning the Image

3.1.1 Standard procedure

The *NAOS/CONICA*-instrument produces 1024 by 1024 pixel images, using an InSb Aladdin 3 detector. The nature of the detector chip itself and the wavelength regime (NIR-MIR) create several problems that have to be dealt with before the actual photometry can commence. For this task, the *dpuser* software[1] provides a number of algorithms.

- Dead/hot pixels on the chip: it needs to be avoided that pixels that either do not respond at all (dead) or always register a very high number of counts (hot) pollute the data (e.g. by mistaking a collection of hot pixels for an actual source). These pixels are detected and their values replaced by an average over the neighboring pixels.
- Flat-fielding: during the photometry, it is assumed that every region of the detector registers a given photon flux as the same number of counts. This is not the case with any real detector, however, since the production process and aging lead to inhomogeneities. To counter this, the detector is illuminated by an artificial light source, and several images are taken with the lamp switched on/off (lamp-flat method). The on and off images are then subtracted, averaged, and the actual data are divided by these *flat-fields*, in order to achieve the same calibrated detector response for the whole image.
- Sky subtraction: flux from emission in the atmosphere itself is a major issue with NIR and MIR observations, and this influence becomes stronger at longer wavelenghts: in the Lp-band, the sky emission exceeds the flux of all but the brightest sources in the GC. This can be compensated by taking images of source-free areas not too far from the main target, and then subtracting these sky exposures from the on-source images. In the H- and Ks-band, taking sky measurements only once or a small number of times during the night is sufficient (depending on observing conditions, a more variable sky necessitates more frequent sky measurements). For Lp-band observations, even small variations of the large sky contribution become important, so a sky exposure is taken after every image of the target.

3.1.2 Pattern removal

Even after the sky-subtraction and flat-fielding, the March 2011 Lp-band images still contained significant patterns. These are not actual structures in the Galactic center itself (as a comparison with previous Lp-band observations reveals, see e.g. Viehmann et al., 2005), but must have been introduced either by the detector itself or possibly by the sky correction. This can happen when the sky exposures contain sources themselves. Due to the high sky flux, these cannot be easily made out and masked, as it can be done in the Ks- or H-band. Two distinct patterns occur in all images: a series of 'stripes' along the East-West-axis and a 'cloudy' structure in the east and west of the FOV. The latter occurs at the same position in each image, while the former is different for each exposure.
The East-West pattern was approximated by averaging over the x-axis of each image (excluding bright pixels, in order to avoid a bias from the stars). The resulting profile was subtracted from the image. This does not introduce a significant bias, since there are no large scale East-West structures expected in this FOV.
In order to remove the stationary pattern, an average image was computed from all individual exposures (excluding the stellar sources) for each polarization channel. This yielded a characteristic pattern for each channel, which was then subtracted from all images.

[1] written by T. Ott, the software is available at *http://www.mpe.mpg.de/~ott/dpuser/*

Before and after the removal of each pattern, each image was shifted to a background level centered around zero. This turned out to be necessary since the background level after sky subtraction varied on the order of 10-20 counts between individual images. With a highly variable sky (due to less-than-optimal observing conditions), this can be expected: the flux from the sky alone reaches 2000-3000 counts per pixel, so a change of 1% between sky and object exposure already produces an offset of 20-30 counts. Unfortunately, this means that the background flux cannot be measured and any information about the background polarization is lost.

3.2 Deconvolution

Even in the optimal case that the influence of the atmosphere can be neglected, the image of a point source produced with any optical system suffers degradations because of the limitations of the instrument. In the ideal case of an aberration-free telescope with a circular aperture, the image of a point source would basically be an Airy pattern. When the effects of the atmosphere and the imperfections of the telescope are added to this, the result is a specific point spread function (PSF). This function is variable with time, due to temporal variations in the instrument itself and turbulence in the atmosphere (which in turn limits the coherence time), and it also varies over the FOV (anisoplanasy).
Thus, the observed signal $g(x,y)$ can be described as a convolution of the observed object $f(x,y)$ with a function describing the PSF, $h(x,y)$, and another function describing other influences like the detector read-out noise, anisoplanasy and other non-linear terms, $c(x,y)$:

$$g(x,y) = f(x,y) \odot h(x,y) + c(x,y) \tag{3.1}$$

with $\odot$ denoting the convolution operator.
Technical improvements like Adaptive Optics and the construction of larger telescopes on the ground and in space are a way to minimize these effects, but some PSF residuals will always remain. The basic idea of deconvolution is therefore to replace the complicated PSF with something that allows easier accurate photometry and also improves the detectability of faint sources, such as a Gaussian PSF with a FWHM of the order of the diffraction limit.
A convolution like this corresponds to a multiplication in Fourier space. Therefore, in pricinple, the Fourier transform of the original object could be (in the ideal case without noise and non-linear effects) determined by a simple divison in Fourier space ($F(u,v)$, $G(u,v)$, $H(u,v)$ denoting the Fourier transforms of $f(x,y)$, $g(x,y)$, $h(x,y)$, with u, v as the spatial frequencies corresponding to the coordinates x and y):

$$F(u,v) = \frac{G(u,v)}{H(u,v)} \tag{3.2}$$

What has to be considered, however, is that any telescope has a limited aperture, which in turn means that $H(u,v)$ will be zero at very high frequencies, and thus information on high spatial frequencies is lost. Also, the image degradation term $c(x,y)$ (non-linear effects, noise) cannot be neglected in any real case, and especially the noise can become dominant at high spatial frequencies. The PSF also cannot be determined with perfect accuracy, as it is usually approximated or extracted from several sources in the image. Therefore, this simple approach does not work, so several methods have been devised to find at least the most probable object distribution. In this work, the *Linear Deconvolution* algorithm and the *Lucy-Richardson Deconvolution* method are used.

3.3 Linear Deconvolution

The linear deconvolution method basically adapts the discussed Fourier division to deal with the issues of an issufficiently determined PSF and noise. For this purpose, a so-called Wiener filter (designated Ψ in the following) for the suppression of high spatial frequencies is introduced. The reconstruction of the object can then be described in Fourier space by the following:

$$O(u,v) = \frac{[G(u,v) + C(u,v)] \times \Psi(u,v)}{H(u,v)} \tag{3.3}$$

The filter then has to be chosen so that the difference between this expression and $F(u,v)$ (the 'real' object) is minimized:

$$\int_{-\infty}^{+\infty} \left| \frac{[(G(u,v)+C(u,v)] \times \Psi(u,v)}{H(u,v)} - \frac{G(u,v)}{H(u,v)} \right|^2 d(u,v) = Minimum \tag{3.4}$$

Deriving this expression with respect to Ψ and setting the result equal to zero leads to

$$\Psi(u,v) = \frac{|G(u,v)|^2}{|G(u,v)|^2 + |C(u,v)|^2} \tag{3.5}$$

It has to be considered that the signal and the noise are uncorrelated, so

$$\int_{-\infty}^{+\infty} (G(u,v) \times C(u,v)) d(u,v) = 0. \tag{3.6}$$

The spectral energy distribution of the signal can be approximated by that of the observed PSF ($|G(u,v)|^2 \approx |H(u,v)|^2$), while the noise spectral energy distribution is reasonably well represented by a delta function ($|\delta(u,v)|^2$). If one takes into account that the power spectrum of a function is given by the product of its fourier transform and the complex conjugate of the fourier transform ($|H(u,v)|^2 = H(u,v) \times \overline{H}(u,v)$), this finally yields (neglecting the noise term in equation 3.3)

$$F(u,v) \approx O(u,v) \approx \frac{G(u,v) \times \overline{H}(u,v)}{|H(u,v)|^2 + |\delta(u,v)|^2} \tag{3.7}$$

3.4 Lucy-Richardson Deconvolution

The Lucy-Richardson (LR) deconvolution algorithm is an iterative process based on the scheme for the rectification of observed probability distributions proposed by Lucy (1974). This scheme consists of the iteration of three steps. First, the current estimate of the object distribution $O_k(x,y)$ is convolved with the PSF estimate $H(x,y)$:

$$L_k(x,y) = O_k(x,y) \odot H(x,y) \tag{3.8}$$

The image obtained this way, $L_k(x,y)$, is compared with the observed image $G(x,y)$:

$$R(x,y) = \frac{G(x,y)}{L_k(x,y)} \odot H(x,y) \tag{3.9}$$

with the PSF acting as a low-pass filter reducing the influence of high frequencies on the result because those are affected much stronger by noise. Finally, a new estimate of the object distribution is obtained by multiplying the original estimate with the correction function $R(x,y)$:

$$O_{k+1}(x,y) = O_k(x,y) \odot R(x,y) \tag{3.10}$$

The convolution with the PSF suppresses high spatial frequencies, thus avoiding the amplification of noise peaks. But also, any details of the image related to high spatial frequencies, like close binary stars, can only be observed after a high number of iterations ($\sim 10^4$). This already points out one big disadvantage of this method, the high amount of computation time that is required. Especially if a large number of images has to be processed, or the same image has to be processed a large number of times like for a completeness correction, this method is slow compared to others (such as Linear Deconvolution). Another disadvantage is the fact that very faint sources and diffuse emission close to bright sources tend to be added to the flux of the bright source. This effect can be observed as a negative residuum around bright sources. The only way to minimize this is a very precise determination of the PSF including its faint wings. Furthermore, the diffuse background of the image tends to be resolved into distinct point sources. These can be excluded by comparing different images, as it is done when creating the common list anyway (see §5.1.1).

4 Observations

4.1 General parameters

All observations used here were carried out with the NAOS-CONICA (NACO) instrument at the ESO VLT unit telescope (UT) 4 on Paranal. The bright super-giant IRS 7 located about 6" north of Sgr A* was used to close the feedback loop of the adaptive optics (AO) system, thus making use of the infrared wavefront sensor installed with NAOS. For the H- and Ks-band observations (including intermediate band data), the sky background was determined by taking several dithered exposures of a region largely devoid of stars, a dark cloud 713" west and 400" north of Sgr A*. In the Lp-band, alternating sky and object exposures were taken using a region 60" west and 60" north of Sgr A* to determine a largely source-free sky.
All images were flat-fielded, sky subtracted and corrected for dead/hot pixels.
In order to determine the quality of individual observations, the Strehl ratio was adopted as a criterion. This parameter describes the ratio of the flux contained in the core of the measured point-spread-function (PSF) in the image to that expected for a theoretical PSF calculated from telescope parameters (for a given wavelength). The Strehl ratio was determined using the *strehl* algorithm in the ESO eclipse software package[1].

4.2 Intermediate band data

The data used for the stellar classification were taken in June/July 2004 and April 2006 (programs 073.B-0084(A), 073.B-0745(A), 077.B-0014(A), see Tab.4.1 for details, datasets N1-N7 and H18), using an H band broadband filter and seven intermediate band filters. The seeing varied for the different observations, within a range of 0.5 to 1.3". A rectangular dither pattern was used for most observations, while some were randomly dithered. This led to a total field-of-view (FOV) of 40.5", corresponding to ∼1.5 pc.
In order to be able to separate early and late type sources using the CO band depth method described in §5.1.6, the photometry has to be accurate enough to clearly identify the feature used for the classification (see §5.1.3). This means that the typical photometric error should be much lower than the typical depth of the classification feature (see §5.1.3 for an estimate of the required accuracy). When observing a large field of view like in this case, a good AO correction can only be achieved within the *isoplanatic patch*, typically a region of ∼10-15" for the available data. This effect leads to a decrease of the Strehl ratio towards the outer regions of the field (see Fig.5.1). This value was computed from the PSFs determined in 12×12 subimages of the IB227 image (with the same PSF stars that were used in the photometry). The Strehl values exhibit a clear trend towards lower values at larger projected distances from the guide star. Sources outside of the isoplanatic patch show a characteristic elongation towards IRS 7. This is a problem when using PSF fitting photometry, while aperture photometry (which is less dependent on the shape of the PSF) is faced with the problem of crowding.

4.3 Polarimetric data

The main polarimetric datasets used in this work were obtained in June 2004 (H-band broadband filter, program 073.B-0084A, dataset P1, see Tab.4.1), May 2009 (Ks-band broadband filter, program 083.B-0031A, dataset P2) and March 2011 (Ks- and Lp-band filters, program 086.C-0049A, datasets P16 and P18. In addition, several polarimetric Ks-band datasets contained in the ESO archive (datasets P3-P15)[2] were used, in order to expand the total FOV and

[1] see N. Devillard, "The eclipse software", The messenger No 87 - March 1997, publicly available at *http://www.eso.org/projects/aot/eclipse/distrib/index.html*

[2] Based on observations collected at the European Organization for Astronomical Research in the Southern Hemisphere, Chile

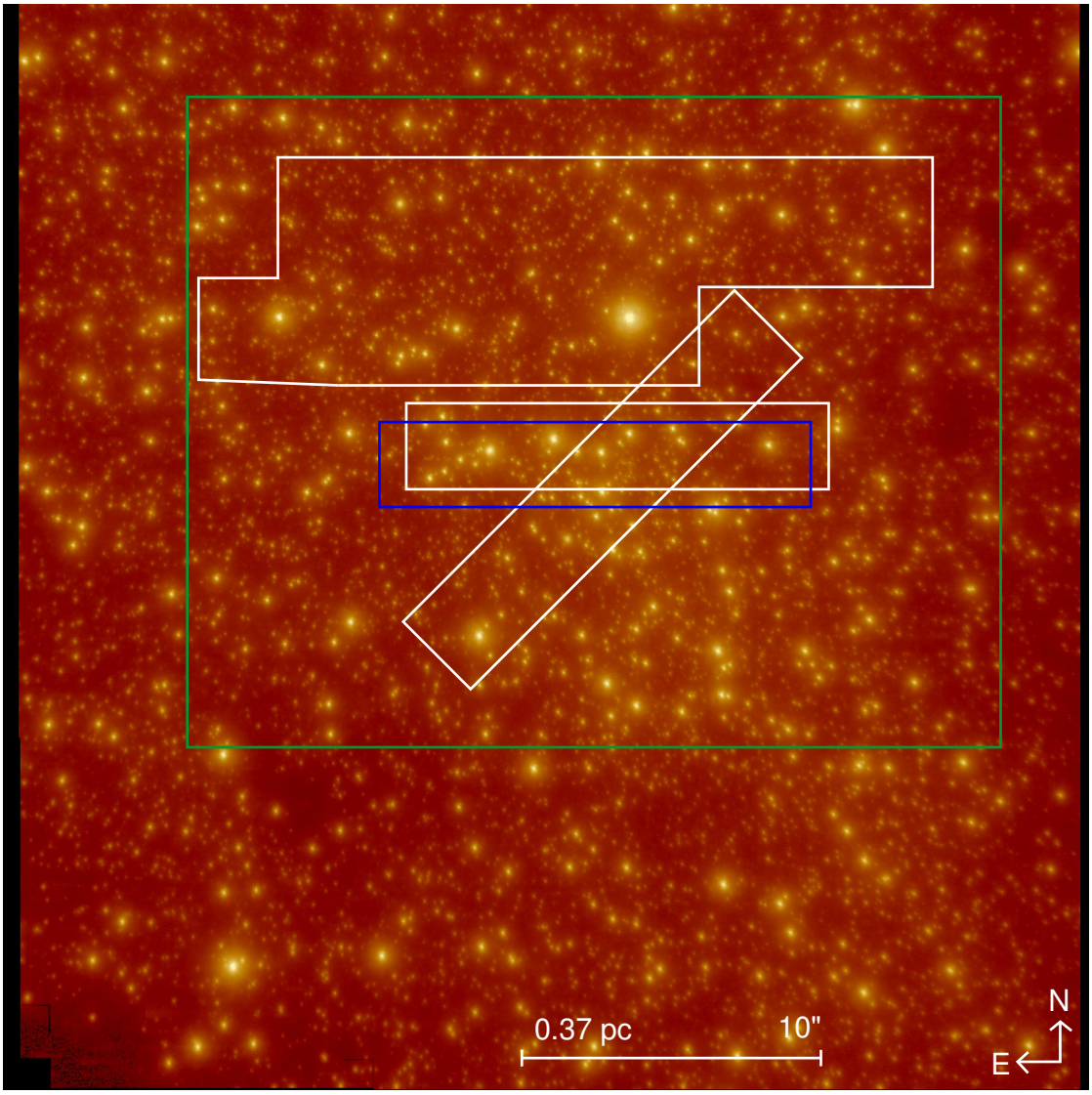

Figure 4.1: Ks-band image of the innermost 40.5" of the GC (ESO VLT NACO image, program 073.B-0084(A). The full image represents the FOV of the intermediate band observations. The lines denote the polarimetric FOVs: white indicates Ks-band, green Lp-band and blue lines H-band.

especially to also cover the bright and strongly polarized source IRS 21. The FOV of these datasets is rotated by 45 degrees compared to e.g. the 2009 Ks-band data.
The seeing during the 2009 Ks-band observations was excellent with a value of ~0.5", while conditions during the H-band observations were less optimal with a seeing of ~0.8". The 2011 observations in both Ks- and Lp-band suffered from less-than-optimal conditions and variable seeing, which in turn greatly complicated achieving sufficiently accurate photometry. The larger FOV of these data was achieved by reducing the depth compared to the 2009 Ks-band (P2) and the H-band data (P1).
The polarization measurements were taken using the Wollaston prism available with NACO in combination with a rotatable half-wave plate. No $\frac{\lambda}{4}$-plate is available with NACO, which means that only linear and no circular polarization can be measured. The two channels produced by the Wollaston prism (0° and 90°), combined with two orientations of the half-wave plate (0° and 22.5°), yielded four sub-images for each of several dither positions. In total, a field-of-view of 3"×16.5" (Ks-band, 2009), 3"×19" (H-band), 8"×28" (Ks-band, 2011), respectively 26"×28" (Lp-band) was covered. This corresponds to 0.11 pc × 0.61 pc, 0.11 pc × 0.70 pc, 0.30 pc × 1.04 pc, respectively 0.96 pc × 1.04 pc (see Fig.4.1, with Ks-band FOV marked with white rect-

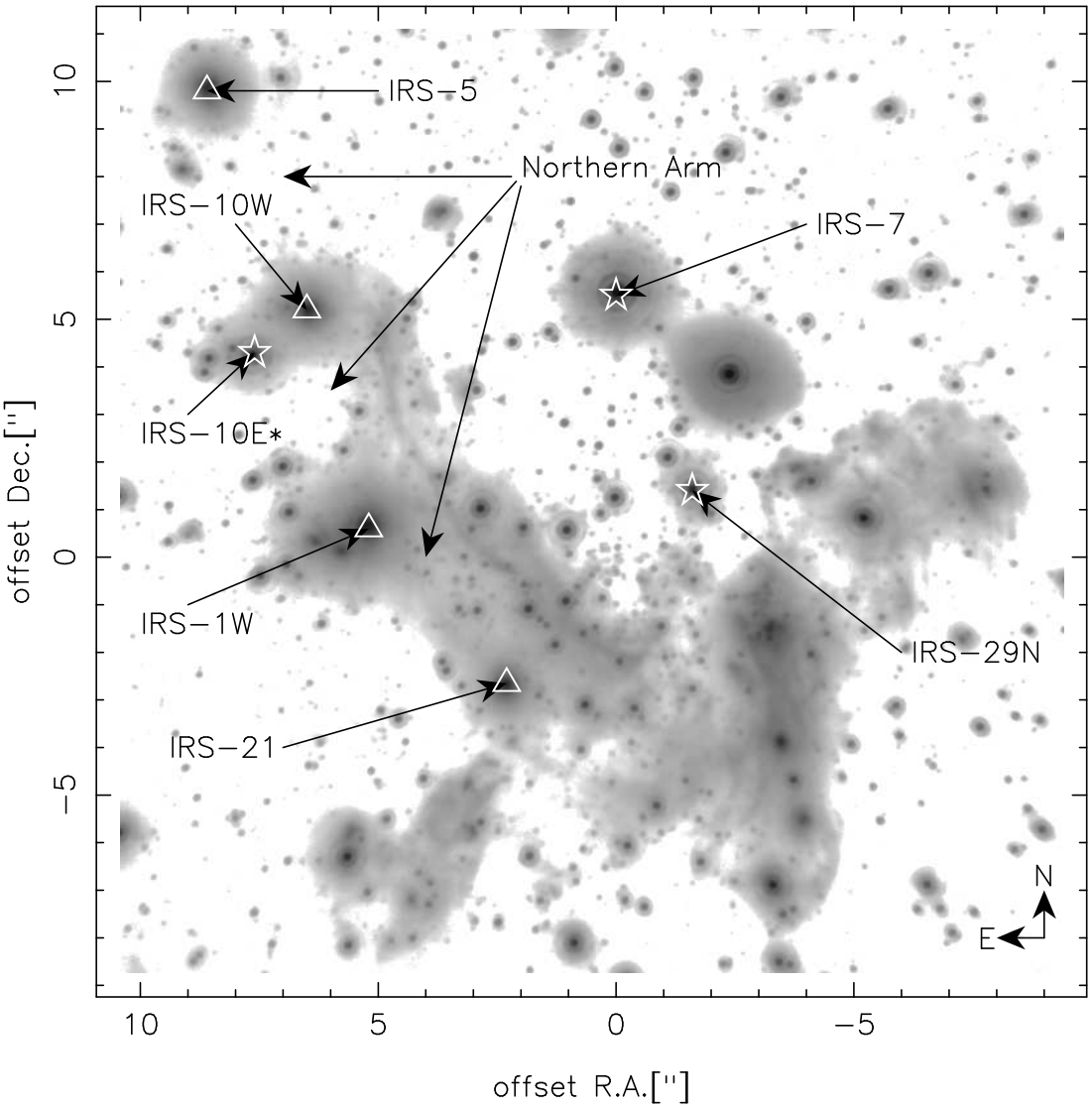

Figure 4.2: Lp-band image of the innermost 20” of the GC (ESO VLT NACO image, program 179.B-0261(A)). Prototypical (bow-shock) sources and location of the Northern Arm are indicated. Stellar sources are marked with stars, bow-shocks are indicated by triangles.

angles, H-band with blue rectangle, and Lp-band with green rectangle, also Fig.4.2).

When flat-fielding polarimetric images, it is essential for a correct calibration that the flat-field observations are taken through the Wollaston as well, because the flat-field shows variations caused by different transmissivity of the channels as well as effects of the inclined mirrors behind the prism (see Witzel et al., 2011). For some data-sets in the archive, only flats taken without the Wollaston are available. Depending on the position of the source in the FOV and its polarization parameters, this can lead to deviations in both polarization degree and angle of the order of a few percent and $\sim 10° - 15°$ (see §5.2.2).

Most data used here were originally taken to examine flares of Sgr A* (see e.g. Eckart et al., 2006; Meyer et al., 2006; Zamaninasab et al., 2010), and this purpose requires the highest possible time resolution. This is the reason why differential polarimetry (channel switching) could not be applied. This technique can eliminate or reduce many instrumental effects and thus increase precision by rotating the imager by 90° between exposures and thus canceling these effects out (effectively switching the 0 and 90° channels). But this also means more time is needed for each exposure, since two images have to be taken for one data-point and the actual rotating takes time as well. Due to these reasons, this technique was also not used in the 2011 observations, since the additonal time required would have further reduced the already limited depth and FOV of

the observations.

4.4 Imaging data

For the variability study of the bow-shock sources, NACO imaging data taken between June 2002 and May 2008 was used (H-, Ks- and Lp-band data contained in the ESO archive). See Tab.4.1 for details on the individual datasets. In total, 45 Ks-band datasets were used, 38 taken in the H-band and 9 observed in the Lp-band.

Table 4.1: Details of the observations used for this work. *Mode* denotes the wavelength filter (H/Ks/Lp broad band or intermediate band, with central wavelength in μm) and the type of observations (imaging (I), Wollaston polarimetry (W or Wr, the latter with a rotated FOV), intermediate band filter (IB)). *N* is the number of exposures that were taken with a given detector integration time (*DIT*). *NDIT* (in sec) denotes the number of integrations that were averaged online by the read-out electronics during the observation. *CAM* indicates the camera optics used (S13, S27 or L27). The Strehl ratio (if given) was measured using the *strehl* algorithm of the ESO eclipse package (see N. Devillard, "The eclipse software", The messenger No 87 - March 1997, publicly available at *http://www.eso.org/projects/aot/eclipse/distrib/index.html*, given here is the average value over all images in each dataset.

	program	date	mode	N	NDIT	DIT	CAM	Strehl
N1	073.B-0745(A)	2004-07-09	2.00, IB	8	4	36	S27	
N2	073.B-0084(A)	2004-06-12	2.06, IB	96	1	30	S27	
N3	073.B-0084(A)	2004-06-12	2.24, IB	99	1	30	S27	
N4	073.B-0745(A)	2004-07-09	2.27, IB	8	4	36	S27	
N5	073.B-0745(A)	2004-07-09	2.30, IB	8	4	36	S27	
N6	073.B-0084(A)	2004-06-12	2.33, IB	99	1	30	S27	
N7	073.B-0745(A)	2004-07-09	2.36, IB	8	4	36	S27	
P1	073.B-0084(A)	2004-06-12	H, W	30	1	30	S13	0.17
P2	083.B-0031(A)	2009-05-18	Ks, W	143	4	10	S13	0.27
P3	179.B-0261(A)	2007-04-01	Ks, Wr	15	2	15	S13	0.13
P4	179.B-0261(A)	2007-04-03	Ks, Wr	70	2	15	S13	0.22
P5	179.B-0261(A)	2007-04-04	Ks, Wr	23	2	15	S13	0.17
P6	179.B-0261(A)	2007-04-05	Ks, Wr	70	2	15	S13	0.10
P7	179.B-0261(A)	2007-04-06	Ks, Wr	51	2	15	S13	0.14
P8	179.B-0261(D)	2007-07-18	Ks, Wr	130	2	15	S13	0.19
P9	179.B-0261(D)	2007-07-19	Ks, Wr	70	2	15	S13	0.08
P10	179.B-0261(D)	2007-07-20	Ks, Wr	70	2	15	S13	0.08
P11	179.B-0261(D)	2007-07-20	Ks, Wr	70	2	15	S13	0.14
P12	179.B-0261(D)	2007-07-21	Ks, Wr	51	2	15	S13	0.14
P13	179.B-0261(D)	2007-07-23	Ks, Wr	124	2	15	S13	0.08
P14	179.B-0261(D)	2007-07-23	Ks, Wr	41	2	15	S13	0.02
P15	179.B-0261(D)	2007-07-24	Ks, Wr	30	2	15	S13	0.08
P16	086.C-0049(A)	2011-03-17	Lp, W	26	150	0.2	L27	
P17	086.C-0049(A)	2011-03-17	Ks, W	11	2	30	S13	
P18	086.C-0049(A)	2011-03-19	Ks, W	37	2	15	S13	
K1	060.A-9026(A)	2002-07-31	Ks, I	60	4	15	S13	
K2	071.B-0078(A)	2003-06-13	Ks, I	102	3	5	S13	
K3	071.B-0078(A)	2003-06-14	Ks, I	120	2	10	S13	
K4	071.B-0078(A)	2003-06-15	Ks, I	183	1	20	S13	
K5	071.B-0078(A)	2003-06-16	Ks, I	211	2	10	S13	
K6	271.B-5019(A)	2003-06-19	Ks, I	223	2	10	S13	

Continued on next page ...

Continued from previous page ...

	program	date	mode	N	NDIT	DIT	CAM	Strehl
K7	073.B-0084(B)	2004-05-07	Ks, I	48	3	10	S13	
K8	073.B-0084(B)	2004-05-07	Ks, I	56	60	0.5	S27	
K9	073.B-0775(A)	2004-07-06	Ks, I	217	2	15	S27	
K10	073.B-0775(B)	2004-08-30	Ks, I	101	2	15	S13	
K11	073.B-0775(B)	2004-09-02	Ks, I	55	2	15	S13	
K12	073.B-0085(C)	2004-09-23	Ks, I	115	2	15	S13	
K13	073.B-0085(I)	2005-04-09	Ks, I	52	15	2	S13	
K14	073.B-0085(E)	2005-05-13	Ks, I	108	60	0.5	S27	
K15	073.B-0085(D)	2005-05-14	Ks, I	181	15	2	S13	
K16	073.B-0085(D)	2005-05-16	Ks, I	185	6	5	S13	
K17	073.B-0085(D)	2005-05-17	Ks, I	32	10	20	S13	
K18	073.B-0085(D)	2005-05-17	Ks, I	34	15	2	S13	
K19	073.B-0085(F)	2005-06-20	Ks, I	77	3	10	S13	
K20	073.B-0085(F)	2005-06-20	Ks, I	24	3	10	S27	
K21	271.B-5019(A)	2005-07-24	Ks, I	60	2	15	S13	
K22	075.B-0093(C)	2005-07-27	Ks, I	145	4	15	S13	
K23	075.B-0093(B)	2005-07-29	Ks, I	37	4	15	S13	
K24	075.B-0093(D)	2005-08-02	Ks, I	78	4	15	S13	
K25	073.B-0085(G)	2005-08-03	Ks, I	47	2	15	S13	
K26	073.B-0085(G)	2005-08-03	Ks, I	42	60	0.5	S27	
K27	077.B-0552(A)	2006-05-28	Ks, I	46	6	5	S27	
K28	077.B-0552(A)	2006-06-01	Ks, I	88	3	10	S27	
K29	077.B-0014(F)	2006-09-23	Ks, I	48	2	17.2	S13	
K30	077.B-0014(F)	2006-09-24	Ks, I	53	2	17.2	S13	
K31	077.B-0014(F)	2006-10-03	Ks, I	48	2	17.2	S13	
K32	078.B-0136(A)	2006-10-19	Ks, I	43	14	2.4	S13	
K33	078.B-0136(A)	2006-10-20	Ks, I	48	14	2.4	S13	
K34	078.B-0136(B)	2007-03-04	Ks, I	48	3	12	S13	
K35	078.B-0136(B)	2007-03-17	Ks, I	48	14	2.4	S13	
K36	078.B-0136(B)	2007-03-17	Ks, I	30	28	2	S27	
K37	078.B-0136(B)	2007-03-20	Ks, I	96	2	17.2	S13	
K38	179.B-0261(A)	2007-04-01	Ks, I	96	6	5	S27	
K39	179.B-0261(A)	2007-04-02	Ks, I	27	1	30	S13	
K40	179.B-0261(A)	2007-04-02	Ks, I	195	6	5	S27	
K41	179.B-0261(A)	2007-04-03	Ks, I	48	3	10	S13	
K42	179.B-0261(A)	2007-04-04	Ks, I	63	3	10	S13	
K43	179.B-0261(A)	2007-04-06	Ks, I	74	6	5	S27	
K44	079.B-0084(A)	2007-05-18	Ks, I	39	4	10	S13	
K45	081.B-0648(A)	2008-05-28	Ks, I	167	2	20	S27	
H1	070.B-0649(B)	2003-03-19	H, I	109	1	10	S13	
H2	070.B-0649(B)	2003-03-20	H, I	32	1	20	S13	
H3	071.B-0077(A)	2003-05-09	H, I	32	6	10	S13	
H4	071.B-0078(A)	2003-06-14	H, I	96	1	20	S13	
H5	071.B-0078(A)	2003-06-15	H, I	120	1	20	S13	
H6	071.B-0078(A)	2003-06-16	H, I	150	1	20	S13	
H7	071.B-0077(C)	2003-07-21	H, I	72	3	20	S13	
H8	071.B-0077(D)	2003-09-05	H, I	32	3	20	S13	
H9	071.B-0077(D)	2003-09-06	H, I	32	30	2	S13	
H10	072.B-0285(B)	2004-03-29	H, I	88	3	10	S13	
H11	073.B-0085(A)	2004-04-29	H, I	76	2	15	S13	

Continued on next page ...

Continued from previous page …

	program	date	mode	N	NDIT	DIT	CAM	Strehl
H12	073.B-0084(A)	2004-06-11	H, I	48	2	15	S13	
H13	073.B-0775(A)	2004-07-06	H, I	49	2	15	S13	
H14	073.B-0775(A)	2004-07-08	H, I	48	1	30	S13	
H15	273.B-5023(C)	2004-07-29	H, I	61	2	15	S13	
H16	073.B-0085(C)	2004-09-24	H, I	17	1	25	S13	
H17	073.B-0085(D)	2005-05-16	H, I	96	15	2	S13	
H18	077.B-0014(A)	2006-04-29	H, I	32	28	2	S27	
H19	077.B-0014(A)	2006-04-29	H, I	48	2	17	S13	
H20	077.B-0014(B)	2006-05-31	H, I	54	2	17	S13	
H21	077.B-0014(B)	2006-06-13	H, I	32	11	5.225	S13	
H22	077.B-0014(C)	2006-06-29	H, I	48	2	17	S13	
H23	077.B-0014(B)	2006-07-24	H, I	64	11	5.225	S13	
H24	077.B-0014(B)	2006-07-27	H, I	52	1	60	S13	
H25	077.B-0014(D)	2006-07-29	H, I	49	2	17	S13	
H26	077.B-0014(D)	2006-08-01	H, I	65	14	2.4	S13	
H27	077.B-0014(E)	2006-08-21	H, I	71	2	17	S13	
H28	077.B-0014(E)	2006-08-28	H, I	32	28	2	S27	
H29	077.B-0014(F)	2006-09-16	H, I	50	2	17	S13	
H30	077.B-0014(F)	2006-10-02	H, I	48	2	17	S13	
H31	078.B-0136(A)	2006-10-15	H, I	48	2	17	S13	
H32	078.B-0136(A)	2006-10-15	H, I	58	14	2.4	S13	
H33	078.B-0136(B)	2007-03-17	H, I	102	2	17	S13	
H34	179.B-0261(A)	2007-04-04	H, I	96	3	10	S13	
H35	179.B-0261(D)	2007-07-19	H, I	48	3	10	S13	
H36	179.B-0261(D)	2007-07-21	H, I	96	3	10	S13	
H37	179.B-0261(T)	2008-06-21	H, I	96	2	17.2	S13	
H38	179.B-0261(T)	2008-06-22	H, I	48	2	17.2	S13	
L1	060.A-9026(A)	2002-08-29	Lp, I	80	150	0.2	L27	
L2	071.B-0077(A)	2003-05-10	Lp, I	35	300	0.2	L27	
L3	073.B-0840(A)	2004-04-25	Lp, I	32	60	0.175	L27	
L4	073.B-0840(A)	2004-04-26	Lp, I	122	60	0.175	L27	
L5	073.B-0085(D)	2005-05-13	Lp, I	48	150	0.2	L27	
L6	077.B-0552(A)	2006-05-29	Lp, I	353	150	0.2	L27	
L7	179.B-0261(A)	2007-04-01	Lp, I	120	150	0.2	L27	
L8	079.B-0084(A)	2007-05-22	Lp, I	194	200	0.2	L27	
L9	081.B-0648(A)	2008-05-26	Lp, I	53	150	0.2	L27	

5 Photometry and calibration

The data-sets used in this work show considerably variations in their quality. This led to the exclusion of two intermediate-band filter data-sets and to only using the best polarimetric data. But the latter was only possible if there were indeed multiple data-sets available for a given FOV. This was the case for the innermost 3"×19" in the Ks-band, which has been observed many times over the last years. But only one polarimetric H-band data-set is available, and the Northern Arm region has also only been observed once in the Ks-band (using NACO, March 2011 data). The Lp-band data-set used here (obtained in March 2011 as well) is the only polarimetric NACO data-set ever taken in that wavelength band, with the exception of a few calibration images taken during the commissioning process of the instrument. Unfortunately, the 2011 data does not nearly match the 2009 Ks-band or the 2004 H-band data in quality. On the one hand, this limits the depth that can be achieved there, while on the other, it means that different photometric techniques have to be applied to the different data-sets in order to avoid specific problems and achieve the maximum in precision that is possible for the individual observations.

5.1 Intermediate band data

5.1.1 Double deconvolution photometry

In order to counter the aforementioned problems and to achieve reliable relative photometry over the entire FOV which is considerably larger than the isoplanatic patch, a two-step deconvolution process was used. Deconvolution is a good way to reduce source confusion in a crowded field, but it can only be applied satisfactorily if the PSF is very well known and uniform over the whole field. The latter is clearly not the case here: sources towards the edges of the field show an elongation towards the guide star. This can be countered by determining the PSF locally, but that depends on the availability of suitable bright, isolated stars. Especially the faint wings of the PSF are easily contaminated by the flux of nearby stars in a crowded field like the GC.
The star that allows to determine the PSF wings with the greatest precision is the guide star itself, IRS 7. Its brightness exceeds that of the stars in the immediate vicinity by several magnitudes. This PSF was then used in the first LR-deconvolution step. The resulting image was divided into sub-images smaller than the isoplanatic patch (8"×8", so the PSF can be regarded as uniform over this area) and deconvolved again with a locally extracted PSF. The fluxes were then measured using aperture photometry. This process is described in detail in Schödel (2010a).
The individual lists of detected stars in the filters were merged to a common list of stars detected in all 8 filters. The number of common sources was limited by the image with the lowest quality to 5914. This number includes almost all brighter sources ($\mathrm{mag}_{Ks} \leq 16$), but several extended sources (like the bow-shock sources in the northern arm of the minispiral) were not detected in all filters with sufficiently low photometric and position uncertainties.

5.1.2 Primary Calibration

The primary calibration done here served a dual purpose: on the one hand, the measured counts for each source in each band were converted into a magnitude (absolute calibration). On the other hand, the bands had to be calibrated relative to each other to ensure smooth spectral energy distributions (SEDs) as they can be expected at this spectral resolution (see Fig.5.3). Only very broad spectral features like CO bandheads and H_2O absorption bands are expected to be observable here. Even the feature around 2.06 μm that appears in the B0V spectrum only causes a decrease of 0.014 mag in that filter compared to the K4.5III spectrum that lacks this feature. This can be neglected compared to other photometric uncertainties.
Atmospheric features can also influence the shape of the measured SEDs and need to be eliminated. But the most important parameter that controls the quality of the data turned out to be the

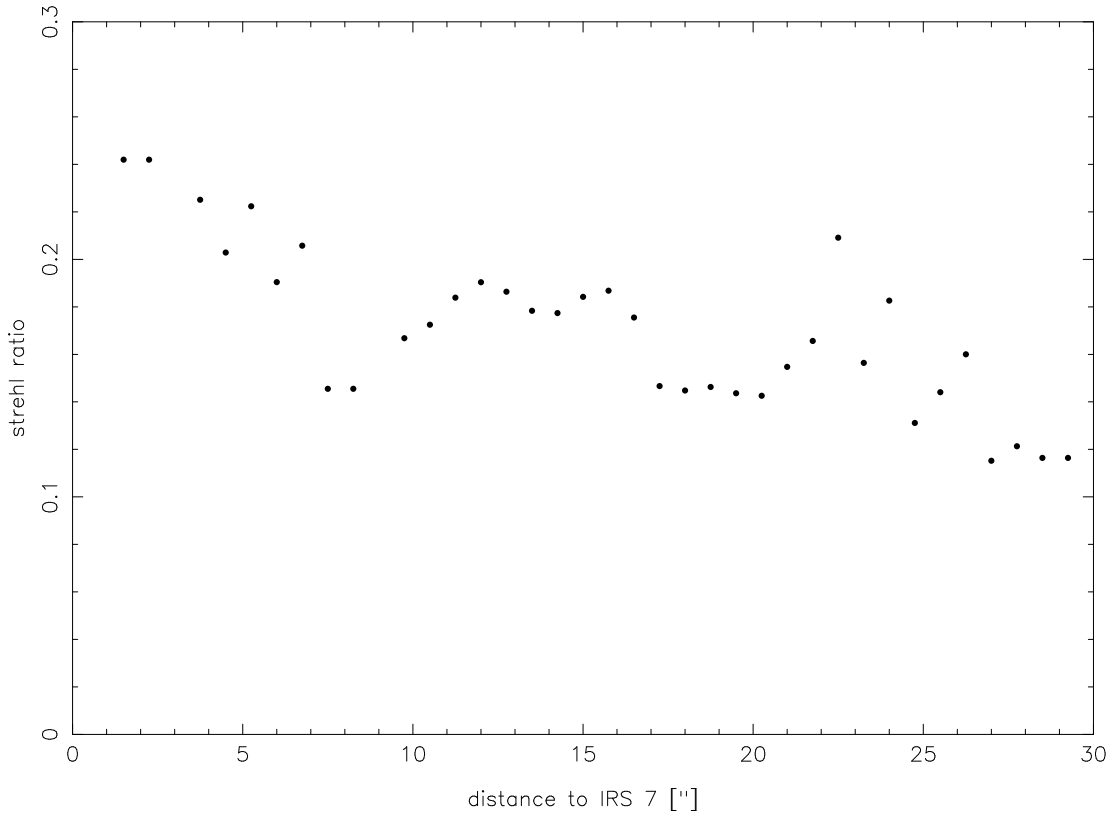

Figure 5.1: The strehl ratio, a value that measures the deviation of the PSFs of the sources from an ideal PSF, decreases with the distance to the guide star.

AO performance, which is why two additional intermediate band datasets (2.12 and 2.18 μm) were not used.
These goals were achieved by calibrating the common list of sources with 11 known OB stars (see Tab.5.1 and Fig.5.2) close to Sgr A*, adopting the classifications of Paumard et al. (2006), who provided a list of 90 early type stars in the central parsec. Stars of this type have some emission lines in the K band (see Fig.5.3 upper right), e.g. the HeI line at 2.058μm, but these lines are narrow enough to be negligible compared to the continuum at the spectral resolution of the data. Thus, the spectra of these stars can be assumed to be featureless, and they can be described by a blackbody spectrum with an effective temperature of ~30000 K. The final calibration has only a minimal dependence on the assumed effective temperature because the Rayleigh-Jeans law is a very good approximation for the SED of hot stars in the near-infrared (using 20000 K instead leads to a difference of only 0.01 mag in the reference magnitudes). Therefore, the same T_{eff} can be used for all calibration sources.
Extinction towards the GC is significant even in the near-infrared. An extinction of ~2.5-3.0 mag (Scoville et al., 2003; Schödel et al., 2010b) has been measured towards the central parsec in the Ks band. In order to minimize calibration uncertainties, individual extinction values were used for each calibration source, taken from the extinction map provided by Schödel et al. (2010b). Since the extinction also depends on the wavelength, the Draine (1989) extinction law was used to calculate an extinction value for each band from the basic value for the Ks band:

$$A_\lambda = A_{Ks} \times \frac{\lambda}{2.18\mu m}^{-1.75} \tag{5.1}$$

Using an extinction law with a different exponent (like $\lambda^{-2.0}$ as proposed by Nishiyama et al. (2008); Schödel et al. (2010b)) would lead to a general offset of about 0.5 mag in extinction, but neither the relative distribution of the extinction values nor the results of the classification would vary, since the same extinction law is used again to fit for the individual extinction of each source in the classification process.

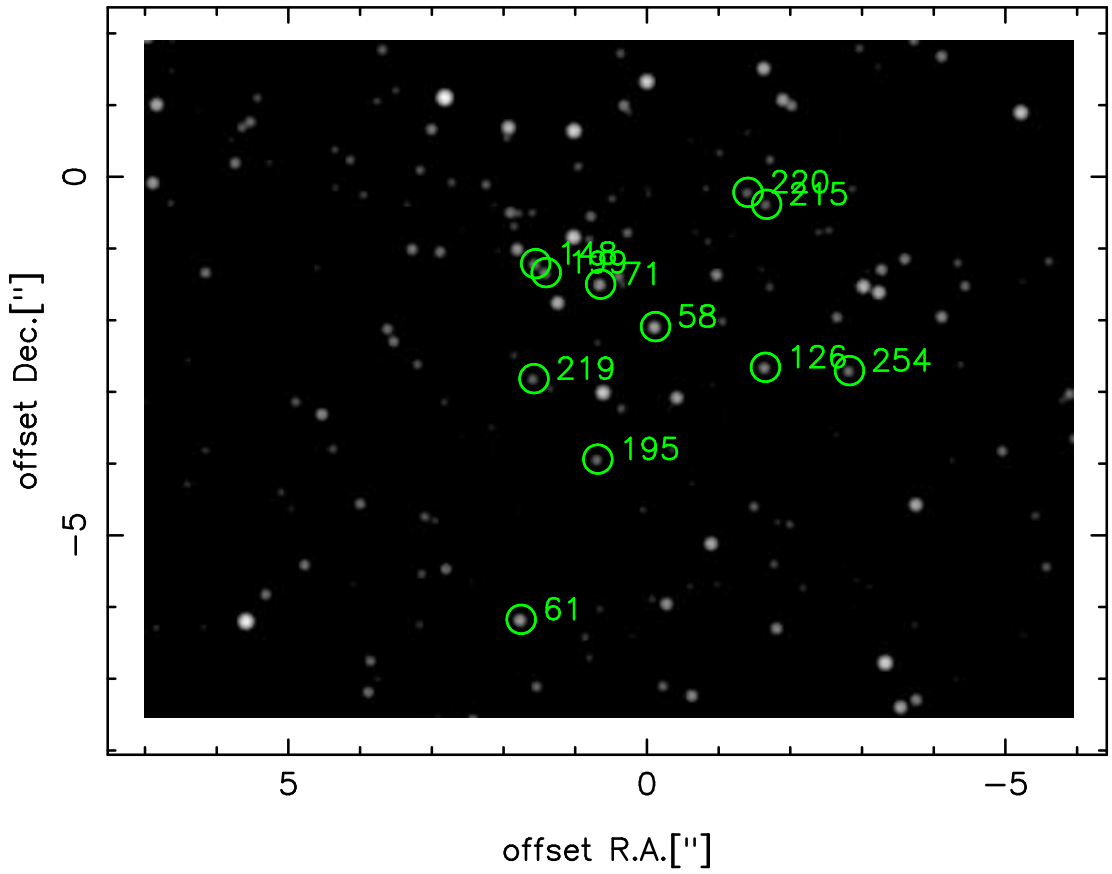

Figure 5.2: Sources used for the primary calibration. Numbers correspond to the numbers in the common list, as also shown in Tab.5.1.

The continuous extincted blackbody spectra were converted to 8 point SEDs by multiplying them with the transmission curve of each filter (see Fig.5.3, lower left). By comparing these theoretical SEDs with the measured counts of the calibration stars, a calibration factor was calculated for each filter to convert the observed counts of each star into a magnitude. This eliminates the influence of any atmospheric features, since they should occur in all sources and thus also in the calibration sources. The magnitude at 2.24μm was adopted as the Ks-band magnitude of the

Table 5.1: Early type calibration stars, used for the primary calibration (names, types and K band magnitudes according to Paumard et al. (2006), approximate values for T_{eff} from *Allen's Astrophysical Quantities*)

name	ID	mag K	type	T_{eff}
E69	61	11.32	early	
E55	195	12.45	B0-1I	~ 20000
E47	219	12.50	B0-3I	~ 18000
IRS 16SSE1	148	11.90	O8.5-9.5I	~ 32000
IRS 16SSE2	199	12.10	B0-0.5I	~ 20000
IRS 16SSW	71	11.45	O8-9.5I	~ 32000
IRS 33N	58	11.22	B0.5-1I	~ 20000
E22/W10	220	12.73	O8-9.5I/III	~ 32000
E25/W14	215	12.58	O8.5-9.5I	~ 32000
E43	126	12.10	O8.5-9.5I	~ 32000
E53	254	12.31	B0-1I	~ 20000

Table 5.2: Stellar types expected to be observable in the central parsec, considering the distance and the extinction towards the GC. Values taken from *Allen's Astrophysical Quantities*, the types shown here are the ones presented in that work that fall into the observational limits for the central parsec.

early types	mag K	T_{eff}	late types	mag K	T_{eff}
B3Ia	11.80	~16000	M6III	~3200	10.78
O6I	12.12	~36000	M4III	~3400	12.32
O7V	13.92	~36000	M2III	3540	12.92
B0V	14.65	30000	M0III	3690	13.57
B2V	16.03	20900	K4.5III	~4100	14.29
B3V	16.33	~19000	K2.5III	~4300	15.37
B7V	17.51	~13000	G8.5III	~4750	16.42
			G7III	~4900	16.50
			G5III	5050	16.62
			G4III	~5100	16.77
			G0III	~5200	17.27

source, since this band is the closest available one to the center of the Ks-band and not affected by absorption features. For the classification algorithm and the analysis, extinction corrected magnitudes were used, i.e. the measured magnitudes were modified with the difference between the individual extinction of each source and the average extinction. This step eliminates the effect that the variable extinction in the observed region has on the brightness of the sources, which is necessary since the cutoff used for the classification depends on the brightness of the source in question. This step also eliminates the effects of spatially variable reddening on the derived luminosity functions. An average extinction in the central parsec of 3.3 mag was assumed here (but see Schödel et al., 2010b, , who find a value of 2.5 mag, using a steeper extinction law).

$$mag_{ext} = mag_{Ks} - A_{Ks} + A_{avg} \tag{5.2}$$

Here, A_{Ks} denotes the measured individual extinction of each source in magnitudes (in the Ks band), A_{avg} = 3.3 mag is the average Ks band extinction in the central parsec, mag_{Ks} represents the measured Ks band magnitude at 2.24 μm.
After the primary calibration, the sources within a few arcseconds of Sgr A* show SEDs that agree very well with SEDs calculated from template spectra of typical stars (Wallace & Hinkle, 1997). The optimum of the calibration is centered around the region where the primary calibration sources are located (close to Sgr A*), and not around the guide star. With increasing distance from the optimum, the SEDs appear to show systematic deviations correlated over areas of a few arcseconds size. There are unfortunately not nearly enough known early type stars over the whole field to extend the primary calibration to the whole central parsec, so an additional local calibration had to be introduced that makes use of another class of stars that are easy to identify and abundant over the whole field: horizontal branch/red clump (HB/RC) stars. It can be assumed that almost all late type stars with Ks band magnitudes between 14.5 and 15.5 are part of this population. This leaves the problem of telling apart late and early type stars. The criterion for this is the same that is used later on in the final classification: the CO band depth (CBD).

5.1.3 CO band depth as a classification feature

Since only very broad spectral features are visible at the low spectral resolution of the data, it is not possible to determine the exact spectral type of every single source. The feature used to distinguish between early and late types is the region beyond 2.24 μm, where late type stars show characteristic CO band head absorption. At the spectral resolution available here, no individual lines or band heads are visible, but a broad feature like the CO absorption alters the shape of the SED in the corresponding region significantly (see Fig.5.4). The presence of CO band heads causes a significant dip in the SED for wavelengths greater than 2.24 μm. In general,

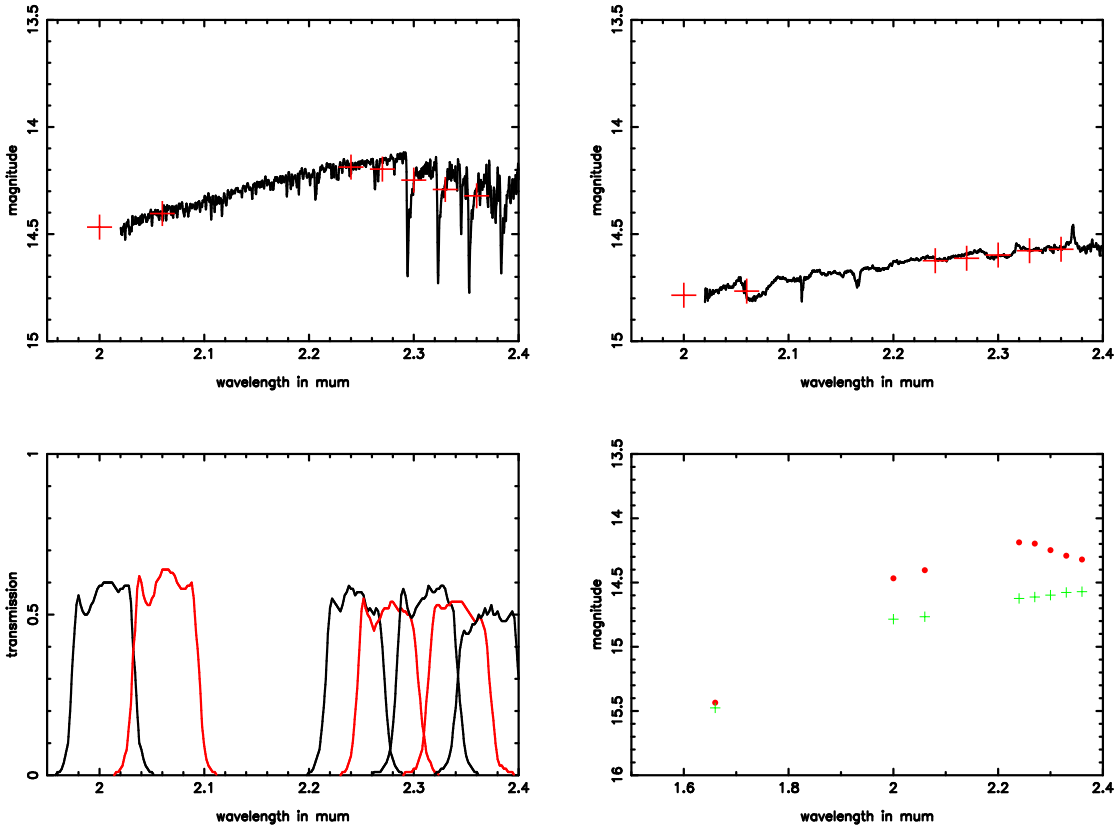

Figure 5.3: Conversion of continuous spectra into template SEDs. Upper left: K4.5 giant spectrum, the crosses indicate the low resolution SED, A_K = 3.3 mag. Upper right: B0 main sequence spectrum, A_K = 3.3 mag. Lower left: transmission curves of IB filters. Lower right: K4.5III and B0V template SEDs with added H band datapoint calculated from effective temperature and extinction.

the presence of this feature leads to the classification of the source as a late type star with this method, while its absence makes the star an early type candidate. Young stellar objects with CO band head emission were not considered in the analysis. If any such objects exist within the data, they would be classified as early-type stars by the algorithm.
This feature also sets the limit for the required photometric accuracy: if a late type source with a Ks band magnitude of 15.5 is expected to show a CO bandhead feature with a depth of 0.1 mag, this corresponds to a difference of ~11% in flux at 2.36 μm and less at shorter wavelengths. Thus, the photometric error should be significantly lower than that value, and the photometric method applied here ensures that for most sources. If the error of a single data-point exceeded 15%, the source was excluded completely.

Table 5.3: Stars close to Sgr A* used to create the HB/RC template. All these sources were classified as late type by the classification algorithm, which serves as another self-consistency test.

ID	mag Ks	ID	mag Ks
3421	15.6	3253	15.7
3369	15.1	2260	15.3
2608	15.6	2248	15.3
2888	15.4	1440	14.6
3896	16.1	2206	14.6
3565	15.1	4448	14.8
4215	15.3	2158	15.0

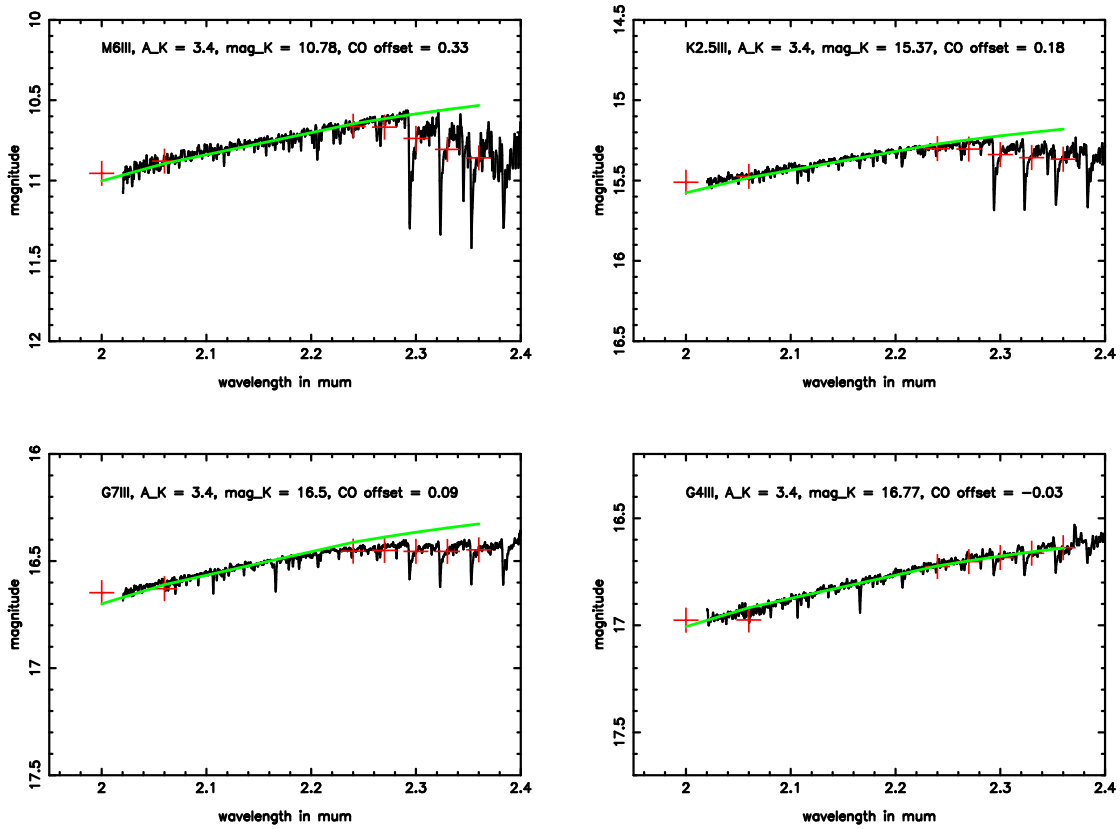

Figure 5.4: Ks-band spectra of late type stars expected in the GC. The crosses mark the corresponding SEDs and the green solid line a fitted extincted blackbody. As can be seen, the CO band heads of G giants are not deep and wide enough to have much influence on the low-resolution SEDs.

The presence of this feature was determined in the following way: an extincted blackbody (T_{eff} = 5000 K, but see §5.1.6 for the effective temperatures used in the final iteration of the fitting process) was fitted to the first 5 data-points ($\lambda \leq 2.27\mu$m). The extinction was varied in a range of 0 to 8 magnitudes in 0.1 magnitude steps. The best fit was chosen based on the reduced χ^2 of the fit. A third order polynomial was then fitted to the complete SED, with the first 5 data-points replaced by the fitted extincted blackbody to ensure a smooth fit. Although it might appear that using only the highest quality filters that are not influenced by possible additional spectral features (like the H band and the 2.24 μm filter) would produce the best results, this would in fact be less reliable than the method used here. Since the GC is a very crowded stellar field, variable AO performance and related variations of the Strehl ratio can cause variations of the measured fluxes of stars. This can easily lead to outliers in the data. Therefore, it is safer to use a larger number of measurements instead of just two or three filters (see §5.1.6 for the special case of AGB stars with intrinsic H_2O absorption features).
For future applications of this method, it would be preferable to also use the intermediate band filter centered at 2.12 μm. The data available at this wavelength had a low Strehl ratio and thus low photometric accuracy. Using the 2.18 μm filter is not advisable, since the data would be influenced by the strong Br γ emission of the minispiral (e.g. Paumard et al., 2004). It would also be possible to make use of the available narrow band filters to probe regions of special interest in the spectra, e.g. Br γ emission or absorption features in early type stars or the 2.20 μm NaI absorption feature in late type stars. But for that, a very careful background subtraction would be necessary to eliminate the strong influence of the minispiral (see e.g. Eisenhauer et al., 2005; Paumard et al., 2006, , the same problem occurs with spectroscopy). Most important would be achieving improved photometric stability and deeper integration.
The shape of both the fitted extincted blackbody and the third order polynomial depend on the local extinction, but the difference between the extrapolated values of the two fits at 2.36 μm

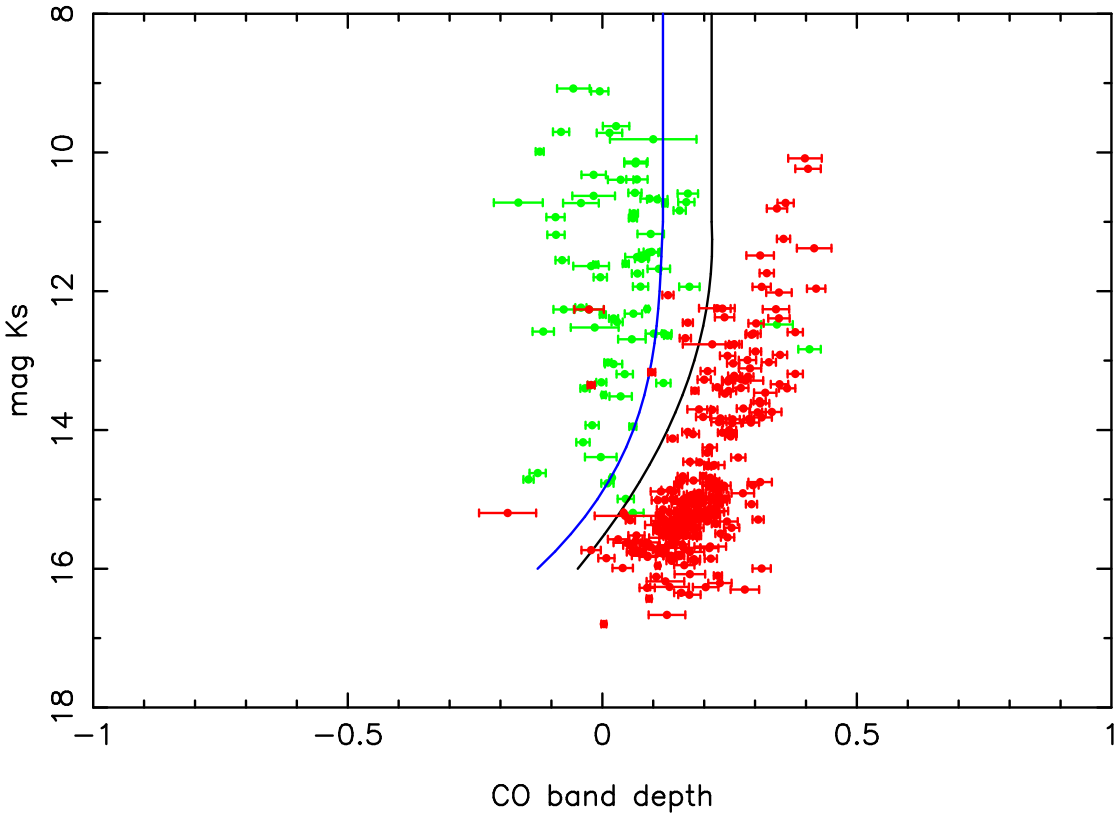

Figure 5.5: CO band depth (CBD) at 2.36 μm for known early type sources found in this sample (Paumard et al. (2006), green) and known late type sources (Maness et al. (2007), red), with the cutoff lines plotted in black (derived from early type sources for inner 12") and blue (based on late type sources, used outside of 12").

is only extremely weakly dependent on extinction. This was tested by artificially reddening a typical late type SED (modeling extinction values of 1.6-6.5 mag) and applying the fitting algorithm to it. The resulting difference of the polynomial and the blackbody varied by less than 0.15%, with slightly higher values for lower extinction. Thus, it can be assumed that this value is independent of the local extinction within an acceptable margin of error, which means it can be used as a good measure for the presence and depth of CO band heads and thus as a classification criterion. But in order to separate early and late type stars based on this value, which will be termed *CO band depth (CBD)* in the following, a reliable cutoff is needed.

5.1.4 Cutoff determination

Although one could expect from template SEDs as shown in Fig.5.3 a CBD close to zero for early type sources and greater than zero for late type sources, which could be separated by a simple general cutoff, the limited signal-to-noise ratio of the data, combined with additional sources of uncertainty, such as photometric errors due to source crowding (see e.g. Ghez et al., 2008) led to considerable scatter in the CBD feature. Therefore, the CBD values of early type stars scatter to positive and negative values. But still, this value can be used as a useful tool to reliably separate early- and late-type stars statistically.
In order to compensate for these difficulties, the CBD values of the sources classified by Paumard et al. (2006); Maness et al. (2007) that are also present in this dataset were compared. As can be seen in Fig.5.5, the early- and late-type sources mostly fall into separate regions when the stellar magnitude is plotted vs. the CBD value. However, there are some (less than 5%) late-type sources present in the early-type region and vice versa. This makes it impossible to use a single smooth cutoff line, let alone a single cutoff value for the whole magnitude range.
Almost all spectroscopically identified early-type sources are concentrated in the innermost 12.9". Therefore, two different smooth cutoff lines were calculated: one that reliably sepa-

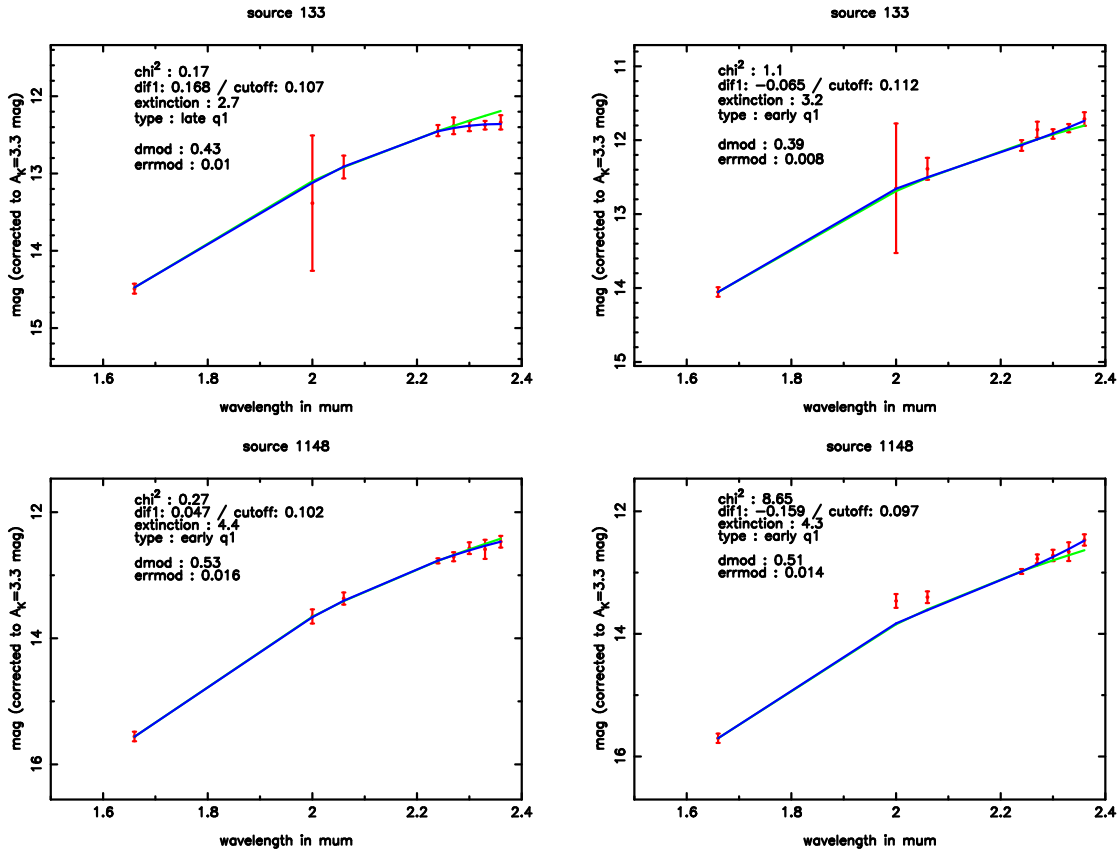

Figure 5.6: Two examples for the effects of the local calibration. Upper right: source fitted as early type, but the SED is noisy which is reflected in the χ^2. Upper left: same source after local calibration, now fitted as late type, with a much better fit. Lower right: source fitted as early type, noisy SED, several data-points do not agree with the fit, large χ^2. Lower left: same source, still fitted as early type, but with much better fit.

rates all known early and late type sources in the inner 0.5 pc, and one for the outer regions that encompassed the known late type sources there (see Fig.5.5). This ensures a more reliable detection of early type stars in the outer region (where the early type density is at best very low. The cutoff line based on the early-type stars will underestimate the number of early type stars, just as using the less strict cutoff based on the late-type stars might overestimate the number of early type stars. Using both cutoff lines allows to estimate the uncertainty of this method.
It was possible to achieve a clear separation of the reference sources with this two-cutoff-method, except a few outliers and noisy sources (see §6.2).
The theoretical lower magnitude limit of this method is determined by the presence of deep enough CO band heads so that the CBD significantly exceeds the photometric uncertainties. This was determined from the Wallace & Hinkle (1997) spectra to be the case for M, K and brighter G giants, corresponding to ~15.5-16 mag at the distance and extinction towards the GC. Fainter G giants and early type stars fainter than B2 have almost identical CBD values (see Fig.5.4). The comparison with published spectroscopic identifications and the shape of the CBD vs. magnitude plot (Fig.5.8) justified the adoption of a magnitude limit of 15.5.

5.1.5 Local calibration

With a classification criterion and a reliable cutoff in place, it was possible to apply a local calibration that significantly improved the results.
Previously published K-band luminosity functions of the central parsec (e.g. Genzel et al., 2003; Maness et al., 2007; Schödel et al., 2007) have shown that the magnitude range of 14.5 to 15.5 is dominated by HB/RC stars outside of the innermost arcsecond. In addition, the density of early type stars decreases steeply outside of the innermost arcsecond (Genzel et al., 2003; Paumard

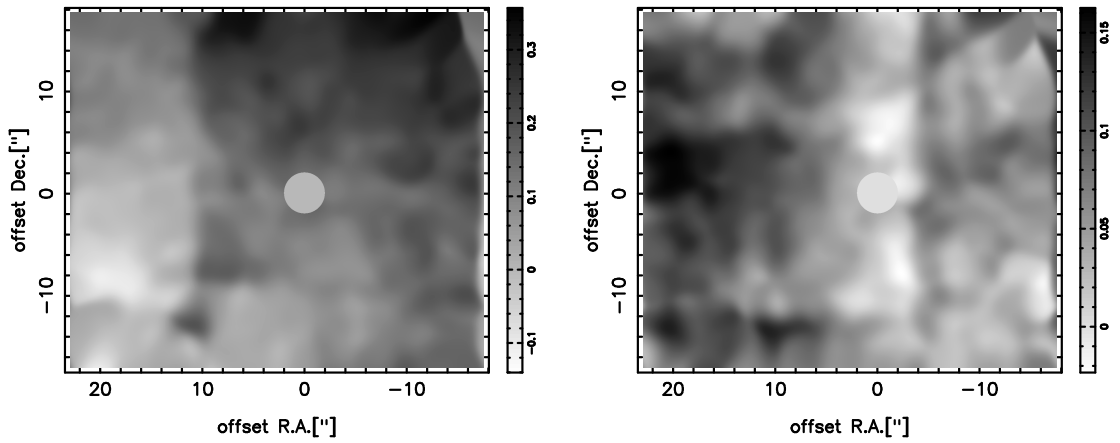

Figure 5.7: Examples of the calibration maps used for local calibration (see §5.1.5) in the 8 bands. Left: 2.00 μm. Right: 2.33 μm. A central region with a radius of 2" was excluded, the calibration factors were set to 0 there. Residuals of the rectangular dither pattern that was applied in the observations can be seen in the calibration maps.

et al., 2006; Lu et al., 2009). So even without knowing the exact type of every source in this magnitude range, they can be used as calibration sources assuming a typical late type SED. This template was determined as the average SED of 14 manually selected late type reference stars (see Tab.5.3) located close to the optimum of the calibration. These stars were selected based on the similarity of their SEDs to the expected shape.
After this, the HB/RC sources in the whole field except the innermost 2" were selected based on two criteria: an extinction-corrected magnitude between 14.5 and 15.5 and a CBD value above the cutoff. The SEDs of these sources were compared to the template HB/RC SED corrected for the determined individual extinction value. This yielded a calibration factor for each source in each band. Due to the uniform distribution of HB/RC sources over the field, these values map the local deviations and can be used to calibrate the SEDs of all sources. The calibration factors were checked for outliers first. If a calibration factor exceeded the median over the closest 20 sources by more than 3σ, it was replaced by that median. On average, 20 sources are contained within an area of $\sim 2 \times 2$", depending on the position in the field. This already leads to a spatial resolution of $\sim$2". The factors were then processed into 8 calibration maps by smoothing the raw maps with a Gaussian with a 2" FWHM (see Fig.5.7).
The final cutoff to be used in the actual classification procedure was calculated in the same way as described in §5.1.4, but with the locally calibrated values for the reference sources. This turned out to be a minor adjustment, so the local calibration process did not have to be reiterated. This local calibration eliminates most systematic local deviations and allows a more reliable classification of the sources towards the outer edges of the field (see Fig.5.6).

5.1.6 Source classification

The fitting process described in §5.1.3 was repeated on the calibrated data. The extinction, CBD, the χ^2 of the fitted polynomial and the uncertainty of the CBD were calculated for each source in several iterations (see below). The reduced χ^2 value for the last five data-points of the polynomial fit was used as a criterion for the quality of the fit. Using a reduced χ^2 for all eight data-points makes less sense than the method used here, since, on the one hand, the first five data-points are replaced by the fitted blackbody for the polynomial fitting, and on the other hand, the first data-points do not have a large influence on the classification anyway. In order to allow a realistic comparison to the cutoff for the final classification, the uncertainty of the CBD was calculated as the average root-mean-square deviation of the last five data-points to the polynomial fit. This value deliberately ignores the individual photometric uncertainties of the data-points, because sources with noisy SEDs with large uncertainties for the last data-points that are crucial for the classification would otherwise have a similar CBD uncertainty as sources with smooth SEDs with the last data-points close to the fitted blackbody. This could lead to

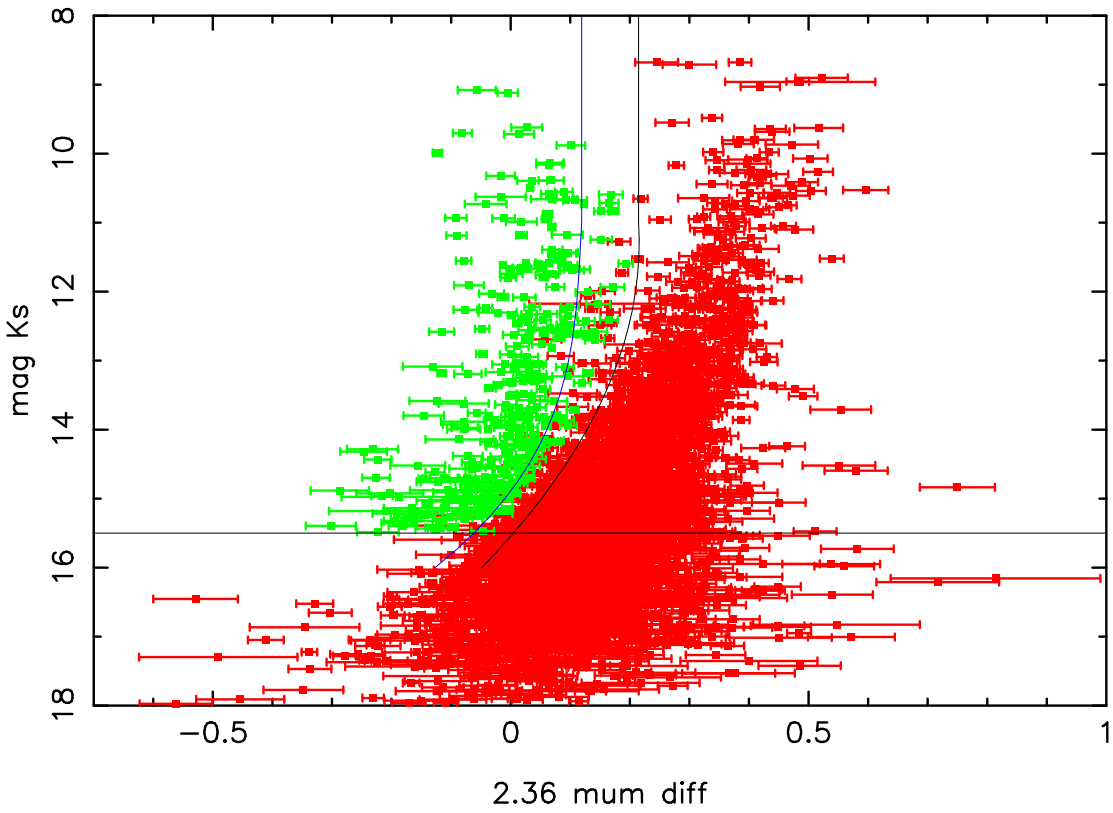

Figure 5.8: CO band depth at 2.36 μm for the sources in the central parsec of the GC, with identified early type (green) and late type (red) sources, separated by the inner (black) and outer cutoff (blue solid line).

erroneous classifications and is not desirable.
The sample of 5914 stars was separated into the following classes:

1. Noisy sources: if the reduced χ^2 of a source was higher than 1.5, this source was rated as too noisy for classification (334 sources). The cutoff of 1.5 was chosen because it excludes the 5% most noisy sources.

2. Foreground sources: these stars are not part of the population of the central parsec and have to be removed prior to any analysis. They are easily recognizable by their low fitted extinction value. Every source with a fitted extinction of less than 2 magnitudes was rated as a foreground source here and excluded. 58 sources were classified as foreground sources.

3. Very red objects: several very strongly reddened objects (like e.g. IRS 3) can be observed in the field. Their SEDs are influenced by other effects in addition to their intrinsic stellar features, e.g. dust shells and bow-shocks. These sources were also excluded from the further analysis since they cannot be compared easily to normal early or late type stars. Sources with a fitted extinction of more than 5 magnitudes were classified as such an object (24 sources). The high fitted extinction here is just a selection criterion that results from the algorithm. The real extinction towards the sources cannot been determined because of the unknown intrinsic SED of the very red objects.

4. Early type sources (quality 1-3): the CBD of every source brighter than 16 magnitudes (extinction corrected) was compared to the applicable cutoff based on their distance to the center: sources closer than 11.9” were compared to the inner cutoff, while any source further away than 11.9” was compared to the outer cutoff. Sources with a CBD below the cutoff were rated as preliminary early type candidates and fitted again with T_{eff} = 30000 K which comes much closer to the actual effective temperatures of early type stars than

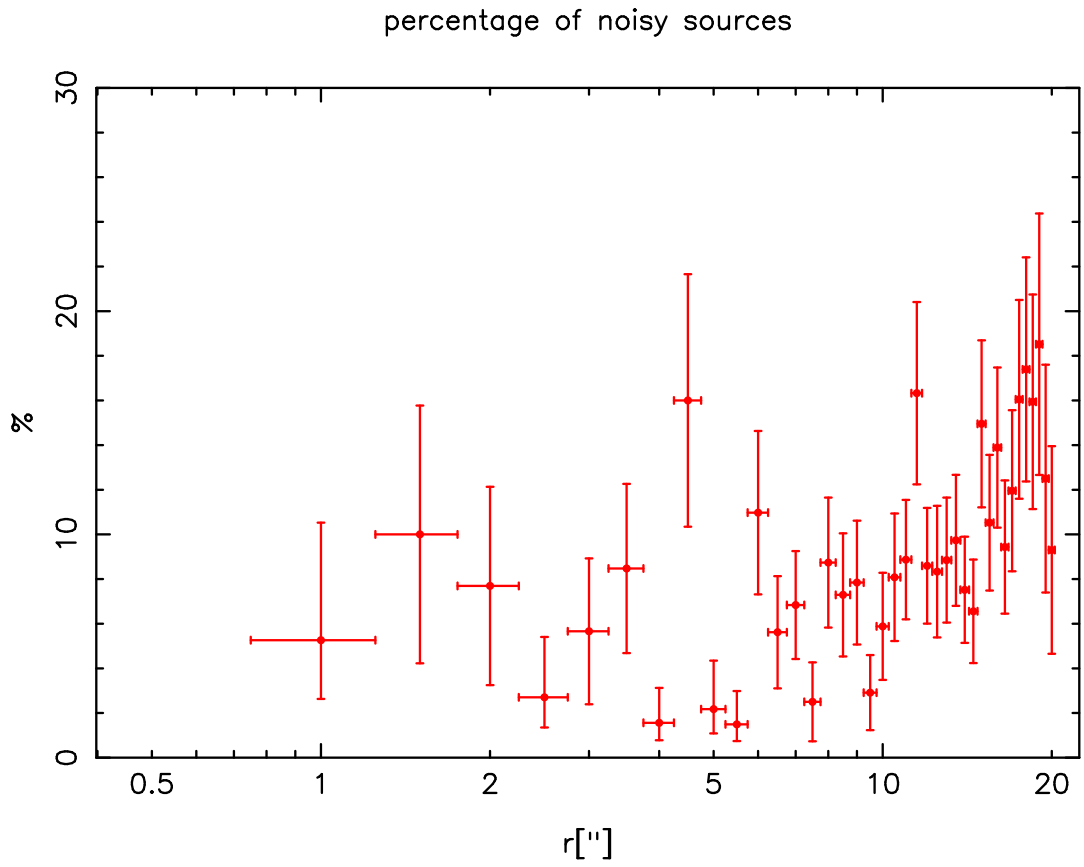

Figure 5.9: Azimuthally averaged density of stars with noisy SEDs. The density profile is practically flat over the inner 15", with a slight increase further out.

the 5000 K that were used in the initial fit. A 30000 K blackbody has a flatter slope in this wavelength regime than a 5000 K blackbody, so the fitted extinction and the CBD that results from the fit also differ. The updated CBD value was compared to the cutoff again. Only sources brighter than 15.5 magnitudes (extinction corrected) were considered. The extinction fitted in this iteration exceeded the previous value by up to ~0.5 due to the flatter slope of the blackbody. This explains the higher magnitude cutoff used in the first step. A classification of fainter sources is not possible with this method, because the depth of the CO band head feature becomes too shallow (Wallace & Hinkle, 1997). If the CBD was more than 3σ lower than the cutoff and the SED was not too noisy (reduced $\chi^2 < 1.5$), the source was rated as an early type with quality 1 (highest quality, 277 sources). If CBD was between 2 and 3σ lower than the cutoff, the source was rated as an early type with quality 2 (25 sources). Sources with a CBD 1-2σ below the cutoff were rated as early type quality 3 (10 sources).

5. Late type sources (quality 1-2): all other sources that did not meet the cutoff criterion to qualify as an early type candidate were fitted again with T_{eff} = 4000 K. This value is typical for the expected late type giants. This again resulted in different extinction and CBD values. The uncertainties of the CBD and the reduced χ^2 of the fit were calculated in the same way as for the early type stars. If the CBD exceeded the cutoff by more than 1σ and the magnitude of the source was brighter than 15.5, the source was rated as a late type star, quality 1 (2955 sources), the others were rated as late type, quality 2 (2231 sources). The late type quality 2 sources are neglected in the analysis of the late type population, since this method does not allow to separate them clearly from early type stars any more.

6. AGB stars: AGB stars are among the brightest sources in the field. Due to their prominent H_2O absorption feature, they are usually fitted with a too flat blackbody/polynomial: the absorption feature leads to a higher magnitude at 2.00 and 2.06 μm that drags the fitted

blackbody and the polynomial "down". This can lead to a CBD below the cutoff and a classification as an early type star. To counter this effect, all sources were checked whether or not these two data-points were more than 1σ below the fitted blackbody. If that was the case, the fitting was repeated without them. When the resulting classification changed, the updated class was adopted as the better result. Putting these objects in a separate sub-category was not deemed necessary, but such a modification could be a way to further improve the classification of early type stars and remove false candidates. Source 1049 is a good example for this effect, especially since it has been identified spectroscopically as a late type source by Maness et al. (2007). This addition to the algorithm resulted in 8 less candidates for early type stars in total, which does not have a big impact on the results as a whole, although it has a noticeable effect on the density distribution in the outer region of the observed area.

Using only two different values for T_{eff} to fit early and late type candidates turned out to be sufficient, since the variations in the fitted extinction stayed within ±0.1mag when the minimum respectively maximum values for T_{eff} as shown in Tab.5.2 were used for the respective classes of objects. The extinction was only determined in steps of 0.1 mag in the first place, so this slight uncertainty can be considered acceptable.

5.2 Polarimetric datasets

5.2.1 Deconvolution-assisted large scale photometry

For all data-sets except the 2011 data, the individual exposures were combined to a mosaic. All photometry was conducted on these mosaics.
Accurate photometry is crucial for polarimetry, especially when the polarization of the targets is of just a few percent. This is the case for the sources in the central parsec in the H-, Ks- and Lp-band, and the effects of crowding and variations of the point-spread-function (PSF) over the FOV complicate photometry even more. For the very bright sources in the FOV, such as the IRS-16 and IRS-1 sources and the extended sources IRS-21 and IRS-1W, crowding is not an issue, but saturation can lead to additional problems. Another problem lies in the presence of extended structures especially in the Lp-band, as this complicates the reliable detection of point sources in the vicinity. These effects have to be countered effectively in order to achieve low photometric errors.
For the deep high-quality data-sets (P1, P2, P4), another photometric method recently presented by Schödel (2010a) was adopted: first, the StarFinder IDL code (Diolaiti et al., 2000) was used to repair the cores of saturated sources (only necessary for some very bright sources in the H-band image) and extract a PSF on the full image from sufficiently bright and isolated sources. For this first step, the most suitable source would again be the guide star IRS 7 itself, since it is several magnitudes brighter than any source within several arcseconds, but this source was not covered by the FOV of all datasets. A PSF determined from several IRS 16 and IRS 1 sources was used instead. Unfortunately, the most suitable of these sources were only contained in the FOV of the Ks-band data, but not covered in the H-band. Since this process is designed to determine the faint wings of the PSF accurately (see Buchholz et al., 2009; Schödel , 2010a), it works worse the fainter the initially used PSF sources are.
This PSF was used for a linear deconvolution (see §3.3). Local PSF fitting photometry was then applied by using StarFinder on overlapping sub-frames of the deconvolved image (~3"×10.6", this generates large overlapping regions and ensures that enough bright sources are contained in each subfield for PSF estimation). This method significantly reduces source confusion and also minimizes systematic errors introduced by variations of the shape of the PSF over the FOV due to anisoplanasy. Despite the relatively small FOV, this effect still occurs since the distance and the angle to the guide star change considerably over the field.
The resulting fluxes in all four channels were normalized to an average of one over all channels for each source and then merged to a common list of sources detected in all channels of each sub-frame. The sub-frame lists were then merged to a common list of all detected sources.
Fig.5.11 show the photometric uncertainties in the H- and Ks-band (data-set P2 only). Only sources brighter than 16 mag (Ks-band) respectively 18 mag (H-band) and with relative photometric errors of less than 3% respectively 6% were used in the subsequent analysis. The lower

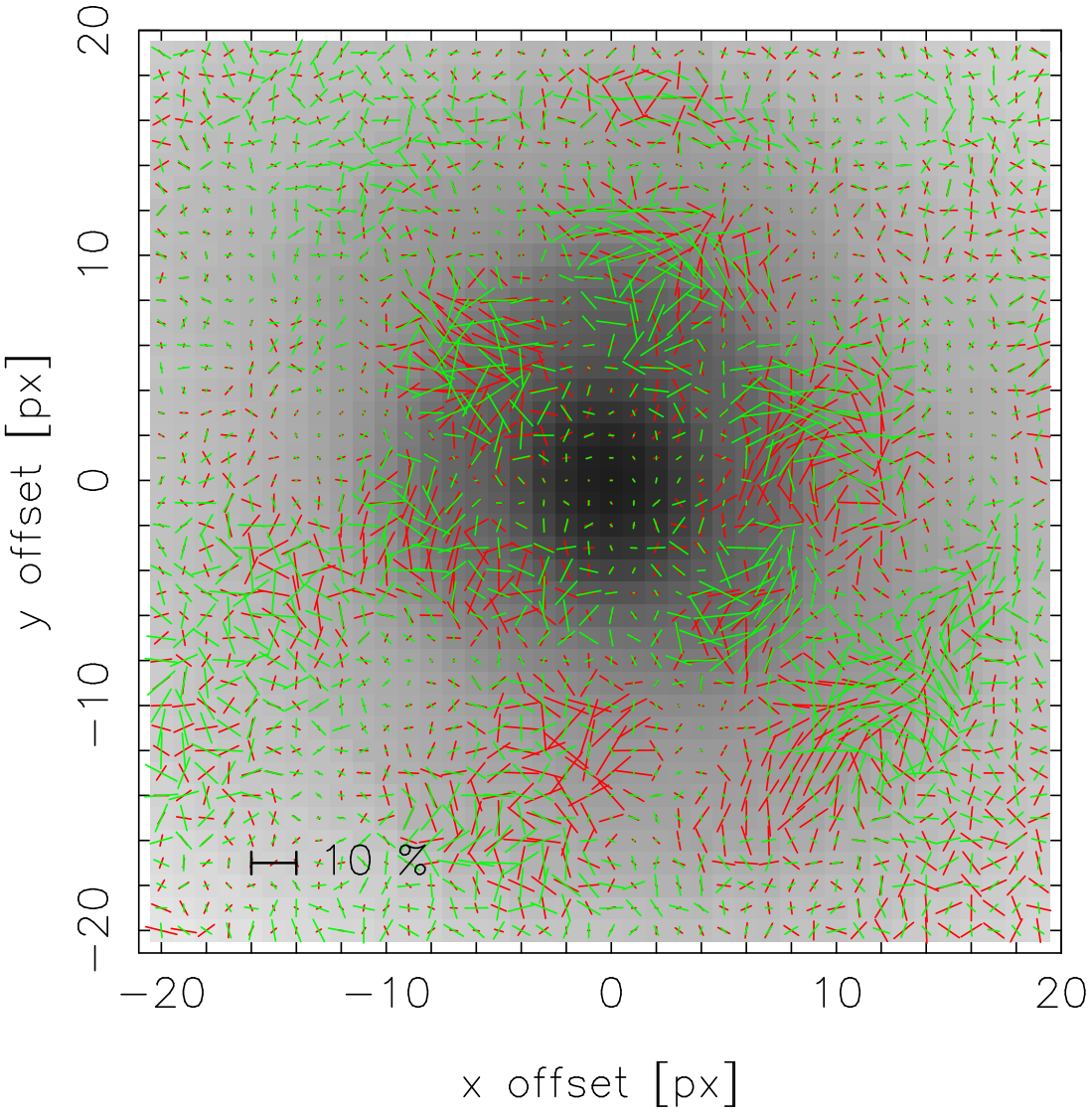

Figure 5.10: Polarization pattern of the PSF used for the first step of the deconvolution-assisted photometry. Red: PSF determined from IRS 16 sources. Green: PSF determined from IRS 1 sources.

brightness limit was chosen in order to avoid problems with insufficient completeness and unreliable photometry, as the errors increase drastically for fainter sources.
In order to counter the effects of the lower depth and data quality of the March 2011 data (P16, P17), different photometric techniques were applied to these data-sets (see §5.2.5).

5.2.2 Error estimation

In general, several effects can contribute to the total flux uncertainty: the basic uncertainty in the counts measured for each pixel, the insufficiently determined PSF (respectively the fact that a PSF determined from several bright sources does not fit every source perfectly) and possible effects of insufficient calibration (e.g. errors in the sky or the flat-field).
When using StarFinder, the formal flux error given by the algorithm represents the first of these three contributions. The algorithm however assumes an independence of all the pixels respectively their measured counts. This is not the case anymore for a deconvolved image. Schödel (2010a) circumvented this problem by introducing a modification factor for these formal errors (determined by simulations). Due to the different instrument setup used here, it was not possible to simply adopt the same factor.

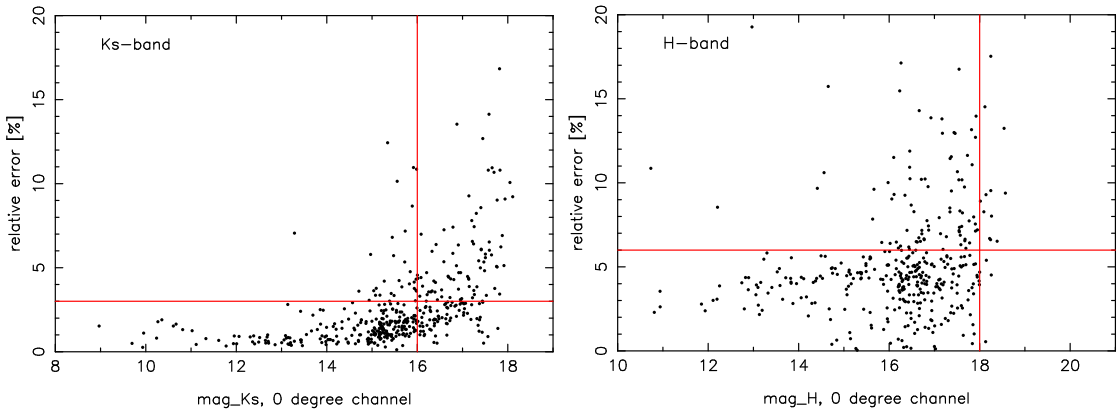

Figure 5.11: Total relative flux errors of the sources detected in the Ks- (upper frame) respectively H-band (lower frame). Only the 0° channel is shown here, but the error distribution is very similar in the other three channels. The values are based on variations between the fluxes measured for the same source at different dither positions. The red lines denote the 16/18 mag respectively 3/6% upper limits (see §5.2.2).

The second contribution stems from a variation of the PSF over the FOV. Generally, the shape of the PSF changes with the relative position of the source to the guide star (anisoplanasy), with greater projected distances leading to higher distortions. The extent of this behavior is highly dependent on the data quality respectively the seeing. The correlation factor provided by StarFinder describes this effect, as it measures how well a source matches the PSF, but it is not clear how to translate this into a flux uncertainty. Therefore this effect was estimated in another way here: three different PSFs were extracted from the western, central and eastern region of the FOV and used for PSF fitting with StarFinder. As it turned out, this does not only produce different fluxes in all 4 channels, but can also lead to a shift in polarization angle and/or degree (depending on the source). A similar effect can be seen when comparing fluxes and polarization parameters measured in different sub-frames of the deconvolved image.
These measurements were compared to aperture photometry applied to two bright sources (IRS 16C, IRS 1C). The results are shown in Figs.5.14,5.15. In general, the values determined by aperture photometry are matched better by the PSF-fitting values the closer the PSF reference sources are to the source in question. The deviations can reach values of up to 1.5% respectively 10° even for these bright sources.
The reason for this behavior is revealed by a closer look at the individual PSFs: these show a polarization themselves, and that pattern changes over the FOV (see Fig.5.10, the polarization vectors are almost perpendicular in several locations, even in areas with significant flux). This lead to the conclusion that the fluxes determined with a ”nearby” PSF are more accurate than those determined with a ”distant” PSF, and therefore the application of a weighted average (based on the distance of the individual source to the average position of the PSF stars) to the photometry on the deconvolved sub-images seems justified. The results provide a better match to the aperture photometry (though it has to be cautioned that the latter is problematic in crowded regions and where large scale extended emission is present, which is why this method is not applied to the image as a whole). The standard deviation of the fluxes over the sub-frames provides an estimate for the contribution of this effect to the total uncertainty.
Using these error contributions to estimate the final, total uncertainty is problematic: the sub-frames are all taken from the same mosaic and are thus not independent measurements, the formal errors given by StarFinder are unreliable and generally far too small for brighter sources, and possible calibration problems (sky, flat-field) are not covered at all.
Therefore, a different approach was used to determine the total flux errors: the same photometric method that was used on the full mosaic was applied to mosaics created from 8 sub-datasets, selected based on the dither position along the East-West axis. This led to sub-sets of about 15 images per dither position, and the resulting mosaics have the same depth respectively signal-to-noise ratio everywhere. Since the original images can be regarded as independent measurements, so can the resulting mosaics, with the additional advantage that fainter stars still have a sufficient

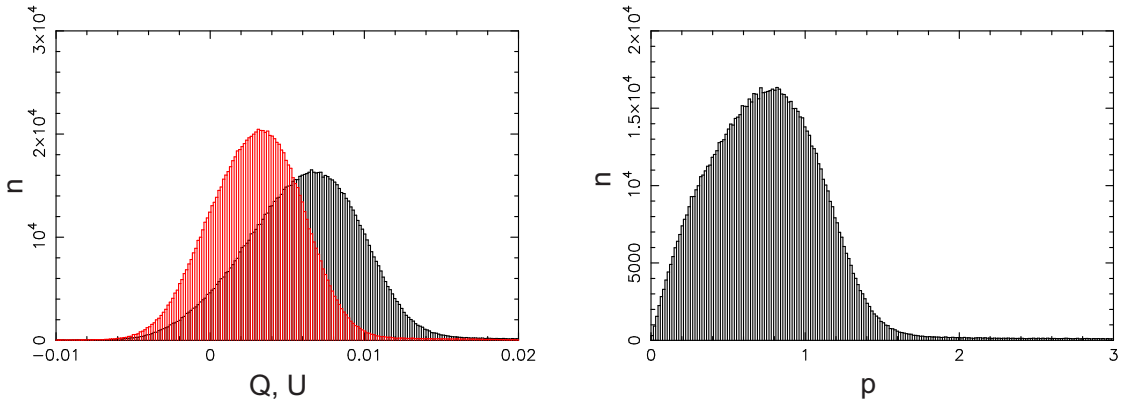

Figure 5.12: Stokes parameters Q and U (left frame) and resulting polarization degree (right frame), measured for each pixel in a wiregrid flat-field.

signal-to-noise ratio (as compared to individual images). The downside of this approach is that all sources in the eastern- and westernmost ~2" are contained in only one of these sub-mosaics. The standard deviation of the fluxes measured in these sub-mosaics was then adopted as the photometric error of each source.
The aperture photometry applied to individual frames shown e.g. in Fig.5.14 reveals two other effects: the measured flux varies over the frames, and in addition to the instrumental polarization (most prominently the "bump" in p), small variations in Q and U (and subsequently p and θ) can be observed. These variations correspond to the dither pattern used in the observation, and they probe the different areas of the Wollaston prism respectively the detector. These deviations are much smaller than the photometric errors, however, so they can be safely neglected respectively averaged over.
Witzel et al. (2011) determined the system-intrinsic systematic uncertainty of polarimetric observations with NACO as 1% in polarization degree and 5° in polarization angle. For a source with 5% polarization (a typical value for GC sources in the Ks-band), this already corresponds to a relative error of 20%. The required accuracy of the photometry so that the final polarimetric errors stay below 3 times (respectively 6 times for the H-band) the systematic uncertainty was simulated. Higher uncertainties in the H-band can be tolerated since the higher polarization there leads to a lower relative error for the same absolute uncertainty of the polarization degree. This led to error thresholds of 3% in the Ks-band and 6% in the H-band. Most of the sources brighter than 16 respectively 18 mag (Ks/H) have errors below these thresholds (see Fig.5.11). This leads to the final error of the polarization parameters being dominated by the statistical photometric errors.

5.2.3 Photometry on extended sources

Applying the PSF fitting algorithm to extended sources leaves large residua, and a simple core subtraction with a stellar PSF does not counter any distortions of the extended component produced by the atmosphere and the telescope. But also here, high precision is necessary. Therefore, a different approach is used here: a small region of the mosaic images was deconvolved with the Lucy-Richardson algorithm (the "ringing" produced by the linear deconvolution complicates the photometry of extended features), using the PSF estimated from the complete mosaic. This resulted in a much clearer view of the extended features (see Fig.8.2), while other sources in the vicinity appear point-like.
The resulting images were shifted to a common reference frame. The extended features were then covered with overlapping apertures (~ 27 mas radius), measuring the flux in each aperture. From these fluxes, the polarization at the position of the apertures was determined. For comparison, the same method was applied to the PSF used for the deconvolution (see §5.2.4). In addition, the total polarization of the two known extended sources in the FOV, IRS 1W and IRS 21, was determined by covering them with apertures of 0.25" radius. This allowed a comparison to previous observations.

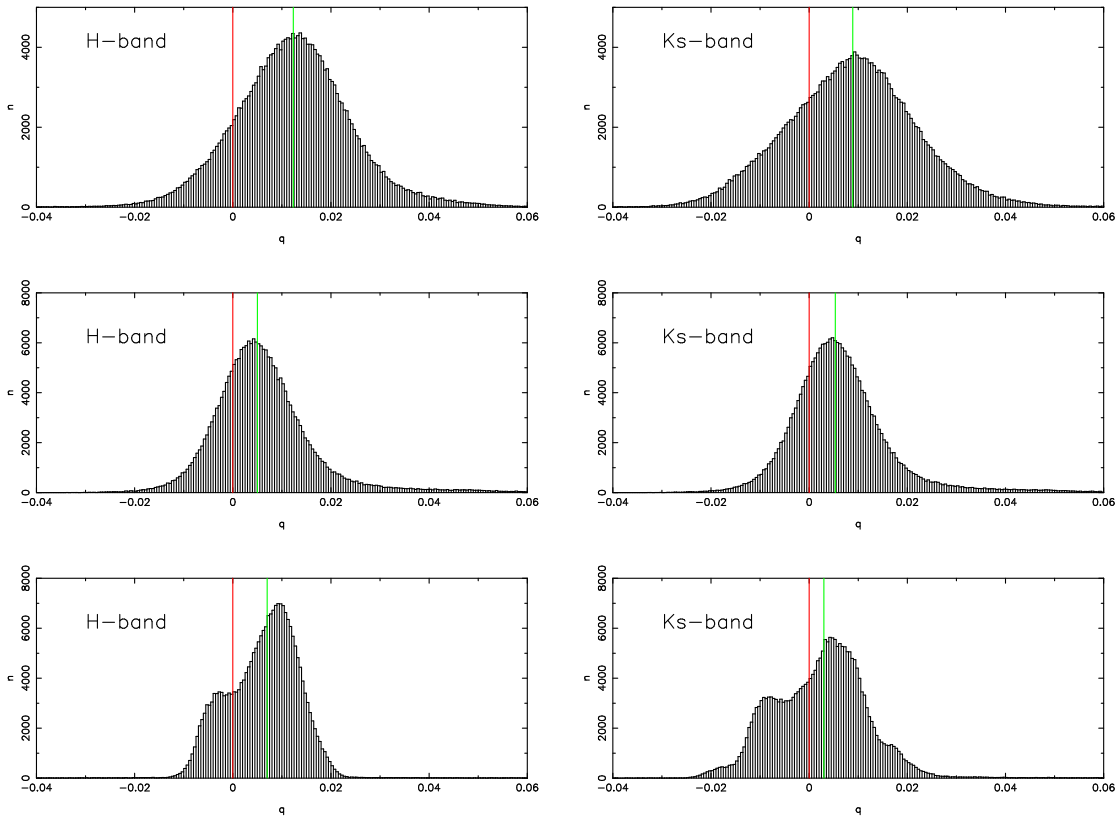

Figure 5.13: Stokes parameter Q measured at each pixel of a flat-field taken with (upper frames) and without (middle frames) the Wollaston prism. The lower frames show Q after dividing the Wollaston flat-field by the flat-field taken without the Wollaston. Left frames: H-band, right frames: Ks-band.

In order to study a possible flux variability of the extended sources (see §8.2), 45 Ks-band and 38 H-band NACO datasets contained in the ESO archive were used (taken between 2003 and 2008). Where the bright point sources were saturated, StarFinder was used to repair their cores. Aperture photometry was then applied to the extended sources and several known bright non-variable sources (see Ott et al., 1999; Rafelski et al., 2006), with additional apertures placed on regions devoid of stars close to the targets in order to get a background estimate. This background was subtracted from the recovered fluxes and the result normalized to the total flux of the chosen non-variable calibration sources for each dataset (the IRS 16 sources except 16SW and 16NE and the IRS 33 sources; IRS 16NE is strongly saturated, while IRS 16SW has been described as an eclipsing binary and therefore shows strong flux variabilities, making it unsuitable as a reference source, see Ott et al., 1999; Rafelski et al., 2006). The uncertainty of each flux measurement was estimated by repeating the aperture photometry on the individual non-mosaiced images of each dataset (which can be assumed to be independent measurements), and adopted the standard deviation of the recovered fluxes as the total flux error. Especially for bright and isolated sources, this yields very small statistical errors of the order of less than 0.5%. Systematic variations of the measured fluxes in the order of about 5% can still be found between the epochs even for sources known to be non-variable on the timescale used here (see Fig.5.16). The latter value provides a more realistic estimate of the photometric accuracy, so an additional flux error of 5% was introduced for all data-points to be able to separate real variability from noise.

5.2.4 LR deconvolution: useful for extended structures?

It is known that Lucy-Richardson deconvolution has a tendency to ”suck up” surrounding flux into a central point source (see e.g. Schödel , 2010a). This impedes or severely hinders the detection of faint sources close to bright ones, introduces astrometric and photometric uncertainties, and makes a reliable background estimation impossible. But unlike linear deconvolution, this

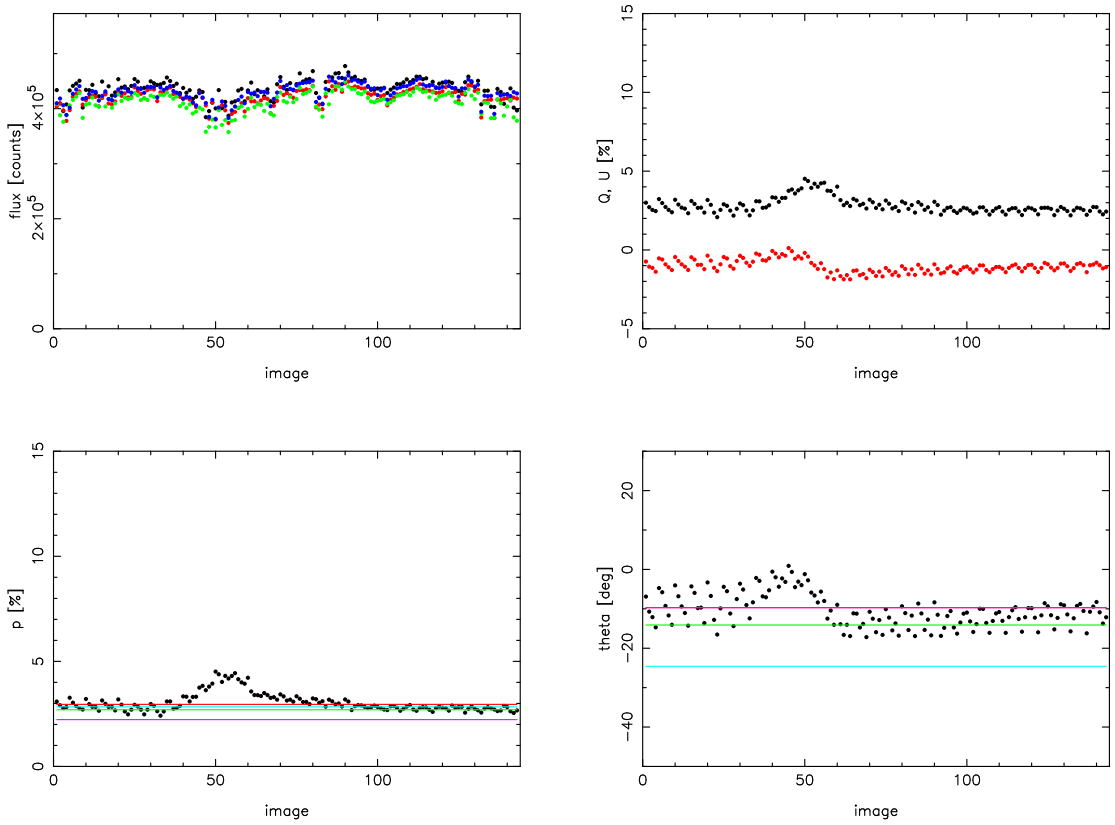

Figure 5.14: Fluxes and polarization parameters of IRS 16C plotted against time of observation. Upper left: flux measured in four channels. Upper right: Q (black) and U (red). Lower left: polarization degree. Lower right: polarization angle. The plotted lines represent the polarization parameters obtained on the complete mosaic by aperture photometry (red), PSF fitting photometry using the IRS 16 stars (light blue) respectively the IRS 1 stars (magenta), respectively the final value after deconvolution assisted PSF fitting photometry (green).

method allows flux measurements on extended structures via simple aperture photometry on the deconvolved images. Can it thus be used to measure the polarization of the extended sources in the GC?
In order to investigate this, images of an artificial bow-shock-like structure next to a point source were created. Several other point sources with different fluxes were added to simulate a crowded field like it is found in the GC. For each filter (0°, 45°, 90° and 135°), all fluxes were modified by a factor calculated for generic polarization parameters of P = 4-5% and δ = -10°-100°:

$$f_{pol,rel} = 1 + P \times cos(\theta - \delta) \tag{5.3}$$

The same was done for the extended feature, with a constant polarization degree of 10% and the polarization angles parallel to the bow-shock structure. An additional foreground polarization of 4% at -15° was then added to the extended feature. The resulting map was convolved with a PSF extracted from the real images. A weakly position dependent background in the shape of a very flat two-dimensional Gaussian similar in level to that found in the actual observations was also added to the images.
These artificial images were deconvolved using the Lucy-Richardson algorithm, followed by aperture photometry on the point sources and the extended structure, mapping the latter with 2 pixel apertures along its length. The structure itself was recovered successfully, although slightly widened. Fig.5.17 shows a comparison of the recovered polarization parameters in comparison to the input values. It appears that the only significant large deviation occurs for the source in the center of the extended feature: the recovered polarization degree is 2.6 percentage points lower than the input value, while the polarization angle is 5° less. This appears to be an effect of the algorithm ”sucking” flux of the extended feature into the central source, thereby changing its

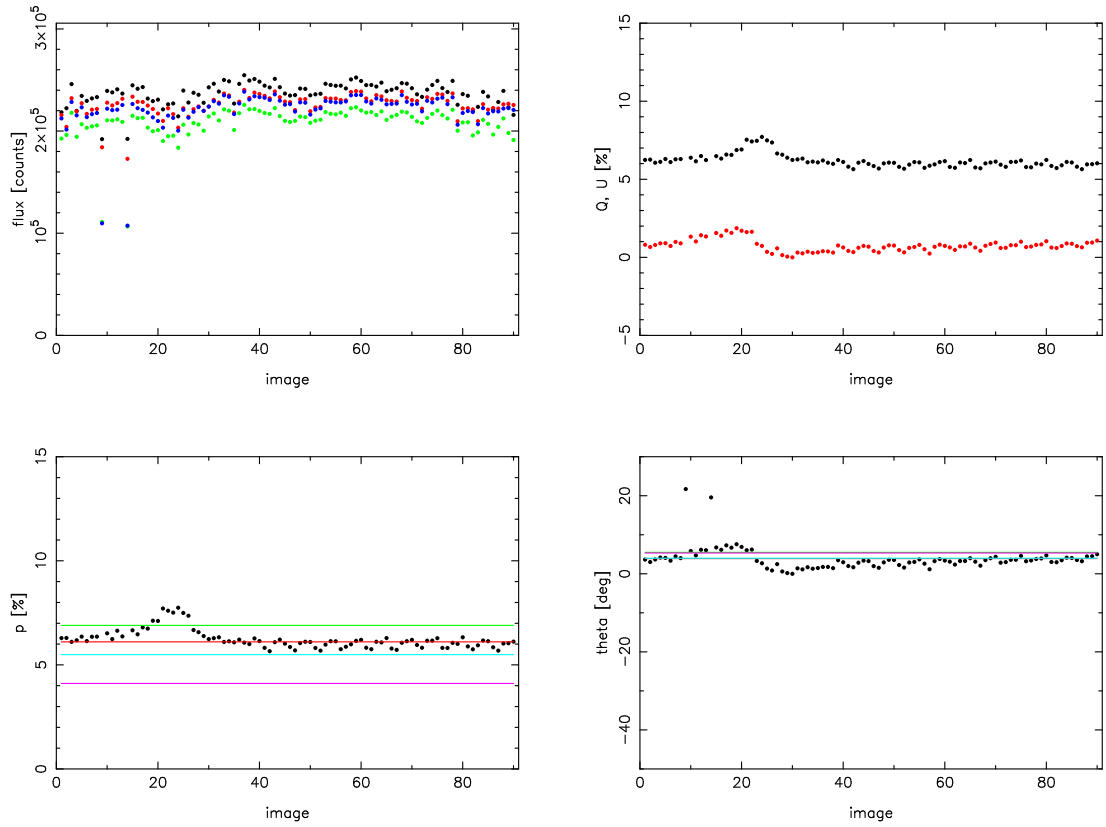

Figure 5.15: Fluxes and polarization parameters of IRS 1C plotted against time of observation. Upper left: flux measured in four channels. Upper right: Q (black) and U (red). Lower left: polarization degree. Lower right: polarization angle. The plotted lines represent the polarization parameters obtained on the complete mosaic by aperture photometry (red), PSF fitting photometry using the IRS 16 stars (light blue) respectively the IRS 1 stars (magenta), respectively the final value after deconvolution assisted PSF fitting photometry (green).

polarization due to the significantly different polarization of the shell. The polarization degrees of several of the very faint point sources were also recovered poorly, while at the same time their recovered polarization angles agreed much better with the input values.
The values recovered for the bow-shock-feature itself show only small deviations compared to the input values, with a maximum difference in polarization degrees of 1.5-2% (less in most cases) and 5-7° in polarization angle. The deviations are even less significant for the brighter stars, with less than 0.5% and less than 1° in most cases. The fainter stars show only slighter higher deviations. This approaches the systematic uncertainties inherent to the instrument. The Lucy-Richardson algorithm can thus be considered sufficiently accurate for the purpose of detecting extended features. The small variances found for the artificial ”bow-shock” also indicate the level of accuracy that can be expected for the polarization parameters determined in §8.2.
Fig.5.10 shows the polarization pattern of two PSFs determined from different bright sources in the FOV (IRS 16 and IRS 1 point sources). There are significant spatial variations, so these variations must occur (to some extent) in all sources in the non-deconvolved images. Since these sources are expected to be essentially point-like before their light enters the atmosphere, polarization patterns like this must be introduced by instrumental or atmospheric effects. This is another reason why deconvolution is an important step to recover polarization patterns of extended sources successfully: the intrinsic patterns would otherwise be masked by the strong spatial variations, with local values for the polarization degree of up to 15% in the PSF pattern (although these values are much lower in the central region with the largest flux, on the order of 1-2%). These effects are removed by the deconvolution process.

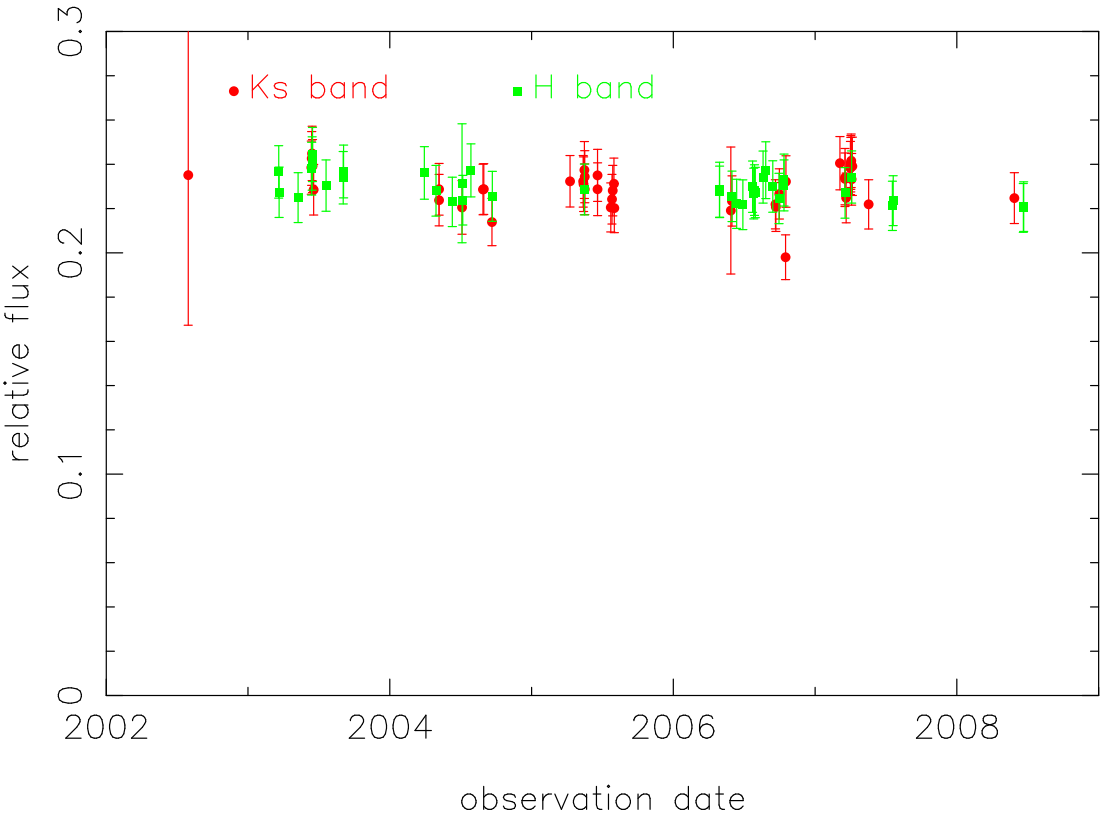

Figure 5.16: H- (green) and Ks-band (red) lightcurve of the known non-variable source IRS 16C.

5.2.5 Large scale aperture photometry

Ks-band

Unlike the older data, where all individual images covered essentially the same FOV in the very center of the GC, the data taken in March 2011 sacrificed depth in order to achieve a much greater FOV. This made mosaic photometry impractical, because the overlapping regions of the images were small, which in turn led to a variable depth over the field.
In addition, the sources detected farther away from the guide star exhibited considerably deformed PSFs. They showed an elongation towards the guide star, a sign of strong anisoplanasy. This effect varied in strength between the individual exposures. About half of the Ks-band exposures had to be discarded because the very low data quality did not allow reliable photometry. This introduced a further complication: in some cases, one of two corresponding 0°/45° images (covering the same FOV and taken in sequence) had a sufficient data quality while the other had to be discarded. Only 21 0°/90° and 25 45°/135° exposures were used, out of 47 taken in total. The different data quality can also introduce offsets in total intensity between the exposures (due to variable AO performance), and this made it necessary to conduct the photometry on each exposure individually.
For this data-set (as well as for the Lp-band data, see below), using PSF-fitting or deconvolution-assisted photometry proved impractical. The guide star IRS 7 was only covered in four of the selected eposures, and while this star would provide an excellent estimate of the PSF including the faint wings, the variation of the shape of the PSF between the different images did not allow to use only this PSF for all other images as well. Local PSF extraction is complicated by the small number of suitable PSF stars in each exposure. The large residua that are produced by using a poorly fitting PSF in this case outweigh any advantage of the photometric methods described above.
It was therefore determined that the best way to achieve reliable photometry on the individual images was aperture photometry, using manually placed apertures for all sources in the FOV. Due to the low depth of the observations, the issue of crowding is far less important than e.g. for the 2009 Ks-band data, especially since precise photometry is not possible for fainter sources

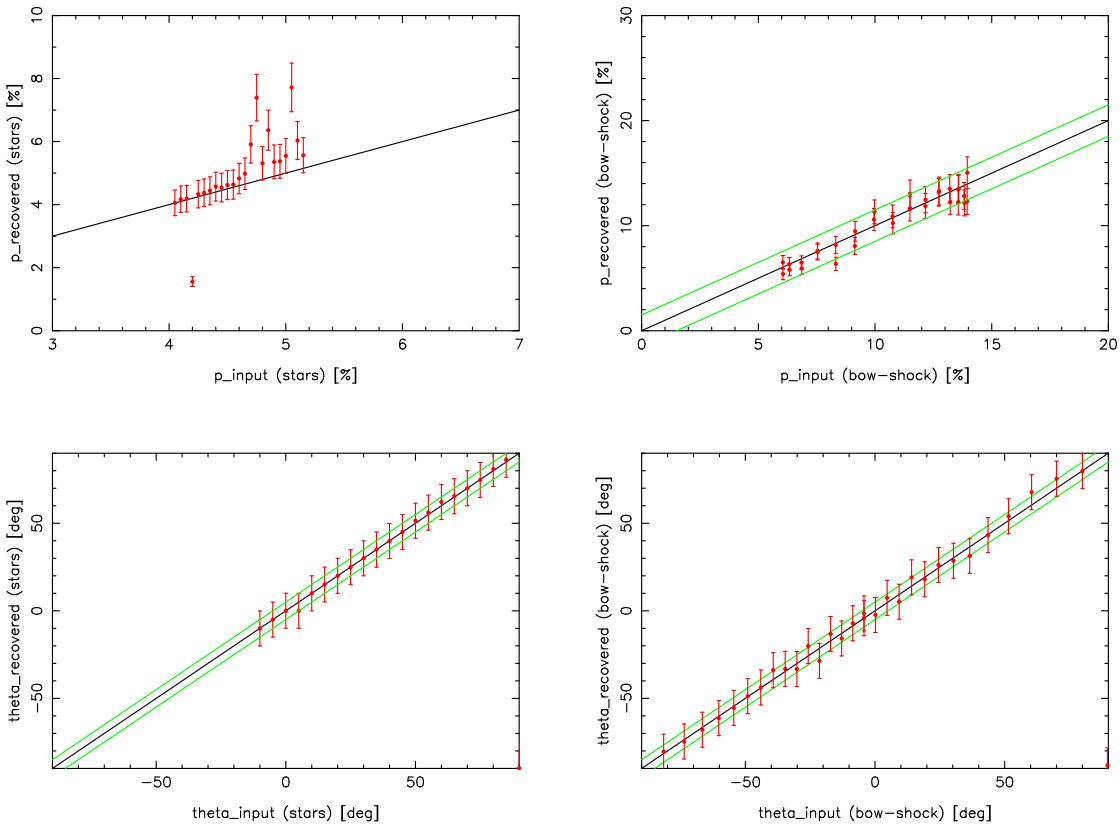

Figure 5.17: Recovered polarization parameters for point sources (left frames) and extended feature (right frames). The green lines indicate a deviation of ±1.5% respectively 5° from a perfect recovery, indicated by the black line.

(15-16 mag) anyway.
The apertures were created based on a mosaic image and were then applied to the sources present in each image. Only apertures fully contained in the respective FOV of each image were used (in order to avoid problems with sources not fully contained in the FOV). The background for each source was estimated using an average over four neighboring background apertures placed in regions with no visible sources. This background flux was then subtracted from the flux measured for the source.
The resulting fluxes were used to calculate the Stokes Q and U parameters for each pair of 0°/90° and 45°/135° exposures (see §5.2.6). These values were then averaged to one Q and U value for each source. This eliminates the bulk of the offset in flux between individual exposures.
The flux errors were determined by calculating the FWHM of the distribution of the fluxes in the background apertures. The value

$$\sigma = \frac{FWHM}{2\sqrt{2ln(2)}} \tag{5.4}$$

was adopted as the flux error per pixel. This led to a total flux error for a given aperture of

$$\sigma_{aper} = \sqrt{2n} \times \sigma \tag{5.5}$$

, with n as the number of pixels contained in the aperture. These flux errors contributed one component to the errors calculated for Q and U (see below). Fig.5.18 shows these flux errors in relation to the measured fluxes. The error distribution shows a clear dependence on the flux, which can be expected since this is basically a Poisson error. This only sets a lower limit for the actual uncertainty of the measured Q and U parameters. The main contribution to the errors that were determined for these values stems from the variation over several exposures (see below).
Using this technique, the fluxes of 148 sources could be measured in a FOV of 8.6”×27.9”.

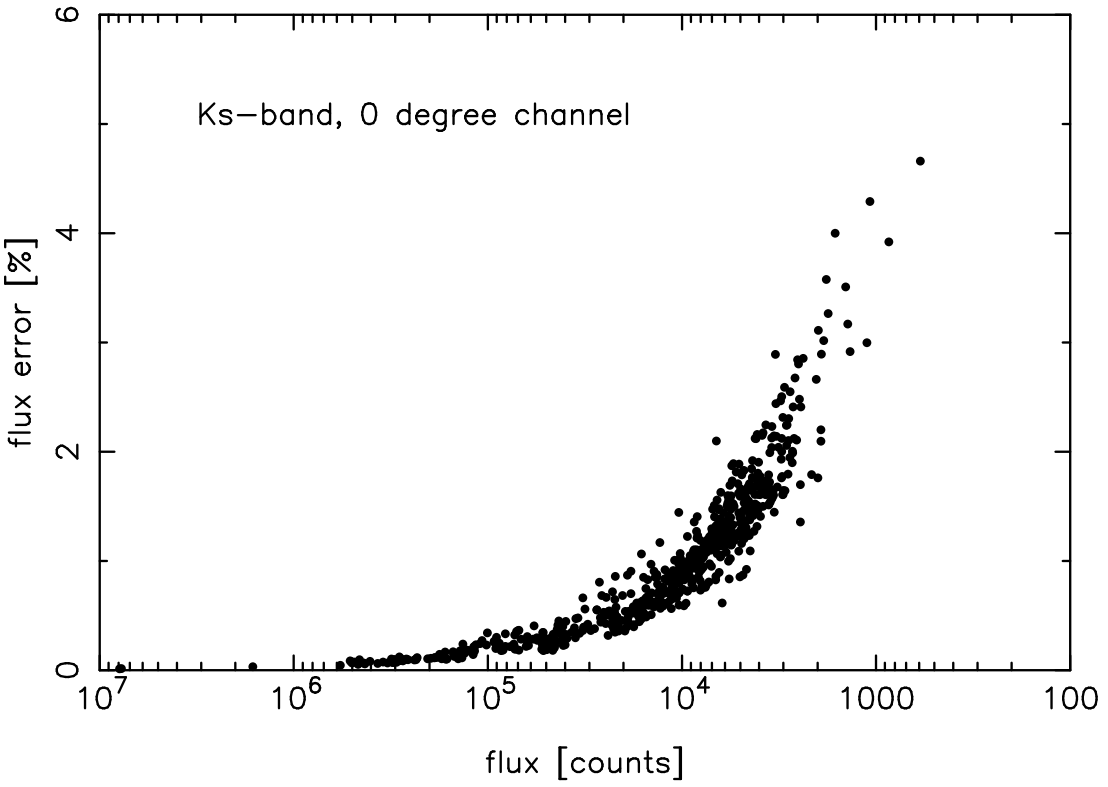

Figure 5.18: Flux errors for the 0 degree channel of the P18 data-set, plotted against the measured fluxes. The errors were determined from the flux variations in background apertures and can therefore only be regarded as lower limit for the actual errors. The other channels show a very similar error distribution.

Compared to the 2009 Ks-band data, the number of detected sources per arcsec^2 is lower by a factor of ∼6. This illustrates the much lower depth and worse data quality of the 2011 data.

Lp-band

The Lp-band images varied much less in quality than the 2011 Ks-band data-set, and all exposures could be used for photometry. The small overlap between the individual images and the fact that most of the FOV was only covered by a single exposure made it necessary to conduct the photometry on the individual images. This was done in a similar way to the Ks-band data-set (see above): the sources in the FOV were covered by manually placed apertures, while the background was determined in a 2 pixel annulus around each aperture. Since the background was shifted to an average of zero for all images before (see §3.1.2), the residual background only contributed a small amount to the total flux measured in each aperture.
Unlike in the Ks-band data-set, each FOV was covered by two corresponding 0° and 45° images. This allowed a direct comparison of the total intensity measured for each source by adding up the fluxes in the 0° and 90° respectively the 45° and 135° channels. For each image pair, the total intensities of all sources were added and a relative calibration factor was determined:

$$c_{totalint} = \frac{\sum_i (f_{00,i} + f_{90,i})}{\sum_i (f_{45,i} + f_{135,i})} \tag{5.6}$$

All fluxes measured in the 45° and 135° channels were multiplied with this factor in order to ensure the same relative flux calibration in all corresponding images. Due to the small overlaps between the images (the two northernmost FOVs showed no overlap at all), a cross-calibration over the full FOV was not possible in this way. Therefore the measured fluxes were normalized to an average of one for each source before combining them to a common list of all detected sources. This ensures that possible differences in flux for sources detected in more than one exposure did not influence the polarization determined for that source.

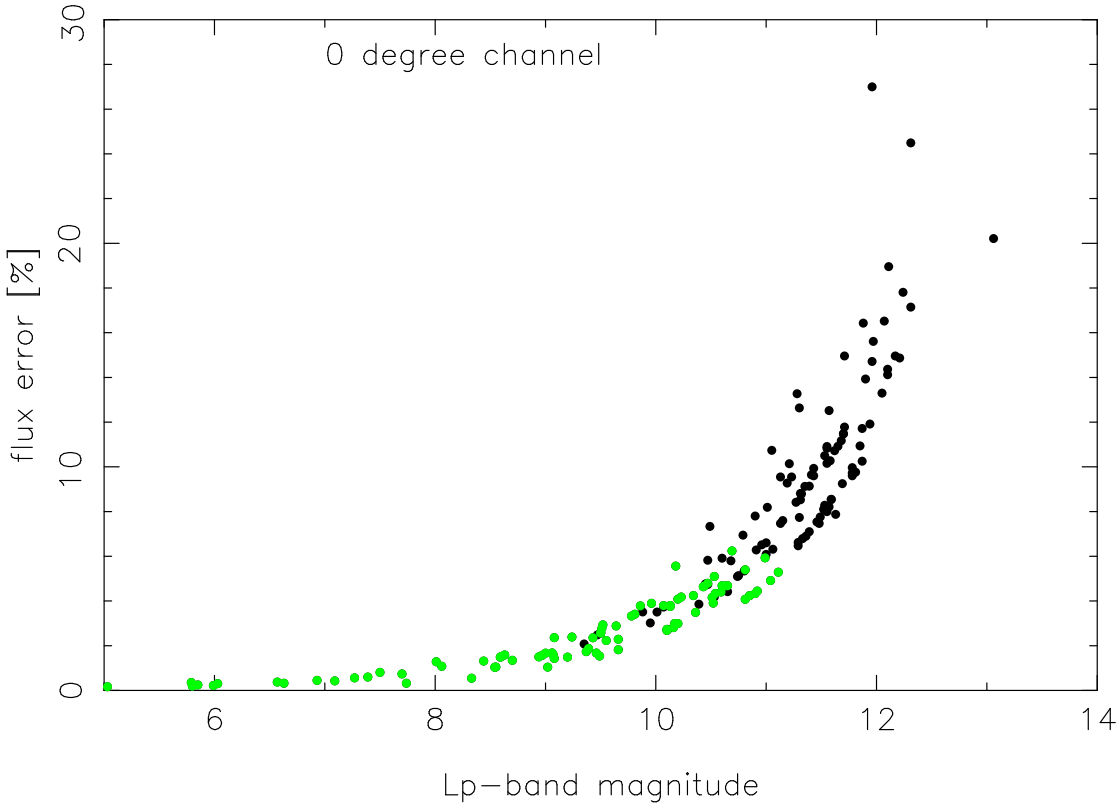

Figure 5.19: Flux errors for the 0 degree channel of the P16 data-set, plotted against the brightness of the sources in magnitudes. The errors were determined from the flux variations in background apertures and can therefore only be regarded as lower limit for the actual errors. The other channels show a very similar error distribution.

The measured fluxes were converted into magnitudes using IRS 16NE as a calibration source. This source has an Lp-band magnitude of ~7.5 (Blum et al., 1996) and shows no variability in the Ks-band (Ott et al., 1999). For a stellar point source, this means that no variability would be expected in the Lp-band as well. Due to possible flux offsets between the sub-fields, this is not an accurate absolute calibration. The resulting Lp-band magnitudes have to be regarded as just an estimate, but that is sufficient for the purposes of this work.
The flux errors per pixel were determined from the FWHM of the distribution of all background pixels of each image (see Eq.5.4), and this value was used to calculate a total flux error for each source (see Eq.5.5). Fig.5.19 shows these errors in relation to the brightness of the sources, and they show the expected distribution of a Poisson error. Only sources with a relative flux error of less than 6% were used in the subsequent analysis. This effectively sets a lower brightness limit of ~11 mag (see Fig.5.20).

5.2.6 Polarimetry

The polarization degree and angle of each source were determined by converting the measured normalized fluxes into normalized Stokes parameters:

$$I = 1$$

$$Q = \frac{f_0 - f_{90}}{f_0 + f_{90}} \tag{5.7}$$

$$U = \frac{f_{45} - f_{135}}{f_{45} + f_{135}} \tag{5.8}$$

$$V = 0$$

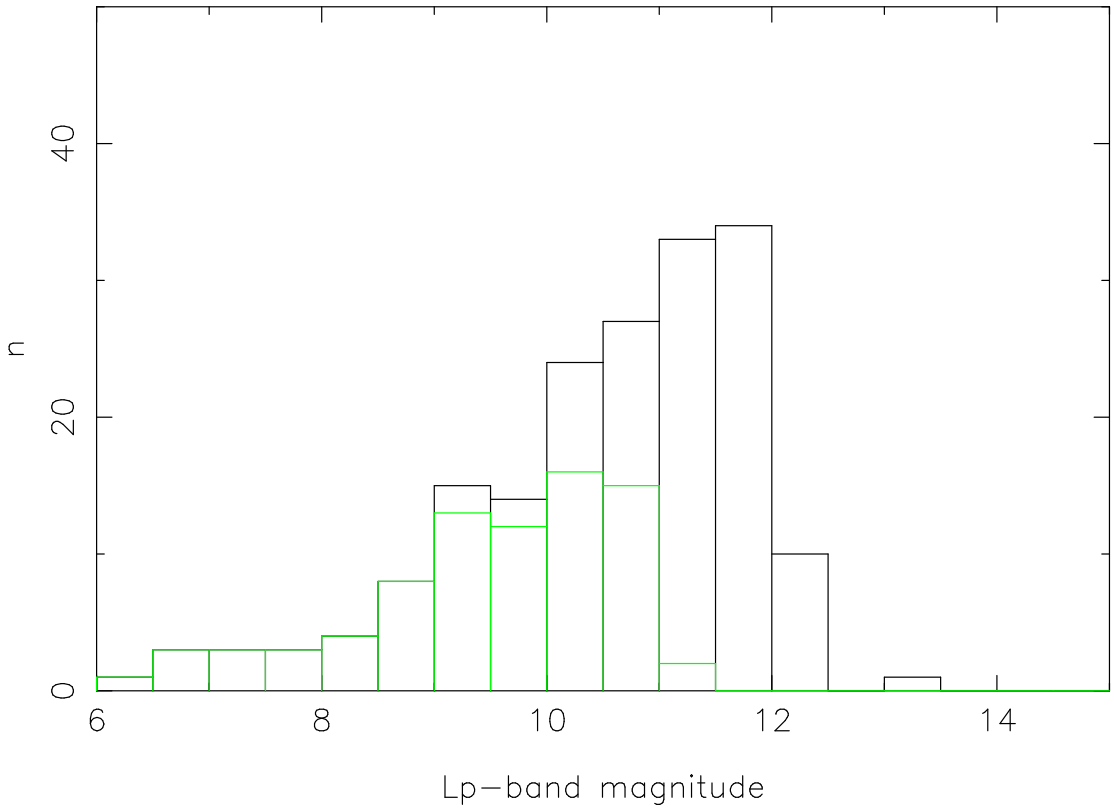

Figure 5.20: Lp-band magnitudes of the sources detected in the polarimetric data-set P16. Black: all sources. Green: sources with reliably measured polarization parameters.

Since NACO is not equipped with a $\frac{\lambda}{4}$ plate, it was not possible to measure circular polarization. However, Bailey et al. (1984) showed that the circular polarization of sources in the GC is at best very small, so it can be assumed here that it can be neglected and set to 0 at the available level of accuracy. Polarization degree and angle can then be determined in the following way:

$$P = \sqrt{Q^2 + U^2} \tag{5.9}$$

$$\theta = 0.5 \times atan\left(\frac{U}{Q}\right) \tag{5.10}$$

Errors for I, Q, U and subsequently p and θ were determined from the flux errors. In order to determine whether or not the polarization of a source was determined reliably, the normalized fluxes that would be expected for the determined values of p and θ were calculated. The difference between these values and the measured fluxes was then compared to the photometric errors of each data-point. The source was only classified as reliable if the root-mean-square of the deviations did not exceed the root-mean-square of the relative photometric errors. The subsequent analysis is only based on these higher quality sources. This method was applied to the data-sets P1, P2, P4 and P16.
Since this method was not applicable to the March 2011 Ks-band data (P18), the final errors of Q and U as well as the reliability were determined differently: dQ and dU were calculated from the photometric errors as it was done for the other data-sets, but the standard deviation over the individual values was added to this in case of multiple detections. Measurements were rated as reliable if the error of the polarization degree did not exceed the value of the polarization degree ($dp < p$).

5.2.7 Calibration of the measured polarization

A first comparison of the Ks- and H-band measurements to known values (Knacke & Capps, 1977; Bailey et al., 1984; Eckart et al., 1995; Ott et al., 1999) revealed significant offsets, es-

pecially in the polarization angles. Instead of the expected orientation along the galactic plane (oriented ∼31.4° East-of-North, in the following, positive angles should be read as East-of-North, negative as West-of-North), polarization angles of about -5° were found. The problem that surfaces here is that NACO was not specifically built for polarimetry, so instrumental effects like this can be expected and have to be countered by a special calibration. Also, the observation technique was developed for the study of short-term variabilities (flares) of Sgr A* and not for high-precision polarimetry on stellar sources.
To reduce this problem, Witzel et al. (2011) developed an analytical model of the behavior of polarized light within NACO. It consists of Müller matrices to be applied to the measured Stokes vector of each source, which then yields the actual Stokes parameters of the source. In general, any optical effect such as reflection, transmission, polarization etc. can be described by a Müller matrix. A combination of effects as it occurs here is then represented by a multiplication of the individual Müller matrices. If the necessary material constants and the construction of the instrument are known, the resulting matrix can be used to significantly reduce systematic offsets and uncertainties. Witzel et al. (2011) show that by using this method, the systematic uncertainties of polarization degrees and angles can be reduced to ∼1% and ∼5°. Applied to the data used here, this causes the final accuracy being limited rather by the photometric uncertainties than by instrumental effects. For a detailed description of the model and the Müller matrices themselves, see Witzel et al. (2011).
Utilizing this new calibration model means that an actual direct calibration can be achieved for the first time at this resolution. Previous studies like Eckart et al. (1995); Ott et al. (1999) had to adopt a calibration based on reference values taken from Knacke & Capps (1977).
The Lp-band measurements were calibrated to match the Knacke & Capps (1977) values for IRS 3 and IRS 7. A direct comparison is possible for those two sources, since they are bright and isolated enough so that even at the resolution of the 1977 data confusion/contamination is not an issue. The parameters of the calibration matrix were adjusted to take the wavelength dependence of the material constants into account.

5.2.8 Correcting for foreground polarization

It can be assumed that the total effect of the foreground polarization can be treated as a simple linear polarizer with a certain orientation θ_{fg} and efficiency p_{fg}. This can be described by a Mueller matrix:

$$\begin{aligned} S_{obs} &= \begin{pmatrix} I \\ Q \\ U \\ V \end{pmatrix} = M_{fg} \times S_{int} = M_{fg} \times \begin{pmatrix} I' \\ Q' \\ U' \\ V' \end{pmatrix} \\ &= M_{rot}(-\theta') \times M_{lin}(p) \times M_{rot}(\theta') \times S_{int} \end{aligned} \tag{5.11}$$

with S_{obs} as the observed total Stokes vector and S_{int} as the Stokes vector of the intrinsic polarization. $M_{lin}(p)$ is the Mueller matrix describing a linear polarizer, producing a maximum of polarization along the North-South-axis:

$$M_{lin}(p) = \begin{pmatrix} 1 & -p & 0 & 0 \\ -p & 1 & 0 & 0 \\ 0 & 0 & \sqrt{1-p^2} & 0 \\ 0 & 0 & 0 & \sqrt{1-p^2} \end{pmatrix}$$

This matrix has to be rotated to the appropriate angle by multiplying it with $M_{rot}(\theta')$, a standard 4×4 rotation matrix:

$$M_{rot}(\theta') = \begin{pmatrix} 1 & 0 & 0 & 0 \\ 0 & cos(2\theta') & sin(2\theta') & 0 \\ 0 & -sin(2\theta') & cos(2\theta') & 0 \\ 0 & 0 & 0 & 1 \end{pmatrix}$$

$\theta' = 90° + \theta_{fg}$ has to be used in the rotation matrix, since the polarization angle θ is defined here as the angle where the flux maximum is measured, while the angle of reference for the Mueller matrix describing the linear polarizer is the angle where the maximum in absorption occurs.
For each source to which the depolarization matrix was applied, the average of the polarization

parameters of the surrounding point sources was used as an estimate for θ_{fg} and p_{fg}.
The resulting matrix can then be inverted and multiplied with the calibrated observed Stokes vector of a source to remove the foreground polarization and leave only the intrinsic polarization. This method was applied to the extended sources (see §8.2), both to their total polarization and the polarization maps, in order to isolate their intrinsic polarization pattern. The relevance of the results depends heavily on the accuracy of the foreground polarization estimate.

6 The stellar population in the central parsec

6.1 Stellar classification

In total, 3349 of 5914 sources[1] have been classified as either early type, late type, foreground or very red sources. 2231 of the remaining sources are too faint to allow a reliable classification with the CBD method, although they can be assumed to be mostly late type sources. The SEDs of 334 sources were too noisy and have been excluded by the classification algorithm.
Unless otherwise indicated, all results shown here are based on the sources with an extinction corrected magnitude brighter than 15.5 (see Eq.5.2). Foreground sources have also been excluded (58 in total), since they do not belong to the population of the central parsec. Very red objects (24 sources) have also not been included in the number of early or late type stars, but have been treated as an extra class of objects. Objects in this class can be of different type: highly extincted background objects (and thus not very relevant for an analysis of the central parsec), sources with dusty envelopes, e.g. IRS 3 (Pott et al., 2008), young stars, whose strong winds interact with the interstellar medium in the form of bow-shocks (e.g. IRS 21, see Tanner et al., 2002, 2003), or even candidates for young stellar objects (Muzic et al., 2008) (examples for the SEDs of these sources are shown in Fig.8.1). Tab.6.1 lists the stars in each (sub)category, while Fig.6.1 shows the spatial distribution of the classified sources.

6.2 Comparison with spectroscopic results and uncertainty estimation

The results of the classification were compared to the lists of spectroscopically classified sources provided by Paumard et al. (2006) and Maness et al. (2007). The list published by Paumard et al. (2006) contains 90 early type stars, 78 of which were contained in the list of common sources. This discrepancy can partly be explained by the nature of the observations used here (different observation dates for the individual filters, 2 years between H band and IB observations, different quality of the datasets): some sources (especially fast moving objects like S2) were not detected at the same position in every image, not detected through all filters or excluded due to too large photometric uncertainties and thus did not make it on the common list. The same effects are probably relevant for the 329 sources classified by Maness et al. (2007), while in addition, parts of this sample are outside of the area covered by the data used here. Only the 266 sources that are also present in this dataset were used for comparison.
67 of the 78 known early type sources were also classified as early type here, 7 had too noisy SEDs and 4 were classified as late type. Of these 4 sources, 3 are borderline cases where a clear identification is very difficult with the CBD method (sources 224, 612 and 1772 respectively E36, E89 and E7 in the Paumard list). Source 3778 (E37 in the Paumard list) shows a clear CO absorption feature. Paumard et al. (2006) classify this source as a potential O8-9 supergiant, but at the same time give it a K band magnitude of 14.8 and an absolute magnitude of -3.3. This is inconsistent with expectations, since a source of this class should be at least two magnitudes brighter (see Tab.5.2). This source is therefore ignored for the uncertainty estimation. This leads to 3 out of 77 sources classified erroneously and 7 out of 77 sources not classified, which corresponds to 3.9% respectively 9.1%. A few well known sources like IRS 16SW and IRS 15NE have noisy SEDs, which in the case of IRS 16SW is probably due to the intrinsic variability of that source. But in general, noisy SEDs mostly stem from problems with the photometry: here, too faint or saturated sources are the biggest issues.

[1] A table of all classified sources is available in electronic form at the CDS via anonymous ftp to cdsarc.u-strasbg.fr (130.79.128.5) or via http://cdsweb.u-strasbg.fr/cgi-bin/qcat?J/A+A/499/483

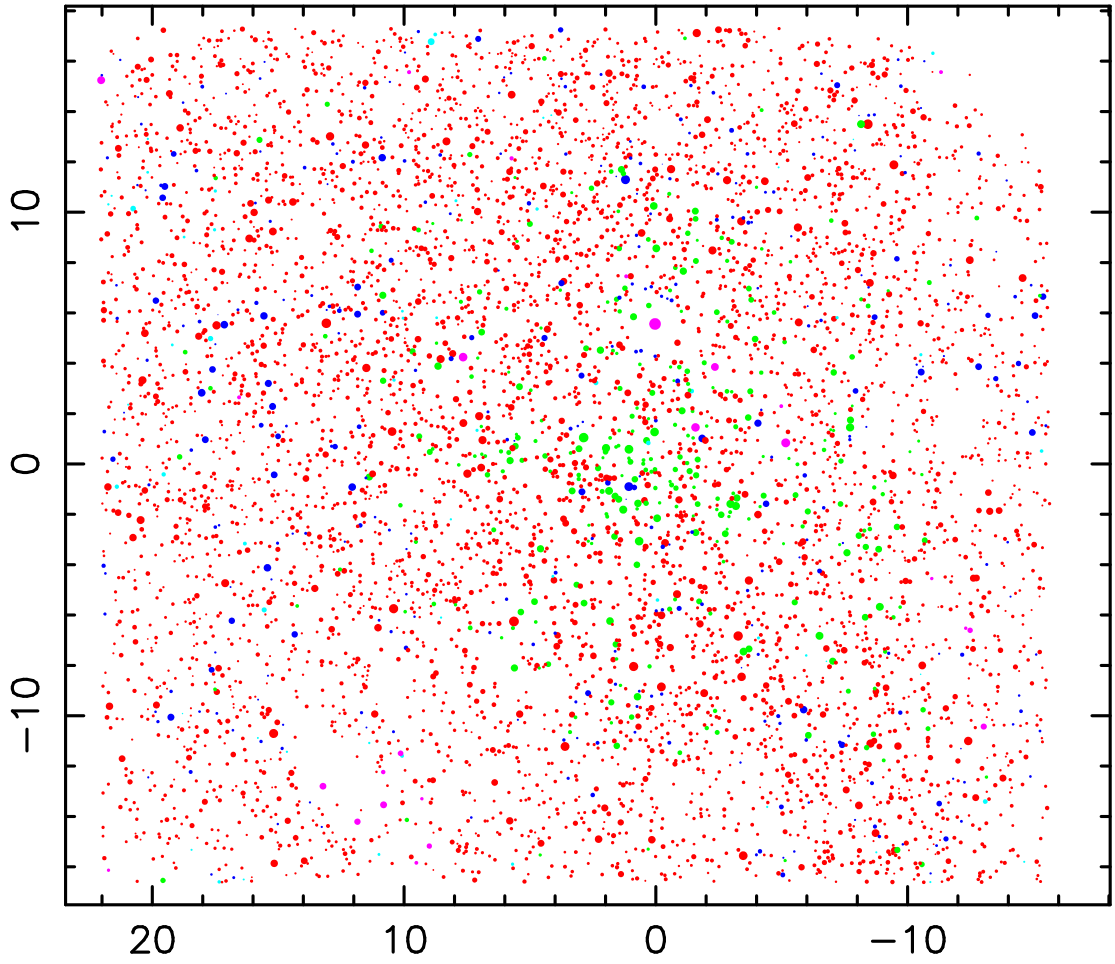

Figure 6.1: Map of the stars in the GC. Red: late type stars. Green: early type candidates. Blue: sources not classified. Light blue: foreground sources. Magenta: extremely red objects. The radii of the circles are linearly dependent on the extinction corrected magnitudes of the sources.

Since the known early type sources are concentrated in the inner 0.5 pc, these values can be adopted as the uncertainties of the number of early type stars in the innermost few arcseconds identified in this work.
258 of the 266 known late type sources have been classified as late types by this method. The SEDs of 7 sources were too noisy and one was classified as early type (source 363, 96 in Maness list). Source 363 does not show a clear CO feature despite being bright enough, and a comparison of the Maness and Paumard lists shows that there is an early type source 0.17” from its position (assuming that the positions given in these works use the same reference frame). In the imaging

Table 6.1: Stars classified in the GC using the method described in Sect.5.1.6.

class	number
early type quality 1	277
early type quality 2	25
early type quality 3	10
late type quality 1	2955
late type quality 2	2231
foreground	58
very red stars	24
noisy sources	334

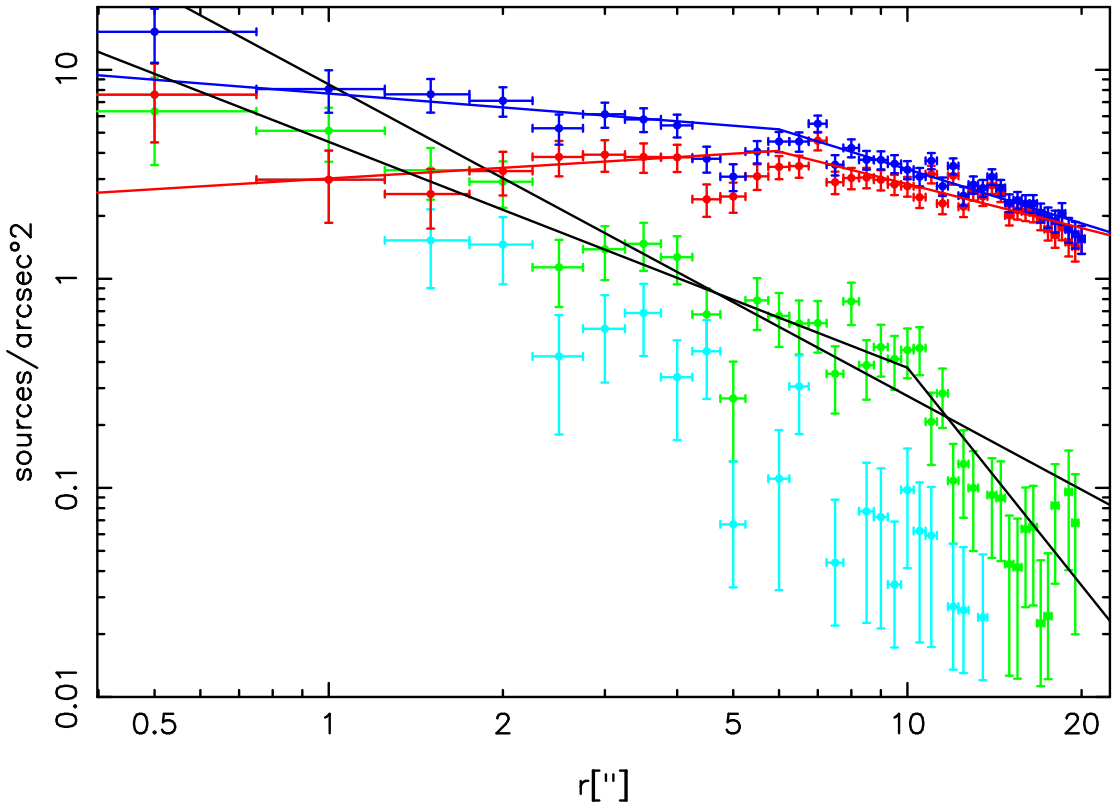

Figure 6.2: Azimuthally averaged stellar surface density plotted against the distance to Sgr A* for Ks magnitudes $\mathrm{mag}_{Ks} < 15.5$. The green points describe the distribution of early type stars, while red stands for late type quality 1 stars and dark blue for all detected stars. This also includes stars rated as noisy and bright enough late type quality 2 sources. The early type stars given in Paumard et al. (2006) are shown in light blue for comparison. The solid lines indicate the power laws fitted to the data.

data that were used for this work, there is only a single source present at the location of source E87 (Paumard) respectively 96 (Maness). It appears sufficiently isolated to rule out confusion with another source. This leads to the assumption that Paumard et al. (2006) and Maness et al. (2007) are looking at the same source there, but classify it differently.
In order to derive an upper limit for the uncertainty and thus the confidence in the CBD method, one erroneous classification in the area covered by the SINFONI observations is assumed. In this region (north of Sgr A*, mostly outside of 0.5 pc), a total number of 11 sources have been classified as early type, including the one star of disputed type. If one of these classifications is assumed to be erroneous, this leads to an uncertainty of ~9% for the number of early type stars outside of 0.5 pc. This can be considered an acceptable level of confidence, considering the low density of early type stars measured this far out.
To be on the conservative side, this value of ±9% is adopted as the uncertainty of the total number of all early type stars, i.e. in the entire field-of-view. It has to be considered, however, that the low total number of sources available for the determination of this uncertainty level limits the confidence in it.

6.3 Structure of the cluster

Fig.6.2 shows the projected stellar density for the total population, the early and late type stars. For comparison, the projected density of the early type stars provided by Paumard et al. (2006) is also shown. Only stars brighter than 15.5 mag have been considered here, in order to allow a clear separation of early and late type stars and to make a completeness correction unnecessary (see Schödel et al. (2007)).
The projected density profile of the late type stars is practically flat within a radius of ~10".

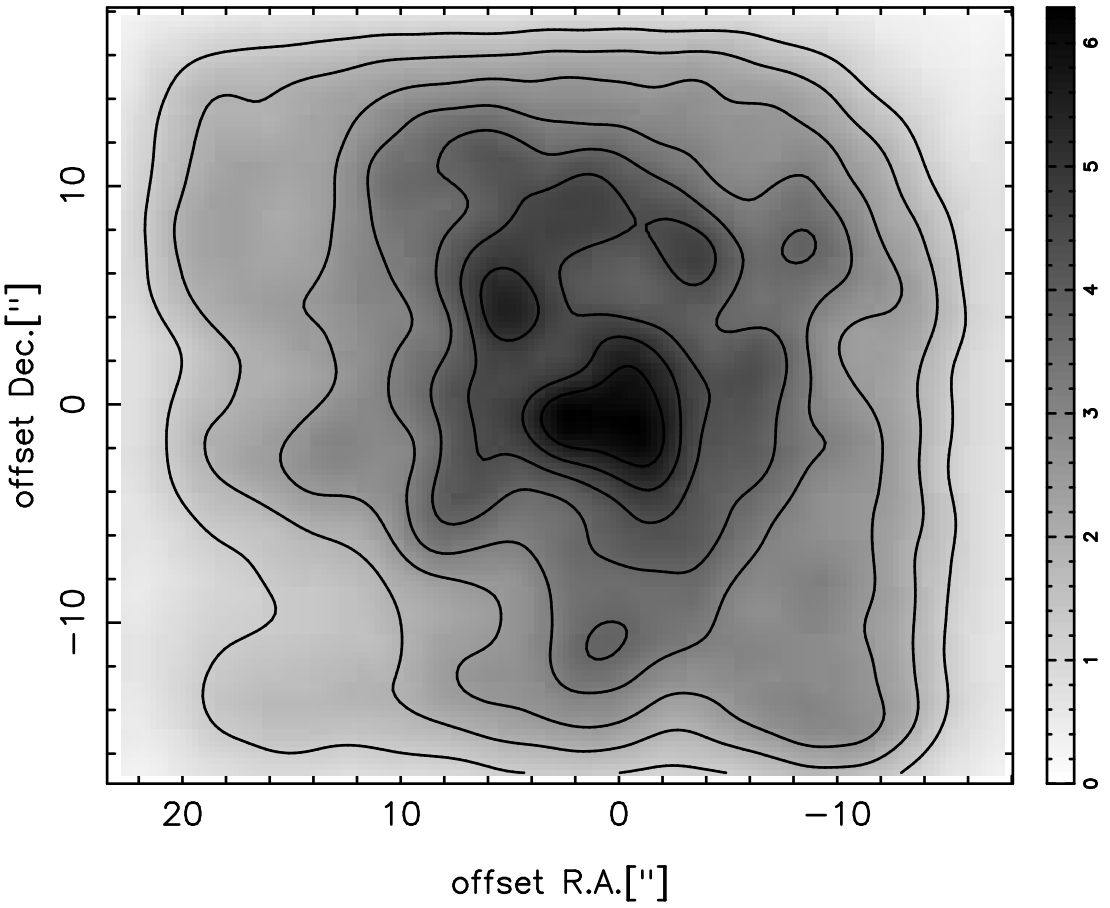

Figure 6.3: Stellar surface density of all stars brighter than 15.5 mag (linear scale, contours trace density in steps of 20, 30 ... 90 percent of maximum density). The density is given in units of sources per arcsec^2.

Within the innermost 5", it can even be fitted with a power law with a positive slope, i.e. the projected density increases with the distance to the center. This flattening or even inversion of the projected surface density profile of the late-type stars combined with the steeply increasing density of early-type stars towards Sgr A* explains the dip in CO band head absorption strength found in early spectroscopic observations of low spatial resolution (Allen et al., 1990; Sellgren et al., 1990; Haller et al., 1996). This is discussed in detail in §6.4.

A dip in the density can be observed at a radius of ∼5" that has already been observed by Schödel et al. (2007) in deep ($mag_K \leq 17.5$) star counts. Zhu et al. (2008) also find a dip at 0.2 pc, which corresponds to the 5" given here and in Schödel et al. (2007). This dip is a significant feature in the density profiles. It is present in both the late- and early-type population, although with a low significance in the latter, due to the small number of early-type stars. The cause for this feature is probably extinction, since there is a ring-like area of high extinction visible in the extinction map at this distance to the center (see Fig.6.7). Since this dip feature seems to appear in two stellar populations that are so different in their age and their dynamical state and since it would be very difficult to reproduce such a feature in a three-dimensional distribution, extinction seems to be the most likely explanation.

A steep increase of the projected density of early type stars can be observed towards the center (except in the innermost arcsecond). This also confirms previous observations. Paumard et al. (2006) proposed that the projected density of the early type stars follows a R^{-2} power law outside of a sharp inner edge at 1" (within the disk(s), so this value is not directly comparable to the findings presented here), with R as the projected distance to Sgr A*. Lu et al. (2009) also confirmed the R^{-2} power law within the clockwise disk. To allow a comparison with the values determined in this work, the projected density of the known early type sources that are contained in the sample presented here was fitted with a power law as well. This yielded a value

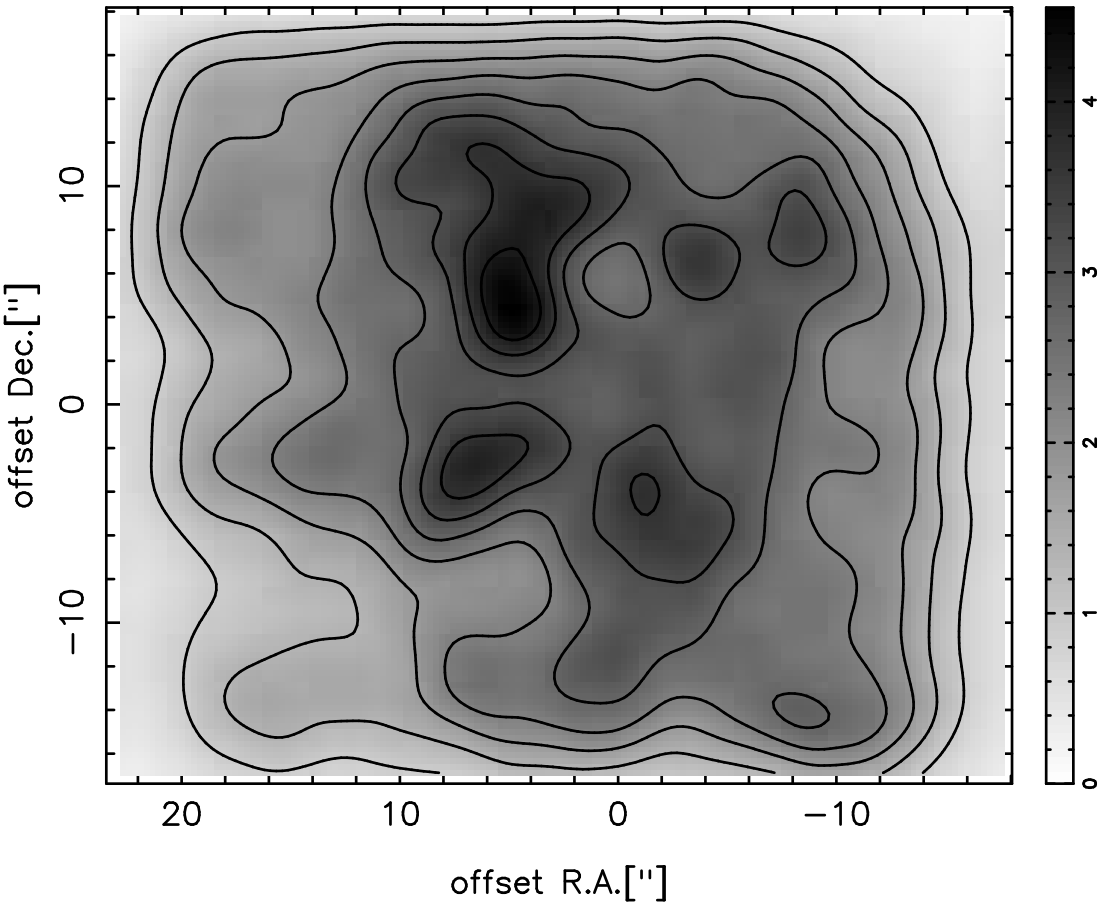

Figure 6.4: Stellar surface density of late type stars brighter than 15.5 mag (linear scale, contours trace density in steps of 20, 30 ... 90 percent of maximum density). The density is given in units of sources per arcsec^2.

of $\beta_{ref} = -1.80 \pm 0.17$. In the following, this value is adopted as a reference.
The projected early type density was fitted with a power law $\rho_{proj.} \propto R^{\beta_{1''}}$, excluding the inner 1". But while providing a value that agrees well with previously published results (Genzel et al., 2003; Paumard et al., 2006; Lu et al., 2009), this single power law does not provide a very good fit to the data. For comparison, the projected early type density was also fitted with a broken power law with a break at 10". This minimizes the deviations from the data, but it introduces an unexplained break at 10".

$$\beta_{1''} = -1.49 \pm 0.12$$
$$\beta_{1-10''} = -1.08 \pm 0.12$$
$$\beta_{10-20''} = -3.46 \pm 0.58$$

It has to be kept in mind that the absolute number of early type stars in the outer regions is much lower than further towards the center, so the uncertainties are considerably larger. The value for R > 1" agrees reasonably well with the values determined by Genzel et al. (2003); Paumard et al. (2006); Lu et al. (2009). Recent observations by Do et al. (2009) ($\beta = 1.5 \pm 0.2$) and Bartko et al. (2010) ($\beta = 1.4 - 1.5$), both using integral field spectroscopy, find projected density power laws for the early type stars that are in excellent agreement with the values presented here.
At R < 1", the early type density is lower than expected from extending the power law inwards. This is a sign of the inner edge of the clockwise disk reported by Paumard et al. (2006) and Lu et al. (2008). In this densest part of the cluster, the stellar surface density is probably also underestimated because source confusion will lead to incompleteness of the data (completeness of the sources at $mag_K \leq 15.5$ is estimated to drop to $\sim$ 80% within 0.5'' of Sgr A*). Outside of 1", a number of early type stars (312 over the whole field compared to 90) is detected that

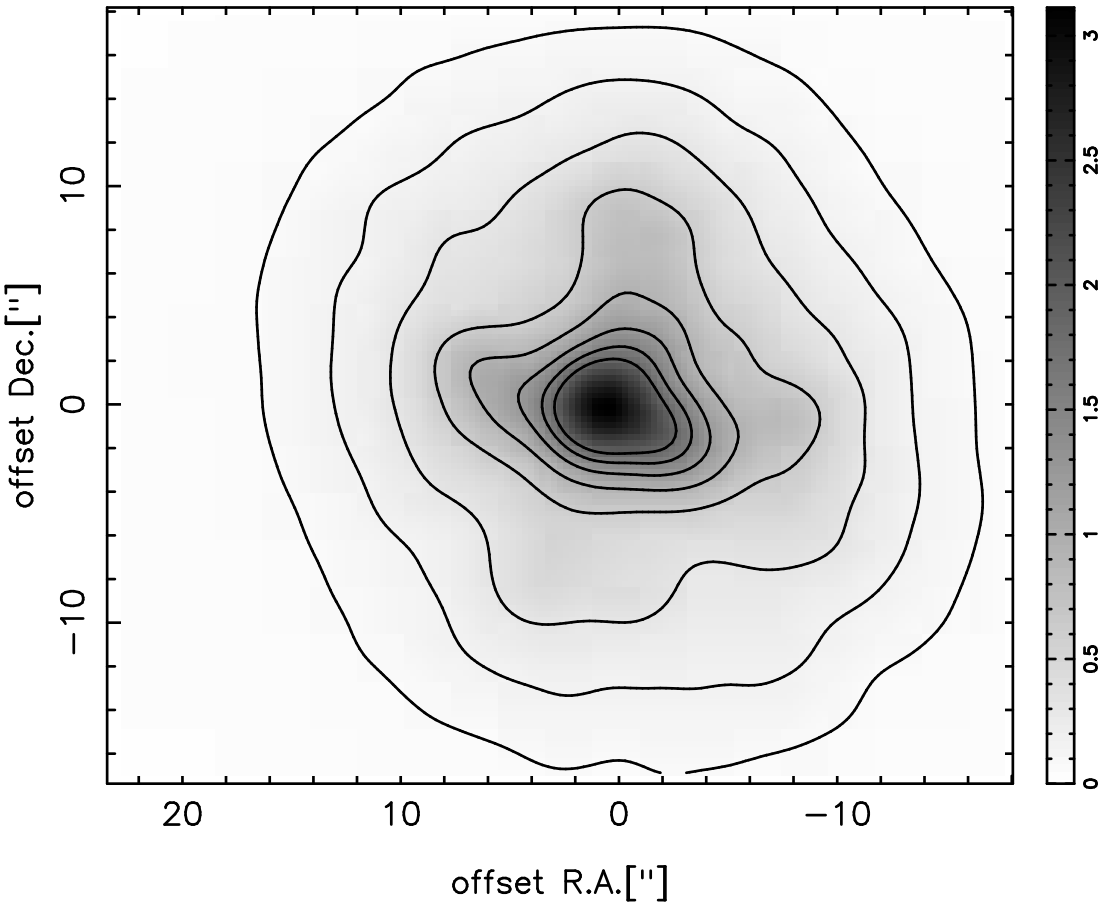

Figure 6.5: Stellar surface density of early type stars brighter than 15.5 mag (logarithmic scale, contours trace density in steps of 2.5, 5, 10, 20 ... 90 percent of maximum density). The density is given in units of sources per arcsec^2.

is by a factor of ∼3 higher than in previous works. Their density profile is similar to that of the previously reported early-type sources. The power law in the inner few arcseconds becomes flatter with the additional early-type stars included, but agrees within the uncertainties with the previously reported values. Towards the edges of the cluster (∼10-20”), a steeper density profile is observed than that presented by Paumard et al. (2006). It may be possible that a different density law applies outside of 10”, but the cause for such a phenomenon is unknown. It has to be considered, however, that the statistics for such a small number of stars at larger distances are not very reliable any more. In addition, two different cutoffs were used for sources inside and outside of 12”. This can also lead to a bias here in the way that the early type density is underestimated outside of 12” and overestimated within that distance to Sgr A*. But this effect should not influence the density on the order of magnitude observed here which leads to the different slopes of the fitted power laws.

The relative stellar density of the sources rated as too noisy (see Fig.5.9) appears to be flat over an inner region with a radius of ∼15”. Outside of 15”, the ratio increases, but that can be expected since the quality of the photometry decreases somewhat toward the edge of the FOV. This is probably due to the rectangular dither pattern used that leads to shallower integration toward the edges of the FOV.

This gives further evidence that the criteria for excluding noisy sources as well as the local calibration applied here are justified, since an even distribution of noisy sources can be expected from a well calibrated data-set. This is the case here, and it means that the exclusion of noisy sources does not lead to a bias in the surface density profiles.

Fig.6.3 shows the two-dimensional density distribution of all stars brighter than $\mathrm{mag}_K = 15.5$ and Fig.6.4 that of the late type stars of the same magnitude range, while Fig.6.5 shows the density of the early type stars in the same way. These maps have been smoothed with a ∼4”

Table 6.2: Power law indices for late type stars and all classified stars, separate fit to sources inside and outside of 6.0”

	β_{inner}	β_{outer}
all stars	-0.22 ± 0.11	-0.86 ± 0.08
late type stars	0.17 ± 0.09	-0.70 ± 0.09

Gaussian. While the late type stars show a similar distribution as the stars in the cluster viewed as a whole (with the exception of the central few arcseconds), the early type stars are concentrated in the center. This result is not surprising since the same can be seen from the azimuthally averaged density. The area in the immediate vicinity of IRS 7 shows a significantly lower stellar density in all maps, because the presence of this extremely bright source impedes the detection of other stars close to it.
The peak of the early type density is, as expected, located close to the position of Sgr A*. The distribution of the early-type stars appears close to circularly symmetric, but indicates extensions along N-S and E-W. An apparent concentration of early-type stars along these directions can also be seen in Fig. 1 of Bartko et al. (2009).
The density distribution of the late type stars clearly shows the relative lack of late type stars in the very center. The map also shows a correlation with the extinction map (see extinction map provided in Schödel et al. (2010b) and Fig.6.7). Areas of higher extinction show a lower density of stars. This effect is not visible in the early type density. But in the areas with higher extinction (e.g. 5” NW of Sgr A*), the early type density is too low for this effect to be relevant, although a trace of it can be seen in the slight dip in the early type density in Fig.6.2. The extinction has two separate effects on the projected density: one effect is that sources behind a lot of extinction appear fainter, so they might be excluded by a simple magnitude cutoff. This effect has been corrected here by using extinction corrected magnitudes. The other problem is that extinction also impedes the detection of sources, especially in filters with lower image quality. This effect of the extinction on the stellar density has not been calculated here and was not compensated.

6.4 Evidence for giant depletion in the center

Figer et al. (2003) examined the radial velocities of 85 cool stars in the GC (mostly M and K giants) and found dynamical evidence for a flattened distribution of late type stars within 0.4 pc (∼ 10”). As Figer et al. (2003) and Zhu et al. (2008) point out, the flat projected surface density profile of the late-type stars implies in fact a *hole/dip* in the 3-dimensional distribution of the late-type stars.
Schödel et al. (2007) described the total population of the central parsec with a broken power law (break radius $R_{break} = 6''.0 \pm 1''.0$, $\beta = -0.19 \pm 0.05$ within R_{break} and $\beta = -0.75 \pm 0.10$ outside of the break radius) for a magnitude limit of 17.75 and using completeness corrected data. This does not allow a comparison of absolute densities to the findings shown here, since that dataset goes much deeper than the one used in this work, but the trend can be confirmed here. It also has to be considered that these results were obtained on the entire population and not separated into early and late type stars.
Broken power laws were fitted to the projected densities of the late type stars and all classified stars (see Tab.6.2). The same break radius of 6.0±1.0” as Schödel et al. (2007) is measured, and the power law indices for the total population also agree with the values given in that work (-0.22±0.11 for the inner region, -0.86±0.06 for R>6” in this work). What is new here, however, is the possibility to obtain separate values for the late type population alone. These values give an even stronger support to the proposed hole/dip in the center: a power law index of -0.70±0.09 is found for the outer region, while the inner region even shows a decline towards the center (0.17±0.09).
This is a very interesting result, since it shows that the previously observed flattening of the density profile of the total population (Genzel et al., 1996; Figer et al., 2003; Genzel et al., 2003; Schödel et al., 2007; Zhu et al., 2008) is an even stronger feature in the late type population. It can therefore be assumed that the stellar population in the innermost ∼0.2 pc is indeed depleted

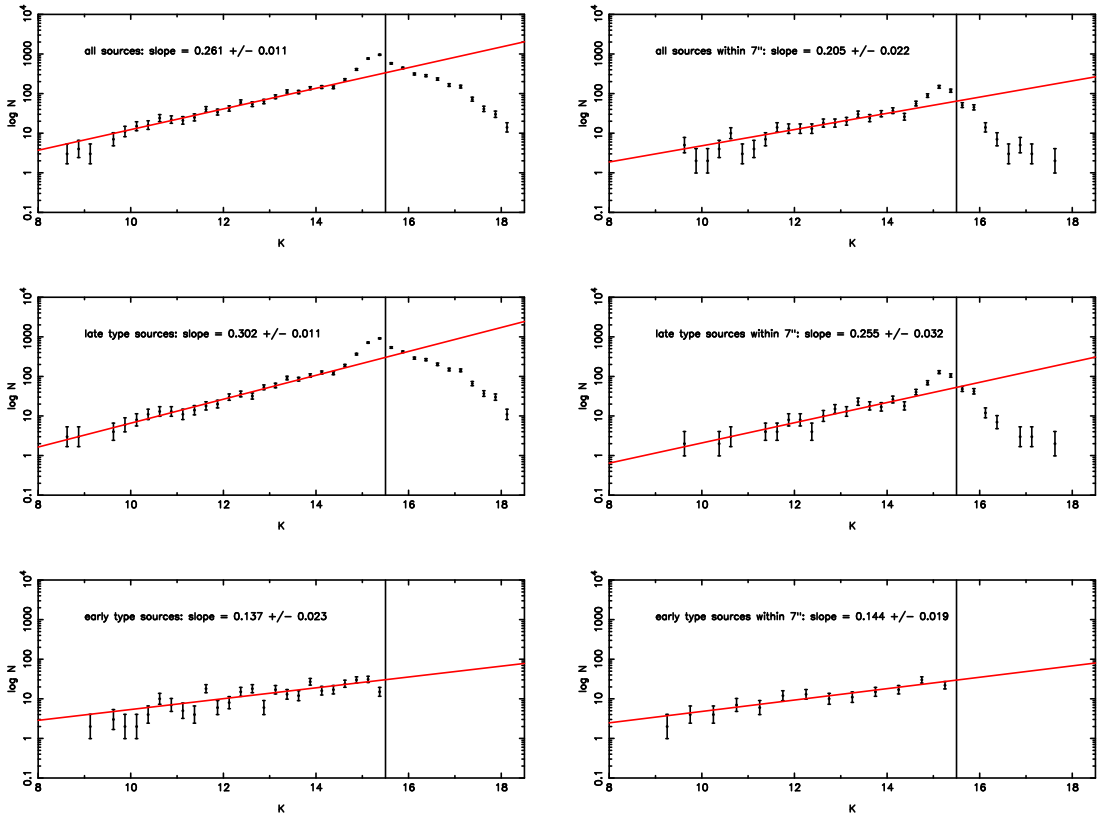

Figure 6.6: Ks-band luminosity function of stars in the central parsec. Each data-point represents the center of a magnitude bin (0.25 mag wide bins, respectively 0.5 mag in lower right frame). Upper left: all stars. Central left: only late type stars. Lower left: only early type stars. Upper right: all stars within 7". Central right: late type stars within 7". Lower right: early type stars within 7".

not only of bright giants, but also of fainter giants down to the magnitude limit of this work of 15.5 mag. These findings have more recently been confirmed in spectroscopic surveys by Do et al. (2009) and Bartko et al. (2010): both find a similar flattening or even decline in the projected densities of the late type stars.
Several causes for this phenomenon have been proposed: Dale et al. (2008) offered an explanation for the under-density of late type stars within 1", claiming that collisions with stellar mass black holes and main sequence stars prevent 1-2 $M_{\odot}$ giants to evolve so that they are not visible in the K band. Their simulations cannot explain the lack of brighter and fainter giants.
Freitag et al. (2008) derived collision probabilities for bright giants in the GC (see especially their Fig.1). They determined that nearly all massive stars within 0.1 pc almost certainly suffer from collisions during their time on the giant branch.
Merritt & Szell (2006) offered yet another explanation: the infall of a second SMBH would destroy the stellar density cusp present around Sgr A*, which would then be built up again in a time-frame of several Gyrs. This process can lead to a practically flat density profile, similar to the one observed here.

Table 6.3: KLF power law indices of the different classified stellar types, calculated for the entire cluster respectively the inner 7"

type	complete cluster	r < 7"
all	0.26 ± 0.01	0.21 ± 0.02
late	0.31 ± 0.01	0.27 ± 0.03
early	0.14 ± 0.02	0.13 ± 0.02

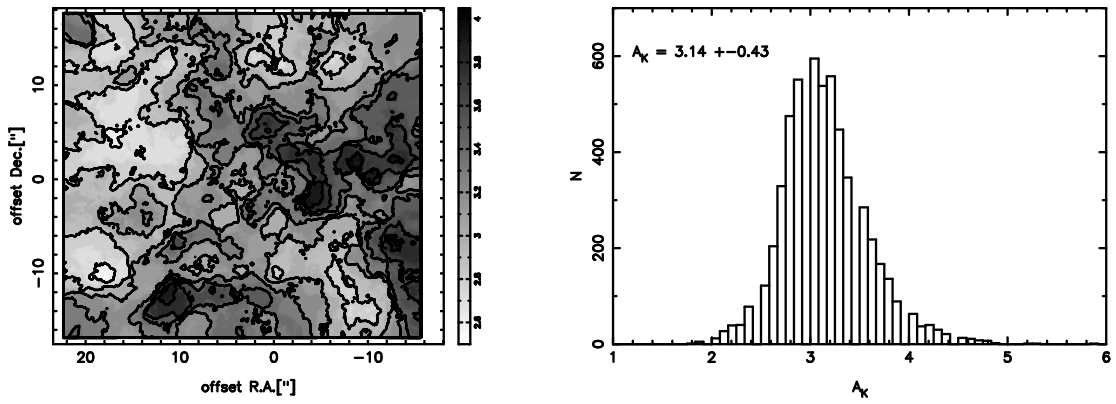

Figure 6.7: Left: Extinction map of the central parsec computed from individually fitted extinction values. Features like the mini-cavity and the mini-spiral are visible. Right: Distribution of extinction values in the central parsec of the GC.

Since these new results were first presented in Buchholz et al. (2009), several further explanations have been discussed: Merritt (2010) proposed a scenario where the nuclear star cluster has not reached a steady state yet under the influence of gravitational encounters. An initial core of ∼1-1.5 pc might have evolved to its present observed size of ∼0.5 pc after about 10 Gyr. Madigan et al. (2011) analyzed the long-term evolution of stellar systems around SMBHs under the influence of resonant relaxation, finding that a depression is produced in the very center due to tidal disruptions (although by a factor of ∼5 smaller than what has been observed).

6.5 K band luminosity function

The general Ks-band luminosity function (Fig.6.6) agrees well with the one presented by e.g Genzel et al. (2003); Schödel et al. (2007). The red clump can clearly be made out at the expected magnitude range of ∼15.0-15.25. The 15.5 mag limit of the observations does not have a significant effect on this feature, since this limit only applies to the separation of early and late type stars, while the photometric completeness limit lies at ∼ 16 mag.
The luminosity functions can be described to the first order by a power law (fitted to the area between 9.0 and 15.5 mag for the early- type stars, respectively 14.5 to exclude the red clump in the other plots):

$$\frac{dlogN}{dK} = \beta \tag{6.1}$$

The power law indices that resulted from this fit are shown in Tab.6.3.Alexander & Sternberg (1999); Tiede, Frogel & Terndrup (1995); Zoccali et al. (2003) measured the power law slope of the bulge population of the milky way several degrees from the center as $\beta \sim 0.3$, while Figer et al. (2004) give the same value for the KLF on 30 pc scales around the GC, claiming that this value agrees very well with the theoretical KLF of an old stellar population, reflecting the rate of evolution of stars along the red giant and asymptotic giant branch. Genzel et al. (2003) give a value of $\beta = 0.21 \pm 0.02$ for the central 9". It is expected that for greater distances to the center, the slope value approaches that of the bulge.
The power law fitted here for the total population of the central parsec is flatter than the one attributed to the bulge population, while the value fitted for the inner 9" matches the value of 0.21 given by Genzel et al. (2003).
The individual KLFs for the late and early types give the reason for this deviation from the bulge power law: since the central parsec (and even more the central few arcseconds) contain a significant number of early type stars and their KLF has a much flatter slope ($\beta_{early} = 0.14 \pm 0.02$), the resulting power law is also flatter than that of the late type population alone. The power law fitted to the KLF of only the late type stars ($\beta_{late} = 0.31 \pm 0.01$) agrees very well with the one observed in the bulge.
Agreeing with Lebofsky & Rieke (1987); Blum et al. (1996); Davidge et al. (1997); Genzel et al. (2003), the data point to the population in the central parsec being an old stellar population

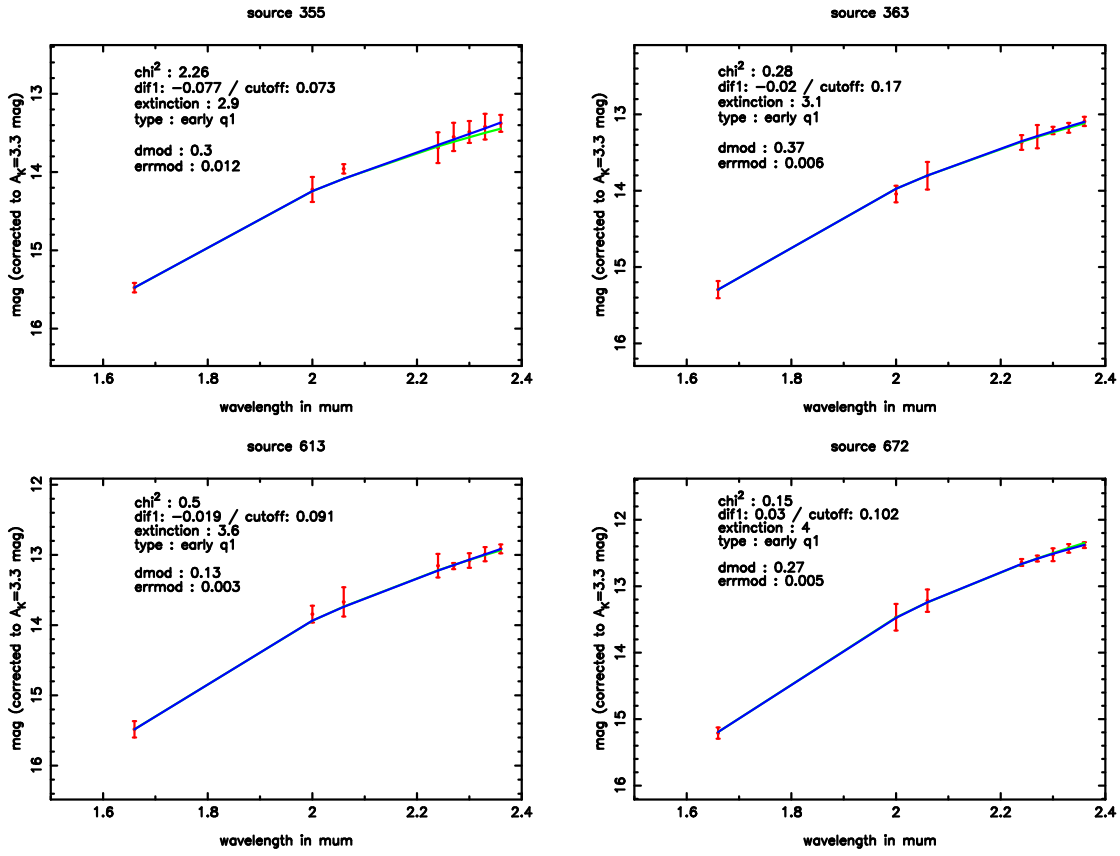

Figure 6.8: SEDs of stars fitted as early type outside of 0.5 pc.

with an admixture of a young, bright component.
The fitted slope value for the inner 9” of 0.21 differs from the one for the total cluster, but otherwise, the shape of the KLF there is very similar. This difference is due to the flatter slope of the late type KLF in this region, while that of the early type KLF stays the same.
Paumard et al. (2006) also presented a KLF for the early-type stars in the disks. They also find a flat KLF, similar to the one presented here. The significant difference is the greater sensitivity achieved in the present work. Paumard et al. (2006) note that their KLF has a spectroscopic completeness limit of ~13.5-14 mag, compared to 15.5 mag here. The fact that the flat slope of the early type KLF can be observed down to that magnitude is an important new result and it strengthens assumptions of a top-heavy mass function since it improves the statistic relevance of the observed flatness. Recent results by Bartko et al. (2010) seem to indicate that the early type KLF for the stars in the disk(s) points to an extremely top-heavy IMF, while it would be consistent with a standard Salpeter/Kroupa IMF for the off-disk population. This might point to different star formation mechanisms responsible for the disk stars opposed to the early type stars located further out and the innermost population, the S-stars.

6.6 Extinction

The average extinction of ~2.5 mag towards the GC is well known (e.g. Schödel et al. (2010b); Fritz et al. (2011)), but this value varies on small scales by up to 1.5-2 mag (Schödel et al., 2007, 2010b) and poses a significant problem for the reliable measurement of apparent magnitudes, colors and intrinsic reddening of stars. Schödel et al. (2010b) are presenting an extinction map based on H-K colors obtained from the same data that is used here, but the individual extinction values obtained in this work can also be used to produce an extinction map. Fig.6.7 shows this map. It agrees well with Schödel et al. (2010b) and exhibits the same large scale structures, while higher overall extinction values are found here. It has to be noted, however, that the Draine(1989) extinction law was used here and that a different law might apply to the GC, as

indeed suggested by Schödel et al. (2010b); Fritz et al. (2011). This may lead to a systematic offset as large as A_K = 0.5 mag, which should be taken into account as a possible systematic uncertainty when interpreting these values.
A histogram of the measured extinction values is shown in Fig.6.7: The distribution is similar to a Gaussian with a mean value and standard deviation of 3.1 ± 0.4. This agrees well with previously published results (Scoville et al., 2003), while it is higher than the value published by Schödel et al. (2010b); Fritz et al. (2011). The latter can be explained by the different power law index of the extinction law derived in the these works. The asymmetry of the histogram is due to the exclusion of foreground stars.

Table 6.4: Early type stars detected outside of 0.5 pc. *x* and *y* denote the position of the star in arcsec relative to Sgr A*, $mag_{K,ext}$ the extinction corrected K band magnitude and A_K the extinction in the K band. *Quality* indicates the confidence in the identification after an additional visual inspection of the SED, with A as the highest confidence and C as the lowest.

x(")	y(")	$mag_{K,ext}$	A_K	CBD	quality
-8.15	13.50	10.7	3.3	0.07±0.04	C
-9.59	-15.33	12.5	3.1	-0.05±0.01	B
15.74	12.87	13.1	2.8	0.03±0.03	B
-8.37	-11.27	13.9	2.7	-0.095±0.019	C
-8.64	-10.74	13.5	3.0	-0.003±0.003	A
-10.57	-15.90	13.0	3.3	0.05±0.01	B
18.92	0.28	13.3	3.2	0.02±0.01	B
-10.62	-9.76	13.2	3.3	0.008±0.017	A
-10.81	-10.51	14.1	3.0	0.01±0.01	B
13.05	14.29	13.3	3.5	0.04±0.02	B
7.39	12.29	13.3	3.5	0.03±0.01	A
13.13	5.08	14.6	2.8	-0.07±0.04	B
19.58	-16.54	12.7	4.0	0.032±0.005	A
4.43	16.11	13.9	3.4	0.028±0.007	B
9.43	9.29	13.6	3.5	-0.008±0.018	B
18.70	4.44	14.0	3.3	-0.08±0.03	B
-10.86	7.20	13.3	3.8	0.05±0.02	B
11.30	8.47	14.0	3.4	0.018±0.004	A
17.69	3.01	14.0	3.4	0.03±0.01	C
10.91	9.44	11.9	4.7	-0.07±0.03	B
-9.05	-11.77	15.2	2.9	-0.089±0.005	A
-12.75	9.77	12.8	4.4	0.05±0.02	B
17.48	11.36	13.7	3.9	0.036±0.008	A
-4.20	14.06	14.9	3.2	-0.08±0.02	B
17.51	-8.95	14.8	3.4	-0.07±0.01	A
9.89	-14.14	13.2	4.4	0.04±0.03	B
14.25	-5.64	14.5	3.8	-0.033±0.005	A
12.55	-4.19	13.2	4.7	0.03±0.02	A
-15.25	6.68	14.1	4.1	-0.09±0.06	B
-13.13	-12.44	15.1	3.6	-0.079±0.004	A
-5.14	-15.75	15.4	3.4	-0.13±0.02	C
4.49	-15.53	15.2	3.6	-0.14±0.03	B
-1.16	16.91	13.8	4.5	-0.06±0.02	B
0.31	-15.30	15.1	3.7	-0.11±0.03	B
8.86	9.55	15.4	3.5	-0.12±0.02	C

6.7 Early type stars outside of 0.5 pc

In addition to not only identifying the well known early type stars in the center of the cluster, but indeed more than tripling the number of early type candidates in the central 0.5 pc, the identification of 35 early type candidates more than 0.5 pc (~12.9") from Sgr A* can also be reported. If the previously derived uncertainty of ~9% (see §6.2) is applied to this value, this leads to a number of 35 ± 3 early type candidates outside of the inner region. This number is most likely underestimated, due to the stricter cutoff criterion used in this region (see §5.1.4). Within the observed area, the distribution of these sources appears to be fairly isotropic, although one has to be cautious here due to the the asymmetry of the observed region and the small number of candidates. The nature of these candidates needs to be confirmed with spectroscopic observations, since the CBD method can only provide a first estimate for the type.
Fig.6.8 shows four examples of what are considered very likely candidates for actual early type stars. The source in the upper right frame of Fig.6.8 does not show a CO absorption feature, but still it has been labeled as a late type source in Maness et al. (2007). Paumard et al. (2006) seem to list it as an early type however. The other sources listed in Tab.6.4 with quality A have similarly smooth SEDs, while quality B and C sources are considerably more noisy.
These findings lead to an average density of early type stars of $(4.6 \pm 0.4) \times 10^{-}2$ sources/arcsec^2 at $R > 12.9''$.
The detection of early type stars this far out in significant numbers is a new result: Paumard et al. (2006) reported no early type stars outside of the central 0.5 pc, citing an 1 σ upper limit of $\sim 10^{-2}$ OB stars per arcsec^2 outside of 13" deduced from SINFONI data, but referring to an unpublished source. The difficulty in identifying these stars in existing data is pointed out by Trippe et al. (2008), who mention very limited coverage of the central cluster and data gathered with several instruments and in different epochs that is very difficult to compare due to different pixel scales, Strehl ratios and completeness. These obstacles have probably impeded the detection of early type stars in the outer region of the central cluster until now. This new method can provide targets for spectroscopic confirmation observations, allowing for a broader search for early type candidates over a large area without the need to cover the whole area with integrated field spectroscopy. Finally, it should be pointed out that it is known that at least one early-type star exists outside of the central 0.5 pc, as has been confirmed by the results of Geballe et al. (2006) on IRS 8.
Recent observations by Bartko et al. (2010, see specifically their Fig.1) confirm the existence of several early type stars outside of the innermost 10", although not all candidates presented first in Buchholz et al. (2009) have been confirmed (*H. Bartko, priv. comm.*). But it has to be considered that the ubiquity of bright sources with CO bandhead absorption might contaminate spectroscopic results at low spatial resolution, so low luminosity early type stars might be identified as late type if only that feature is used.
As Fig.6.2 shows, there are two possible fitting solutions for the early type density. While the single power law fitted to the projected density of early type stars agrees with the previously published power law, the slopes of the broken power law show a significant difference in the outer and inner region. If a single power law distribution can be assumed, this would indicate that these stars merely represent the continuation of the disk and the off-disk population. But if the much steeper decline outside of 10" is indeed a significant and real feature, this might point to a change in the population respectively so far unknown effects on the density distribution.

7 Stellar polarization

7.1 Ks-band polarization

7.1.1 2009 data-set (P2)

It was possible to measure reliable polarization parameters for 194 sources[1] brighter than 16 mag in the 2009 Ks-band dataset (P2). For fainter sources, the photometric uncertainty becomes too large to determine the polarization reliably, and this limit also helps to avoid issues with insufficient completeness and source crowding, which could generate a bias in averaged values. The subsequent analysis and the comparison to the H-band data is only based on this dataset (no H-band data covering the FOV of dataset P4 or P17/P18 are available, unfortunately).
The polarization angles in the central arcseconds mostly follow the orientation of the galactic plane within the uncertainty limits (31.4°, see Reid et al., 2004), while angles of ~25-30° are found in this work), while they are slightly steeper (~5-15°) towards the eastern edge of the FOV (see Fig.7.1). A small number of sources west of Sgr A* also shows similar steep angles, but there are too few reliable sources there to allow any conclusions.
The distribution of the polarization angles (see Fig.7.2, lower left frame) can be fitted with a single Gaussian, peaked at 20° with a FWHM of 30°. Using the FWHM as a measure for the uncertainty (with $\sigma = \frac{FWHM}{2\sqrt{2\times ln(2)}}$), this yields $\theta = 20° \pm 13°$. Using a fitting function with two Gaussian peaks yields a significantly lower χ^2 (by a factor of 3). The two peaks are fitted at $\theta_1 = 10° \pm 4°$ (FWHM of 10°) respectively $\theta_2 = 26° \pm 8°$ (FWHM of 20°). Considering the uncertainties of the polarization angles shown in the lower right frame of Fig.7.2, which are of the order of up to 15°, it can be questioned if these two peaks are indeed a real feature, with the distance between the peaks in the order of these typical errors.
The polarization degree also appears to vary over the field, with values of 4-5% in the central region and 8-10% towards the eastern edge (and for some western sources, but with the same caveat as for the polarization angle). Especially sources in the area around the IRS 1 sources show these higher polarization degrees. The logarithms of the polarization degrees were fitted with a Gaussian (peaked at (5.1 ± 1.7)%, FWHM of 4.0%, see Fig.7.2, upper left frame), and just as it was the case for the polarization angles, the fit was quite poor. Repeating the fit with a double Gaussian yielded two peaks at (4.6 ± 0.8)% respectively (7.7 ± 1.2)%, with FWHMs of 1.8% respectively 2.8% and a significantly better χ^2 (by a factor of 8). The relative uncertainties of the polarization degree are of the order of up to 30% (see Fig.7.2, upper right frame), and this limits the confidence in the two fitted peaks.
Comparing the two fitted Gaussian distributions for both parameters reveals that a similar number of stars are contained in the 10° and the 7.7% peak (~25-30%), respectively the 26° and 4.6% peak (~70-75%). This confirms the general trends found in Fig.7.1 and indicates that the fitted peaks indeed correspond to a real feature.
Fig.7.10 (left frame) shows the Ks-band polarization degrees plotted versus the polarization angles, and there appears to be a trend that larger polarization degrees coincide with steeper polarization angles, despite the large errors.

7.1.2 2007 data-set, rotated FOV (P4)

Reliable polarization parameters were measured for 186 sources brighter than 16 mag. This dataset has a lower Strehl ratio (on average) than the 2009 data (22% compared to 27%). No H-band data with this FOV is available for a comparison, but several bright sources are also contained in the Lp-band dataset.

[1] A table containing the polarization parameters of all reliably measured sources in data-sets P1, P2, and P4 is available in electronic form at the CDS via anonymous ftp to cdsarc.u-strasbg.fr (130.79.128.5) or via http://cdsweb.u-strabg.fr/cgi-bin/qcat?J/A+A/534/A117

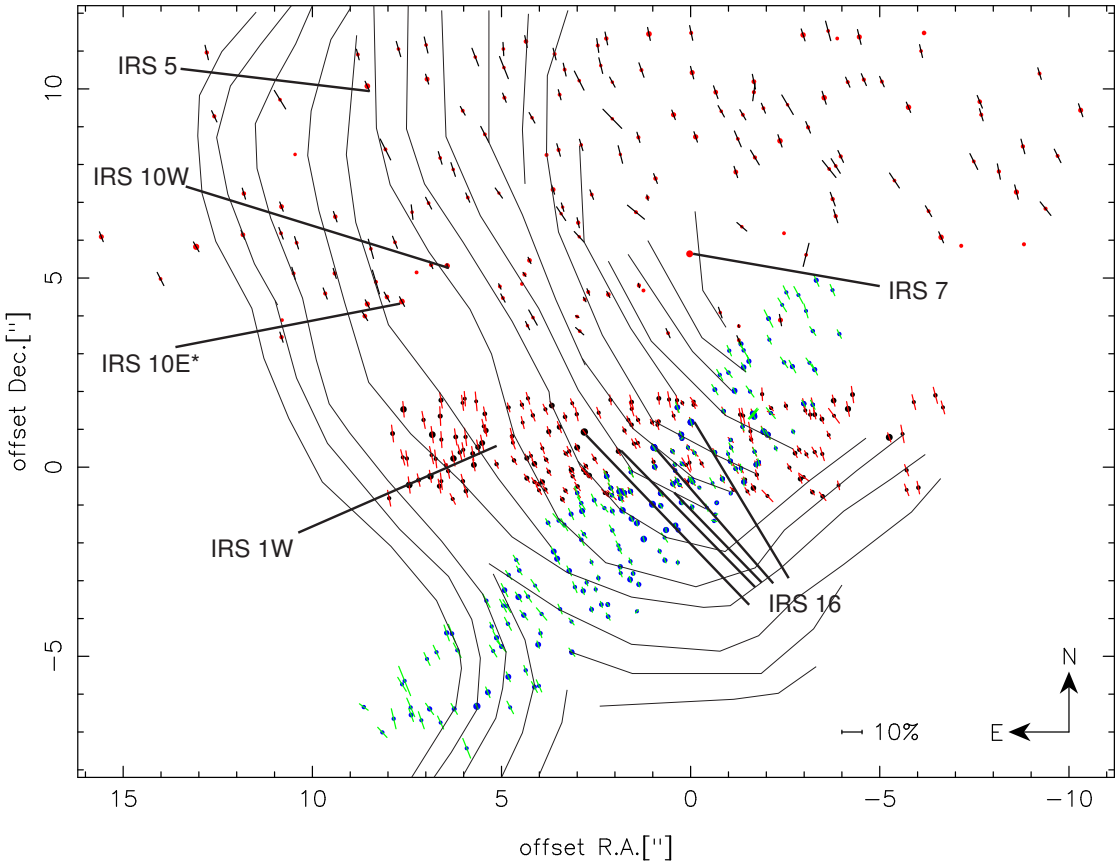

Figure 7.1: Ks-band polarization map of stars in the Galactic center. Only reliably measured polarization values are shown here. Black circles and red lines: dataset P2. Blue circles and green lines: dataset P4. Red circles and black lines: dataset P18). The diameter of the circles corresponds to the brightness of the source. Thin black lines in the background denote magnetic fields determined from MIR data (Aitken et al., 1998, , based on a 1.5" beam). The brightest sources are also indicated.

The trends found here are similar to those in the main dataset: the polarization angles appear aligned with the Galactic plane (see Fig.7.1), but no similar shift in polarization angle towards the east of the FOV is observed. What can be found, however, is an increase in polarization degree towards the south-east, similar to the increase found in the 2009 data towards the east. Both the distribution of the polarization degrees (logarithmic) and the polarization angles can be fitted with a single Gaussian with sufficient accuracy (see Fig.7.3), with peaks fitted at (4.6 ± 2.1)% respectively 26° ± 8° (FWHM of 5% respectively 20°). The FWHM of the distribution of the polarization degrees is comparable to that found for the 2009 data, but a single Gaussian provides a much better fit here. The larger uncertainties would however lead to a blurring of the two Gaussians, if indeed two were present.
The relative errors of the polarization degree (see Fig.7.3, upper right frame) mostly stay below 30%, with some outlier values of up to 40-50%. This exceeds the errors found for dataset 2, but this can be expected due to the lower data quality. The errors found for the polarization angles are also higher on average than those measured for dataset 2.

7.1.3 2011 data-set (P18)

Despite the much wider FOV compared to the older data, only the polarization parameters of 131 sources could be measured reliably, but that still increases the number of sources by a factor of 4 compared to Eckart et al. (1995) (who measured the polarization of ∼ 30 sources in this area, while Ott et al. (1999) did not cover this region at all).
As in the deeper data-sets, the polarization angles show the expected alignment with the Galac-

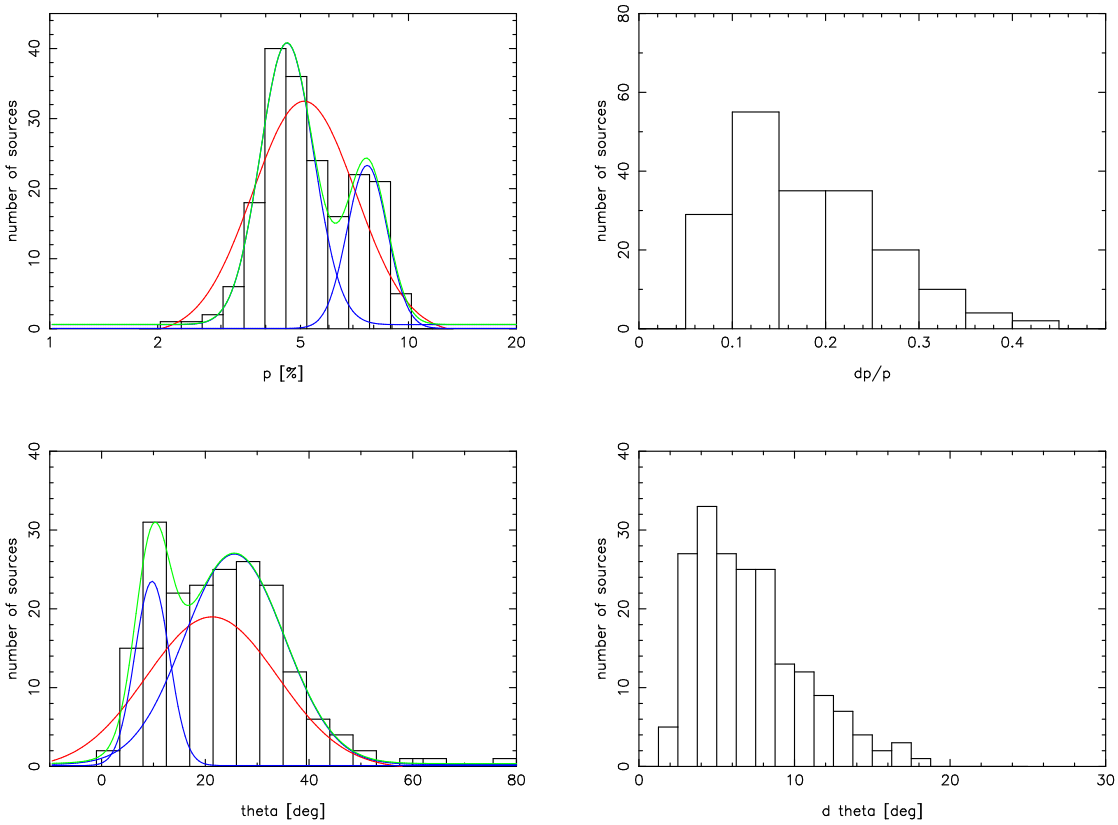

Figure 7.2: Ks-band polarization degrees (plotted on logarithmic scale, upper left) and angles (lower left) of stars in the Galactic Center (2009-05-18, dataset P2). The red line denotes the fit with one Gaussian distribution, while the green respectively blue lines denote the fit with a double Gaussian (green: sum, blue: individual Gaussians). Upper right: relative errors of the polarization degrees. Lower right: absolute errors of the polarization angles.

tic plane (see Fig.7.1). There may be a trend of larger polarization degrees towards the north compared to the southern center, but it is not as clear as the trend found in the P2 data-set.
Fitting the distribution of the polarization angles a single Gaussian yields a peak at 20°± 7° (see Fig.7.4, lower left frame). For comparison, the distribution was also fitted with a double Gaussian, which led to two peaks at 16°± 1° and 22°± 7°. This improves the reduced χ^2 by a factor of 3, but the fact that the secondary peak lies within the FWHM of the primary peak reduces the confidence in this feature. The distribution of the angles does not differ much from what was found for data-sets P2 and P4, and the fitted single Gaussian peaks agree within the uncertainties. The double Gaussian fit is also consistent with data-set P4: the two peaks fitted here match the values found for the peaks in data-set P2 within one respectively two sigma (peaks at 10°/16° respectively 26°/22°).
The polarization degrees seem to show lower values towards the southern-central part of the FOV, which would link up well with the results found for data-set P2 (see Fig.7.1). On average, the polarization degrees are slightly higher than those found in data-sets P2 and P4 (see Fig.7.4, upper left frame): fitting the logarithms of the polarization degrees with a single Gaussian yields a peak at (6.1 ± 1.3)% (which still agrees with the values found for P2 and P4 within the uncertainties). Again, fitting the logarithmic distribution with a double Gaussian resulted in a lower reduced χ^2 (by a factor of 2), with peaks fitted at (5.7 ± 1.0)% and (8.0 ±2.1)%. This is also consistent with the two peaks fitted for P4, but the second feature found here is a lot less pronounced than that in the P4 data-set.
The errors of the polarization angle mostly stay below 15° (see Fig.7.4, lower right frame), and this further limits the confidence in the second peak due to its small offset from the primary feature. The relative errors of the polarization degree reach up to 50% (except a few outliers, see Fig.7.4, upper right frame).

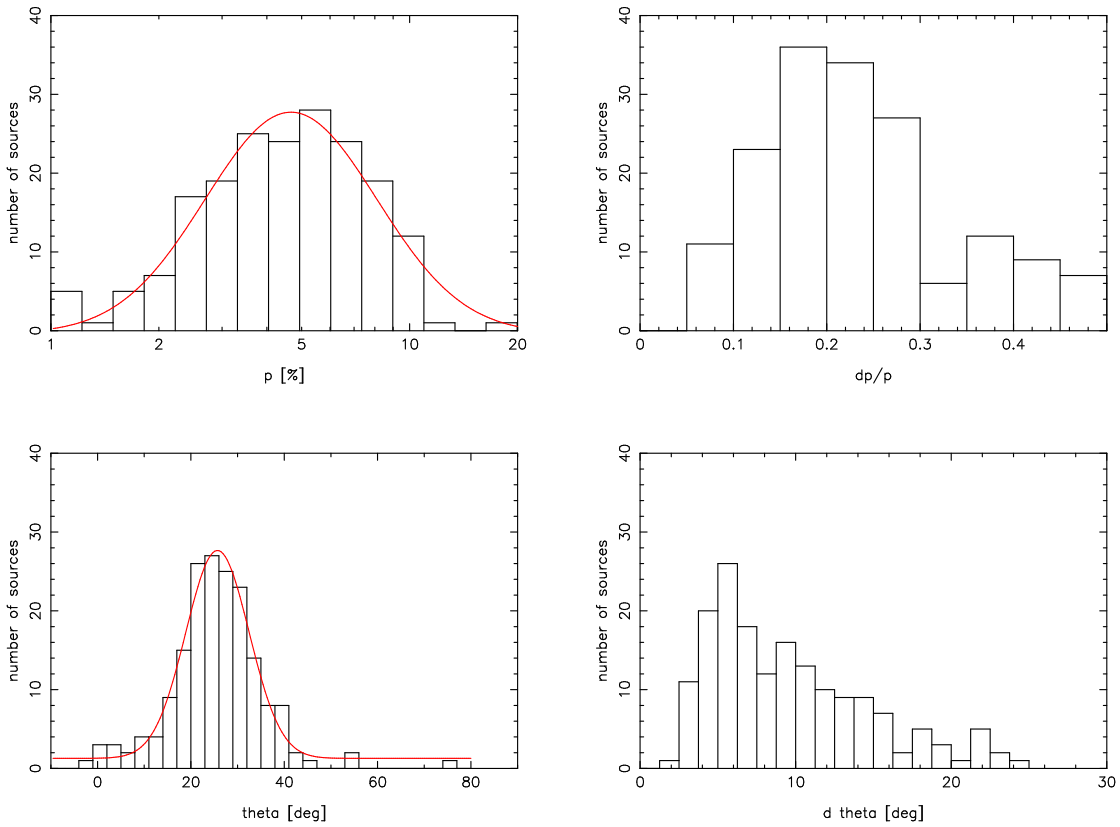

Figure 7.3: Ks-band polarization degrees (plotted on logarithmic scale, upper left) and angles (lower left) of stars in the Galactic Center (2007-04-03, dataset P4). The red lines denotes fits with a Gaussian distribution. Upper right: relative errors of the polarization degrees. Lower right: absolute errors of the polarization angles.

7.1.4 Comparing the common sources

In the overlapping area of dataset P2 and P4, the sources for which reliable measurements could be obtained in both datasets show very similar polarization parameters (see Fig.7.5). The polarization degrees and angles of 82% of the common sources agree within 1 sigma, viewing the parameters individually. Both parameters agree within 1 sigma for 69% of the common sources. For 93% of the common sources, both parameters agree within 2 sigma, and 98% (all but one source) show an agreement within 3 sigma.
The relation between the polarization degrees respectively the difference of the polarization angles of the sources in the common region of both datasets was fitted with a Gaussian (see Fig.7.5), finding peaks at $\frac{p_2}{p_4} = 1.2 \pm 0.2$ (FWHM of 0.5) and $\theta_2 - \theta_4 = 1° \pm 7°$ (FWHM of 17°). The uncertainties of these values provide an estimate for the general accuracy of the Ks-band measurements, so they are plotted as an errorcone in Fig.7.1.
This reinforces the confidence in the measured values in both datasets. Unfortunately, the overlapping part of the FOVs is only about 8 arcsec^2, and no data with a different FOV exists for the regions that show an excess in polarization degree/angle in both datasets.
The FOV of the 2011 data does not overlap with that of any previous NACO-observations, so no direct comparison is possible. But since the fitted peaks of the parameter distributions and the large scale trends (see Fig.7.1) appear very similar, the three data-sets will be treated as consistent for the purposes of this work.

7.2 H-band polarization (P1)

Reliable results could be obtained for 163 sources brighter than 18 mag. The limit of 18 mag was chosen because this corresponds to the limit of 16 mag in the Ks-band, assuming a typical H-Ks

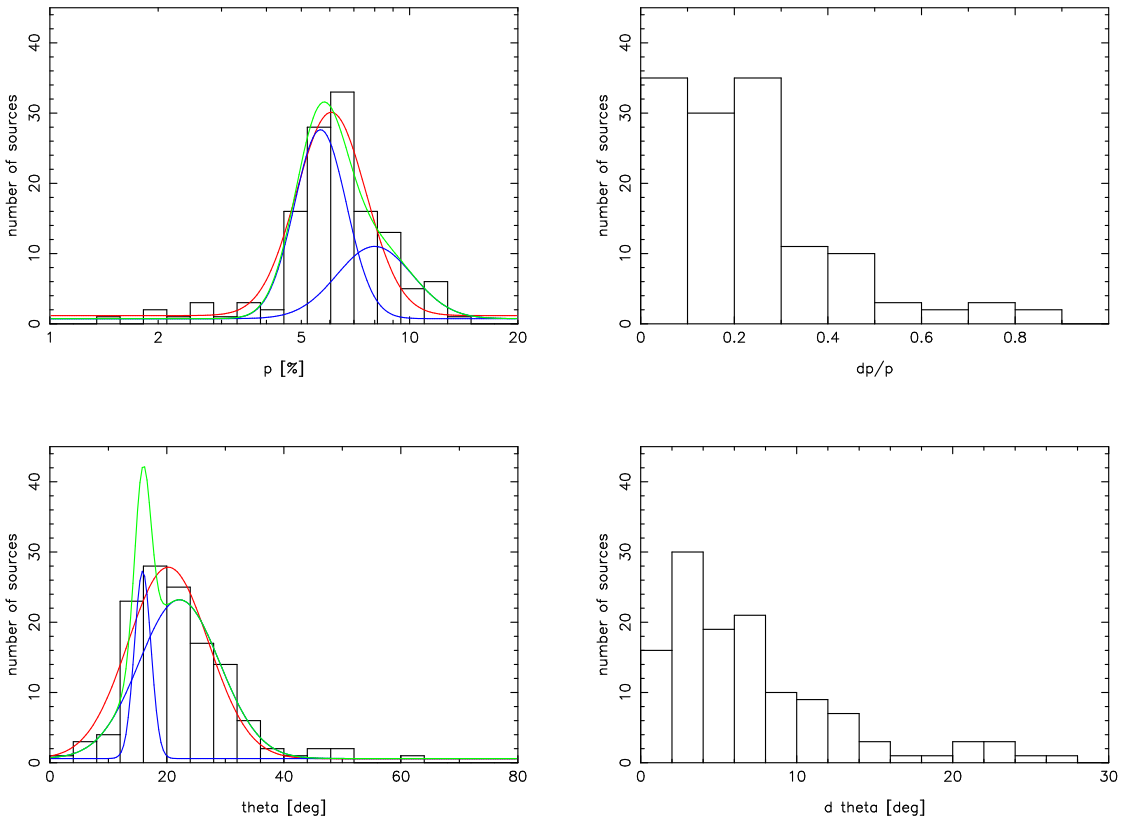

Figure 7.4: Ks-band polarization degrees (plotted on logarithmic scale, upper left) and angles (lower left) of stars in the Galactic Center (2011-03-19, dataset P18). The red lines denotes fits with a single Gaussian distribution, while the green respectively blue lines denote the fit with a double Gaussian (green: sum, blue: individual Gaussians). Upper right: relative errors of the polarization degrees. Lower right: absolute errors of the polarization angles.

of ∼2 mag (with H-$Ks_{intrinsic}$ ∼0 mag and A_H-A_{Ks} ∼2 mag, see e.g. Schödel et al., 2010b). The lower number of sources with reliable polarization compared to the Ks-band can be attributed to the significantly lower Strehl ratio of the H-band data (0.17 compared to 0.27 in the Ks-band) and the slightly different FOV, but the latter is a minor effect. The polarization angles found here are very similar to those in the Ks-band, but with a more uniform distribution over the FOV (see Fig.7.6). The distribution of the polarization angles can be fitted well with a single Gaussian, peaking at $20° \pm 8°$ (FWHM of 19°, see Fig.7.7, lower left frame). Fitting this distribution with a double Gaussian produces a slightly better χ^2, but this can be expected for increasing the number of fitting parameters. A single Gaussian fits the distribution with sufficient accuracy, compared to the poor fit with a single Gaussian function for the Ks-band polarization angles. Typical errors of the polarization angle reach about 12° (see Fig.7.7, lower right frame).
The polarization degree also appears to be quite uniform over the FOV, with typical values of 8-12%. Fitting the logarithms of the polarization degrees with a single Gaussian leads to a peak at (9.8 ± 0.7)% (FWHM of 1.7%), satisfyingly matching the data (see Fig.7.7, upper left frame). The data was also fitted with two Gaussian peaks for comparison, but as it was the case for the polarization angles, this only improves the fit marginally. The relative uncertainties of the polarization degree are of the order of up to 40% (see Fig.7.7, upper right frame).
Unfortunately, no high-resolution H-band measurements with a different FOV are available for a comparison.
As for the Ks-band, the H-band polarization degrees were plotted versus the polarization angles (see Fig.7.10, right frame). No large scale trend is visible, both parameters appear concentrated around ∼20° respectively ∼9%.

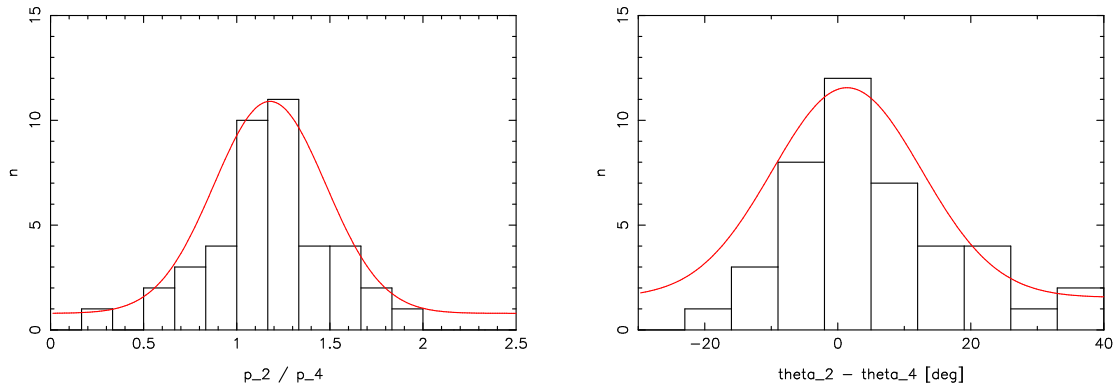

Figure 7.5: Comparison between polarization degrees (left frame) and angles (right frame) measured on sources common to dataset P2 (2009) and dataset P4 (2007). Plotted are histograms of $\frac{p_2}{p_4}$ respectively $\theta_2 - \theta_4$, with Gaussians fitted to both values (red lines).

7.3 Lp-band polarization (P16)

The polarization of 84 sources in the Lp-band data-set could be determined reliably. Considering the size of the FOV, this number appears small compared to the H- and Ks-band data, but Lp-band polarimetry suffers from much larger difficulties than what is encountered at shorter wavelengths. Fig.7.8 shows that while there is an overall trend of polarization along the Galactic plane (as seen in the H- and Ks-band), there is a significant number of outliers with either strongly deviating polarization angles or much weaker/stronger polarization degrees than what is expected for pure foreground polarization. Considering the complex structures observed in the Lp-band in the central parsec (large-scale dust structures, bow-shocks, embedded sources), this is not surprising.
Despite these additional complications, the distribution of polarization angles (see Fig.7.9, lower left frame) shows a clear peak at 20°±5° when fitted with a single Gaussian. A small secondary feature might be present at ∼35°, and a fit with a double Gaussian indeed has a better reduced χ^2 (by a factor of 2.5). But considering the small number of sources contained in this feature compared to the number of the other, more widely distributed outliers, this may not be a significant feature at all. In addition, the single Gaussian fits the distribution with sufficient accuracy, and it does not differ much from the first peak of the fitted double Gaussian.
In the same way, the distribution of the logarithms of the polarization degrees shows a slightly widened peak at (4.5 ± 1.4)% (see Fig.7.9, upper left frame), which can also be fitted with a double Gaussian for a better reduced χ^2 (by a factor of 5). This produces a secondary peak at ∼6%, but again, this may not be significant, considering the width of this peak and the fact that it is within the FWHM of the fitted single peak. The single Gaussian provides a sufficient fit.
Fig.7.9, upper right frame, shows the relative errors of the polarization degree. These errors

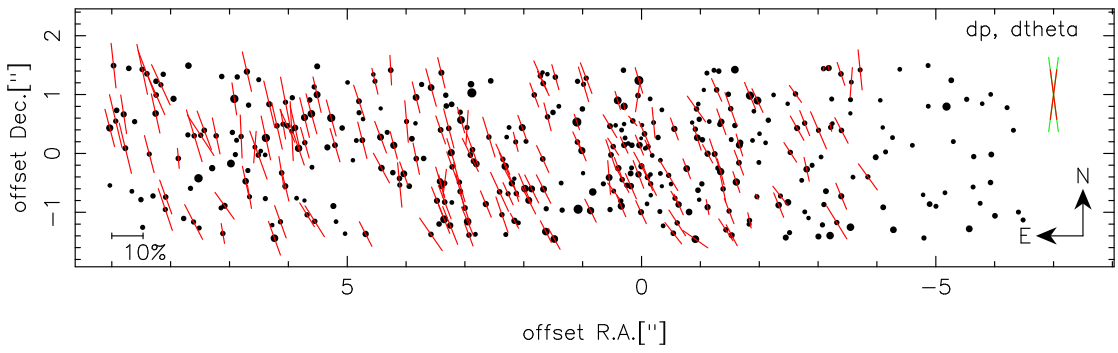

Figure 7.6: H-band polarization map of stars in the Galactic Center (dataset P1). Only reliably measured polarization values are shown here. Typical errors plotted as error cone (upper right), adopted from Ks-band data.

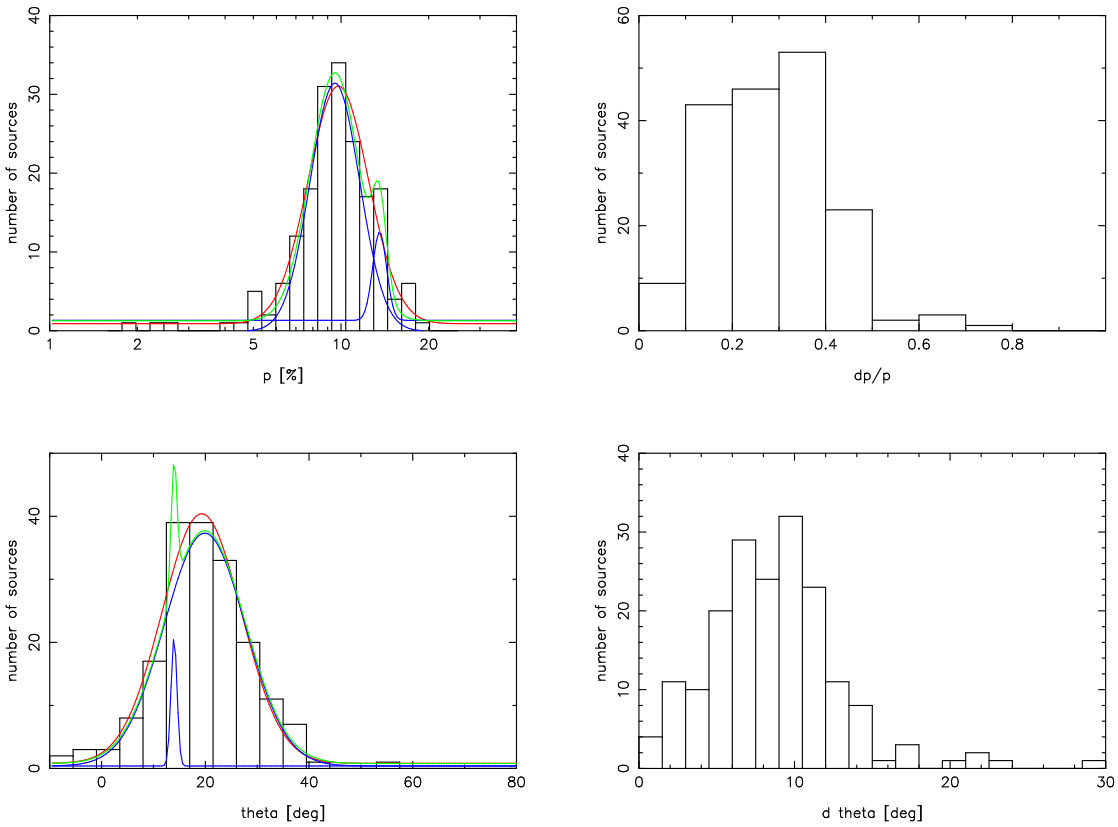

Figure 7.7: H-band polarization degrees (plotted on logarithmic scale, upper left) and angles (lower left) of stars in the Galactic Center (dataset P1). The red line denotes the fit with one Gaussian distribution, while green respectively blue lines denote the fit with a double Gaussian (green: sum, blue: individual Gaussians). Upper right: relative errors of the polarization degrees. Lower right: absolute errors of the polarization angles.

mostly stay below ~60%, a value significantly larger than what was found for the relative errors of the other data-sets. This again indicates the problems of Lp-band polarimetry (difficult photometry combined with lower polarization degrees compared to the H/Ks-band). The uncertainties of the polarization angles (see Fig.7.9, lower right frame) reach up to ~25°, which is also higher than what was found in the other data-sets. The errors of the polarization parameters further decrease the confidence in the significance of the small secondary features found in both distributions.

7.4 Comparison to previous results

The polarization degrees and angles of 30 sources from Eckart et al. (1995) and 13 sources from Ott et al. (1999) were compared to the values determined from the 2009 Ks-band data (P2). These two studies were calibrated based on polarization parameters determined by Knacke & Capps (1977) and Lebofsky et al. (1982). 87% of the Eckart sources agree with the values presented in this study within 3 sigma in polarization degree (and 83% in polarization angle). The Ott sources (with a slightly different FOV) show agreement within 3 sigma in 77% of the cases for both polarization degree and angle.
A comparison with the 2011 values shows larger deviations: only 47% of the 32 sources found both in the Eckart et al. (1995) study and the P18 data-set show an agreement in polarization degree within 3σ or less. 63% of the sources show a 3σ agreement for the polarization angles. The FOV of this data-set and that of Ott et al. (1999) do not overlap, so no comparison was possible.
Differences between these older studies and the new measurements can probably be attributed to the lower spatial resolution of the former. Both older studies show average polarization angles

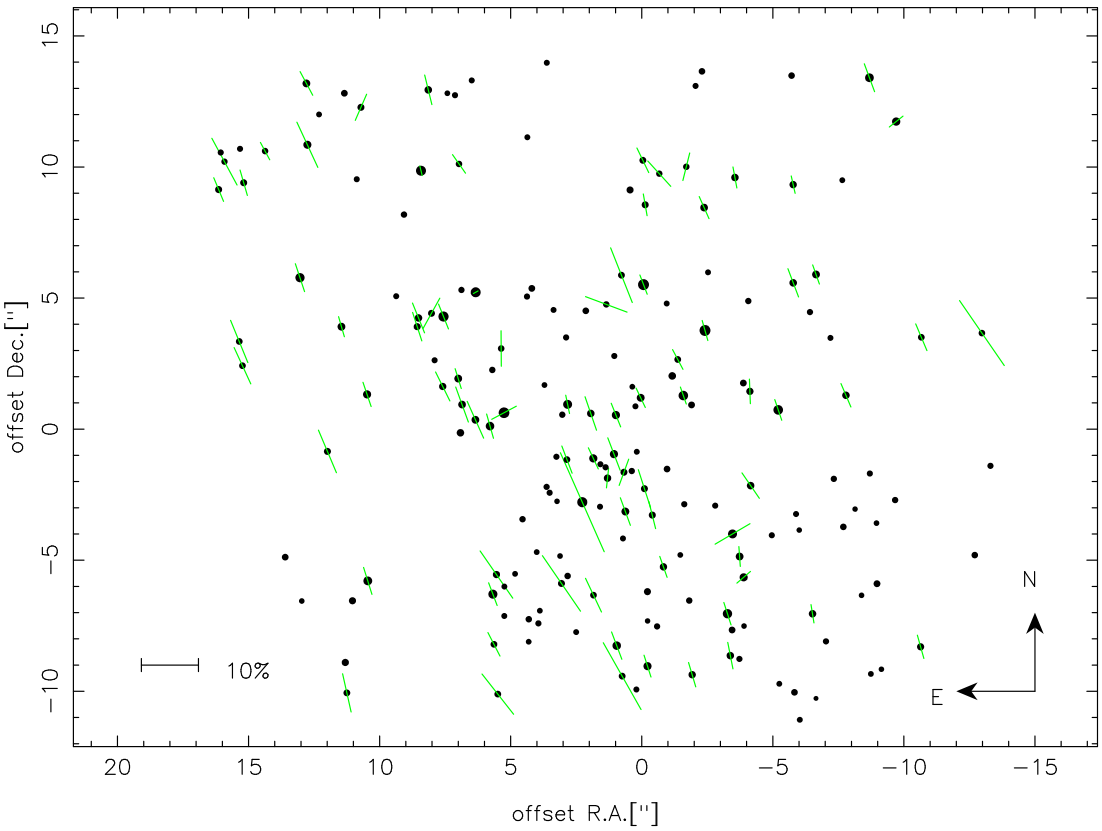

Figure 7.8: Lp-band polarization map of stars in the Galactic Center (dataset P16). Only reliably measured polarization values are shown here.

generally parallel to the Galactic plane, on average at 25° respectively 30°. Similar results are found here for the much larger new sample of sources. The average polarization degree is slightly higher, but this can be expected since the inclusion of IRS 7 with its polarization degree of only 3.6% in both older surveys lowered the flux weighted average that was calculated there considerably.

Another aspect has to be considered here: for the first time, an absolute polarimetric calibration was applied to high angular resolution data. That such good agreement can be found with data where a relative calibration based on the Knacke & Capps (1977) values was used increases the confidence in both this study and the results of the mentioned previous works.

There are only a few sources in the FOV of the presented data-set that can be compared directly to the K-band results of Knacke & Capps (1977): IRS 7 is bright and isolated enough to be detected as a single source even in the old data, while the total polarization of the sources in the vicinity of IRS 1W can be compared to the value given for IRS 1 in the older work. IRS 3 would also be suitable for such a comparison, but this source is not fully contained (i.e. located on the edge of the FOV) in any of the 2011 images.

Knacke & Capps (1977) measured a polarization of (3.0 ± 0.3)% at 20°± 5° for IRS 7, and the value found here matches that results quite well: (2.9 ± 1.0)% at 13°± 10° have been measured base on the 2011 data, but it has to be cautioned that the saturation of the source might influence these results.

In the IRS 1 region, a flux-weighted average polarization of (4.3 ± 0.5)% at 14°±10° is measured in a 3.5” aperture, which matches the value given in the older study ((3.5 ± 0.5)% at 16° ± 5°). The flux-weighted average was calculated by summing up the fluxes of the individual stars contained in the aperture for each channel and calculating Q and U (and subsequently p and θ) from these total values. This corresponds to a flux-weighted average over Q and U.

The reason why this value is much lower than the polarization found generally in this area is the contribution of IRS 1W with its large flux and an intrinsic polarization that is almost perpendicular to that of the sources in the vicinity.

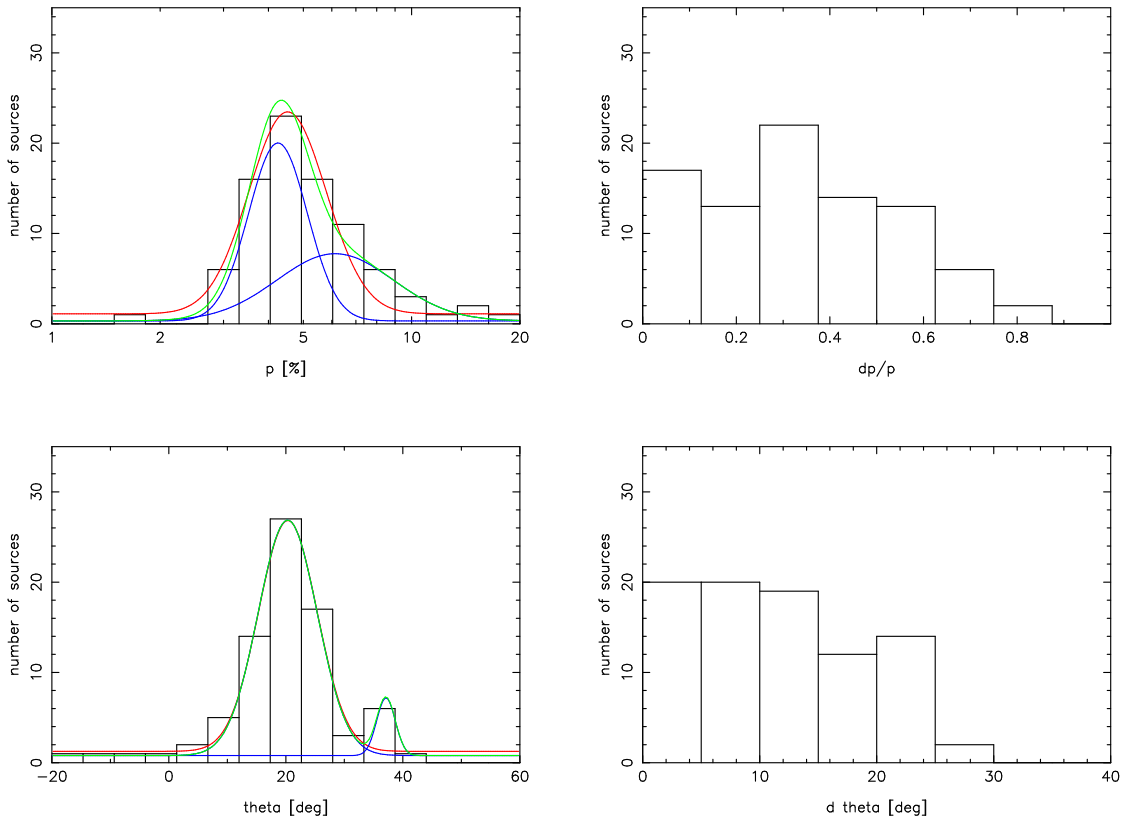

Figure 7.9: Lp-band polarization degrees (plotted on logarithmic scale, upper left) and angles (lower left) of stars in the Galactic Center (dataset P16). The red line denotes the fit with one Gaussian distribution, while green respectively blue lines denote the fit with a double Gaussian (green: sum, blue: individual Gaussians). Upper right: relative errors of the polarization degrees. Lower right: absolute errors of the polarization angles.

This further supports the detection of higher polarization degrees towards the eastern edge of the FOV: in order for the total polarization to be on the order of 4% (including IRS 1W), the surrounding sources must have a significantly higher polarization degree.
Very few H-band polarization measurements are available for a comparison. The most recent survey with an aperture not exceeding the FOV of this study was conducted by Bailey et al. (1984) in the J-, H- and K-band, who presented polarization parameters for two sources contained in this study, IRS 1 and IRS 16 (treating these complexes as a single source each, using a 3.0” aperture). That study measured $9.9 \pm 0.6\%$ at $20° \pm 1°$ for IRS 1 respectively $10.2 \pm 0.2\%$ at $8° \pm 1°$ for IRS 16 in the H-band. Calculating a flux weighted average in a 3.0” aperture around the IRS 1 respectively IRS 16 sources based on the new data yields values of $10.9 \pm 0.5\%$ at $15° \pm 10°$ for IRS 1 and $7.2 \pm 0.5\%$ at $21° \pm 10°$ for IRS 16. This agrees well for IRS 1, while the polarization degree found for IRS 16 deviates considerably. But it has to be considered that both sources were only very poorly resolved at the time of that study, not all IRS 16 sources are contained in this study, and only sources with reliably measured polarization were used for the comparison.
The polarization degrees and angles measured here are also compatible to the larger scale polarization maps presented by Nishiyama et al. (2009) in both the H- and the Ks-band. The authors of that study find polarization angles of ~20° in the area around the FOV used here, which itself is not covered due to insufficient resolution and crowding.
The situation in the Lp-band is similar to the H-band: Lebofsky et al. (1982) (5.8” beam) and Knacke & Capps (1977) (7” beam) are the only studies to date that measured L-band polarization. Only two sources can be compared directly: Knacke & Capps (1977) measured the polarization of IRS 3 as $(3.4 \pm 1.0)\%$ at $16° \pm 8°$, while they give values of $(2.6 \pm 0.3)\%$ at $43° \pm 5°$ for IRS 7. Lebofsky et al. (1982) do not provide values for IRS 3, but measured $(3.2 \pm 0.5)\%$ polarization at 13° for IRS 7. The values found in the new observations for these two

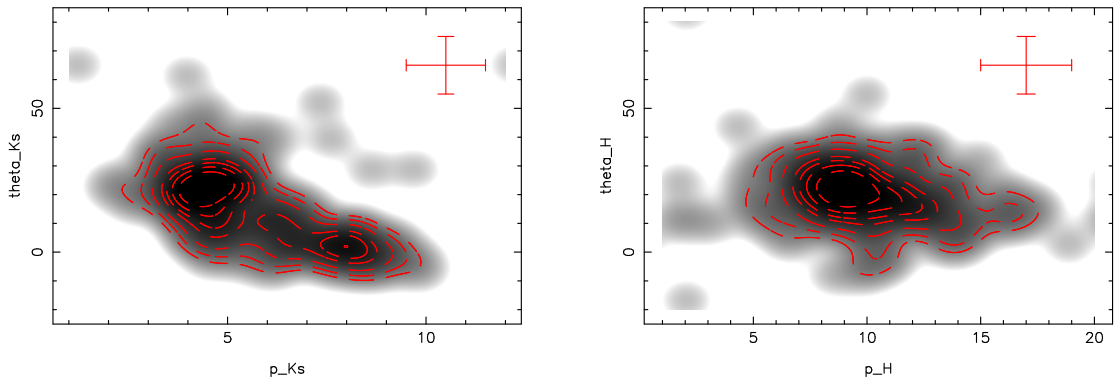

Figure 7.10: Polarization angle vs. polarization degree, plotted as logarithmic smoothed point density, with typical error indicated by red bars (upper right corners). Contours were plotted to guide the eye. Left frame: Ks-band, right frame: H-band

sources, about 30 years and several instrument/telescope generations later, agree relatively well: the polarization of IRS 3 is measured as (3.7 ± 0.1)% at 16.0° ± 0.7°, which is in very good agreement with the Knacke & Capps (1977) value. IRS 7 exhibits a polarization of (3.6 ± 0.1)% at 20.9° ± 0.7°. This matches the Lebofsky et al. (1982) values better, while the measured angle deviates from Knacke & Capps (1977). The good agreement of these polarization parameters shows that the calibration applied to the new data also works in the Lp-band.

7.5 Comparison between the wavelength bands

7.5.1 H- and Ks-band

The H-band data-set (P1) has almost the same FOV as the Ks-band data-set P2 and a comparable depth and data quality. The H/Ks-band comparison is therefore only based on these two data-sets.
By comparing the positions of the sources detected in each datasets, 133 sources with reliable polarization parameters could be identified in both the H- and the Ks-band data. The missing sources are mostly found outside the other data-set's FOV, in addition to a small number of very fast moving sources (like the S-stars), which are difficult to identify due to the time of 2.5 years between the H- and Ks-band observations. In addition, photometric errors tend to be higher in the westernmost region of the FOV due to the lack of suitable close bright stars for PSF determination. This leads to the number of sources with reliable polarization parameters being small there. The common sources are used for the following, source-by-source comparison.

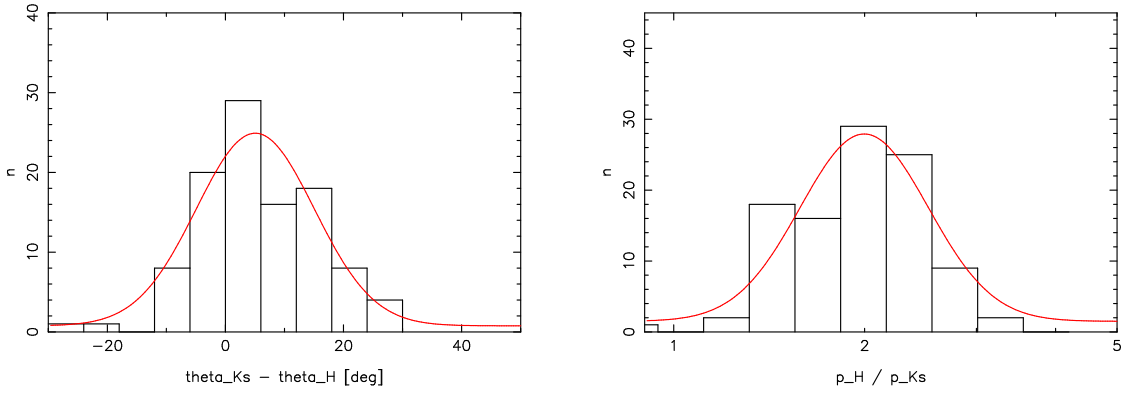

Figure 7.11: Left frame: difference between H- and Ks-band polarization angle. Right frame: relation of H- to Ks-band polarization degree (logarithmic plot). The red line represents a Gaussian fitted to the histograms.

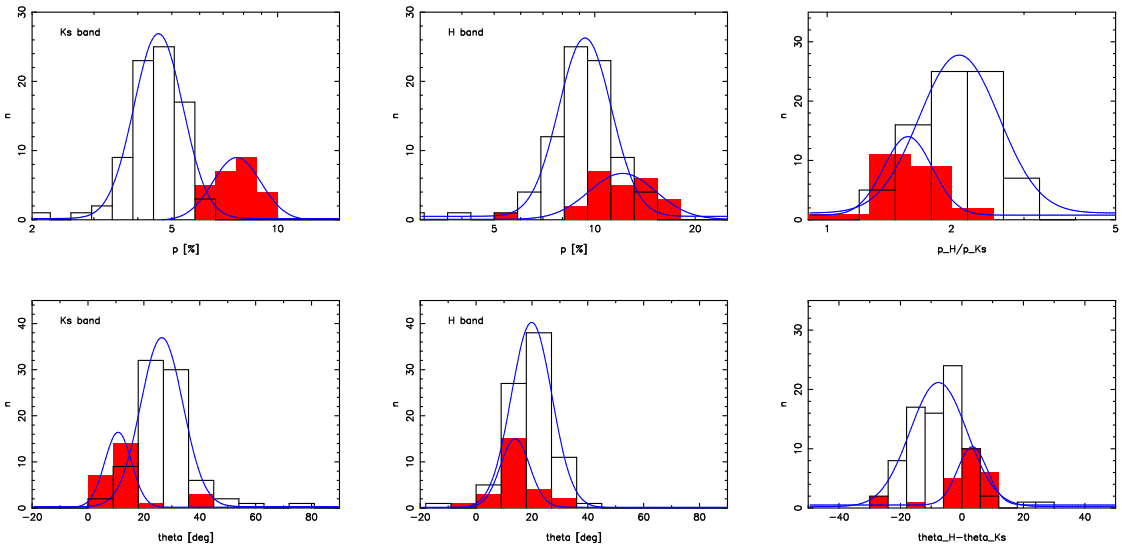

Figure 7.12: Sources detected in H- and Ks-band, separated by Ks-band polarization. White columns: $p_{Ks} < 6\%$. Red columns: $p_{Ks} > 6\%$. Upper/lower left frame: Ks-band polarization degree/angle, Upper/lower middle frame: H-band polarization degree/angle, upper right frame: relation of H- and Ks-band polarization degree (logarithmic plot). Lower right frame: difference between H- and Ks-band polarization angle. Blue lines represent Gaussian fits to the histograms.

The polarization angles measured in the H- and Ks-band seem to agree well in the center and the western part of the FOV, while there appears to be an offset in the eastern region. Fig.7.11 shows both the difference in polarization angle as well as the relation of H- and Ks-band polarization degrees. $\theta_H - \theta_{Ks}$ can be fitted well with a Gaussian distribution and shows a peak at $4° \pm 8°$

Table 7.1: Results of Gaussian fits to polarization parameter histograms for the complete dataset respectively sub-datasets separated based on p_{Ks} respectively position along the East-West-axis. Polarization degrees given in %, angles given in degrees.

separation	value	peak 1	σ_1	peak 2	σ_2
none	p_{Ks}[%]	4.6	0.8	7.7	1.2
none	p_H[%]	9.8	0.7		
none	θ_{Ks}[°]	28	3	12	6
none	θ_H[°]	20	8		
none	$\frac{p_H}{p_{Ks}}$	1.9	0.4		
none	$\theta_H - \theta_{Ks}$[°]	2	8		
p_{Ks}	p_{Ks}[%]	4.6	0.6	7.5	1.0
p_{Ks}	p_H[%]	9.3	1.3	12.1	2.1
p_{Ks}	θ_{Ks}[°]	28	6	11	6
p_{Ks}	θ_H[°]	20	6	13	6
p_{Ks}	$\frac{p_H}{p_{Ks}}$	2.0	0.3	1.6	0.3
p_{Ks}	$\theta_H - \theta_{Ks}$[°]	-5	4	4	5
E-W pos	p_{Ks}[%]	4.6	0.6	7.7	1.0
E-W pos	p_H[%]	9.3	1.4	11.8	2.1
E-W pos	θ_{Ks}[°]	29	6	10	7
E-W pos	θ_H[°]	21	6	13	6
E-W pos	$\frac{p_H}{p_{Ks}}$	2.0	0.3	1.7	0.3
E-W pos	$\theta_H - \theta_{Ks}$[°]	-5	4	3	5

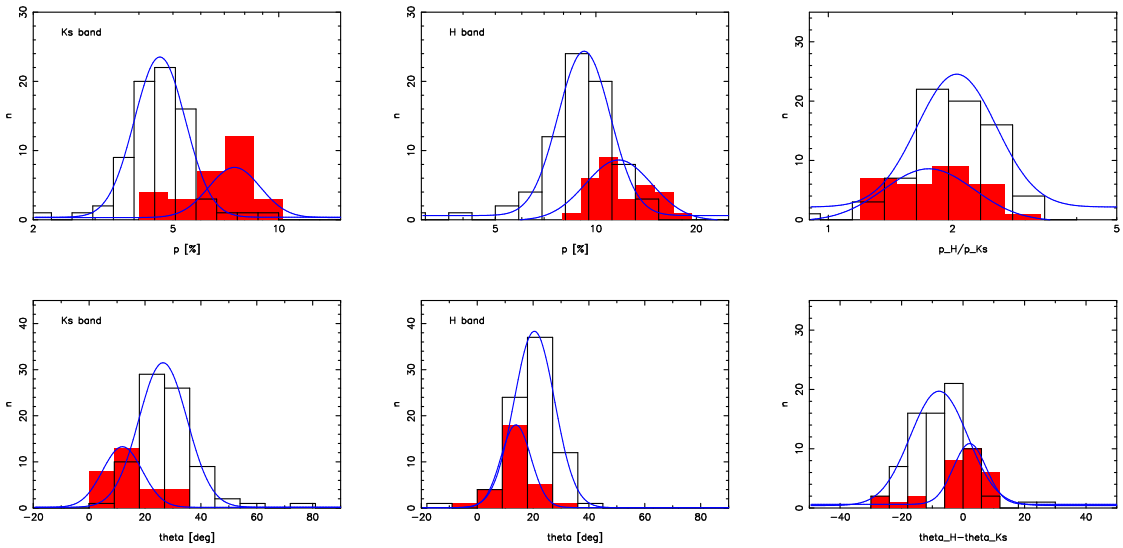

Figure 7.13: Sources detected in the H- and Ks-band, separated by position along the East-West-axis. White columns: sources less than 4.1" east of Sgr A*. Red columns: sources more than 4.1" east of Sgr A*. Upper/lower left frame: Ks-band polarization degree/angle, upper/lower middle frame: H-band polarization degree/angle, Upper right frame: relation of H- and Ks-band polarization degree (logarithmic plot). Lower right frame: difference between H- and Ks-band polarization angle. Blue lines represent Gaussian fits to the histograms.

(FWHM of 20°). Considering the width of the peak, this offset is not significantly different from zero. $\frac{p_H}{p_{Ks}}$ can be fitted quite well with a log-normal distribution, peaking at 1.9 ± 0.4 (FWHM of 0.9). For a complete list of the fitting results, see Tab.7.1 (which also contains the values referred to in the following paragraphs).

Assuming the two peaks found for both the polarization degree and angle in the Ks-band are real, the stars with reliable polarization parameters in both H- and Ks-band were separated into two samples: stars with $p_{Ks} < 6\%$ (pK^-) and with $p_{Ks} > 6\%$ (pK^+). Fig.7.12 shows histograms of the different polarization parameters of the pK^- and pK^+ sources in the two bands, namely the polarization degrees and angles, $\theta_H - \theta_{Ks}$ and $\frac{p_H}{p_{Ks}}$. All histograms were fitted with a Gaussian, and although these fits are poor in several cases, the fitted peaks show at least the trends present in the data.

The pK^+ sources show systematically lower polarization angles than the pK^- sources in the Ks-band (peak offset of 18°). The peaks fitted here match the ones fitted to the complete dataset (see §7.1). A similar, yet smaller offset exists in the H-band (7°, well within the uncertainties, and the fitted peaks also correspond to those determined in §7.2). Accordingly, $\theta_H - \theta_{Ks}$ also shows an offset of 9°, but that value is relatively close to zero for both sub-datasets considering the large FWHM of the peaks.

Looking at the polarization degrees reveals similar offsets: for the Ks-band, the pK^+ peak is found at a polarization degree which is higher by a factor of 1.6 than where the pK^- peak is fitted. The relative difference found in the H-band is smaller, with the pK^+ peak found at a polarization degree which is larger by a factor of 1.3 than that of the pK^- peak. This manifests itself in the $\frac{p_H}{p_{Ks}}$ histogram, which is found peaked at 1.6 for pK^+, and at 2.0 for pK^-.

Since the higher polarized pK^+ sources are mostly found in the eastern part of the FOV (in the general area of the Northern Arm), the sources were also divided into two samples based on their position along the East-West-axis: pK-E (sources more than 4.1" east of Sgr A*) and pK-W (sources less than 4.1" east of Sgr A*). Fig.7.13 shows histograms of the polarization parameters for both sub-datasets. The results obtained there are very similar to those found for a separation based on p_{Ks}, with practically identical peaks and offsets (pK-E corresponding to pK^+, pK-W to pK^-).

How can these findings be explained? For interstellar polarization in general, the H-band polarization degrees are expected to be significantly larger than the Ks-band values, while the

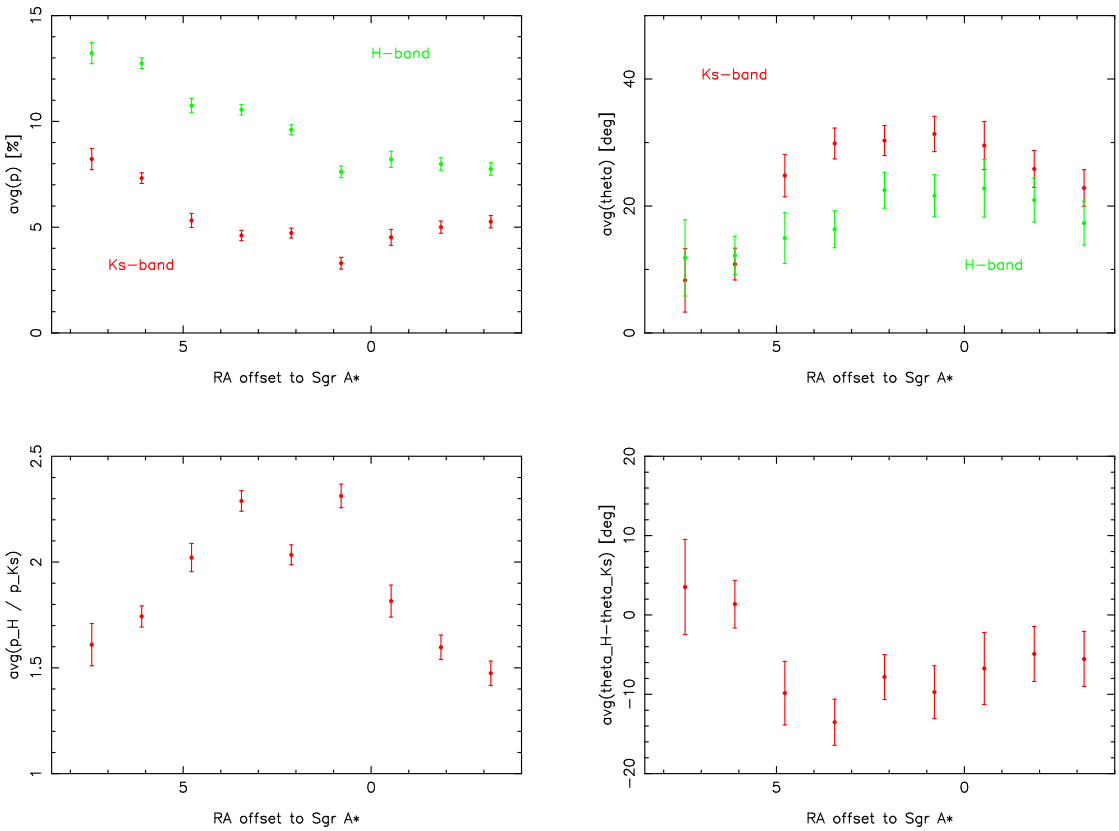

Figure 7.14: H- and Ks-band polarization parameters, averaged over 1.3” bins along the East-West axis. Upper left: polarization degrees, red: Ks-band, green: H-band. Upper right: polarization angles, red: Ks-band, green: H-band. Lower left: $\frac{p_H}{p_{Ks}}$. Lower right: $\theta_H - \theta_{Ks}$.

angles in both bands should be the same within the uncertainties. This is expected from both the Serkowski law and the power law relation presented by Martin et al. (1990). According to the semi-empirical Serkowski law, the polarization at a given wavelength in relation to the polarization maximum is dependent on the wavelength where that maximum occurs:

$$\frac{p(\lambda)}{p_{max}} = exp\left[-K \times ln^2\left(\frac{\lambda_{max}}{\lambda}\right)\right] \tag{7.1}$$

with $K = 0.01 + 1.66\lambda_{max}$ (Whittet et al., 1992). It appears, however, that polarization in the NIR, specifically in the J-, H- and K-band, is only very weakly dependent on λ_{max} (Martin et al., 1990). Keeping this in mind, and considering the availability of only two data-points for each source and the large FWHM of the Gaussian fits to $\frac{p_H}{p_{Ks}}$, only rough estimates can be given here. The peak fitted to the complete dataset (1.9 ± 0.9) agrees best with $\lambda_{max} \sim 0.7\mu m$. Of the two fitted peaks for the sub-datasets, the value of 2.0 ± 0.7 would agree with $\lambda_{max} \sim 0.7\mu m$ as well, while the peak at 1.6 ± 0.7 points to a λ_{max} which is either much smaller ($\sim 0.25\mu m$) or larger ($\sim 1.25\mu m$). Bailey et al. (1984) give a value of $\lambda_{max} \approx 0.80\mu m$ (using J, H-and K-band data), which approximately matches the first two values found here. It is stated in that work itself that the agreement with the semi-empirical law is only rough. It also has to be considered that this law was established for sources with only very weak polarization in the NIR, so it does not describe observations in that wavelength regime very well. All this leads to the conclusion that the presented data is clearly not sufficient to give a reliable estimate for this parameter.
Using the power law relation proposed by Martin et al. (1990)

$$\frac{p_H}{p_{Ks}} = \left(\frac{\lambda_H}{\lambda_{Ks}}\right)^{-\alpha} \tag{7.2}$$

yields a power law index of $\alpha = 2.4 \pm 1.7$ for $\frac{p_H}{p_{Ks}} = 1.9 \pm 0.9$, while the two sub-dataset peaks

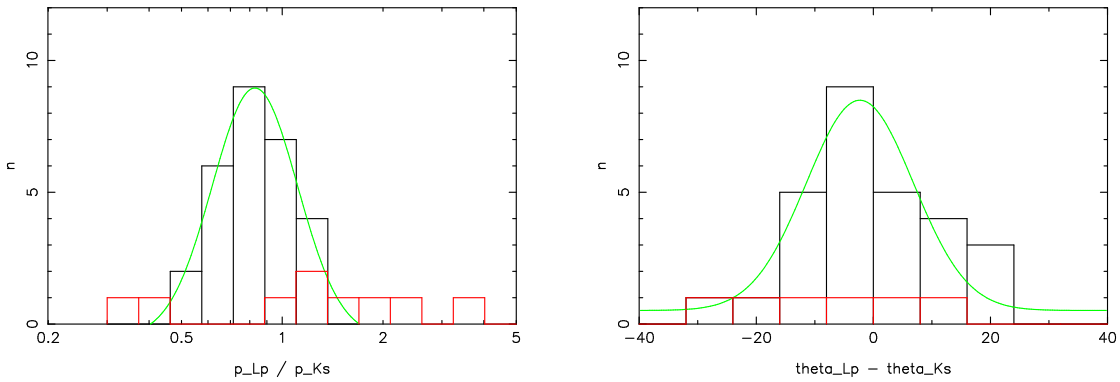

Figure 7.15: Left frame: relation of Lp- to Ks-band polarization degree (logarithmic plot). Right frame: difference between Lp- and Ks-band polarization angle. In both frames, the red columns represent suspected intrinsically polarized sources, while the white columns contain sources affected only by the foreground polarization. The green lines represent Gaussians fitted to the histograms.

lead to $\alpha = 1.7 \pm 1.6$ respectively $\alpha = 2.5 \pm 1.3$. These values agree with the range of 1.5-2.0 given by Martin et al. (1990), although the uncertainties are quite large. It has to be stressed that these values have been obtained on a relatively small region and that a study of a much larger region is necessary before any reliable conclusions can be drawn on this issue.
Fig.7.14 shows binned plots of the H- and Ks-band polarization parameters. Only the common reliable sources were used for these maps, averaging the polarization parameters for all the sources contained in 1.3" wide bins along the East-West axis.
The same large scale trends are seen here as the ones found based on the histograms, and the first impression points towards the same effects being present in both Ks- and H-band for both polarization degree and angle. Looking at the plots of $\frac{p_H}{p_{Ks}}$ and $\theta_H - \theta_{Ks}$, however, the differences between the two bands become apparent: as seen in Fig.7.13, $\frac{p_H}{p_{Ks}}$ is found to be around 2-2.2 in the center and more towards 1.5-1.6 east of Sgr A*. A similar trend is visible towards the western edge, but the number of sources is small there and there may be an influence of edge effects. The $\theta_H - \theta_{Ks}$ plot also confirms the trends found earlier: an offset of $\sim 10°$ can be seen in the center and the west and one of $\sim 0°$ towards the east.
These results raise the question what could cause the observed deviations of the polarization parameters over the FOV, assuming those deviations are indeed real and not some sort of instrumental effect that was not compensated. The comparison of the 2009 Ks-band dataset (P2) with dataset P4 shows that while a similar increase in polarization degree exists there as well, no accompanying shift in polarization angle is found. If this was indeed an instrumental effect, one would expect the same pattern in both parameters. Fig.5.14 shows a residue of the dither pattern in both Q and U, but these variations are far too small to lead to a significant deviation over the FOV as it is observed here.
This issue cannot be solved completely without further (calibration) observations, but for the purposes of this study, it can be assumed that thed observed effect is indeed real.
As possible explanations, two basic mechanisms come to mind here:

Variable LOS extinction The extinction towards the central parsec is known to be "patchy" (see Schödel et al., 2010b), which in turn indicates different dust column densities and/or dust parameters along individual lines-of-sight towards different regions in the FOV. This could lead to differences in the polarization measured at different locations. But the situation is even more complex. Not only the densities are important, but also possible different alignment in individual dust clouds (so passing through an additional cloud on one LOS compared to another could even lower the total polarization degree for that LOS). Another problem is that a smaller effect is found in the H-band (and thus the impact on $\theta_H - \theta_{Ks}$ and $\frac{p_H}{p_{Ks}}$). This would require significantly different average dust parameters from one LOS to the other (which in turn requires even more dramatic changes for a large percentage of the individual dust clouds along the LOS). Such a

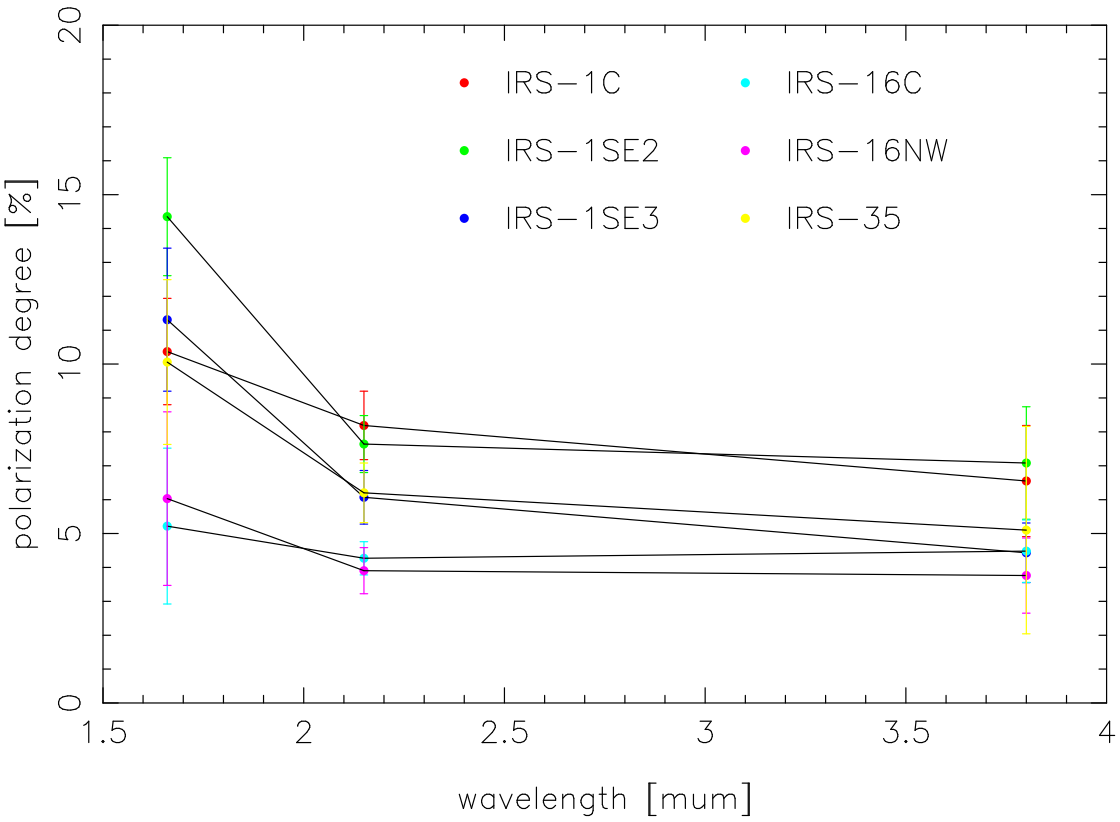

Figure 7.16: Polarization degrees measured for 6 sources in the H/Ks/Lp-band. The sources are indicated by the different colors and by the lines connecting the data-points (to guide the eye).

configuration is possible, but the highly specific arrangement required to produce a pattern as observed here seems very unlikely.

Local influences The area where this effect occurs coincides with the position of a known local feature, the Northern Arm of the Minispiral. This feature is clearly visible in the L-band (see Fig.4.2), faint in Ks and not detectable in the H-band. Both the light from the stellar sources itself, which passes through the stream of aligned grains in the Northern Arm, as well as scattered and/or emitted light from these grains themselves may contribute to some extent to the polarization measured in this region. This would have a larger impact in the Ks-band compared to the H-band, due to the sizes and temperatures of the involved grains, this far matching the findings. The question however remains how large such a contribution could be.
Under conditions as they are found in the filaments, grain alignment by the Davis-Greenstein mechanism would be almost perfect, especially due to the strong magnetic fields (lower limit of ~2 mG close to IRS 1W, see Aitken et al., 1998). By coincidence, the local grain alignment angle in the Northern Arm matches that measured for the LOS polarization (Aitken et al., 1998). This means that local dichroic extinction would increase the observed total polarization degree, while scattering/emission would decrease it (as it is indeed found for IRS 1W, see below). This leads to the conclusion that the former effect, local dichroic extinction, is the most likely cause for this effect, although the likely extent of this contribution cannot be determined from the available data on dust parameters and configurations both along the LOS and in the GC itself.
This immediately leads to the next question: are these trends mirrored by the behavior of the extinction measured in the FOV?

7.5.2 Ks- and Lp-band

For 37 sources, Ks-band and Lp-band polarization parameters have been measured. This is less than half of the available Lp-band sources, but that can be expected considering the respective fields-of-view observed in both bands (see Fig.4.1). The relation between Ks- and Lp-band

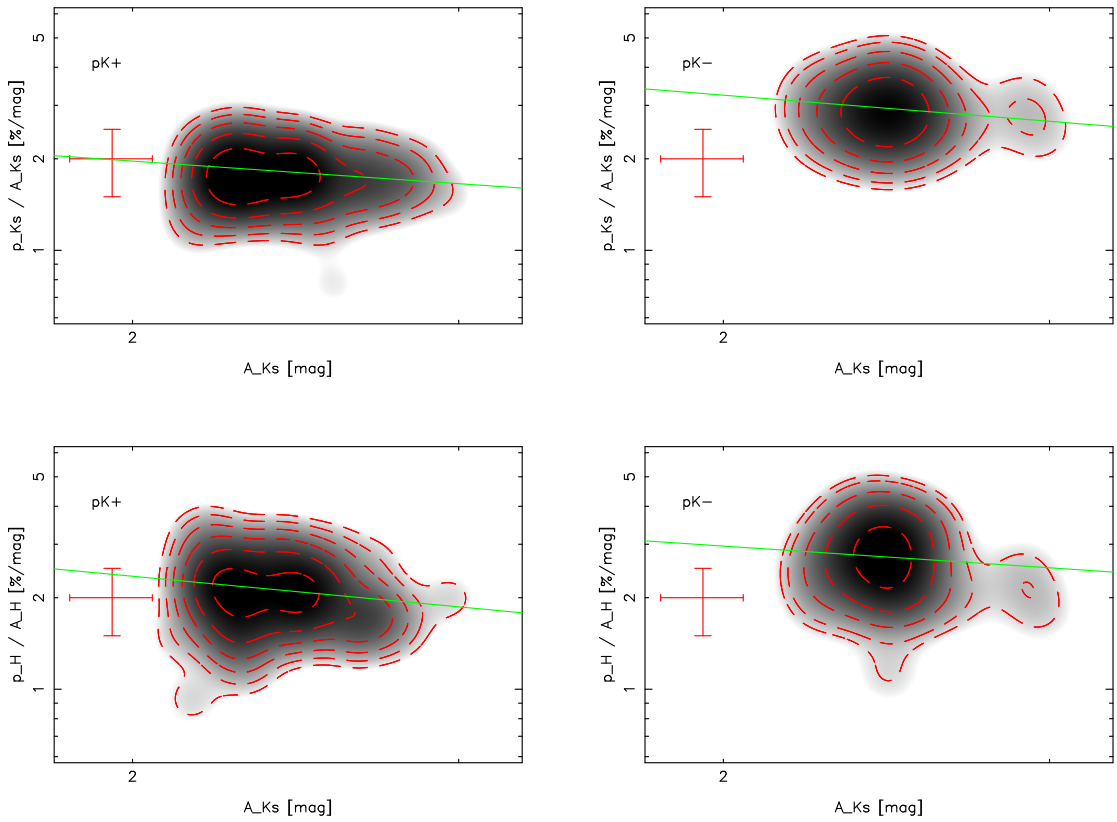

Figure 7.17: Polarization efficiency in data-set P2 (Ks-band, upper frames) and data-set P1 (H-band, lower frames), compared to Ks-band extinction, plotted as point density, with typical error represented on the left. pK^+ and pK^- sources shown separately in left respectively right frames for both bands. Green lines represent the fitted power-law relation.

polarization of a source can provide a strong indication of intrinsic polarization: if $\frac{p_{Lp}}{p_{Ks}}$ is significantly higher or lower than the value expected for foreground polarization (~0.7-0.8 towards the GC, see Jones, 1990) or if the polarization angles deviate strongly between the two bands, the source can be regarded as intrinsically polarized. The reason for this is that at least in the foreground component, the same grains should be responsible for the polarization in all NIR (and optical) bands. So a purely foreground-polarized source should show the same polarization angle over these wavelength bands, and if it does not, another component must be contributing. Of the 37 common sources, 9 candidates for intrinsic polarization have been found based on this method. Tab.7.2 shows the polarization parameters of the common sources, as well as the classification of each source as intrinsically or foreground polarized. Several bright intrinsically polarized sources are examined in more detail in §8.2. Fig.7.15 shows the distribution of $\frac{p_{Lp}}{p_{Ks}}$ and the difference between the polarization angles. Most of the outlier values can be assumed to be affected by intrinsic polarization (plotted in red), while the distribution of the foreground-polarized sources shows clear peaks at 0.8 ± 0.3 ($\frac{p_{Lp}}{p_{Ks}}$) respectively -2°± 9° ($\theta_{Lp} - \theta_{ks}$). The latter value agrees with zero within the uncertainties, which is expected if indeed the same grain population (or at least grains aligned in the same direction) is responsible for the polarization at both wavelengths. The former exceeds the value expected from theoretical and semi-empirical models: while the Serkowski et al. (1975) law does not work well in the NIR anyway (see §7.5.1), the model proposed by Mathis (1986) and the power law relation suggested by Martin et al. (1990) predicts too small values as well. Jones (1990) compared these relations to data obtained on local sources and observations on three GC sources, IRS 7, IRS 9 and GCS 9. The GC sources showed an even higher excess than the local sources compared to the results of the models/relations, with $\frac{p_{Lp}}{p_{Ks}}$ around 0.7. This is confirmed here for a much larger number of sources, while the cause remains uncertain. As suggested by Jones (1990), polarimetric observations at even longer wavelengths and spectropolarimetric observations in the Lp-band

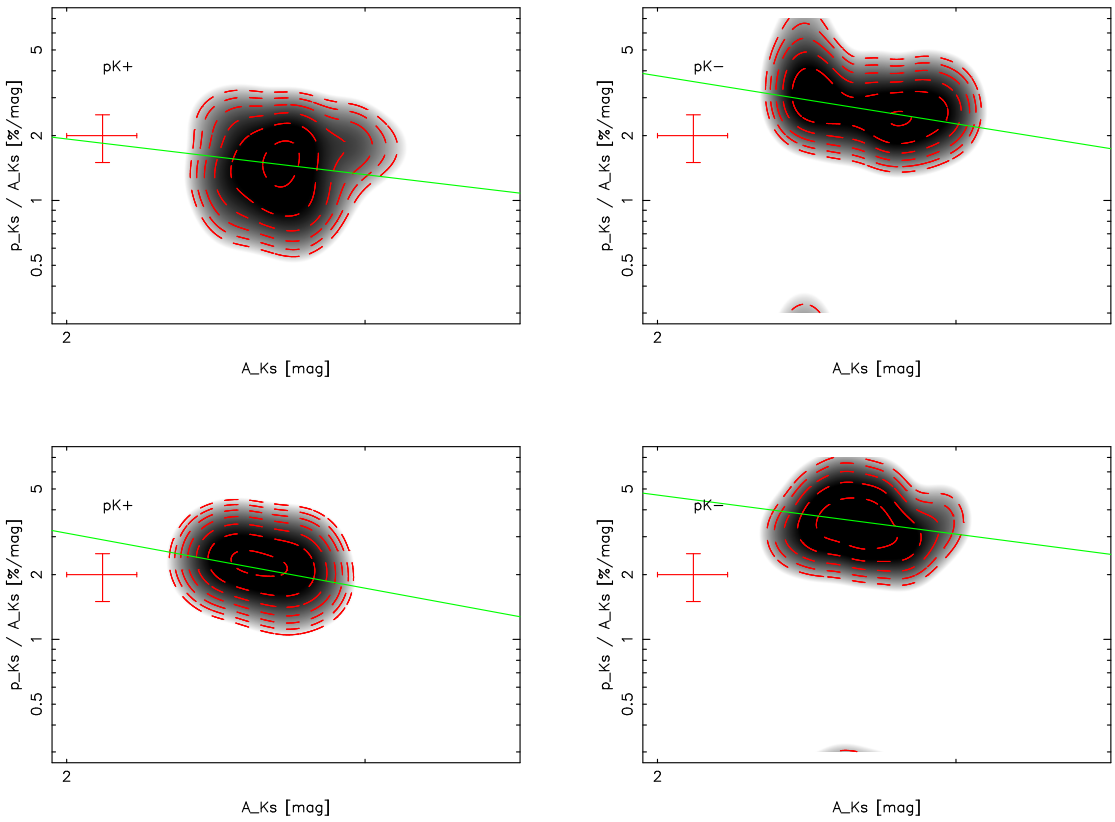

Figure 7.18: Polarization efficiency in data-set P4 (Ks-band, upper frames) and data-set P18 (Ks-band, lower frames), compared to Ks-band extinction, plotted as point density, with typical error represented on the left. pK^+ and pK^- sources shown separately in left respectively right frames for both bands. Green lines represent the fitted power-law relation.

might help to answer this question, but such measurements are anything but easy.

7.5.3 Sources found in H-, Ks- and Lp-band

Only 6 sources were detected in all three bands. The small H-band FOV and the low depth of the Lp-band data are the limiting factors here. See Tab.7.3 for the polarization parameters found for the individual sources. The polarization angles agree well within the uncertainties for each source, which indicates that these sources are not affected by intrinsic polarization in these wavelength bands and that their polarization can be treated as typical for the LOS towards the GC. Fig.7.16 shows the measured polarization degrees for these 6 sources. While the relation between the H- and Ks-band values matches the expectations from the Serkowski et al. (1975) law and the Martin et al. (1990) power-law relation (as discussed for a broader sample including these sources in §7.5.1), the Lp-band polarization is higher than what would be expected from both laws (as found in §7.5.2 for all sources common to Ks- and Lp-band).

7.6 Correlation with extinction

The H- and Ks-band polarization values were compared to the extinction map presented by Schödel et al. (2010b). Fig.7.17 shows the polarization efficiency $\frac{p_\lambda}{A_\lambda}$ for the data-sets P1 and P2 plotted against the Ks-band extinction A_{Ks} taken from the extinction map at the location of each source. As it turns out, almost the same distribution of A_{Ks} is found for the pK^+ and the pK^- sources (see Fig.7.20), which in turn leads to an offset between the two sub-datasets in polarization efficiency. They are therefore plotted separately in Fig.7.17.
For the sources found in the P4 and P18 data-sets, a clear separation into two distinct groups of sources based on the Ks-band polarization is not as evident as for the P2 data-set, but the polar-

ization degrees still show a wider distribution than the clear peaks of the P2 distribution. In order to investigate if this coincides with an offset in polarization efficiency as well, a separation at 6% (P4) respectively 7.3% (P18) was also introduced here (using the pK^+ and pK^- nomenclature for this separation as well) . These values were chosen based on Figs.7.4 and 7.3. Sources with less than 3% polarization were exluded, since this low value indicates either a foreground source or intrinsic polarization perpendicular to the foreground (e.g. in IRS 1W and 10W, see §8.2). In both of these cases, a comparison with an extinction map would not produce meaningful results.

Table 7.2: Polarization parameters of the sources detected in the Ks- and Lp-band. *ID* indicates the number of the source in the list contained in the *online* material. *Class* gives the classification of the source as intrinsically or foreground polarized.

ID	p_{Ks} [%]	p_{Lp} [%]	θ_{Ks} [°]	θ_{Lp} [°]	class
1	2.67 ± 0.6	3.3 ± 0.6	35 ± 11	12 ± 8	foreground
2	4.27 ± 0.6	4.5 ± 0.9	25 ± 5	22 ± 7	foreground
5	8.19 ± 1.0	6.6 ± 1.6	8 ± 6	20 ± 9	foreground
7	7.77 ± 0.8	5.7 ± 2.3	5 ± 5	26 ± 14	foreground
8	7.64 ± 0.8	7.1 ± 1.7	11 ± 5	24 ± 8	foreground
11	6.07 ± 0.8	4.4 ± 0.9	11 ± 5	16 ± 8	foreground
12	3.91 ± 0.8	3.8 ± 1.1	26 ± 10	25 ± 10	foreground
184	7.49 ± 0.5	4.3 ± 2.4	11 ± 5	4 ± 24	foreground
187	4.84 ± 0.8	3.8 ± 0.5	19 ± 8	18 ± 5	foreground
195	2.94 ± 0.9	4.2 ± 0.5	26 ± 16	20 ± 5	intrinsic
196	2.66 ± 0.9	3.5 ± 1.6	17 ± 17	-6 ± 23	intrinsic
197	3.90 ± 1.0	4.1 ± 0.8	24 ± 9	25 ± 6	foreground
199	2.06 ± 0.9	4.9 ± 3.0	4 ± 19	-20 ± 21	intrinsic
201	6.20 ± 0.9	5.1 ± 3.1	26 ± 5	21 ± 22	foreground
284	3.12 ± 0.7	6.1 ± 0.7	20 ± 14	21 ± 5	intrinsic
300	2.77 ± 0.8	3.2 ±0.5	24 ± 11	19 ± 5	foreground
305	5.01 ± 0.7	3.9 ± 2.8	25 ± 5	28 ± 25	foreground
389	5.59 ± 0.5	5.2 ± 0.5	30 ± 5	18 ± 5	foreground
399	7.4 ± 0.5	8.8 ± 0.9	13 ± 5	25 ± 5	intrinsic
400	5.19 ± 0.5	4.0 ± 3.1	17 ± 5	35 ± 23	foreground
401	5.4 ± 0.5	1.8 ± 0.5	24 ± 5	14 ± 5	intrinsic
403	2.10 ± 0.5	0.9 ± 0.5	6 ± 5	-61 ± 5	intrinsic
404	5.40 ± 0.5	4.7 ± 0.5	28 ± 5	22 ± 5	foreground
405	4.72 ± 0.5	5.6 ± 1.2	28 ± 5	22 ± 7	foreground
406	5.29 ± 0.5	5.3 ± 2.7	32 ± 5	18 ± 17	foreground
407	5.6 ± 0.5	6.1 ± 2.7	30 ± 5	-29 ± 16	intrinsic
411	6.41 ± 0.9	4.8 ± 2.4	15 ± 5	26 ± 17	foreground
412	6.73 ± 0.5	6.0 ± 3.5	20 ± 5	42 ± 16	foreground
413	7.52 ± 0.6	5.0 ± 3.1	12 ± 5	-14 ± 24	foreground
414	6.80 ± 0.5	3.8 ± 1.1	18 ± 5	11 ± 13	foreground
421	5.54 ± 0.5	3.1 ± 1.3	22 ± 5	13 ± 19	foreground
422	6.48 ± 0.5	4.3 ± 1.1	18 ± 5	24 ± 9	foreground
424	5.47 ± 0.6	3.9 ± 2.0	19 ± 5	10 ± 23	foreground
427	2.87 ± 0.5	3.6 ± 0.5	13 ± 10	21 ± 5	foreground
432	5.93 ± 4.9	3.6 ± 1.1	24 ± 10	19 ± 12	foreground
515	5.78 ± 4.8	3.7 ± 0.5	10 ± 15	16 ± 5	foreground
526	2.29 ± 0.5	7.8 ± 3.9	16 ± 8	70 ± 13	intrinsic

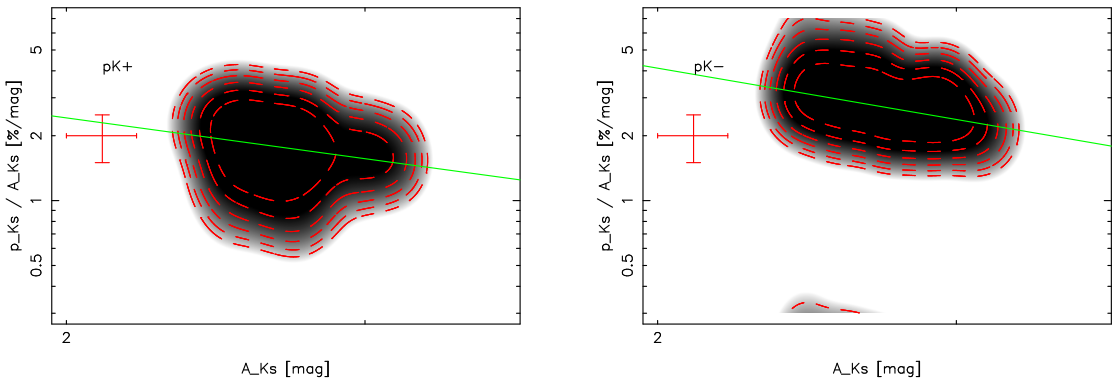

Figure 7.19: Polarization efficiency over three Ks-band data-sets (P2, P4 and P18), compared to Ks-band extinction, plotted as point density, with typical error represented on the left. pK^+ and pK^- sources shown separately in left respectively right frame. Green lines represent the fitted power-law relation.

In all cases, the distributions can be fitted with a power law:

$$\frac{p_\lambda}{A_\lambda} \propto A_{Ks}^{\beta} \tag{7.3}$$

, yielding the following power law indices:

$$\begin{aligned}
\beta_{P1,-} &= -0.6 \pm 0.6 \\
\beta_{P2,-} &= -0.4 \pm 0.4 \\
\beta_{P4,-} &= -0.9 \pm 0.2 \\
\beta_{P18,-} &= -1.4 \pm 0.3 \\
\beta_{P1,+} &= -0.4 \pm 1.5 \\
\beta_{P2,+} &= -0.5 \pm 0.7 \\
\beta_{P4,+} &= -1.3 \pm 0.3 \\
\beta_{P18,+} &= -1.0 \pm 0.5
\end{aligned}$$

Despite the large errors which stem from considerable scatter of the parameters, the pK^+ and pK^- values match the relation found by Gerakines et al. (1995) for the Taurus dark cloud as well as the results of Whittet et al. (2008) for Ophiuchus (both in the Ks-band). This is not directly comparable, since the GC is obscured by more than one dust cloud with possibly different dust alignment. A more general study by Jones (1989), examining a large number of sources covering a range in optical depth of about a factor of 100, finds a power law relation with $\beta \sim -0.25$. In that study, the author proposed a model where the magnetic field along the LOS consists of a constant and a random component (see also Heilis, 1987), thus leading to different grain alignment in each section along the LOS. This reproduces the findings in that study quite well, and it is also consistent with the results presented here within the uncertainties.
Compared to the pH/K^- values, a significant offset in polarization efficiency is detected for the

Table 7.3: Polarization parameters of the 6 sources detected in all three wavelength bands (H, Ks, Lp).

name	p_H [%]	p_{Ks} [%]	p_{Lp} [%]	θ_H [°]	θ_{Ks} [°]	θ_{Lp} [°]
IRS 1C	10.4 ± 1.6	8.2 ± 1.0	6.6 ± 1.6	8 ± 1	8 ± 6	20 ± 9
IRS 1SE2	14.4 ± 1.7	7.6 ± 0.8	7.1 ± 1.7	12 ± 3	11 ± 4	24 ± 8
IRS 1SE3	11.3 ± 2.1	6.1 ± 0.8	4.4 ± 0.9	19 ± 6	11 ± 3	16 ± 8
IRS 16C	5.2 ± 2.3	4.3 ± 0.5	4.5 ± 0.9	19 ± 10	26 ± 5	22 ± 7
IRS 16NW	6.0 ± 2.6	3.9 ± 0.7	3.8 ± 1.1	17 ± 12	25 ± 8	25 ± 10
IRS 35	10.0 ± 2.4	6.2 ± 0.9	5.1 ± 3.1	23 ± 8	26 ± 5	21 ± 22

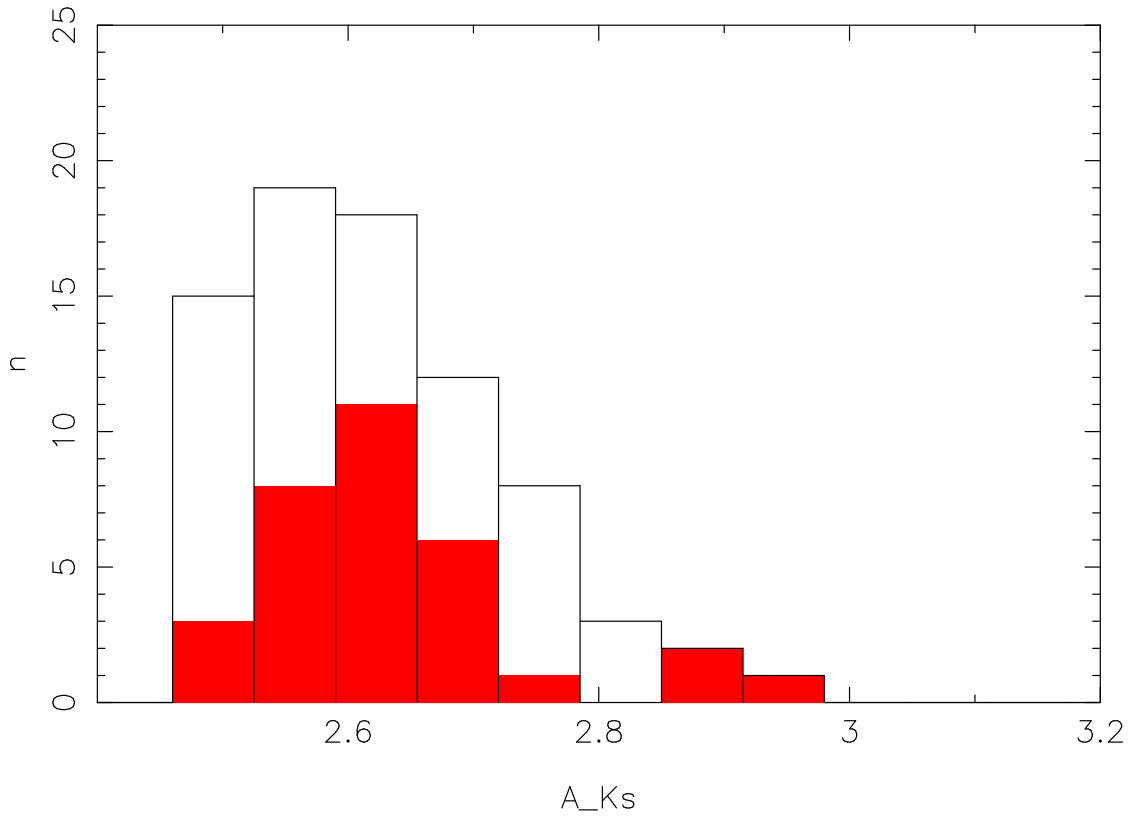

Figure 7.20: Ks-band extinction for sources with $p_{Ks} < 6\%$ (open columns) respectively $p_{Ks} > 6\%$ (filled columns).

pH/K$^+$ sources, while the underlying power law appears to be very similar. This might indicate that the additional polarization is indeed caused by a local contribution, likely by dust in the central parsec itself. In order to produce such a deviation along the LOS, a very specific and therefore unlikely dust configuration would be required. It has to be noted, however, that the offsets found for the P4 and P18 sources are smaller compared to the P2 sources, and this limits the confidence in this conclusion.
The distribution of the polarization efficiency combined for the three Ks-band data-sets is shown in Fig.7.19. Fitting a power law to the polarization efficiency leads to

$$\beta_{total,-} = -1.1 \pm 0.2$$
$$\beta_{total,+} = -1.3 \pm 0.2$$

These values agree with the results found for the individual data-sets within the uncertainties. A similar offset between the higher and lower polarized sources is also found here, but there is a considerable overlap between the sub-groups. This stems from the different selection criteria applied to the different data-sets.

8 Bow-shocks and dusty sources in the central parsec

8.1 Extremely red objects

Several stars in the central parsec show an SED that can be fitted with an extinction on the order of A_{Ks} ~5-6 mag. This is caused by a very red spectrum, which may be an indication either for local dust (if the source is enshrouded in a dusty shell) or for a source viewed through the material in the central parsec (and thus located behind the NSC from the observers point of view). Bright dust-enshrouded sources usually appear extended in the NIR (depending on local conditions like dust temperature and optical depth, IRS 21 for instance appears as an unremarkable point source in the H-band compared to the Ks- and Lp-band, while IRS 1W shows an extended structure in all of these three bands). Unfortunately, the photometric methods applied to produce the intermediate-band SEDs do not work well on such extended sources. However, several of these prominent objects have been studied spectroscopically in previous works already (e.g. Krabbe et al., 1995; Moultaka et al., 2004, 2009), specifically IRS 1W and IRS 21, where featureless red spectra were found in the NIR.

8.2 Examining the extended sources

The polarimetric data presented here covers several bright extended sources in the central parsec: IRS 1W, IRS 5, IRS 10W and IRS 21. In addition, the MIR-excess source IRS 5NE (Perger et al., 2008, Ks- and Lp-band) and the sources in the IRS 2 complex are examined in the following (only Lp-band available, these sources are located in a region of strong extended emission). Other bright MIR sources, like IRS 3, IRS 9 and IRS 12, do not seem to show intrinsic polarization.
IRS 1W is contained in the H-, Ks- and Lp-band data, while the others have only been observed in the Ks- and Lp-band. IRS 1W shows a clear horseshoe shape as it is expected for a bow-shock source in high-quality Ks-band images, while the other sources appear more blurred. Due to its large apparent polarization, IRS 21 would be interesting as a polarimetric calibration source, but only if the polarization is not variable. In order to further constrain the nature of these sources, a flux variability analysis was conducted on IRS 21 and other extended sources in the FOV of the polarimetric data and several NACO imaging datasets, which were taken between 2002 and 2009 in the H-, Ks- and Lp-band.

8.2.1 IRS 1W

Source morphology

IRS 1W shows the characteristic horseshoe-shape of a bow-shock source (see e.g. Tanner et al., 2005). This shape can already be made out in the raw images, but it becomes even more apparent in a Lucy-Richardson deconvolved image (using a PSF obtained from bright IRS 16 sources, see Fig.8.2). The observed shape agrees very well with the relative velocities of the streaming material of the Northern Arm (Lacy et al., 1991) at the location of the source and the proper motion of IRS 1W itself (Schödel et al., 2009, velocities plotted in Fig.8.2).

Spatially resolved polarimetry

The total polarization of IRS 1W was measured as (1.8 ± 0.5) % at (-37 ± 5)° East-of-North in the Ks-band after application of the Mueller matrix to account for instrumental polarization. Ott et al. (1999) provide values of (4.6 ± 2.5) % at (-85 ± 8)° East-of-North. It has to be considered that instrumental effects take place in the same order of magnitude as the measured polarization

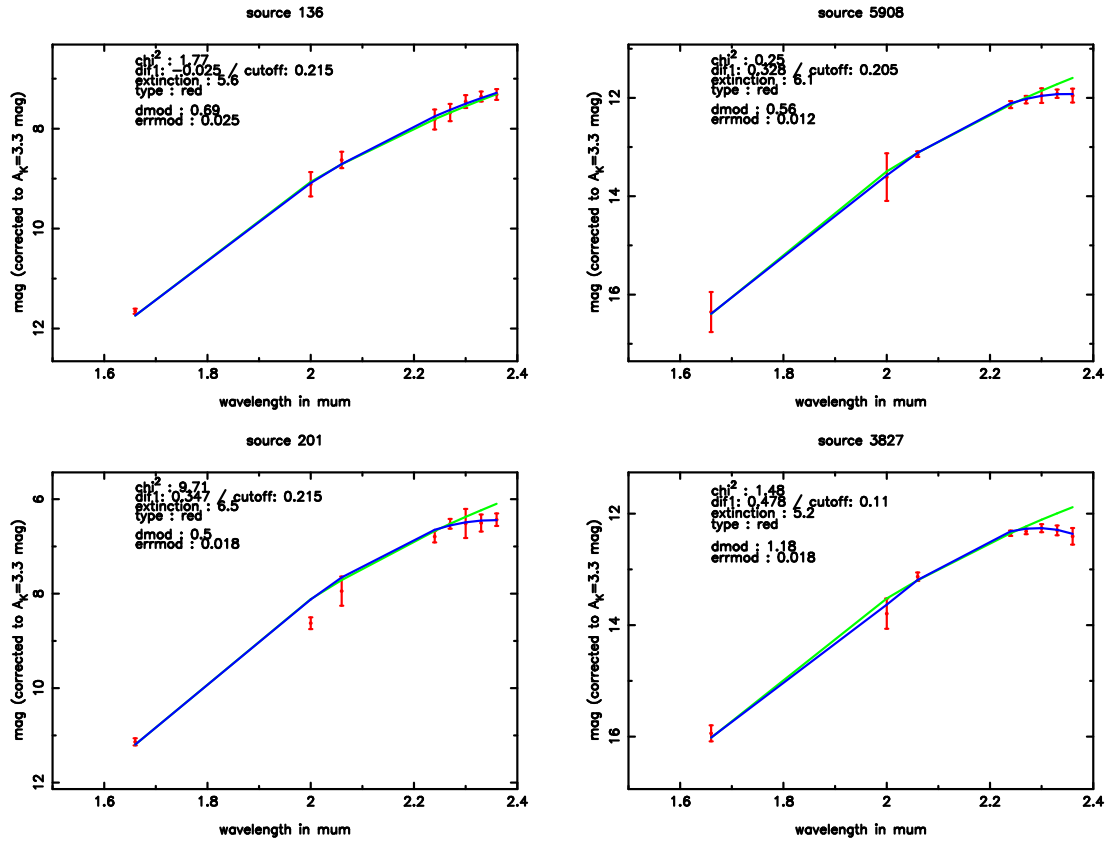

Figure 8.1: SEDs of Extremely Red Objects. Upper left: source NW of Sgr A*, no CO feature, but strongly reddened. Upper right: source NW of Sgr A*, here a CO feature is visible. This source is located near a local maximum of extinction, so it may just be a normal late type star. Lower left: source located in the northern arm of the mini-spiral. Lower right: source located in the far SE of Sgr A*, also in a region of very high extinction. The CO feature suggest a late type star, maybe towards the back of the cluster.

degree, which may explain the large offset in polarization angle compared to the older values where these effects were not compensated. The lower total polarization degree found here can be attributed to the better angular resolution and thus less influence from neighboring sources. The values provided by Eckart et al. (1995) are clearly influenced by neighboring stellar sources, with (3.0 ± 1.0) % at (10 ± 7)°.

If it is assumed that the foreground polarization for this source is the same as for the surrounding objects and a depolarization matrix with the parameters for $p = 7.6\%, \theta = 9.2°$ is applied, this yields a total intrinsic polarization of (7.8 ± 0.5) % at (-75 ± 5)°.

In the H-band, the total polarization of IRS 1W is measured as (5.2 ± 0.5) % at (12 ± 5)° East-of-North. The polarization angle appears typical for a stellar source affected by foreground polarization, but the polarization degree is much lower than the ∼12% found for stellar sources in the vicinity. The application of a depolarization matrix with $p = 12\%, \theta = 15°$ leads to an intrinsic polarization of (6.9 ± 0.5) % at (-73 ± 5)°.

The values found for the Lp-band confirm this trend: while a total polarization of (4.9 ± 0.5)% at (-62 ± 5)° is measured, applying a depolarization matrix with $p = 4\%, \theta = 25°$ yields an intrinsic polarization of (8.9 ± 0.5)% at (-63 ± 5)°. The polarization angle appears consistent over the three bands, which suggests that the same process is responsible, while the increase of the intrinsic polarization degree towards longer wavelengths points to the higher influence of the extended dust component compared to that of the central source.

In order to investigate the polarization pattern in different regions of this extended source, the polarization was measured in small apertures in the deconvolved images, and the foreground polarization was subtracted using a Mueller matrix as described in §5.2.8. The results are shown in Fig.8.2. This yielded polarization degrees of about 10-20 % with very similar polarization

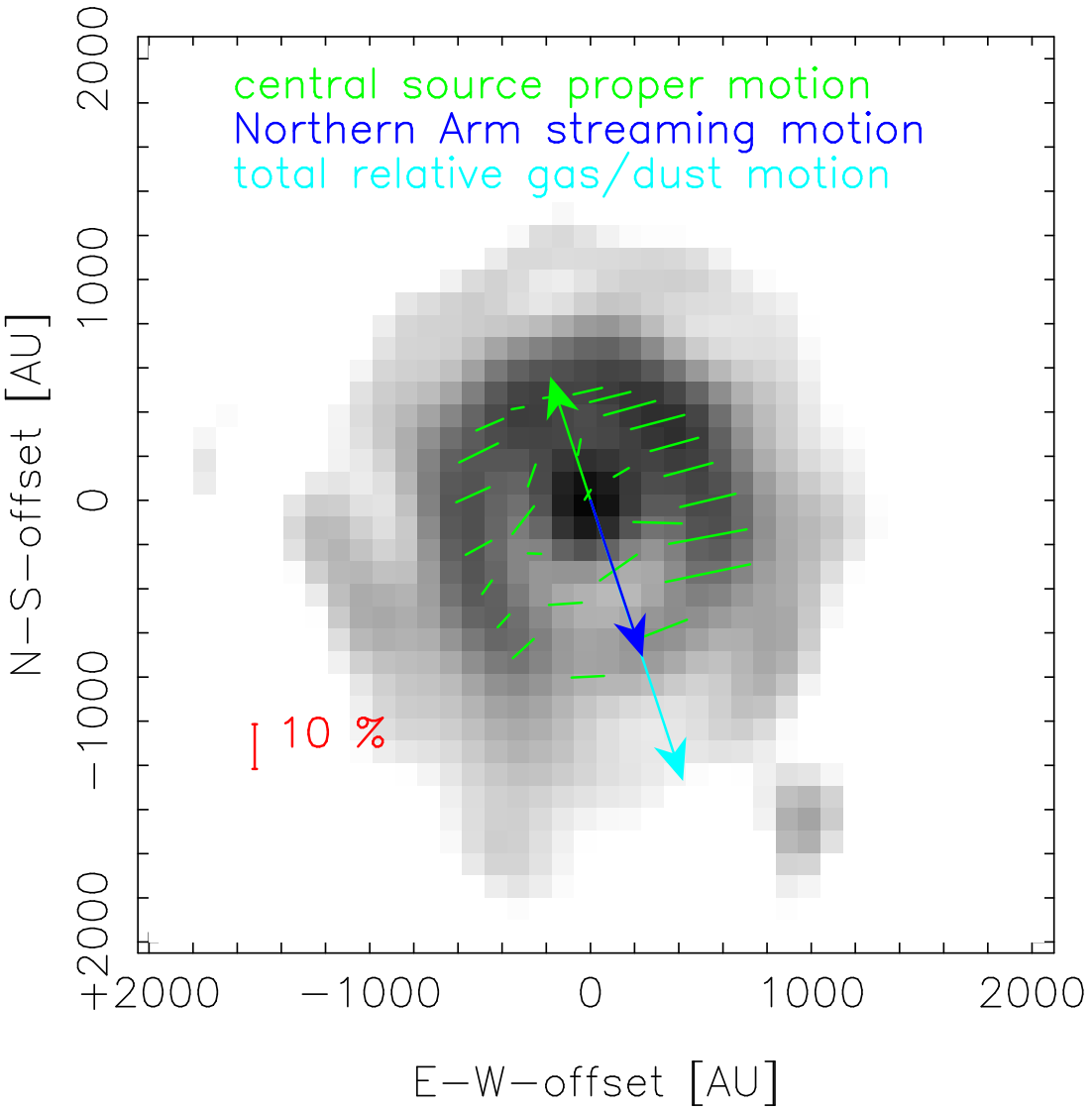

Figure 8.2: Map of the intrinsic Ks-band polarization of the extended source IRS 1W. The arrows indicate the proper motions of the central source, the motion of the Northern Arm material and the motion of both relative to each other.

angles for regions with significant flux. Apparently, the polarization degree is lower by a factor of up to ~3 around the apex compared to the tails.
The same technique was applied to the H-band dataset, and Fig.8.3 shows the result for the immediate area around IRS 1W. The polarization pattern is comparable to that found in the Ks-band, with polarization degrees of about 10-20 % at very similar polarization angles for regions with significant flux, and much lower polarization degrees in the central region. There is no significantly lower polarization degree towards the apex, as it was found in the Ks-band, but it has to be noted that the horseshoe shape is much less pronounced in the H-band anyway. The angles agree with those determined from the Ks-band data.
Fig.8.4 shows the polarization pattern in the Lp-band, and the similarity to both the H- and the Ks-band pattern is quite apparent, despite the much lower depth. The polarization increases in the tails of the bow-shock, while the apex shows signs of depolarization.
The total intrinsic polarization and the spatially resolved pattern of IRS 1W can be explained from the combination of the motion of the source itself, the streaming velocity in the Northern Arm and the magnetic fields present in that structure.
Aitken et al. (1998) mapped the polarization of the Northern Arm at 12.5 μm and inferred the magnetic field orientation by assuming that the polarization was produced by emission from

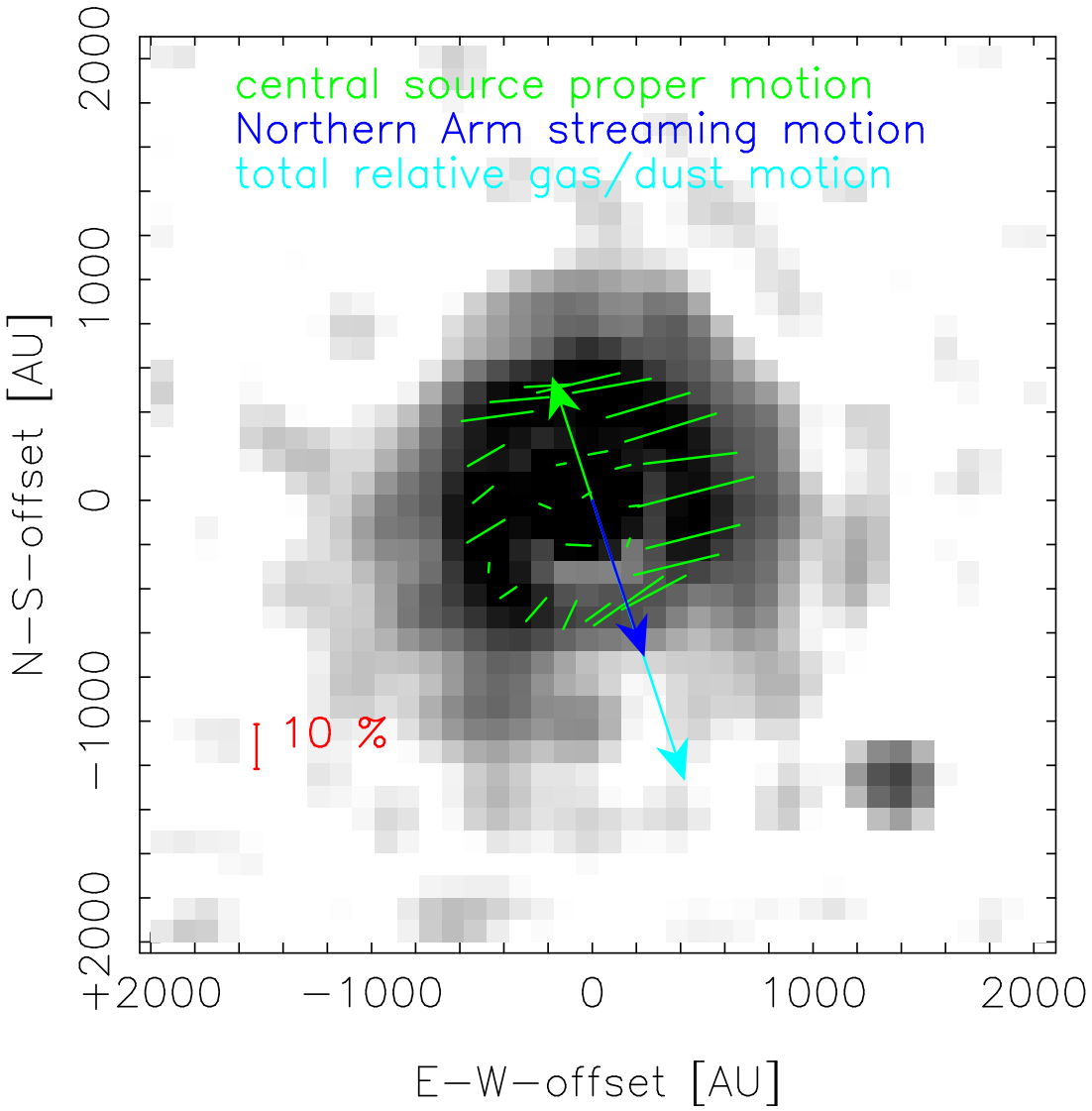

Figure 8.3: Map of the intrinsic H-band polarization of the extended source IRS 1W. The arrows indicate the proper motions of the central source, the motion of the Northern Arm material and the motion of both relative to each other.

magnetically aligned elongated dust grains. The magnetic field at the location of IRS 1W is perpendicular to the polarization angles found here for this source. The projected velocity of the source (Schödel et al., 2009) is parallel to the field lines and also parallel to the streaming motion in the Northern Arm itself (Lacy et al., 1991). This leads to the field lines following the morphology of the shock around the source. At the apex, this causes a weakening of the field, while it is compressed in the tails. This in turn leads to a weaker respectively stronger grain alignment in the apex respectively the tails.
Grain temperatures in the Northern Arm reach up to ~200-300 K (Smith et al., 1990; Gezari, 1992), and this is sufficient to explain the observed 12.5 μm emission. But for significant emission in the H- and Ks-band, much higher grain temperatures of ~1000 K would be required. This raises the question if the extended emission in the bow-shock is emission from or scattering on the aligned grains. One possibility is that the temperature in the shock is indeed high enough for significant emission. Geballe et al. (2004) suggest that such higher temperatures could be reached by very small grains (~0.001-0.01 μm, which is by a factor of 10 smaller than typical grains expected here) if they are heated by occasional high energy photons or stochastic collisions with high energy electrons or ions. Moultaka et al. (2004) find that the spectrum measured for IRS 1W (including the bow-shock) matches a 900 K blackbody. At this higher temperature,

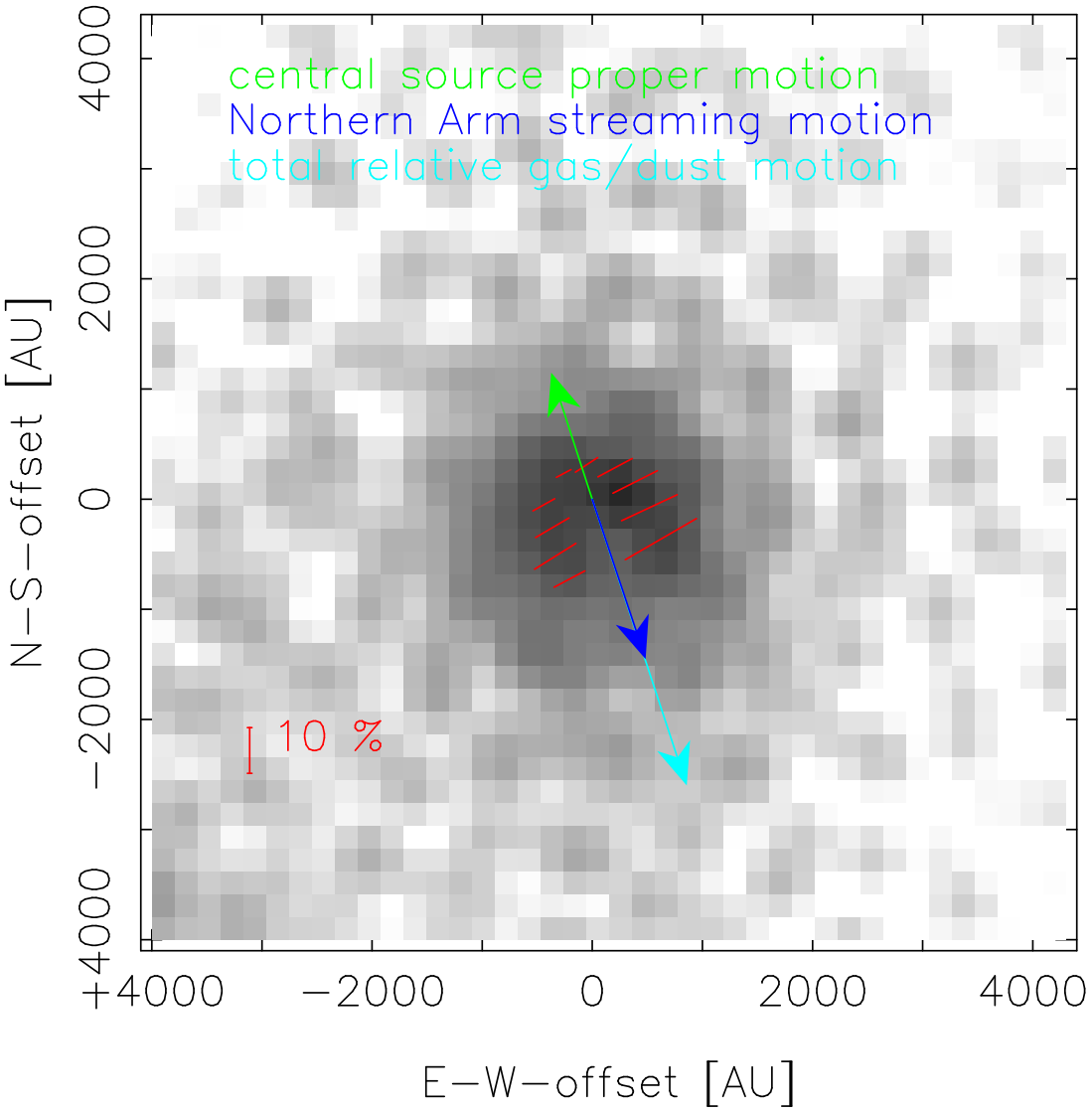

Figure 8.4: Map of the intrinsic Lp-band polarization of the extended source IRS 1W. The arrows indicate the proper motions of the central source, the motion of the Northern Arm material and the motion of both relative to each other.

emission from heated aligned dust grains should contribute to the NIR polarization.
This leaves the question of the survival of these very small grains in a bow-shock environment and at this temperature. In addition, these grains would have to be aligned to produce the observed polarization. But the very same processes which would heat the small grains to high temperatures would also randomize any previous alignment, unless the alignment mechanism is much faster than the randomization. This may be the case here, since strong frozen-in and compressed magnetic fields provide an even stronger and faster alignment than in other regions of the Northern Arm. This might also add to the lower polarization at the apex due to turbulence, which could lead to a partial randomization of grain alignment, before the stronger field and uniform streaming motion in the tails increase the alignment again.
In addition to emission, scattered light from the central source enclosed in a dusty envelope could contribute to the observed polarization. This process is known to occur in planetary nebulae and dusty young stellar objects (YSOs) (e.g. Lowe & Gledhill, 2007; Lucas & Roche, 1998). In the ideal case of pure Mie-scattering on spherical dust grains, most of the light would be scattered forward, but a significant portion is scattered perpendicular to the incident direction. This latter part is linearly polarized, with the polarization vector in the plane of the sky and perpendicular to the original propagation direction of the light. If a source like this is viewed face-on, no

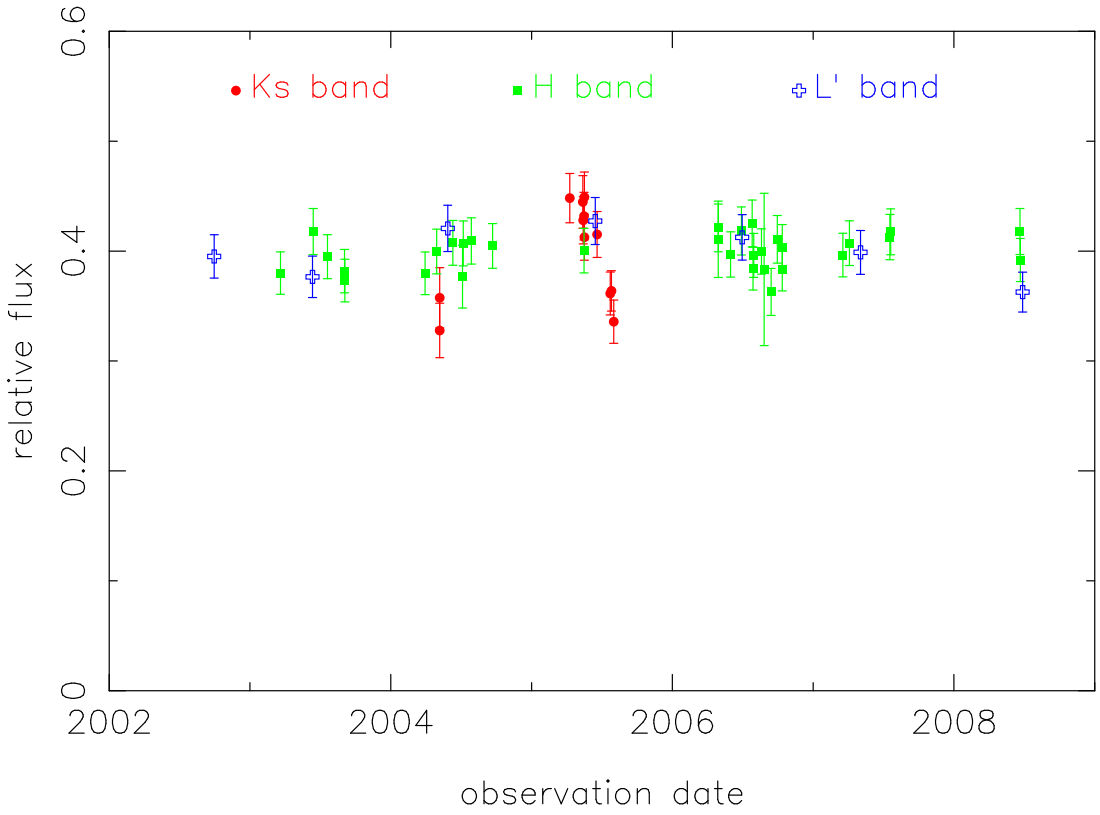

Figure 8.5: Ks-band (red circles), H-band (green squares) and Lp-band (blue open crosses) lightcurves of IRS 1W. Shown here is the flux of the source normalized to the flux of non-variable reference sources in the respective band. H- and L-band values were multiplied by a constant factor to match the average Ks-band values.

total intrinsic polarization is detected, since the polarizations of the regions surrounding the central source cancel each other out. If the source is inclined, any total polarization angle can be produced. Spatially resolved polarimetric measurements of such sources however show a characteristic centrosymmetric pattern of the polarization vectors. Clearly, this is not the kind of pattern found here.

But what if the grains are not spherical, but elongated and aligned as it is the case here at least for a significant part of the grain population? Lucas & Roche (1998) find patterns of aligned polarization vectors similar to the ones found here in the central regions of a minority of the sources examined in their study. They claim that these patterns cannot be explained by scattering on spherical grains, but that aligned elongated grains must play a role there. Whitney & Wolff (2002) modeled scattering and dichroic extinction for non-spherical dust grains, finding a variety of polarization patterns for different input values for optical depth, degree of grain alignment and inclination of the source. In general, at low optical depths they find polarization vectors perpendicular to the axis of grain alignment (i.e. the orientation of the angular momentum vector of the spinning grains), while high optical depth leads to a predominance of dichroic extinction and thus to polarization vectors parallel to the axis of grain alignment. This study is focussed on spherical dust configurations and disk-like structures, so the results are not directly applicable to a bow-shock source.

Multiple scattering may play a role in the depolarization observed towards the apex, but again, the alignment of the grains has to be considered. If the local dust density is high enough for multiple scattering to become important, would this also already suffice for a significant contribution by local dichroic extinction? While the former process would lead to a depolarization by a randomization of the polarization angles, the second would produce polarization perpendicular to the emissive/single scattering polarization angle, which does not match the observations.

In the light of these results, it can be considered likely that scattering on elongated grains contributes to the observed patterns in the H- and Ks-band data. Both scattering and emission should

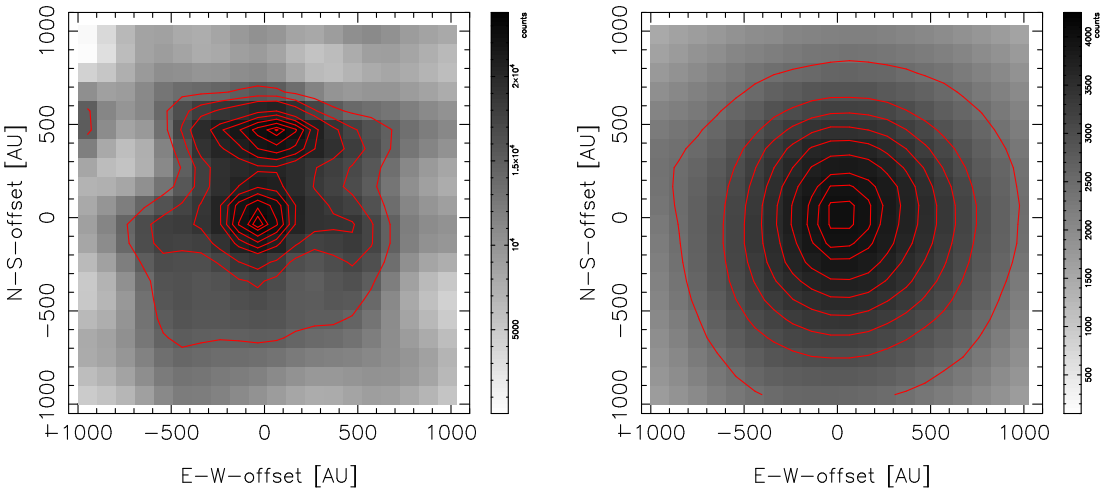

Figure 8.6: IRS 21 observed on 2004-08-30, right: image before Lucy-Richardson deconvolution, left: image after deconvolution (logarithmic gray-scale, contours trace 10, 20, 30, 50, 60, 70, 80, 90, 95% of maximum flux in the left frame, respectively 40, 50, 60, 70, 80, 90, 95, 99% in the right frame.

produce polarization at the same angle. Without thoroughly modeling the conditions in such a bow-shock environment, it cannot be determined which process is dominant, only that both probably contribute. The longer the wavelength, the more important the contribution of emission becomes (at the dust temperatures considered here). In the Lp-band, emission is probably the dominant process.

Flux variability

The total flux of IRS 1W can be difficult to determine, since the center of this source is saturated in a large number of images. Unfortunately, the repairing algorithm included in StarFinder only works on point sources, since it assumes that the saturated source has a PSF similar to that of non-saturated sources in the vicinity. This is obviously not the case for an extended source like IRS 1W. Therefore only data were used where the peak fluxes at the location of IRS 1W stayed below the saturation threshold. Fig.8.5 shows the flux of IRS 1W in relation to the reference

Table 8.1: Polarization parameters measured for IRS 21. The average over all observations respectively the standard deviation is given in the last line.

	date	p[%]	dp[%]	θ [deg]	d θ [%]
1	2007-04-01	10.4	0.5	15	5
2	2007-04-03	9.3	0.5	16	5
3	2007-04-04	8.9	0.5	15	5
4	2007-04-05	8.8	0.5	17	5
5	2007-04-06	9.0	0.5	16	5
6	2007-07-18	9.4	0.5	16	5
7	2007-07-19	9.0	0.5	17	5
8	2007-07-20	9.1	0.5	16	5
9	2007-07-20	9.0	0.5	18	5
10	2007-07-21	8.4	0.5	17	5
11	2007-07-23	9.2	0.5	16	5
12	2007-07-23	8.3	0.5	18	5
13	2007-07-24	9.5	0.5	16	5
avg		9.1	0.2	16.4	0.3

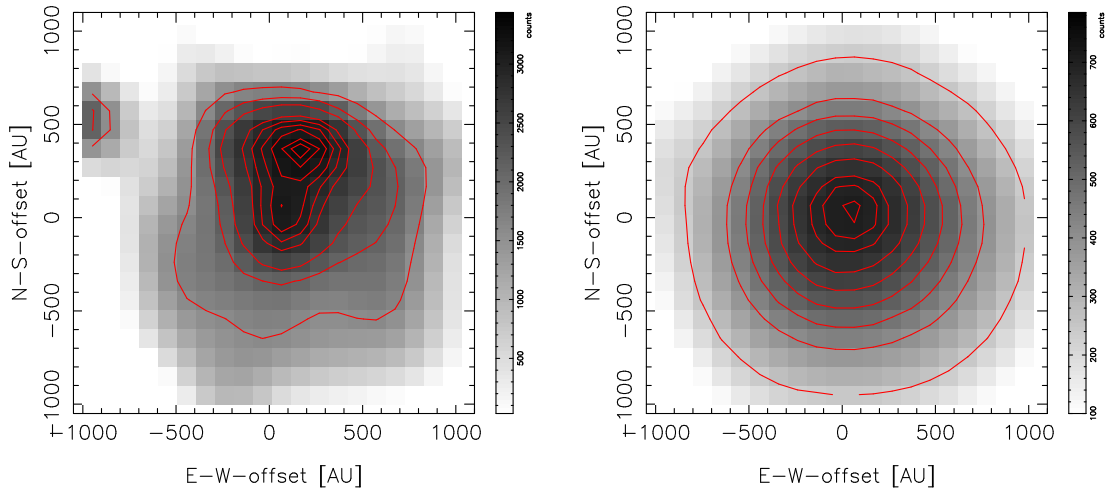

Figure 8.7: IRS 21 observed on 2005-05-14, right: image before Lucy-Richardson deconvolution, left: image after deconvolution (logarithmic gray-scale, contours trace 10, 20, 30, 50, 60, 70, 80, 90, 95% of maximum flux in the left frame, respectively 40, 50, 60, 70, 80, 90, 95, 99% in the right frame.

flux in the H-, Ks- and Lp-band. The flux appears to be variable by ~30% in the Ks-band, while the H-band value is inconclusive. No clear periodicity is apparent, which might indicate either an erratic variability or a period in the order of or below the time resolution of the data. The flux variability exceeds that found for IRS 16C (see Fig.5.16), but this may in part be due to the difficult photometry on IRS 1W. In the L-band, the flux rises to a maximum in 2005 and drops again by ~15 %. This is consistent with a constant flux within the uncertainties, especially since there is no correlated behavior over the H-, Ks- and L-band. In total, the available observations do not allow a conclusion whether or not IRS 1W shows a source-intrinsic flux variability.

8.2.2 IRS 21

Source morphology

Previous studies show IRS 21 as a roughly circular, yet extended source in the Ks-band (Tanner et al., 2002, 2005). The same is found for the data presented here, but after applying a Lucy-Richardson deconvolution, this changes significantly: Fig.8.6 and 8.7 show IRS 21 before and after deconvolution for two datasets (2004-08-30 respectively 2005-05-14). There is no clear bow-shock shape visible prior to deconvolution. After the LR process, there is still no clear horseshoe shape, but it is clear that the source is not circular in projection and thus most likely not spherical. The deconvolved images appear to contain a central source with a bow-shaped northern extension. It has to be noted that this shape is not this apparent in all available datasets, but the resolution that can be achieved on an extended feature like this depends critically on the data quality, especially in a very dusty environment like that of IRS 21. The LR algorithm also tends to 'suck up' flux of extended features into a central source (see §5.2.4). For all but a few periods, however, the deconvolved images show an extended structure at this location, with an east-western bar/bow to the north and a point-source-like feature to the south. This shape is deemed to be consistent with a marginally resolved bow-shock type source. These findings match those presented by Tanner et al. (2004), who find a similar spatial structure and position angle of the bow-shock in the Lp-band. Furthermore, the relative motion of the Northern Arm material Lacy et al. (1991) and the proper motions of IRS 21 (e.g. Tanner et al., 2005) would agree with a bow-shock in this direction (see projected velocities plotted in Fig.8.8). The recent Lp-band observations agree with the presence of such a structure as well (see Fig.8.9), although the insufficient depth of the observations prohibits the resolution of fainter features like the tails of the bow-shock.
From the images where the bow-shock shape was visible, a projected distance between the peaks of the southern and the northern feature of ~ 400 ± 100 AU was determined (see Fig.8.6, this is

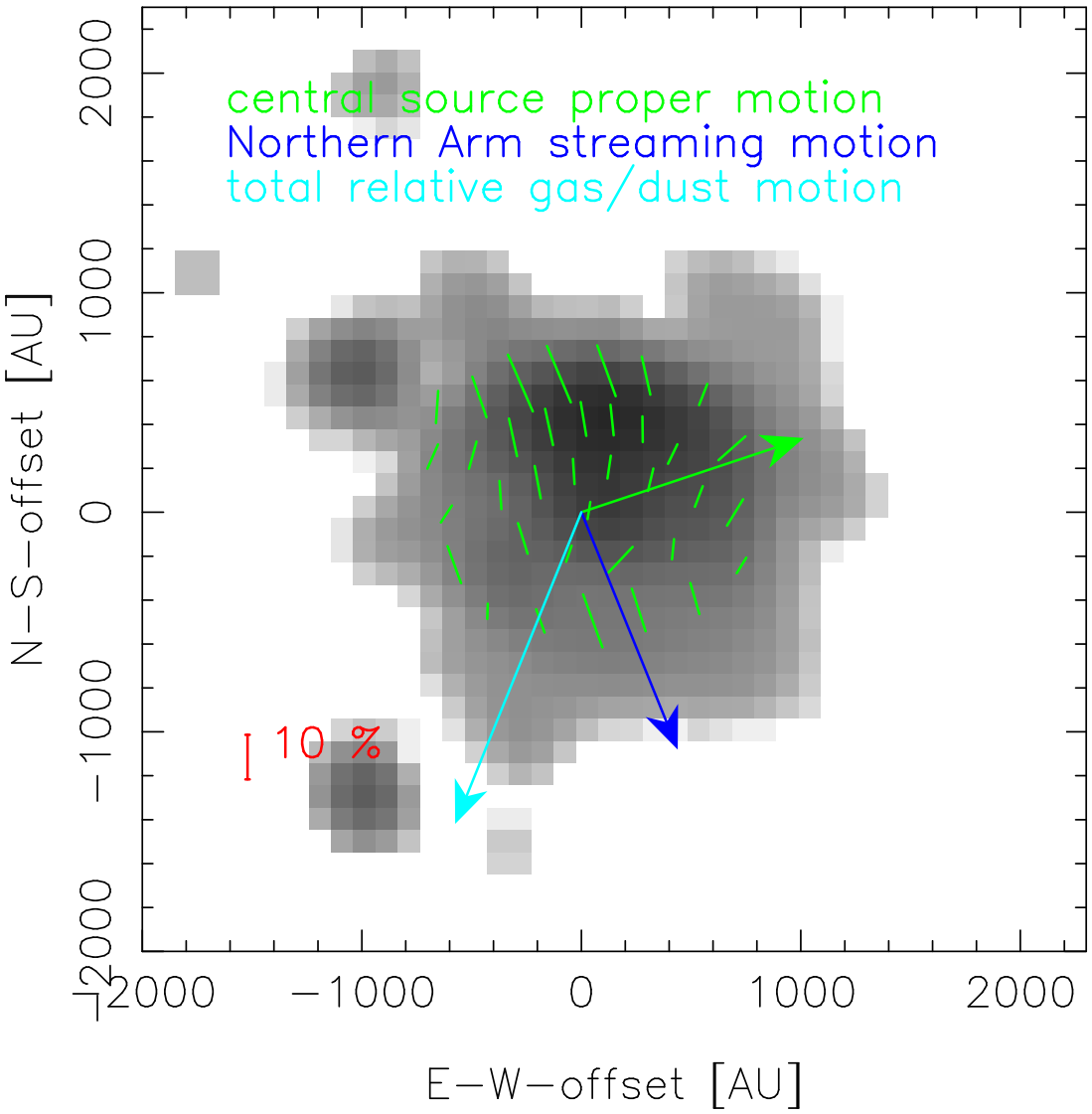

Figure 8.8: Map of the intrinsic Ks-band polarization of the extended source IRS 21. The arrows indicate the proper motions of the central source, the motion of the Northern Arm material and the motion of both relative to each other.

also consistent with the Lp-band image, Fig.8.9). The projected distance was almost the same for all images, and the error given here is just a rough estimate. Considering a possible inclination of the source, this constitutes a lower limit for the standoff distance between the central source and the apex of the bow-shock. Tanner et al. (2002) provide modeled standoff distances for candidate central objects, using the Ks-band radius they measure for IRS 21 of ~650 AU as an estimate for the standoff distance. Using the radius makes this value an upper limit for the projected standoff distance. They find that this value agrees best with the following stellar types: an AGB type star, W-R, Ofpe/WN9 or W-R WC9. Especially a Wolf-Rayet (W-R) type star would be able to produce a wide range of possible standoff distances (310-10100 AU). The value determined here agrees with these possibilities as well.

Spatially resolved polarimetry

IRS 21 is not covered by the 2009, high quality polarimetric dataset (P2), so its total polarization was measured in several other datasets with lower Strehl ratios (see Tab.4.1, datasets P3-P15, the data quality is still sufficient for polarimetry on bright sources). The values found for the individual data-sets are shown in Tab.8.1. Considering the uncertainties, these measurement allow the conclusion that both the polarization degree and angle of IRS 21 can be treated as

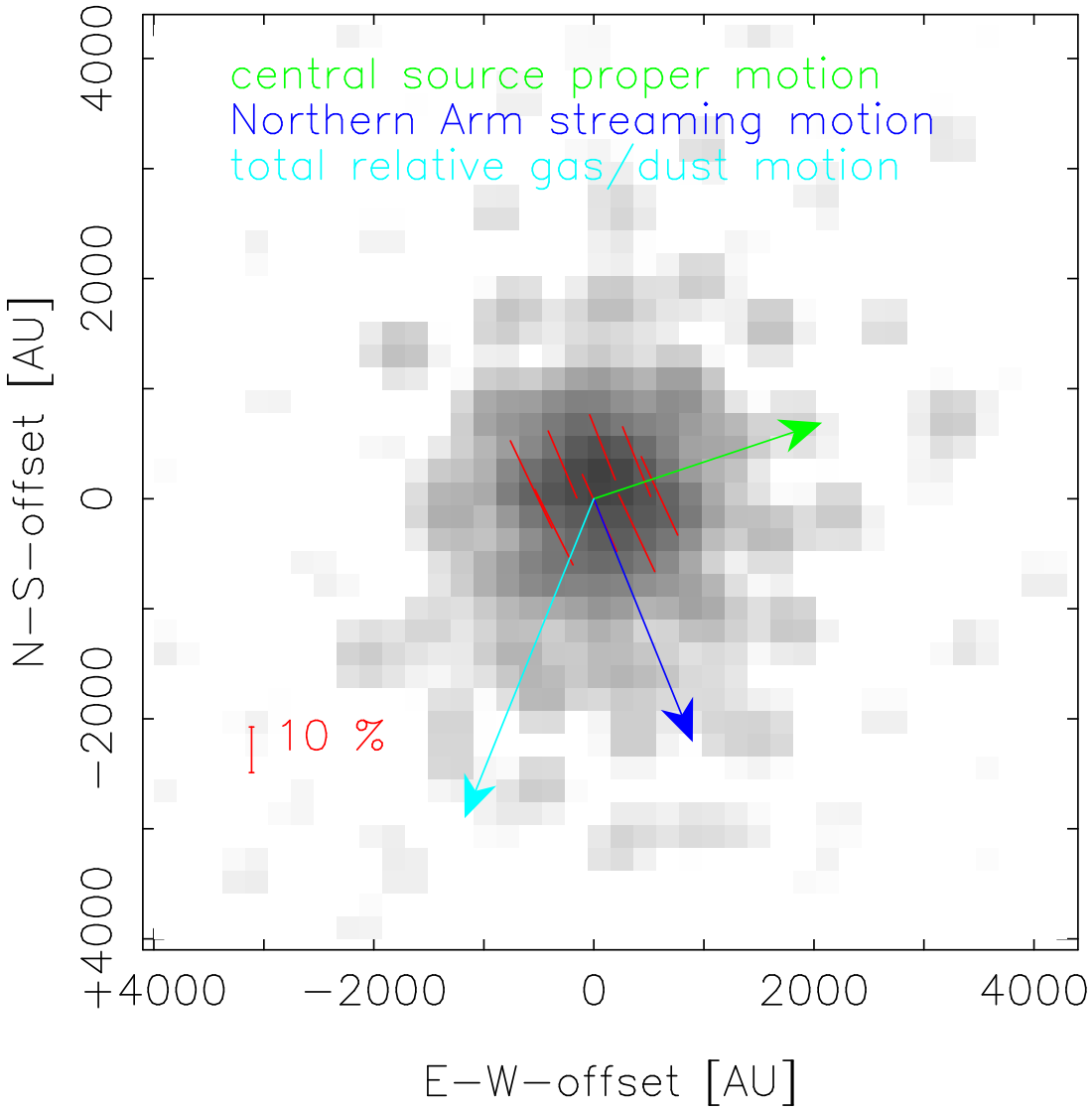

Figure 8.9: Map of the intrinsic Lp-band polarization of the extended source IRS 21. The arrows indicate the proper motions of the central source, the motion of the Northern Arm material and the motion of both relative to each other.

constant within the margin of error. The measurements yield an average value of (9.1 ± 0.2) % at (16.4 ± 0.3) degrees, which agrees very well with the polarization measured by Ott et al. (1999) and also with the polarization angle determined by Eckart et al. (1995). The latter study measured a polarization degree which is ~60% higher than the value measured here. Ott et al. (1999) explained this difference by different apertures used and that might indeed be the case. No clear indication of a variable polarization degree of IRS 21 has be found in the available data, although several, low quality datasets led to some outlier values. Since this coincided with large variations in the polarization of other sources, this is not considered a significant effect.

After applying a depolarization matrix with polarization parameters determined from the surrounding point sources (5% at 30°, determined on two sources close to IRS 21 and thus not as reliable as the values for IRS 1W), IRS 21 appears to have a total intrinsic polarization of (6.1 ± 0.5) % at (5 ± 5) degrees. The polarization degree is slightly lower than that of IRS 1W, while both sources have very different intrinsic polarization angles. Again, the angle found here is perpendicular to the magnetic field orientation in this region given by Aitken et al. (1998). Unfortunately no polarimetric H-band data covering IRS 21 are available.

In the Lp-band, IRS 21 shows a much stronger polarization compared to the Ks-band. The total polarization amounts to (19.0 ± 0.5)% at (24 ± 5)°, and subtracting the foreground polarization

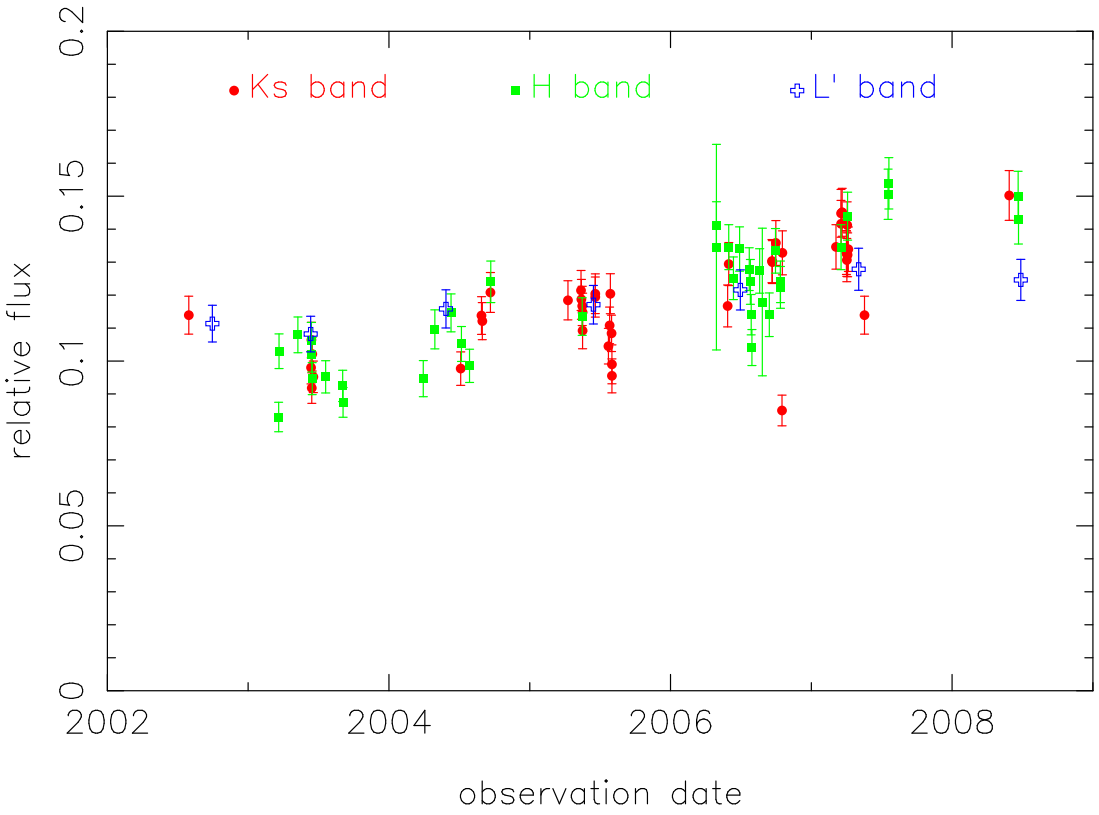

Figure 8.10: Ks-band (red circles), H-band (green squares) and Lp-band (blue open crosses) lightcurves of IRS 21. Shown here is the flux of the source normalized to the flux of non-variable reference sources in the respective band. H- and L-band values were multiplied by a constant factor to match the average Ks-band values.

reveals an intrinsic polarization of (15.0 ± 0.5)% at (24 ± 5)°.
Fig.8.8 shows the Ks-band polarization of individual regions. Polarization degrees of about 3-8 % are measured here, with less uniform polarization angles than those found for IRS 1W in regions with significant flux. In addition, rather an increase than a decrease of the polarization degree is detected towards the apex. The polarization angle shows more variation compared to IRS 1W. By comparison, the polarization pattern in the Lp-band (see Fig.8.9) appears more uniform: polarization degrees on the order of 15% are detected in regions with significant flux, with very similar polarization angles of 20-25°. As in the Ks-band, no clear substructure (as it was found for IRS 1W) is apparent.
Again, the relation of the source motion and the local magnetic fields and streaming motions offer an explanation for the observed polarization in both bands. The source moves almost perpendicular to the field, so the field lines are likely compressed in front of the shock and diluted towards the flanks. This leads to a higher polarization at the apex. If this field orientation is indeed preserved over the whole structure, it could explain the observed polarization pattern, since the polarization angles would be perpendicular to the field lines. This would be the expected behavior for emission/scattering producing the polarization.
For this grain alignment, dichroic extinction would be expected to produce polarization angles perpendicular to what is observed here. This would reduce the overall intrinsic polarization, but it is questionable if the optical depth of the dust surrounding IRS 21 is sufficient for a significant contribution of this process. While a detailed model of bow-shock polarization using measurements at more NIR/MIR wavelengths or even spectropolarimetry as input parameters would be desirable to clarify the extent and relative importance of these processes, a rough estimate may already be possible from the Ks- and Lp-band values alone: compared to the Ks-band, the total intrinsic polarization is increased by a factor of ~2.5 in the Lp-band, compared to an increase by a factor of 1.1 that was found for IRS 1W. Moultaka et al. (2004) fitted the Lp-band spectrum of IRS 21 with a 1200 K blackbody, which is hotter than the value found for IRS 1W in the

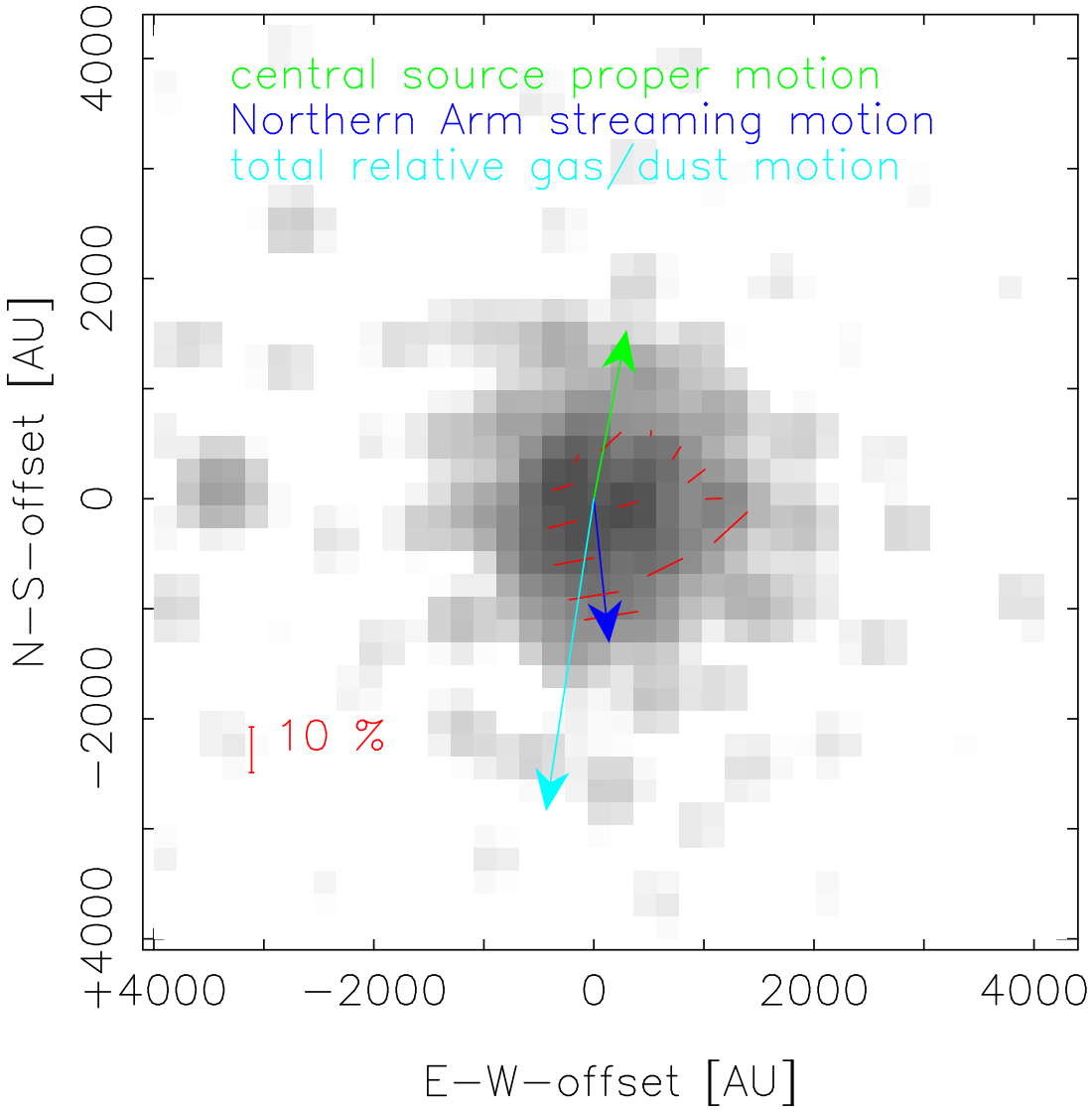

Figure 8.11: Map of the intrinsic Lp-band polarization of the extended source IRS 10W. The arrows indicate the proper motions of the central source, the motion of the Northern Arm material and the motion of both relative to each other.

same study (~900 K). This would lead to a higher emission at shorter wavelengths, and if dust emission is dominant for both sources, why is the polarization of IRS 1W and IRS 21 almost the same in the Ks-band, while the latter source has a much higher polarization in the Lp-band? The answer might be that the optical depth respectively dust extinction also has to be considered: the shape of IRS 21 suggests a higher optical depth since no clear central source can be made out even in the Ks-band (where the central source of IRS 1W is clearly discernible). Thus, the light from the central source of IRS 21 is mostly absorbed at shorter wavelengths (which produces polarization perpendicular to the emissive polarization) or affected by multiple scattering (which depolarizes the light). Even if this contribution stays the same in the Lp-band, the dust primarily emits at longer wavelengths, so the highly polarized dust emission becomes more and more dominant towards the Lp-band. The emissive polarization in the Ks-band is in turn reduced by the absorption/multiple scattering component. For IRS 1W, these two processes would not play a significant role due to the much lower optical depth towards the central source.
In order to further clarify this relation and to investigate a possible substructure in polarization, further observations with higher depth would be required.

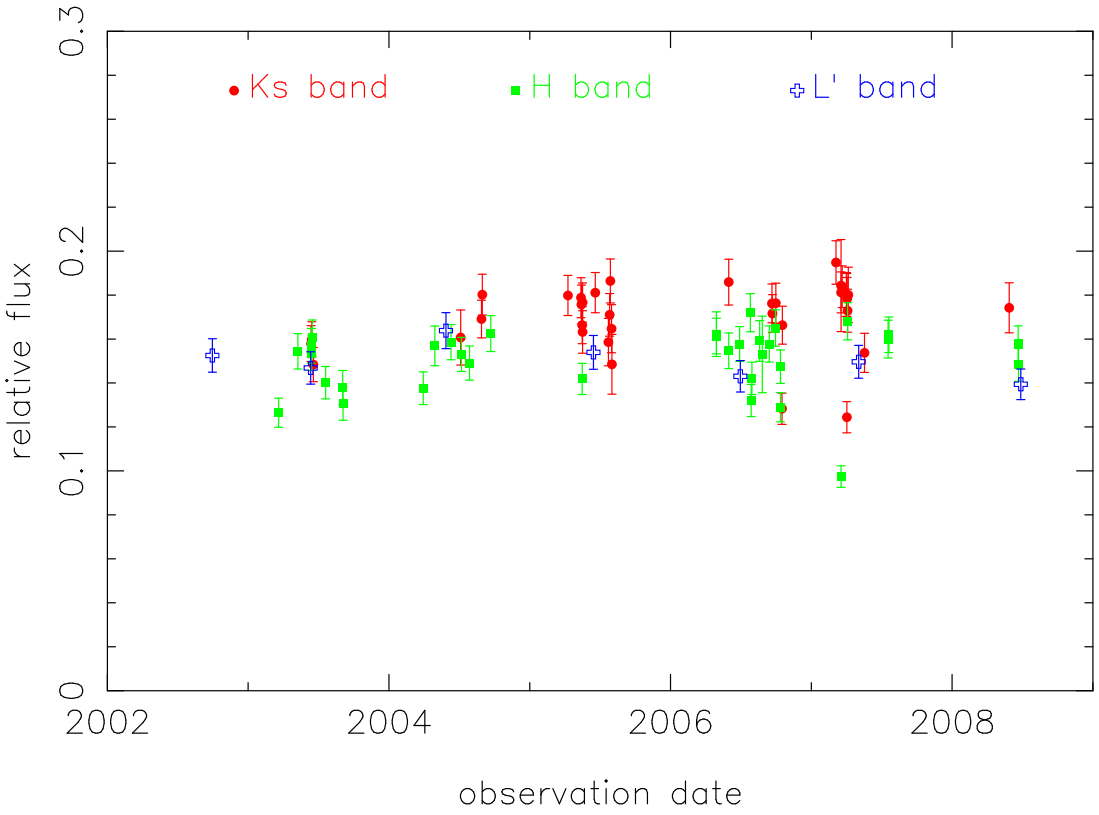

Figure 8.12: Ks-band (red circles), H-band (green squares) and Lp-band (blue open crosses) lightcurves of IRS 10W. Shown here is the flux of the source normalized to the flux of non-variable reference sources in the respective band. H- and Lp-band values were multiplied by a constant factor to match the average Ks-band values.

Flux variability

Fig.8.10 shows the flux of IRS 21 in relation to the reference flux. For both the H- and the Ks-band data, there appears to be a significant and steady increase in flux of about 50% over the observed period (June 2002 to May 2008). This corresponds to an increase in brightness of about 0.4 mag. The fact that the same increase is detected in both bands suggests that it is intrinsic to the source itself, because the H-band is dominated by the stellar component, while the Ks-band source is dominated by the dust enshrouding the stellar source. A smaller (~20%) correlated flux increase is found in the Lp-band data as well. What could cause this increase in flux?
From the available data, it cannot be determined whether this is a periodic variability or not since only a steady increase in flux is observed. This would be possible for all the candidates presented by Tanner et al. (2002): both AGB-stars and Wolf Rayet stars may show such an increase in luminosity in this time-frame, especially if they are in a mass-losing phase.

8.2.3 IRS 10

Spatially resolved polarimetry

IRS 10W is contained in the FOV of the 2011 Ks- and Lp-band data. No polarimetric H-band observations of this source are available.
The quality of this Ks-band data-set is insuffiecent for spatially resolved polarimetry, so only total values could be obtained: the total polarization of IRS 10W was measured as (2.1 ± 0.5)% at (6 ± 5)° in the Ks-band. Applying a depolarization matrix with the polarization of IRS 10E* used as the foreground value (this source is point-like and does not show signs of intrinsic polarization, with (5.4 ± 0.5)% at (28 ± 4)°) yielded an intrinsic polarization of (4.2 ± 0.5)% at (-52 ± 5)°. In the Lp-band, similar values are found: the total polarization is measured as

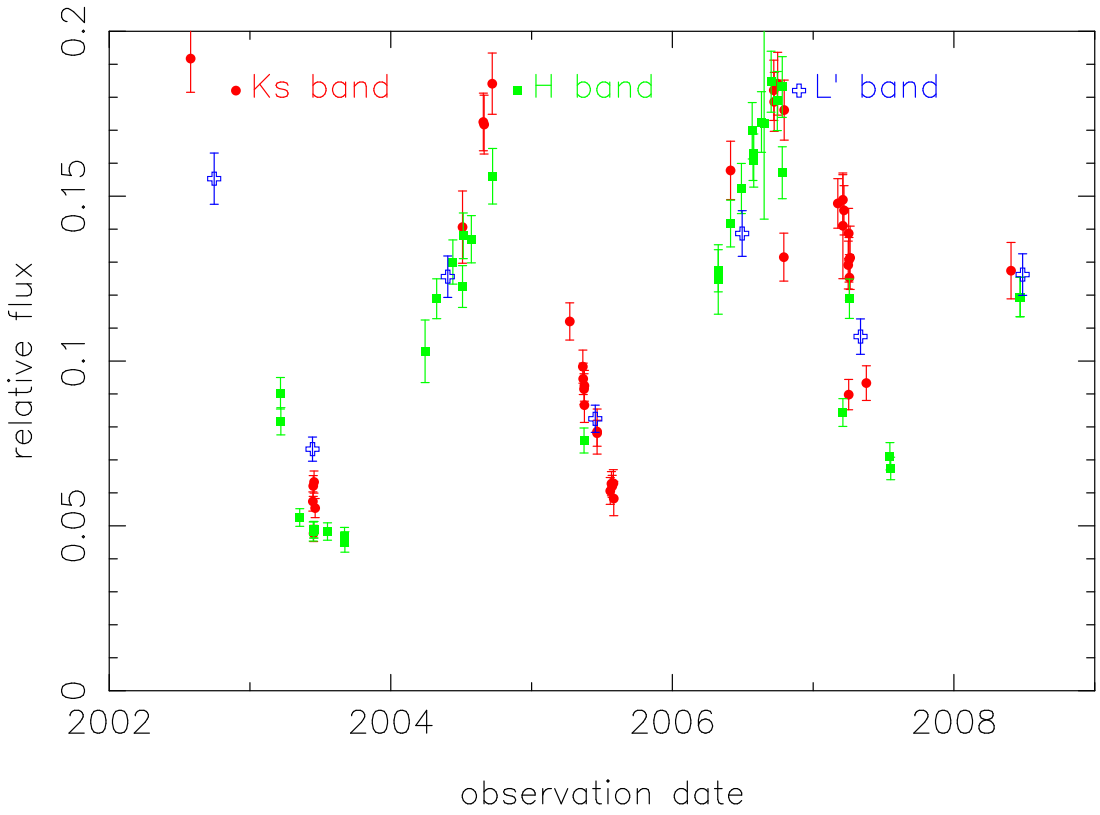

Figure 8.13: Ks-band (red circles), H-band (green squares) and Lp-band (blue open crosses) lightcurves of IRS 10E*. Shown here is the flux of the source normalized to the flux of non-variable reference sources in the respective band. H- and Lp-band values were multiplied by a constant factor to match the average Ks-band values.

(0.9 ± 0.5)% at (-61 ± 5)°, which yields an intrinsic polarization of (5.6 ± 0.5)% at (-67 ± 5)°, assuming a foreground polarization of (4.7 ± 0.5)% at (22 ± 5)°, which was again estimated based on IRS 10E*.
The intrinsic Lp-band polarization measured here is higher by a factor of ~1.3 than the Ks-band value. This resembles the increase found for IRS 1W. But while that source shows a clear bow-shock morphology, this is not the case for IRS 10W (see Fig.8.11). Tanner et al. (2005) fitted this source with a bow-shock like shape, but the authors of that study themselves cautioned that the angle of the best-fit solution did not agree with the observed proper motions of the source and the dynamics of the Northen Arm. They instead suggested that the observed shape was produced by the additional influence of an outflow from IRS 10E*, a highly variable source about 2" to the south-east (see below). The resolved Lp-band polarization (see Fig.8.11) is also not consistent with a bow-shock with the apex towards the east. The pattern found here would agree well with a bow-shock oriented at about 30° East-of-North, which would be consistent with the source proper motions and the Northern Arm flow here. The polarization pattern is less symmetric than that found for IRS 1W, and the uncertainties are larger, but these findings seem to confirm the suggestion of Tanner et al. (2005) that the bright region in the south-east is indeed not the apex of the bow-shock.
The total polarization measured in the Ks- and Lp-band supports this argument as well: an intrinsic polarization angle perpendicular to the bow-shock angle would be expected, and therefore the observed angles of -52° respectively -67° would indicate a bow-shock angle of about 20-40°.

Flux variability

IRS 10W shows a flux variability in all three bands, but there is no clear periodic behavior (see Fig.8.12). The Ks- and H-band fluxes vary by about ~30%, while the L-band flux only shows

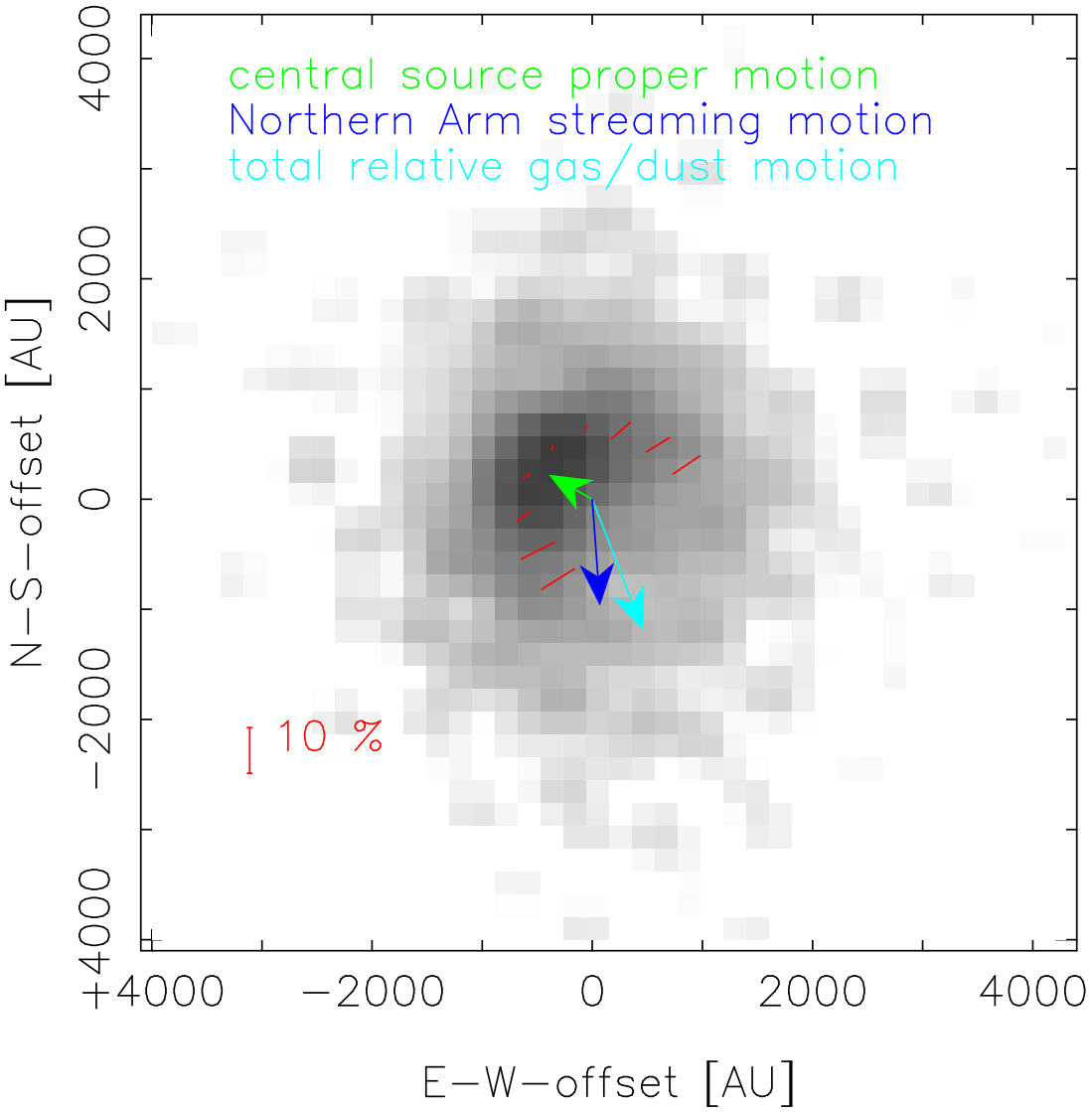

Figure 8.14: Map of the intrinsic Lp-band polarization of the extended source IRS 5. The arrows indicate the proper motions of the central source, the motion of the Northern Arm material and the motion of both relative to each other.

about 10% variability. This is not considered a reliable detection of intrinsic variability, since no systematic trends are visible at the observable timescale. By comparison, IRS 10E* shows a strong and clear periodic variability with the flux increasing by a factor of 3 and a period of about 2 years (see Fig.8.13). The variability is correlated in the H-, Ks and Lp-band. This source has been classified as a late-type Mira variable by Tamura & Werner (1996), while Ott et al. (1999) label it as a long-period variable. The results obtained here agree with these classifications.

8.2.4 IRS 5

Spatially resolved polarimetry

IRS 5 also shows a bow-shock shape in the Ks- and the Lp-band (as found by e.g. Tanner et al., 2005), and the total polarization measured in both bands at least partly agrees with the observed morphology: in the Ks-band, the source shows a total polarization of (5.4 ± 0.5)% at (24 ± 5)°. Most sources in the vicinity seem to exhibit a stronger polarization (see Fig.7.1) on the order of 7.5% at 24°. This yields an intrinsic polarization of (2.1 ± 0.5)% at (-62 ± 5)° for IRS 5. Note that this estimate, however, depends critically on the accuracy of the foreground value.
Looking at the Lp-band, the source also shows a deviation in polarization from the sources

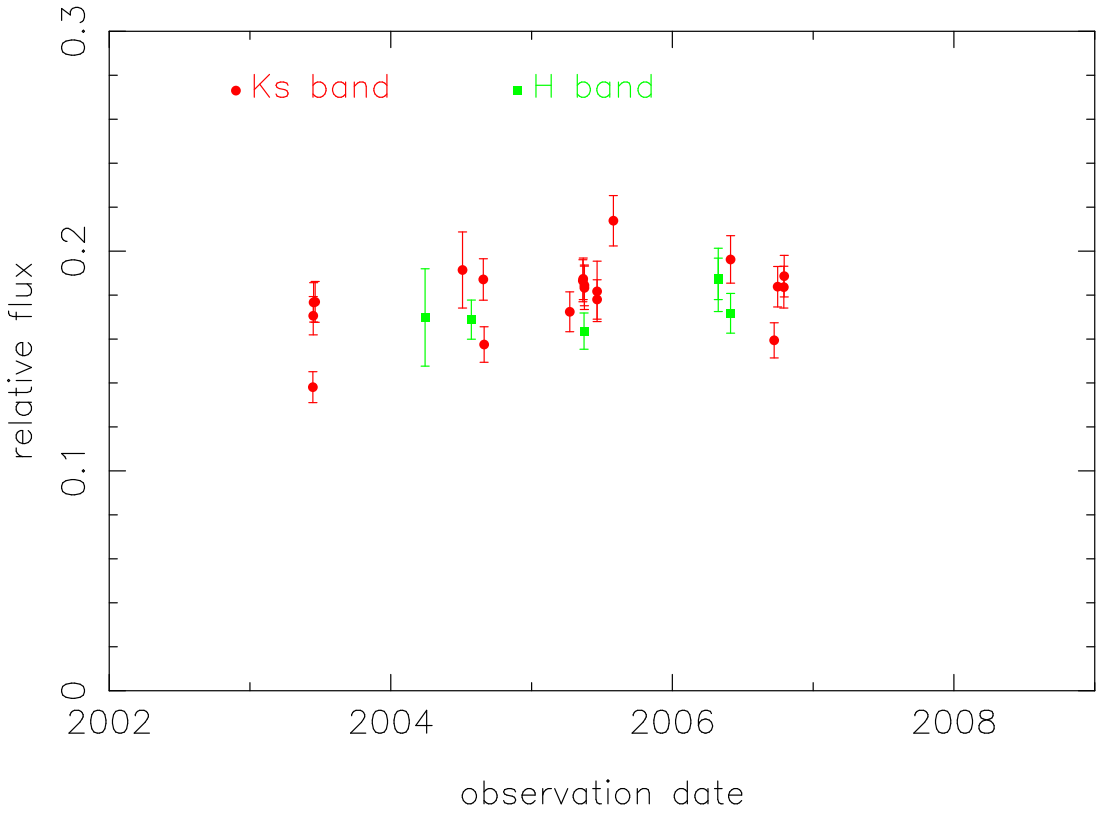

Figure 8.15: Ks-band (red circles), H-band (green squares) and Lp-band (blue open crosses) lightcurves of IRS 5. Shown here is the flux of the source normalized to the flux of non-variable reference sources in the respective band. H-band values were multiplied by a constant factor to match the average Ks-band values.

around it: a value of (1.8 ± 0.5)% at (14 ± 5)° was measured, and with a foreground polarization of 4% at 25° this leads to an intrinsic value of (2.5 ± 0.5)% at (-57 ± 5)°. The angle found here coincides with the Ks-band angle and with the expectations from the observed orientation of the bow-shock, while the polarization degree is increased by a factor of ~1.2 compared to the Ks-band value. This also matches what was found for IRS 1W.
The resolved Lp-band polarization pattern (see Fig.8.14) resembles that of IRS 1W closely, with stronger polarization found in the tails of the bow-shock, a decrease towards the apex and very uniform polarization angles. As for IRS 10W, the Ks-band data quality does not allow spatially resolved polarimetry. The observed pattern in the Lp-band agrees very well with the proper motions of the source and the streaming motion in the Northern Arm, as do the total intrinsic polarization parameters. This suggests that the same mechanism is responsible for the bow-shock polarization as proposed for IRS 1W (see §8.2.1).

Flux variability

IRS 5 also shows a flux increase in the Ks-band between 2002 and 2008 (see Fig.8.15), although the increase is not as strong and clear as that found for IRS 21. The H-band data is much less clear for this source, and while it appears to be variable at that wavelength as well, the variability seems quite erratic. Therefore it cannot be concluded that this is an intrinsically variable source on the observed timescale.

8.2.5 IRS 2

The IRS 2 region, located south of IRS 13 (see e.g. map by Viehmann et al., 2005), is made up of three main bright sources: the extended sources IRS 2L in the north and IRS 2S in the south, and a more compact source between the two, here referred to as IRS 2C. Polarimetric data is only available in the Lp-band for these sources.

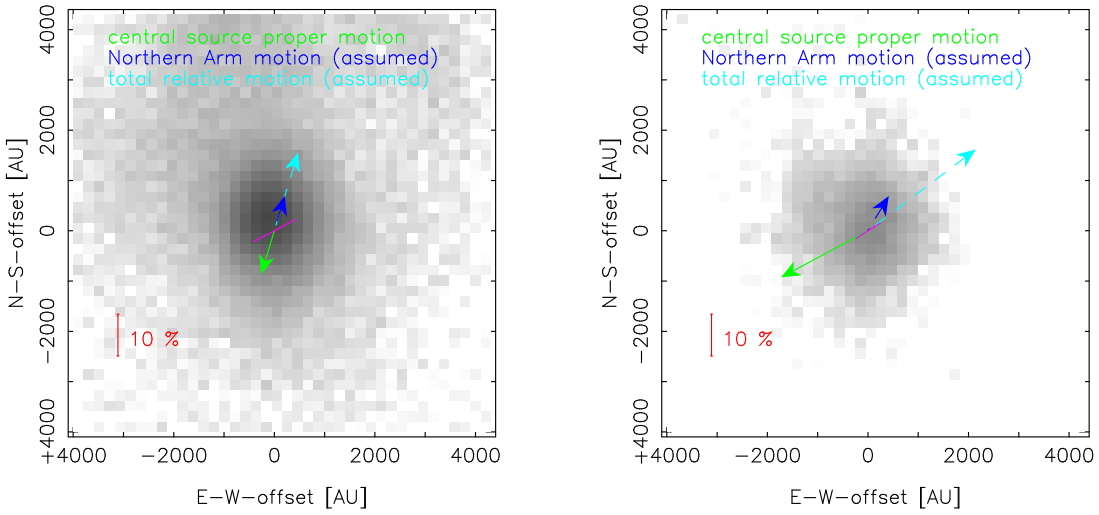

Figure 8.16: Lp-band image of the MIR excess source IRS 2L (left) and IRS 2S (right) after LR deconvolution. The arrows indicate the proper motions of the central source, the (assumed) motion of the local medium and the (assumed) motion of both relative to each other. The magenta line indicates the polarization.

A total polarization of (7.1 ± 0.5)% at (-60 ± 5)° is found for IRS 2L, and with an assumed foreground polarization of 4% at 25° based on neighboring sources, this source shows an intrinsic polarization of (11.1 ± 0.5)% at (-62 ± 5)°. IRS 2S exhibits a weaker total polarization at a similar angle, with (3.2 ± 0.5)% at (-49 ± 5)°. With the same foreground polarization, this leads to an intrinsic value of (6.9 ± 0.5)% at (-58 ± 5)°. IRS 2C, located in projection directly between these two sources, shows only the foreground value and no signs of intrinsic polarization. This can easily be explained if this source simply lies in front of the dust feature that stretches from IRS 13 down to IRS 2, while the other two sources are embedded in this structure and affected by it. This is supported by the shape of the sources in Lp-band images, where IRS 2C appears point-like and the other two are visibly extended. The fact that both other sources show the same polarization angle but different polarization degrees may indicate a different dust column density towards these sources, and indeed it seems as if the dust structure they are embedded in becomes fainter towards the south (see e.g. Fig.4.2).
No direct measurements of the projected velocities of the local medium are available in this region (IRS 2 lies outside of the region where velocities were mapped by Paumard et al., 2004). If the local magnetic field (see Aitken et al., 1998) follows the velocity field as it is the case for the Northern Arm, this would indicate a local streaming motion with an angle of 20-30° to the North-South axis. If these sources are indeed embedded in a structure that is on an infalling orbit around the center (in a way similar to the Northerm Arm), the local streaming motion should be towards the north-west. Fig.8.16 shows an assumed motion of the local medium (of ~120 km/s, dashed blue line), and the resulting relative motion. If these were bow-shock sources, the polarization angle would be expected to be perpendicular to the relative motion, and this is clearly not the case here: for IRS 2L, the observed angle differs by about 45° from the expected value, while for IRS 2S, it is even perpendicular to what would be exptected for a bow-shock. In addition, the observed angles differ about 30° from the MIR angles determined for the extended emission by Aitken et al. (1998). These findings indicate that the observed polarization may be influenced significantly by the local extended dust distribution and the interaction of the central sources with the medium. Without examining the spatial polarization patterns and comparing them over different wavelength bands, it is not possible to determine whether these sources are bow-shocks or not.

8.2.6 IRS 5NE

IRS 5NE, one of the sources east of IRS 5 that where examined in detail by Perger et al. (2008), shows a total Ks-band polarization of (7.4 ± 0.5)% at (13 ± 5)°. The polarization parameters

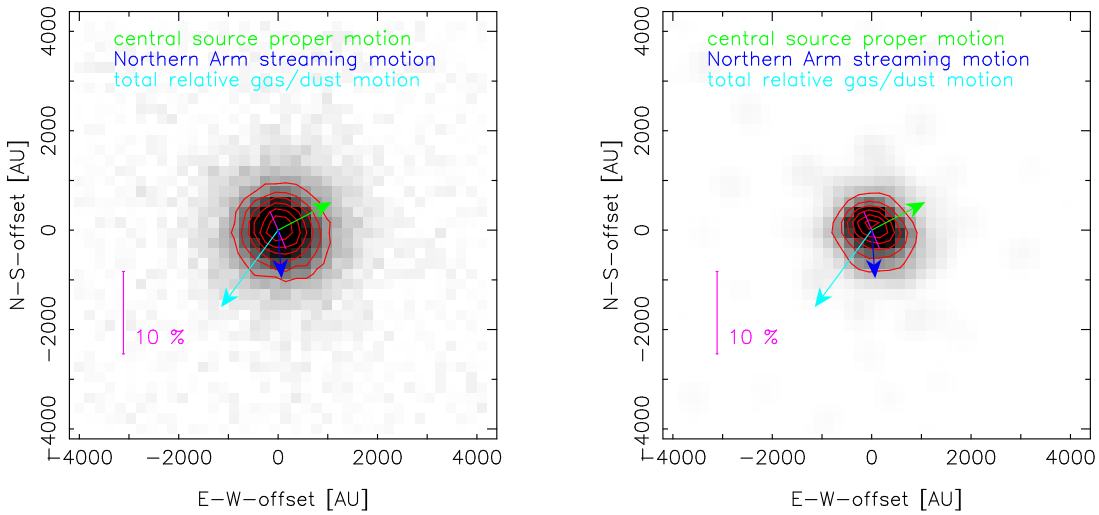

Figure 8.17: Left: Lp-band image of the MIR excess source IRS 5E before LR deconvolution. The arrows indicate the proper motions of the central source, the motion of the Northern Arm material and the motion of both relative to each other. The magenta line indicates the polarization. Right: The same source after LR deconvolution. The elongation of the source, the relative motion vector and the polarization all consistently indicate a bow-shock source. Contours plotted to guide the eye.

agree with the expected foreground polarization (see §8.2.4. In the Lp-band, there appears to be a significant polarization excess, with a total polarization of (8.8 ± 0.5)% at (24 ± 5)° compared to a value of 4% at 25° in the vicinity. This leaves (4.8 ± 0.5)% at (23 ± 5)° of intrinsic polarization. While Perger et al. (2008) described this source as compact with no apparent bow-shock morphology or other extended component, they suggest that the very red color points to the influence of a dust envelope and that candidate sources include a dust-enshrouded low-luminosity AGB star or possibly a young stellar object still in its dust shell. IRS 5NE may thus be a low luminosity variant of the brighter bow-shock sources in the central parsec.
With the higher resolution available here and after a Lucy-Richardson deconvolution, IRS 5NE appears clearly extended in the Lp-band (although no apparent bow-shock shape can be observed, see Fig.8.17). The shape of the source would be marginally consistent with a bow-shock considering its proper motions and the local streaming motion of the Northern Arm (which seems to extend even further eastward than IRS 5 and 10, see Paumard et al., 2004). The intrinsic polarization also suggests a dusty source, and the polarization angle found here is almost perpendicular to the relative motion of the source through the surrounding material (Paumard et al., 2004; Perger et al., 2008) and the observed elongated feature. The source is too faint and the depth of the available data is too low for resolved polarimetry, but the findings mentioned above already make a good case for IRS 5NE being a bow-shock source, similar to IRS 1W and IRS 5.

9 Summary and Conclusions

9.1 Stellar Classification

This newly developed method of stellar classification has confirmed several previously obtained results and has proven to be able to classify sources of known type reliably. It cannot compete with spectroscopic identifications of individual sources, but due to the ability to classify a large number of sources with a relatively small need for observation time, it can provide important statistical information about a stellar population which can later be refined by observing the early type candidates with spectroscopic methods. The analysis presented here extends the sensitivity limit of stellar classification by about 1.5 magnitudes compared to previous works, thus providing a statistically stronger basis for conclusions on the stellar population.
The following results could be obtained:

1. A larger number of early type candidates has been detected than in any previous study, 312 sources compared to the known 90. It was possible to identify known early type sources with 87% accuracy, while 96% of the known late type sources were classified correctly. The different percentages stem from the different selection criteria of the reference sources in the cited publications: Maness et al. (2007) already selected their late type sources by the presence of sufficiently deep CO band heads, which is the same feature that the new method makes use of. The early type sources published by Paumard et al. (2006) were selected based on narrow emission lines that are not visible at the spectral resolution available here.
   These high rates of correct classifications increases the confidence in the presented results, but the new detections need to be confirmed spectroscopically, especially the early type candidates.

2. The spatial distribution of the early type stars follows a power law, with $\beta_{1''} = 1.49 \pm 0.12$, which is flatter than the values of the value of $\beta = -1.8$ that was computed from the data published by Paumard et al. (2006); Lu et al. (2009), but still compatible at the 3σ limit. It is also possible to fit the early type density with a broken power law with $\beta_{1-10''} = -1.08 \pm 0.12$ and $\beta_{10-20''} = -3.46 \pm 0.58$. This broken power law fits the density distribution better than the single power law, but it remains unknown what causes the density drop observed at $\sim$10". The significance of this feature should be examined by further observations that extend to larger distances from Sgr A*.

3. The previously reported flat projected surface density profile of the late type stars in the innermost arcseconds could be confirmed with much higher source numbers and therefore significantly improved statistics. The flat (or even inversed) surface density of late type stars must imply a central *dip or hole* in their 3D distribution. This together with the steep early type density profile explains the observed drop in CO absorption. It has to be emphasized that this result signifies a change in the perception of the nuclear star cluster. Separating the early- and late-type population shows clearly that the GC cluster does *not* have a *cusp* (see discussions in Genzel et al. (2003); Schödel et al. (2007)). To the contrary, the late-type, old stellar population, which appears to make up the vast majority of stars in the GC cluster, shows a flat or even slightly inverted power-law in projection within about 0.2 pc from Sgr A*. These results have recently been confirmed by Do et al. (2009); Bartko et al. (2010). This may indicate that there is some kind of *hole* in the late-type population near the center, as has been pointed out by Figer et al. (2003). The exact cause is still not understood, but various explanations have been suggested. One often discussed possibility is the destruction of the envelopes of giant stars by collisions with main-sequence stars, post-main sequence stars, and stellar remnants in the dense environment near Sgr A* (Rasio & Shapiro, 1990; Davies et al., 1991; Genzel et al., 1996;

Alexander et al., 1999; Davies et al., 1998; Bailey & Davies, 1999; Dale et al., 2008). Another possible explanation for the non-existent cusp of late-type stars is that the cusp may have been destroyed by the infall of a second black hole (Merritt & Szell, 2006) and that there may not have been sufficient time yet to re-grow the cusp. The central parsec might thus not have reached a steady state at all (Merritt, 2010). Tidal disruptions may also play a role in creating a depression in the very center (Madigan et al., 2011).

4. The late type KLF has a power law slope of 0.30±0.01. This resembles closely the KLF that has been measured for the bulge of the Milky Way. This is surprising considering that the nuclear star cluster is probably a dynamically separate entity from the bulge (see Böker et al. (2008) for an overview of the properties of nuclear star clusters in galaxies). It implies a similar star formation history for the NSC and the bulge. The early type KLF has a much flatter slope of (0.14 ± 0.02). The fact that the flatter early type KLF could be confirmed down to a magnitude limit of 15.5 mag is an important extension of previous works that had a completeness limit of ∼13-14 mag. Recent work by Do et al. (2009) confirms this result, while Bartko et al. (2010) fins an even flatter KLF for parts of the early type population. Paumard et al. (2006) claimed that their flat early type KLF agreed best with stellar evolution models using a top-heavy initial mass function (IMF), but did not give a value for the slope of the KLF itself (Fig.13 in that work). The early type KLF found here seems to show a very similar shape down to the magnitude limit and thus also appears to support the proposed top-heavy IMF, but an accurate comparison is not possible due to the lack of a value for the slope in Paumard et al. (2006). Bartko et al. (2010) proposed an extremely top-heavy IMF for the disk stars, while claiming that the off-disk population is matched best with a regular Salpeter-Kroupa IMF.

5. Early type stars have been detected outside of 0.5 pc, in a density that still agrees with the power law density profile in the inner region, so these sources could well be part of the known disk/off-disk population, if the single power law is valid. If the edge observed at ∼10” is a real feature, this may point to a more complicated situation. This result is of course pending spectroscopic confirmation. A larger number of early type sources is detected in the whole cluster with the density distribution following the same power law as in Paumard et al. (2006). This means that the power law found here still agrees with the early type density outside of 0.5 pc, which is higher than the upper limit provided in that work. The new results by Bartko et al. (2010) also show several early type stars outside of the innermost 10”.

6. Both foreground stars and strongly reddened objects could be detected or excluded easily based on their fitted extinction. Unfortunately not all known bow-shock and mini-spiral sources could be observed, due to position and photometric uncertainties.

It is still not decided which one of the two main scenarios serves best to explain the presence of the early type stars in the central half parsec, in-situ formation or infall and dissolution of a cluster formed at several parsecs distance from the GC. Recent publications lean towards favoring the scenario of *in-situ* star formation (e.g. Paumard et al. (2006); Nayakshin & Sunyaev (2005); Bartko et al. (2009). The results obtained in this work also seem to agree best with this model: the steep power law decline of the projected early type density that agrees much better with the R^{-2} power law expected for that scenario than with the $R^{-0.75}$ of the *in-spiraling cluster*. It is important to note that the cluster infall scenario predicts that less massive stars are stripped from the cluster at larger distances (Guerkan & Rasio, 2005). This analysis probes, for the first time, the density of late-O/early B-type stars in the entire central parsec. These stars are less massive than the early-type stars reported from spectroscopic observations (Paumard et al., 2006; Bartko et al., 2009). Although a somewhat flatter power-law for the density of the early-type stars is found here, the improved statistics still imply a steep decrease of the early-type stellar density with distance from Sgr A*. This supports the *in situ* scenario, but it is not possible to clearly rule out or confirm one scenario based on the current data.
Further observations that cover a larger area should be undertaken in the future, as well as spectroscopic confirmations of the new early type candidates. Lu et al. (2009) suggest covering at least the inner 5 pc of the GC, and while observations of such an area require an extreme

amount of time with an instrument like SINFONI, the method presented here may be the key to explore large areas like this for features like tidal tails of an in-falling cluster or a continuation of the early type population of the central parsec.

9.2 Polarimetric results

1. Like several previous polarimetric surveys of the central parsec at much lower resolution, the polarization found in this study follows the Galactic plane in general. This confirms that the polarization can indeed be attributed to aligned dust grains between the Galactic Center and the observer (foreground polarization). However, both systematic and individual deviations from this general pattern are detected. Over the FOV, the polarization degrees and angles seem to change towards the eastern region around IRS 1. This behavior occurs in both both H- and the Ks-band data, with larger relative deviations in the Ks-band. That can be expected if this is indeed a local effect produced by dust grains in the Northern Arm, since typical temperatures and grain sizes in this region lead to a much larger impact of radiation from this grain population at longer wavelengths. This is supported by a systematic change of $\frac{p_H}{p_{Ks}}$ over the FOV, with values of 2.0±0.3 in the center and 1.6±0.3 in the Northern Arm region. The larger one of these values leads to a polarization maximum at $\sim 0.7\mu$m, which matches previous findings of $\lambda_{max} \sim 0.8\mu$m by Bailey et al. (1984), based on JHK observations of a larger region in the GC. This value represents dust parameters, specifically typical grain sizes, and it can be expected that local contributions by distinct dust masses lead to a different value than the average along the LOS. Unfortunately, no further constraints for the local dust can be derived based only on these two bands, other than that the dust grains responsible for the local effects must be elongated and aligned (see Aitken et al., 1998), and that their temperature and size must be sufficient for their influence in the H/Ks-band.

2. A correlation between the spatially variable extinction towards the central parsec and the polarization efficiency, $\frac{p_\lambda}{A_\lambda}$ is found. This relation appears to be different for the two groups of sources detected in the FOV (sources only affected by LOS polarization respectively sources where local contributions are significant): for the foreground-polarized sources, a power law relation with a similar power law index for the H- and the Ks-band ($\beta_H = -0.6 \pm 0.6$, $\beta_{Ks} = -0.4 \pm 0.4$) can be fitted. This is compatible with the measurements respectively the model by Jones (1989), who assume a combination of a constant and a random component of the galactic magnetic field along the LOS to align the dust grains. For the population of higher polarized sources, a higher polarization efficiency in general is measured, while the power law index for both bands resembles that of the sources with lower polarization (with $\beta_H = -0.4 \pm 0.7$ and $\beta_{Ks} = -0.5 \pm 1.5$, although it has to be cautioned that these fits are poor due to the small number of sources). The higher polarization efficiency points to the influence of local dust grains, which only contribute a small amount to the total extinction. But since these grains are aligned, they add a significant component to the total polarization, since this alignment is not (partially) compensated by averaging over other dust populations with different alignment as it is the case for every individual dust configuration along the LOS. These findings further support the previous conclusion that the influence of local dust is quite significant not only in the MIR, but also in the H- and Ks-band.

3. For the first time, Lp-band polarimetry was conducted with an 8m telescope, yielding polarization parameters for 84 sources brighter than 11 mag in the central parsec. The results confirmed the findings by Jones (1990) of a deviation in the Lp-band from the NIR wavelength dependency of the foreground polarization based on a much larger number of sources.

4. Intrinsic polarization takes place in several sources in the central parsec, not only at longer wavelengths as shown first by Knacke & Capps (1977), but also in the H- and Ks-band (e.g. Ott et al., 1999). Using the Müller calculus, the intrinsic component can be isolated for point sources and maps of extended features. The resulting total intrinsic polarization

angles for several known extended sources such as IRS 1W, IRS 5, IRS 10W and IRS 21 agree very well with what can be expected from source morphology and relative motion of gas/dust in the northern Arm and the sources themselves. Very similar intrinsic polarization degrees are measured for IRS 1W and IRS 21, with (7.8 ± 0.5) % at (-75 ± 5)° for IRS 1W and (6.1 ± 0.5) % at (5 ± 5)° for IRS 21 (both Ks-band). Contrary to the wavelength dependency seen in the foreground polarization, the H-band polarization degree is slightly lower for IRS 1W compared to the Ks-band: (6.9 ± 0.5) % at (-73 ± 5)°. The fact that the central source contributes a larger amount of flux in the H-band compared to the extended component, while the intrinsic polarization mostly stems from the bow-shock, explains this discrepancy.
In the Lp-band, the intrinsic polarization degree of these two sources deviates considerably (while the angles are still very similar): IRS 21 shows a much stronger Lp-band polarization of (15 ± 0.5)% than IRS 1W with (8.9 ± 0.5)%. This may be an effect of a much higher dust density and therefore higher optical depth towards the former source.
The spatially resolved intrinsic polarization patterns of the bright extended sources in the FOV do not show a centrosymmetric shape as it would be expected for Mie scattering on spherical grains. Instead, the pattern found for IRS 1W suggests that scattering on aligned elongated grains must play a significant role, possibly combined with thermal dust emission (in the Ks-band), since the grains in the bow-shocks may reach temperatures on the order of 1000 K (see Moultaka et al., 2004). Both effects would produce polarization parallel to the long axis of the grains and thus perpendicular to their angular momentum. It therefore appears that the angular momentum of the grains in the bow-shock surrounding IRS 1W is aligned parallel to the relative motion of the source through the Northern Arm material. Taking the magnetic fields in the Northern Arm into account, this is most likely due to the field lines being warped around the flanks of the bow-shock. This in turn compresses the field lines and thus increases the local field strength, which is then sufficient for fast magnetic alignment of the grains.
For IRS 21, a different polarization pattern is detected. It appears that the polarization vectors are mostly parallel to the relative motion of the source through the surrounding material. Combined with the local field orientation, this again leads to the same dominant mechanism of scattering/emission as for IRS 1W, if it is assumed that the field lines are compressed in front of the shock that is moving perpendicular to them. The patterns found in the Lp-band agree with the Ks- and H-band measurements.

5. IRS 5 and IRS 10W show a relation between Ks- and Lp-band polarization similar to what was found for IRS 1W (at lower total polarization degrees). It seems that the intrinsic polarization degree in both bands declines from IRS 1W to IRS 5, with IRS 10W inbetween. This may point to a decrease in grain alignment (and therefore magnetic field strength?) from south to north along the Northern Arm, but drawing such conclusions based on only three data-points is risky at best. The resolved patterns also resemble that found for IRS 1W, and they also agree well with the observed proper motions and the streaming motion of the local medium, so it appears that the same mechanism is at work there.

6. After deconvolution, IRS21 clearly does not show a circular shape in the Ks-band. Instead, its shape is consistent with that of a poorly resolved bow-shock with its apex north of the central source. This is consistent with the Lp-band shape presented by Tanner et al. (2004) and the expectations from the proper motions of the source in relation to the streaming motion of the Northern Arm. The standoff distance is measured as ~400 AU, and this agrees with the upper limit given by Tanner et al. (2002). It is difficult to constrain the nature of the central source by this parameter alone, and most stellar types with strong winds, such as Wolf-Rayet stars, would be likely candidates (see Tanner et al., 2002).

7. Of the MIR excess sources contained in the observed FOV, only IRS 5NE, IRS 2L and IRS 2S seem to show significant intrinsic polarization (IRS 9, for instance, is apparently purely foreground-polarized). Considering the known proper motions of these sources and the known (or in case of the IRS 2 sources, assumed) streaming velocities of the local medium, the polarization of IRS 5NE would agree very well with a lower luminosity

version of the bow-shocks observed in IRS 1W, 5 and 10W, while no clear conclusions can be drawn for the IRS 2 sources. The latter may show an influence of local dust emission in addition to their own interaction with the medium. It may thus be possible to use Lp-band polarimetry as a tool to indentify possible, unresolved bow-shocks, and especially to distinguish them from disk-like dust configurations as they would be expected for YSOs.

8. Several bow-shock sources in the central parsec show a flux variability: IRS 21 shows a flux increase of ~50% over 6 years in the H- and Ks-band (less, but still significant in the Lp-band). Especially the H-band measurement indicates that this variability must be intrinsic to the central source and not only to the envelope. The candidates suggested for the central source by Tanner et al. (2002) could all show such a variability, especially a source that is currently in a mass-losing phase.
   While a possible flux variability is also detected for IRS 5, IRS 1W and IRS 10W in all three bands, no clear periodicity or trend is apparent for these sources at the available time resolution. Therefore it cannot be determined if these sources show a true intrinsic variability or not. The known periodicity of IRS 10E (~2 yrs) in the Ks-band could be confirmed, and the same variability was detected in the H- and Lp-band as well.

Several effects appear to contribute to the observed polarization in the central parsec of the GC, in addition to the foreground polarization. While the latter is dominant in most sources in all three observed wavelength bands, large scale trends and intrinsic effects play a very important role and may be used to further investigate the interstellar medium in the GC as well as possibly very young objects, such as the sources in the IRS 13N cluster. These are the best candidates for recently formed objects in the central parsec, so a confirmation of their nature might provide valuable insight into star formation mechanisms in such a hostile environment as the immediate vicinity of a SMBH.
The recently achieved polarimetric calibration of NACO (Witzel et al., 2011) and the first successful polarimetric Lp-band observations in nearly 30 years offer the possibility to use these tools to further enhance the knowledge of the stellar population and the ISM in the vicinity of Sgr A*.

Bibliography

Aitken, D., Smith, C., Moore, T.,& Roche, P., 1998, MNRAS 299, 743

Alexander, T. 1999, ApJ, 527, 835-850

Alexander, T., & Livio, M. 2004, ApJ, 606, L21

Alexander, T., & Sternberg, A. 1999, ApJ, 520, 137

Allen, D. A., Hyland, A. R., & Hillier, D. J. 1990, MNRAS, 244, 706

Bailey, J., Hough, J. H., & Axon, D. J., 1984, MNRAS 208, 661

Bailey, V. C., & Davies, M., B. 1999, MNRAS, 308, 257-270

Bartko, H., Martins, F., Fritz, T. K., Genzel, R., et al. 2009, ApJ 697, 1741

Bartko, H., Martins, F., Trippe, S., Fritz, T. K., Genzel, R., Ott, T., Eisenhauer, F., et al. 2010, ApJ 708, 834

Becklin, E. E., & Neugebauer, G. 1968, ApJ 151, 145

Becklin, E. E., Mathews, K., Neugebauer, G., & Willner, S. P. 1978, ApJ, 219, 121

Blum, R. D., Sellgren, K., & DePoy, D. L. 1996, AJ, 112, 1988

Blum, R. D., Ramírez, S. V., Sellgren, K., & Olsen, K. 2003, ApJ, 597, 323

Böker, T., et al. 2008, Journal of Physics: Conference Series, Volume 131, Proceedings of ”The Universe Under the Microscope - Astrophysics at High Angular Resolution”, held 21-25 April 2008, in Bad Honnef, Germany. Editors: Rainer Schödel, Andreas Eckart, Susanne Pfalzner and Eduardo Ros, pp. 012043

Böker, T., 2010, IAU Symposium Proceedings, 266, 58-63

Buchholz, R. M., Schödel, R., & Eckart, A. 2009, A&A 499, 483

Capps, R. W., & Knacke, R. F. 1976, ApJ 210, 76

Dale, J. E., Davies, M. B., Church, R. P., & Freitag, M. 2008, MNRAS 393, 1016

Davidge, T. J., Simmons, D. A., Rigaut, F., Doyon, R., & Crampton, D. 1997., AJ, 114, 2586

Davies, M. B., Benz, W., & Hills, J. G. 1991, ApJ, 381, 449-461

Davies, M. B., Blackwell, R., Bailey, V. C., & Sigurdsson, S. 1998, MNRAS, 301, 745-753

Davis, L., & Greenstein, J., 1951, ApJ 114, 206

Diolaiti, E., Bedinelli, O., Bonaccini, D. Close, L., Currie, D., & Parmeggiani, G. 2000, A&A Supplement Series, vol. 147 (no. 2), Editions de Physique, p335

Do, T., Ghez, A. M., Morris, M. R., Lu, J. R., Matthews, K., Yelda, S., & Larkin, J. 2009, ApJ 703, 1323

Draine, B. T., Interstellar extinction in the infrared (Infrared Spectroscopy in Astronomy, Proceedings of the 22nd Eslab Symposium held in Salamanca, Spain, 7-9 December, 1988. Edited by B.H. Kaldeich. ESA SP-290, European Space Agency, 1989, p.93), 93-+

Eckart, A., Genzel, R., Hofmann, R., Sams, B. J., & Tacconi-Garman, L. E. 1993, ApJ 407, 77

Eckart, A., Genzel, R., Hofmann, R., Sams, B. J., & Tacconi-Garman, L. E. 1995, ApJ 445, 23

Eckart, A., Ott, T., Genzel, R., & Lutz, D. 1999, Proceedings IAU Symposium No. 193

Eckart, A., Genzel, R., Ott, T., & Schödel, R. 2002, MNRAS, 331, 917

Eckart, A., Baganoff, F. K., Morris, M., et al. 2004a, A&A 427, 1

Eckart, A., Moultaka, J., Viehmann, T., Straubmeier, C., & Mouawad, N. 2004b, ApJ, 602, 760

Eckart, A., Baganoff, F. K., Schödel, R., et al. 2006, A&A 450, 535

Eisenhauer, F., Genzel, R., Alexander, T., et al. 2005, ApJ 628, 246-259

Figer, D., Gilmore, D., Sungsoo, S., Morris, M., Becklin, E. E., McLean, I., Gilbert, A., Graham, J., Larkin, J., Levenson, N., & Teplitz, H. 2003, ApJ, 599, 1139-1156

Figer, D. F., Rich, R. M., Sungsoo, S. K., Morris, M., & Serabyn, E. 2004, ApJ, 601, 319

Freitag, M., Dale, J. E., Church, R. P., & Davies, M. B. 2008, Proceedings IAU Symposium No. 245, 2007

Fritz, T. K., Gillessen, S., Dodds-Eden, K., Lutz, D., Genzel, R., Raab, W., Ott., T., Pfuhl, O., Eisenhauer, F., & Yusef-Zadeh, F. 2011, arXiv:1105.2282v2

Geballe, T. R., Rigaut, F., Roy, J.-R., & Draine, B. T. 2004, ApJ, 602, 770

Geballe, T. R., Najarro, F., Rigaut, F., & Roy, J.-R. 2006, ApJ, 652, 370-375

Genzel, R., Thatte, N., Krabbe, A., Kroker, H., & Tacconi-Gharman, L. E., 1996, ApJ, 472, 153

Genzel, R., Schödel, R., Ott, T., Eisenhauer, F., et al. 2003, ApJ, 594, 812

Gerakines, P. A., Whittet, D. C. B., & Lazarian, A. 1995, ApJ 455, 171

Gerhard, O., 2001, ApJ, 546, L39

Gezari, D. 1992, in Blitz L., ed., The Center, Bulge and Disk of the Milky Way, Kluwer, Dordrecht, p.23

Ghez, A. M., Duchêne, G., Matthews, K., Hornstein, S. D., Tanner, A., et al. 2003, ApJ 586, L127

Ghez, A. M., Salim, S., Hornstein, S. D., Tanner, A., Morris, M., Becklin, E. E., & Duchene, G. 2005, ApJ 620, 744

Ghez, A. M., Salim, S., Weinberg, N. N., Lu, J. R., Do, T., Dunn, J. K., Matthews, K., Morris, M., Yelda, S., Becklin, E. E., Kremenek, T., Milosavljevic, M., & Naiman, J. 2008, ApJ 689, 1044

Gillessen, S., Eisenhauer, F., Trippe, S., Alexander, T., Genzel, R., Martins, F., & Ott, T. 2009, ApJ 692, 1075

Gold, T., Nature 169, 322

Goodman, J. 2003, MNRAS 339, 937

Gosling, A. J., Bandyopadhyay, R. M., & Blundell, K. M., 2009, MNRAS 394, 2247

Groenewegen, M. A. T., Udalski, A., & Bono, G. 2008, A&A 481, pp.441-448

Guerkan, M. A. & Rasio, F. A., 2005, ApJ 628, 236

Gustafson, M., Ravkilde, T., Kristensen, L. E., Cabrit, S., Field, D., & Pineau des Forêts, G. 2010, A&A 513, 5

Haller, J. W., & Rieke, M. J., Rieke, G. H., Tamblyn, P., Close, L, & Melia, F. 1996, ApJ 456, 194

Heilis, C. 1987, in Interstellar Processes, ed. D Hollenbach and H. Thronson (Boston:Reidel), p.171

Holland, S., et al. 1998, AJ 115, 1916-1920

Jones, T. J. 1989, ApJ 346, 728

Jones, T. J. 1990, AJ, Vol. 99, Number 6, 1894

Kim, S. S. & Morris, M., 2003, ApJ 597, 312

Kim, S. S., Figer, D. F. & Morris, M., 2004, ApJ 607, L123

Knacke, R. F., & Capps, R. W. 1977, ApJ 216, 271

Kobayashi, Y., Kawara, K., Kozasa, T., Sato, S., & Okuda, H., 1980, Publ. Astron. Soc. Japan 32, 291

Krabbe, A., et al. 1995, ApJ 447, L95

Lacy, J. H., Achtermann, J. M., & Serabyn, E., 1991, ApJ 380, L71

Lazarian, A., 2003, Journal of Quantitative Spectroscopy & Radiative Transfer, v.79-80, p.881.

Lazarian, A., & Hoang, T., 2007, MNRAS 378, 910

Lebofsky, M. J., Rieke, G. H., Deshpande, M. R., & Kemp, J. C., 1982, ApJ 263, 672

Lebofsky, M. J., & Rieke, G. H. 1987, AIP Conf. 155, The Galactic Center, ed. D. C. Backer (New York:AIP), 79

Levin, Y. & Beloborodov, A. M., 2003, ApJ 590, L33

Lowe, K. T. E., & Gledhill, T. M., 2007, MNRAS 374, 176

Lu, J. R., Ghez, A. M., Hornstein, S. D., Morris, M. R., & Becklin, E. E., 2005, ApJ 625, L51-L54

Lu, J. R., Ghez, A. M., Hornstein, S. D., Morris, M. R., Becklin, E. E., & Matthews, K., 2009, ApJ 690, 1463

Lucas, P. W., & Roche, P. F., 1998, MNRAS 299, 699

Lucy, L. B. 1974, AJ 19, 745

Madigan, A.-M., Hopman, C., & Levin, Y. 2011, ApJ 738, 99

Maillard, J. P., Paumard, T., Stolovy, S. R., & Rigaut, F. 2004, A&A 423, 155-167

Maness, H., Martins, F., Trippe, S., Genzel, R., et al. 2007, ApJ 669, 1024-1041

Martin, P. G., & Whittet, D. C. B., 1990, ApJ 357, 113

Martins, F., Genzel, R., Hillier, D. H., Eisenhauer, F., Paumard, T., et al. 2007, A&A 468, 233-254

Mathis, J. S. 1986, ApJ 308, 281

McMillan, S. L. W. & Portegies Zwart, S. F., 2003, ApJ 596, 314

Merritt, D. 2010, ApJ 718, 739

Merritt, D., & Szell, A. 2006, ApJ 648, 890-899

Meyer, L. Schödel, R., Eckart, A., et al. 2006, A&A 460, 15

Milosavljevic, M. & Loeb, A., 2004, ApJ 604, L45

Mishchenko, M. I., Travis, L. D., & Macke, A. 2000, in: Light Scattering by Nonspherical Particles, ed. M. I. Mishchenko, J. W. Hovenier, & L.D. Travis (San Diego: Academic), 147

Morris, M. 1993, ApJ 408, 496

Morris, P. W., Eenens, R. P. J., Hanson,. M. M., Conti, P. S., & Blum, R. D. 1996, ApJ 470, 597

Moultaka, J., Eckart, A., Viehmann, T., Mouawad, N., Straubmeier, C., Ott, T., & Schödel, R. 2004, A&A 425, 529

Moultaka, J., Eckart, A., Schödel, R., Viehmann, T., & Najarro, F. 2005, A&A 443, 163

Moultaka, J., Eckart, A., & Schödel, R. 2009, ApJ 703, 1635

Murakawa, K. 2010, A&A 518, 63

Muzic, K., Schödel, R., Eckart, A., Meyer, L., & Zensus, A. 2008, A&A 482, 173-178

Najarro, F., Hillier, D. J., Kudritzki, R. P., Krabbe, A., Genzel, R., Lutz, D., Drapatz, S., & Geballe, T. R. 1994, A&A 285, 573

Najarro, F., Krabbe, A., Genzel, R., Lutz, D., Kudritzki, R. P., & Hillier, D. J. 1997, A&A 325, 700

Nayakshin, S. & Cuadra, J., 2005, A&A 437, 437

Nayakshin, S., & Sunyaev, R. 2005, MNRAS 364, L23-L27

Nishiyama, S., Nagata, T., Tamura, M., Kandori, R., Hatano, Sato, S., & Sugitani, K. 2008, ApJ 680, 1174

Nishiyama, S., Tamura, M., Hatano, H., Kanai, S., Kurita, M., Sato, S., et al., 2009, ApJ 690, 1648

Nishiyama, S., Hatano, H., Tamura, M., Matsunaga, N., Yoshikawa, Z., et al. 2010, ApJ 722, 23

Ott, T., Eckart, A., & Genzel, R. 1999, ApJ 523, 248

Paumard, T., Maillard, J. P., Morris, M., & Rigaut, F. 2001, A&A 366, 466-480

Paumard, T., Maillard, J.-P., & Morris, M. 2004, A&A 426, 81

Paumard, T., Genzel, R., Martins, F., et al. 2006, ApJ 643, 1011-1035

Perger, M., Moultaka, J., Eckart, A., Viehmann, T., Schödel, R., & Muzic, K. 2008, A&A 478, 127

Portegies Zwart, S. F., McMillan, S. L. W., & Gerhard, O., 2003, ApJ 593, 352

Pott, J.-U., Eckart, A., Glindemann, A., Schödel, R., Viehmann, T., & Robberto, M. 2008, A&A 480, 115

Purcell, E.M., & Spitzer, L., 1971, ApJ 167, 31

Rafelski, M., Ghez, A. M., Hornstein, S. D., Lu, J. R., & Morris, M. 2006, ApJ 659, 1241-1256

Rasio, F. A., & Shapiro, S. L. 1990, ApJ 354, 201-210

Reid, M. J. 1993, ARA&A 31, 345-372

Reid, M. J., & Brunthaler, A. 2004, ApJ 616, 872

Rieke, G. H., Rieke, M. J., & Paul, A. E. 1989, ApJ 336, 752

Schödel, R., et al. 2002, Nature, 419, 694

Schödel, R., Ott, T., Genzel, R., Eckart, A., Mouawad, N., & Alexander, T. 2003, ApJ 596, 1015

Schödel, R., Eckart, A., Alexander, T., et al. 2007, A&A 469, pp.125-146

Schödel, R., Merritt, D., & Eckart, A., A&A 502, 91

Schödel, R. 2010a, A&A 509, 58

Schödel, R., Najarro, F., Muzic, K., & Eckart, A. 2010b, A&A 511, 18

Schödel, R. 2010c, The Galactic Center: a Window to the Nuclear Environment of Disk Galaxies. Proceedings of a workshop held at Shanghai, China on October 19-23, 2009. Edited by Mark R. Morris, Q. Daniel Wang, and Feng Yuan. San Francisco: Astronomical Society of the Pacific, 2011, p.222

Scoville, N. Z., Stolovy, S. R., Rieke, M., Christopher, M. & Yusef-Zadeh, F. 2003, ApJ, 594, 294

Sellgren, K, McGinn, M. T., Becklin, E. E., & Hall, D. N. 1990, ApJ 359, 112

Serkowski, K., Mathewson, D. S., & Ford, V. L., 1975, ApJ 196, 261

Smith, C. H., Aitken, D. K., & Roche, P. F. 1990, MNRAS 246, 1

Tamura, M., & Werner, M. W. 1996, ApJ 467, 645

Tanner, A., Ghez, A. M., Morris, M., et al. 2002, ApJ 575, 860

Tanner, A., Ghez, A. M., Morris, M., & Becklin, E. E. 2003, ASN 597-603

Tanner, A., Ghez, A. M., Morris, M., & Becklin, E. E. 2004, AN 324, No. S1, 597

Tanner, A., Ghez, A. M., Morris, M., & Christou, J. C. 2005, ApJ 624, 742

Tiede, G. P., Frogel, J. A., & Terndrup, D. M. 1995, AJ 110, 2788

Trippe, S., Gillessen, S., Gerhard, O. E., Bartko, H., Fritz, T. K., Maness, H. L., Eisenhauer, F., Martins, F., Ott, T., Dodds-Eden, K., & Genzel, R. 2008, A&A 492, 419

van Marle, A. J., Meliani, Z., Keppens, R., & Decin, L. 2011, ApJ 734, L26

Viehmann, T., Eckart, A., Schödel, R., Moultaka, J., Straubmeier, C., & Pott, J.-U., A&A 433, 117

Wallace, L., & Hinkle, K. 1997, ApJS v.111, p445

Whitney, B. A., & Wolff, M. J. 2002, ApJ 574, 205

Whittet, D. C. B., Martin, P. G., Hough, J. H., Rouse, J. A., Bailey, J. A., & Axon, D. J. 1992, ApJ 386, 562

Whittet, D. C. B., Hough, J. H., Lazarian, A., & Hoang, T. 2008, ApJ 674, 304

Witzel, G., Eckart, A., Buchholz, R. M., et al., 2011, A&A 525, 130

Zamaninasab, M., Eckart, A., Witzel, G., Dovciak, M., Karas, V., Schödel, R., et al. 2010, A&A 510, 3

Zhu, Q., Kudritzki, R., Figer, D., Najarro, F., Merritt, D. 2008, ApJ 681, 1254-1278

Zoccali, M., et al. 2003, A&A, 399, 931

Acknowledgements

I would like to thank everybody who supported me during my work on this thesis. First and foremost, my thanks go to Prof. Dr. Andreas Eckart for the opportunity to work on this fascinating topic under his supervision, and especially for the unique working atmosphere in the 'aegroup'. I am very grateful as well to Dr. Rainer Schödel, now in Granada, who provided valuable comments and reviews (not only) to my first publications, and whose suggestions got me back on the right track a few times.
I also have to thank the entire 'aegroup', who of course contributed to the working atmosphere mentioned above, and who were always open for discussions not only about work, but far beyond. For many helpful suggestions and comments (and also really interesting off-topic discussions), I would especially like to thank Gunther Witzel, Mohammad Zamaninasab, Markus Bremer, Jens Zuther, Sebastian Fischer, Constanza Araujo-Hauck, Kora Mužić, and everybody I forgot to mention. Also, my thanks go to Christoph Rauch and Markus Bremer for proof-reading this thesis and their helpful comments.
For generous financial support during my thesis, my thanks go to Renia GmbH, Cologne. Also, I wish to thank the entire ESO-Paranal staff for their support during the March 2011 observations. Last but not least, I would like to thank my friends and my family for their support and encouragement over the past years.

Erklärung

Ich versichere, dass ich die von mir vorgelegte Dissertation selbständig angefertigt, die benutzten Quellen und Hilfsmittel vollständig angegeben und die Stellen der Arbeit – einschliesslich Tabellen, Karten und Abbildungen –, die anderen Werken im Wortlaut oder dem Sinn nach entnommen sind, in jedem Einzelfall als Entlehnung kenntlich gemacht habe; dass diese Dissertation noch keiner anderen Fakultät oder Universität zur Prüfung vorgelegen hat; dass sie - abgesehen von unten angegebenen Teilpublikationen - noch nicht veröffentlicht worden ist sowie, dass ich eine solche Veröffentlichung vor Abschluss des Promotionsverfahrens nicht vornehmen werde. Die Bestimmungen der Promotionsordnung sind mir bekannt. Die von mir vorgelegte Dissertation ist von Prof. Dr. A. Eckart betreut worden.

Köln, den 19. Dezember 2011

(Rainer M. Buchholz)

Teilpublikationen

- *Composition of the galactic center star cluster: Population analysis from adaptive optics narrow band spectral energy distributions*, **R. M. Buchholz**, R. Schödel, A. Eckart, 2009, Astronomy and Astrophysics 499, 483

- *Composition of the galactic center star cluster*, **R. M. Buchholz**, R. Schödel, A. Eckart, 2011, in *The Galactic Center: A Window to the Nuclear Environment of Disk Galaxies*, ASP Conference Series, Vol. 439, ed. by M. Morris, Q. Wang, and F. Yuan

- *Adaptive-optics assisted near-infrared polarization measurements of sources in the Galactic center*, **R. M. Buchholz**, G. Witzel, R. Schödel, A. Eckart, M. Bremer, K. Mužić, 2011, Astronomy and Astrophysics 534, A117

Weitere Publikationen

- *The extreme luminosity states of Sagittarius A**, Sabha, N., Witzel, G., Eckart, A., **Buchholz, R. M.**, Bremer, M., Giessübel, R., Garcia-Marn, M., Kunneriath, D., Mužić, K., Schödel, R., Straubmeier, C., Zamaninasab, M., Zernickel, A., 2010, Astronomy and Astrophysics 512, 2

- *Signatures of strong gravity with GRAVITY*, Eckart, A., Zamaninasab, M., Straubmeier, C., Fischer, S., Araujo-Hauck, C., Garcia-Marin, M., Wiest, M., Witzel, G., **Buchholz, R. M.**, Sabha, N., Mužić, K., Eisenhauer, F., Paumard, T., Yazici, S., Perrin, G., Brandner, W., Perraut, K., Amorim, A., Schöller, M., 2010, Optical and Infrared Interferometry II.

Edited by Danchi, William C., Delplancke, Franoise, Rajagopal, Jayadev K. Proceedings of the SPIE, Volume 7734, pp. 77340X-77340X-11

- *Comet-shaped sources at the Galactic center. Evidence of a wind from the central 0.2 pc* Mužić, K., Eckart, A., Schödel, R., **Buchholz, R. M.**, Zamaninasab, M., Witzel, G., 2010, Astronomy and Astrophysics 521, 13

- *The instrumental polarization of the Nasmyth focus polarimetric differential imager NAOS / CONICA (NACO) at the VLT. Implications for time-resolved polarimetric measurements of Sagittarius A** Witzel, G., Eckart, A., **Buchholz, R. M.**, Zamaninasab, M., Lenzen, R., Schödel, R., Araujo, C., Sabha, N., Bremer, M., Karas, V., Straubmeier, C., Mužić, K., 2011, Astronomy and Astrophysics 525, 130

- *Coordinated Multi-Wavelength Observations of Variable Emission from the Galactic Center*, Eckart, A., Zamaninasab, M., Sabha, N., Garcia-Marn, M., Kunneriath, D., Straubmeier, C., Mužić, K., Witzel, G., Bremer, M., Valencia-Schneider, M., Karas, V., Dovciak, M., Morris, M. R., Baganoff, F., Schödel, R., Moultaka, J., **Buchholz, R. M.**, Duschl, W., Zensus, A., 2011, in: The Galactic Center: a Window to the Nuclear Environment of Disk Galaxies. Proceedings of a workshop held at Shanghai, China on October 19-23, 2009. Edited by Mark R. Morris, Q. Daniel Wang, and Feng Yuan. San Francisco: Astronomical Society of the Pacific, 2011, p.294

- *The near-infrared spectral index of Sagittarius A* derived from Ks- and H-band flare statistics*, Bremer, M., Witzel, G., Eckart, A., Zamaninasab, M., **Buchholz, R. M.**, Schödel, R., Straubmeier, C., Garcia-Marin, M., Duschl, W., 2011, Astronomy and Astrophysics 532, 26

Lebenslauf

Name	Buchholz
Vorname	Rainer Matthias
Geburtsdatum	5. Dezember 1980
Geburtsort	Köln, Deutschland
Familienstand	ledig
Staatsangehörigkeit	deutsch

Schulausbildung

1987 – 1991	Kath. Grundschule Fussfallstrasse, Köln-Merheim
1991 – 2000	Heinrich-Heine-Gymnasium, Köln-Ostheim
Juni 2000	Abitur
2000 – 2001	Wehrdienst bei 6./342. PzGrenBtl, Koblenz

Hochschulausbildung

2001 – 2008	Studiengang Physik an der Universität zu Köln
2007 – 2008	Diplomarbeit am I. Physikalischen Institut der Universität zu Köln: *Composition of the Galactic Center star cluster*
2008 – 2011	Doktorarbeit am I. Physikalischen Institut der Universität zu Köln: *NIR Polarimetry and Stellar Classification in the Galactic Center*
seit 2008	Angestellter der Firma Renia GmbH, Köln